Oxidation of Uranium Dioxide

By

JACEK MICHAL WASIK

School of Physics
UNIVERSITY OF BRISTOL

A dissertation submitted to the University of Bristol in accordance with the requirements of the degree of DOCTOR OF PHILOSOPHY in the Faculty of Science.

SEPTEMBER 2020

Word count: 76 304

Abstract

This thesis investigates the influence of the crystallographic orientation of the UO_2 on the oxidation process and phase transition into U_3O_8. The samples were prepared by DC magnetron sputtering and a new sputtering system was constructed. A new method to produce poly-epitaxial columns of UO_2 with controlled grain size was developed and used. X-ray characterisation of single crystal epitaxial thin films revealed the best long range order for the (001) orientated samples. The truly polycrystalline character of the poly-epitaxial thin films, without preferred orientation, was demonstrated by x-ray diffraction and electron backscatter diffraction.

Utilising these idealised systems, fundamental studies have been conducted to explore the oxidation behaviour of uranium dioxide. The in-situ oxidation studies performed on poly-epitaxial UO_2 revealed a fastest oxidation rate for (001) orientation, in contradiction to the literature data. This discovery was further investigated using single crystal samples. In situ High Temperature-Environmental Scanning Electron Microscopy observations showed disintegration of the UO_2 structure after phase transition to U_3O_8, for the (111) and (110) oriented single crystal, while there was no loss of integrity for the initially (001) oriented structure. Additionally, in-situ X-ray diffraction studies revealed an epitaxial relationship between the (130) plane of U_3O_8, rotated 45°, on the (001) plane of UO_2. This was identified as a topotactical phase transition, with sigmoidal nucleation and growth kinetics.

In conclusion, this thesis has discovered a new epitaxial relationship between the (001) plane of UO_2 and (130) plane of U_3O_8. This match was also attributed to the faster oxidation rate observed for (001) oriented grains in polycrystalline systems, as possibly lower energy is required for phase transition in this oxidation route. This new insight into the oxidation process of the most common nuclear fuel can help improve the efficiency, reliability and safety throughout the nuclear fuel cycle, and might potentially apply to other oxide systems.

ACKNOWLEDGEMENTS

I would like to thank Bristol Alumni for providing funding for this project, and Bristol Centre for Functional Nanomaterials for giving me this opportunity and support throughout the entire project.

I wish to express my special thanks to my supervisor Ross Springell for his guidance, insightful comments, and support. I would like to thank everyone from the Interface Analysis Centre research group especially

- Keith Hallam for his help with general paper work and RA's, as well the discussions over a wide range of topics and explanation of British culture.
- Mattia Cattelan and Neil Fox for the aid at the nanoESCA laboratory.
- Oliver Payton and Loren Picco for their knowledge and advice regarding HS-AFM
- Antonios Banos for general support with SIMS operation and analysis.
- Adel El-Turke, Joseph Sutcliffe and Chris Jones for training and support on the FEG-SEM EBSD, as well for advice on sample polishing process.
- Peter Heard and Siqi He for their support with operation of DB microscope.
- Tom Scott and Natasa Vasiljevic for usefully discussion and advice during my APMs.
- Entire thin film group: Joseph, Sophie, Eleanor, Daniel, Lottie, Angus, Jarrod and Rebecca.

I would like to express my deepest gratitude to the physics mechanical workshop team led by Adrian Crimp for the advice during the design stage, and later for fabrication of the parts without which I wouldn't be able to complete construction of the sputtering system.

I want to thank Renaud Podor form the Institute for Separation Chemistry in Marcoule(ICSM)for his general help with collection of HT-ESEM data. Mark Isaacs from HarwellXPS for support with XPS mapping experiment.

I would like to thank all my office friends Macarena, Chong, Ian, Haris, Antonios, Jonathan, Gareth, Fahed, Ilemona, Siqi and Dimitris for a great time and international lunches. I am very grateful to my family for their support. Finally big thanks to Nadia, who has had motivated and encourage to finish my PhD, for her patience with correcting my misspellings during the write-up, and keeping up with me during the stressfully period of PhD combined with the COVID-19 pandemic.

AUTHOR'S DECLARATION

I declare that the work in this dissertation was carried out in accordance with the requirements of the University's Regulations and Code of Practice for Research Degree Programmes and that it has not been submitted for any other academic award. Except where indicated by specific reference in the text, the work is the candidate's own work. Work done in collaboration with, or with the assistance of, others, is indicated as such. Any views expressed in the dissertation are those of the author.

SIGNED: ..... DATE: .....

TABLE OF CONTENTS

List of Tables

List of Figures

CHAPTER 1

INTRODUCTION

Global energy consumption is predicted to increase every year [1]. The main factors responsible for the energy consumption growth are increase of the population and increase of the energy consumption per head. The current estimation shows that every year population will increase by 83 million people [2]. Furthermore, due to development of electronics, average energy consumption for a single person will increase to power a laptop, a smartphone, a smartwatch, a smartband, smart glasses etc.

A recent mathematical model [3], used to provide future estimates by taking into account factors such as the development and adoption of new technologies to predict energy demand showed that studies assuming near 100% renewable power by 2050 are flawed as they do not sufficiently account for reliability of the supply. The lack of firm backup energy systems , such as nuclear or power plants with carbon capture systems, would lead to so often fails of the power supply system, making it deemed inoperable.

It is very important to meet the demands for energy in an environmentally friendly way. The European Union is trying to increase the contribution of "green" renewable sources by law (30% in 2030) [4]. However, renewable energy depends on weather conditions and time of the day, so an stable source of energy with low carbon emission is required to cover the basics off peak needs for energy. Nuclear power is the perfect candidate as it provides a reliable, carbon-free solution.

Nuclear power plants, according to data from April 2017, are working in 30 countries worldwide with 449 nuclear reactors in total [5]. The number of nuclear power plants will increase, as 60 are curently under construction [6]. In 2014, nuclear power plants produced 11% of the world's electricity. The most nuclear energy is generated in USA, and countries such as: France, Slovakia, Ukraine, Belgium, and Hungary where most than 50% of electricity generation comes from nuclear power plants [5]. Amongst the 50 most polluted cities in Europe 33 are in Poland (the biggest European nation to have never had nuclear power plants), where most energy produced is by coal-based power plants [6, 7].

To produce energy, the nuclear power plant needs fuel, one of the most common fuels is uranium dioxide. Uranium dioxide has been studied for more than 60 years, allowing the safe and economic operation of nuclear power plants. A lot of research was focused on the oxidation process of UO_2, due to its importance throughout the full fuel cycle. This includes uranium mining and storage, behaviour of uranium dioxide during operation in nuclear core, disposal and reprocessing of used fuel.

This chapter will briefly describe the context of the PhD. Firstly the UO_2 fuel cycle process will by described, followed by a description of the fuel material. Higher oxidation states of uranium, with current knowledge about the oxidation process will then be considered, highlighting the influence of the crystallographic structure of uranium dioxide on the oxidation rate, which is the one of main interest points of this thesis. A thin film approach as a surrogate to investigate properties of the bulk material will be then reviewed. Finally an outline of the thesis will be given.

1.1 Nuclear fuel cycle

Uranium is a naturally occurring element formed in supernovae. It is estimated that uranium occurs in the Earth's crust 40 times more often than silver, which makes it almost as common as zinc or tin [8]. Uranium is at low levels in rock or sands, therefore not all deposits are economically optimal for mining. The highest amount of uranium (29% of the world's supply), can be found in Australia, where the high grade ore can have 200 000 ppm of U [9]. A list of countries with their

Country	Tonnes U	Percentage of World
Australia	1,664,100	29%
Kazakhstan	745,300	13%
Canada	509,000	9%
Russian Fed	507,800	9%
South Africa	322,400	6%
Niger	291,500	5%
Brazil	276,800	5%
China	272,500	5%
Namibia	267,000	5%
Mongolia	141,500	2%
Uzbekistan	130,100	2%
Ukraine	115,800	2%
Botswana	73,500	1%
USA	62,900	1%
Tanzania	58,100	1%
Jordan	47,700	1%
Other	232,400	4%

Table 1.1: Recoverable Resources of Uranium 2015

recoverable uranium resources in shown in Tab. 1.1.

Uranium can be excavated in a traditional way like ores of other material. This include underground and open pit mining. Underground mining is used typically to harvest the resources stored deeper than 120m. For resources closer to the surface, pit mining can be applied. In this case huge amounts of ground must be removed in order to uncover the uranium ore and to prevent the pit walls from collapsing.

In 2014 more than a half of the uranium production became mined using a new technique called In Situ Leach (ISL) or In Situ Recovery (ISR). This technique is also known as a solution mining as the underground uranium oxide is dissolved and harvested at the surface in a solution. To leach the uranium generally three solutions are used: hydrogen peroxide (Kazakhstan), hydrogen peroxide with lower concentration together with sulfuric acid as complexing agent (Australia), and alkali leach (USA). The last one is used in USA due to the presence of gypsum and limestone, which consumes high amounts of acid. The factors limiting the use of this technology are permeability of the orebody and the location to prevent contamination of the groundwater.

Once the ore is harvested it needs to be separated from the waste rock, before it is packed and shipped. Then the ore is crushed and ground in a milled to form a fine slurry. Then is leached

using sulfuric acid or alkaline solutions [10]. Apart of extracting uranium from the ore, the leaching agent extracts heavy metals including vanadium, molybdenum, iron, lead, selenium and arsenic. After drying and filtrating a final product called Yellowcake is formed. The Yellowcake contains more than 80% of uranium, and the name comes from the color of the powder produced in early mills, when it was contaminated with $(NH_4)_2U_2O_7$ [11]. Typical yellowcake contains between 70% to 90% of triuranium octoxide (U_3O_8), and other oxides including uranium dioxide (UO_2) and uranium trioxide (UO_3) [12].

Before the uranium from yellowcake can be used in nuclear power plant it has to go through an enrichment process, as it contains only 0.7% of fissile isotope U-235. The rest of it is U-238 (which potentially could be used in fast-neutron reactors) and trace amounts of U-234. Before the enrichment process happens, the milled uranium oxide is converted to one of two substances. When the power plant dos not require enriched fuel, it is converted to uranium dioxide. The second option, used for most of the reactors, is converting the leached U_3O_8 into uranium hexafluoride (UF_6) to make it suitable for the enrichment process.

To convert uranium oxide into uranium hexafluoride two methods can be used, a dry process and a wet process. In the first one, uranium is simply calcined, then agglomerated and crushed. In the wet procces uranium oxide is first dissolved in nitric acid to form $UO_2(NO_3)2.6H_2O$, which goes under countercurrent solvent extraction process in tributyl phosphate dissolved in kerosene or dodecane. To collect uranium the organic extractant is used and washed by weak nitric acid solution and then concentrated by evaporation, after which is calcinated in fluidised bed ractor into UO_3 [9].

Uranium trioxide from the wet process and crushed triuranium octoxide from the dry process are then reduced to uranium dioxide. The reduction is done in hydrogen atmosphere in a kiln, what represents the reactions shown on equation 2.3. After the reduction, UO_2 is treated with hydrogen fluoride (HF) in another kiln to convert into uranium tetrafluoride (UF_4) as shown on equation 2.4. Then the uranium hexafluoride (UF_6) is produced using gaseous fluorine (2.5.

$$U_3O_8 + 2H_2 \rightarrow 3UO_2 + 2H_2O$$

(1.1) $$or$$

$$UO_3 + H_2 \rightarrow UO_2 + H_2O$$

(1.2) $$UO_2 + 4HF \rightarrow UF_4 + 2H_2O$$

(1.3) $$UF_4 + F_2 \rightarrow UF_6$$

The UF_6 can be enriched to required concentration of the fissionable isotope U-235 using isotope separation methods. The most popular are gaseous diffusion (no longer in use [13]) and gas centrifuge, which are physical processes based on mass difference between U-235 and other isotopes [14]. The U-235 atoms are about 1% lighter. New methods for separation are under investigation including aerodynamic process [15], electromagnetic process [16], plasma separation [17] and variety of laser based methods [18].

The gas centrifuge is a very economical method used since 1940s with a big development in the 1970s-80s for nuclear fuels [16]. The UF_6 gas is fed into a vacuum tube with a rotor and spin rapidly. the example of such centrifuge is shown on picture 1.1. That allows heavier isotopes to concentrate at the edge of the cylinder, while the U-235 will be near the center. Use of countercurrent flow set up by a thermal gradient allows to be pulled axially the enriched product with lighter molecules on one side and heavier on another.

Before enriched uranium which is a form of UF_6 can be used in a power plant, it needs to undergo a preparation process. The first step is to convert it back to UO_2 powder. Then uranium dioxide is pressed and sintered at high temperature to form ceramic pellets. The pellets are then stacked inside corrosion resistance tubes forming the so called fuel rods [19]. The full nuclear fuel assemblies are tailored for particular types of reactors, the picture 1.2 shows an example of nuclear fuel assembly for Mitsubishi PWR rector.

Typically fuel is used for 18-36 months. During this time the amount of fission product will increase making it no longer practical to use. In typical used fuel, the concentration of U-235 is

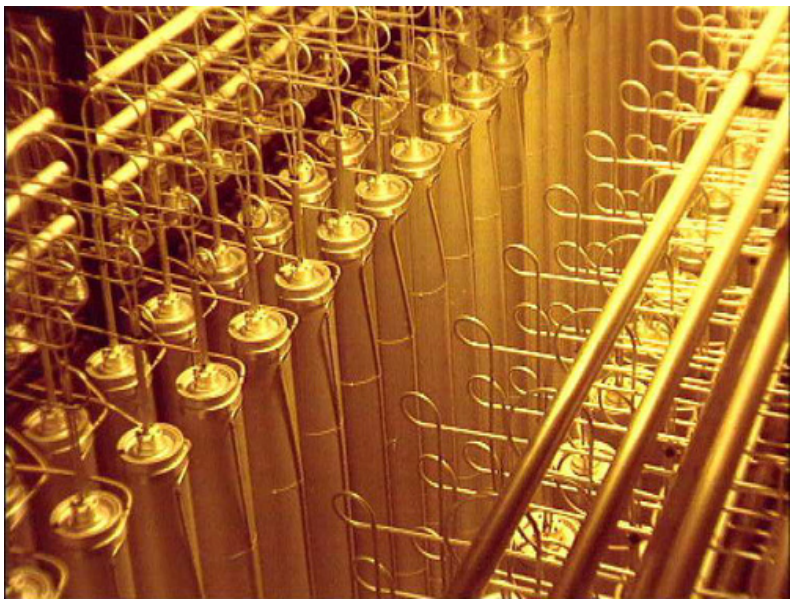

FIGURE 1.1. Uranium centrifuges at the Urenco Group. Figure from [14].

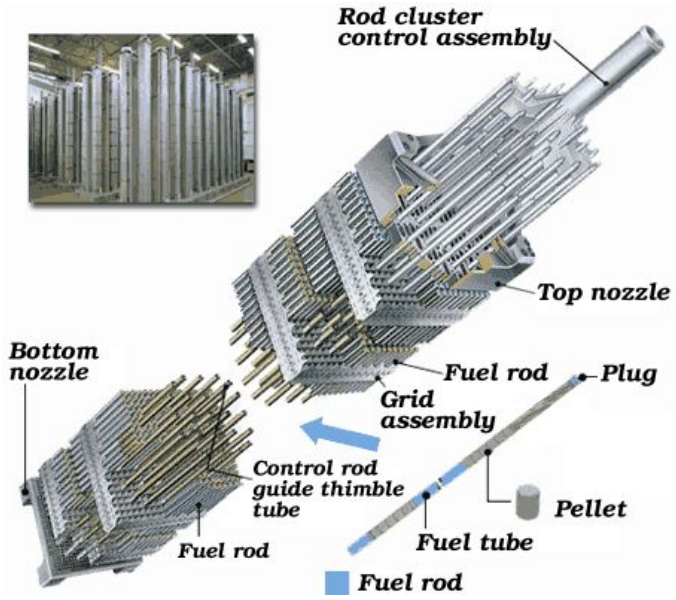

FIGURE 1.2. Mitsubishi PWR nuclear fuel assembly schematic. Figure from [19]

about 1% with 0.6% of fissile plutonium and about 3% of fission products and minor actinides. The most of it is still U-238 (around 95%). The used fuel after being removed from the reactor is transferred inside a storage pond next to the reactor, as it emits radiation and heat. Ponds have water shielding for radiation and also the heat is absorbed by water 1.3.

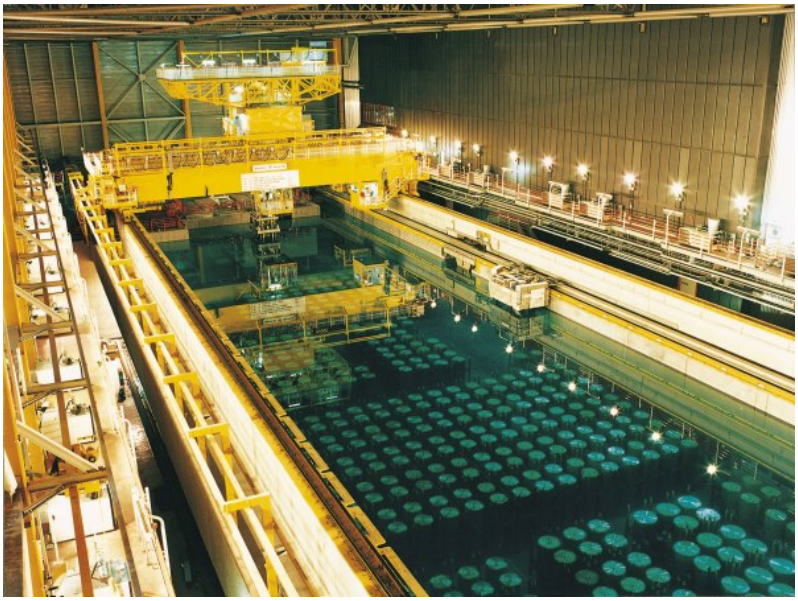

FIGURE 1.3. Storage pond at the UK's Sellafield for the used fuel. Figure from [20].

Used fuel after several months or even years of storing in ponds has two possible paths. It can be reprocessed by recovering fissile and fertile materials or can be prepared for long term storage and final disposal. Recycling used fuels can increase the energy from the original uranium by 25%-30%. It also helps to reduce the amount of materials that needs to be disposed, as well as the radioactivity level of it.

Throughout the fuel cycle, uranium is present in different oxide forms, with UO_2 being the most important. To ensure safe and efficient handling of this material, knowledge about structures and properties as well as oxidation mechanisms are necessary. A brief review is presented in the next section.

1.2 Uranium dioxide

Uranium dioxide has been extensively studied for more than 60 years. This oxide of uranium is naturally occurring as a uranium ore product in the minerals pitchblende and uraninite [21]. The UO_2 exhibits only one structure, the cubic fluorite crystal structure as shown on Fig. 1.4, with an $Fm\bar{3}m$ space group. The arrangement of the uranium atoms is a face centered cubic (fcc), with a lattice parameter a=5.468 Å, the oxygen atoms are on a cubic sublattice with an edge length

of 2.734 Å, which has been confirmed by recent neutron studies [22]. In that arrangement the uranium atom occupy the (0,0,0) position, an the oxygen atoms the $(\frac{1}{4},\frac{1}{4},\frac{1}{4})$.

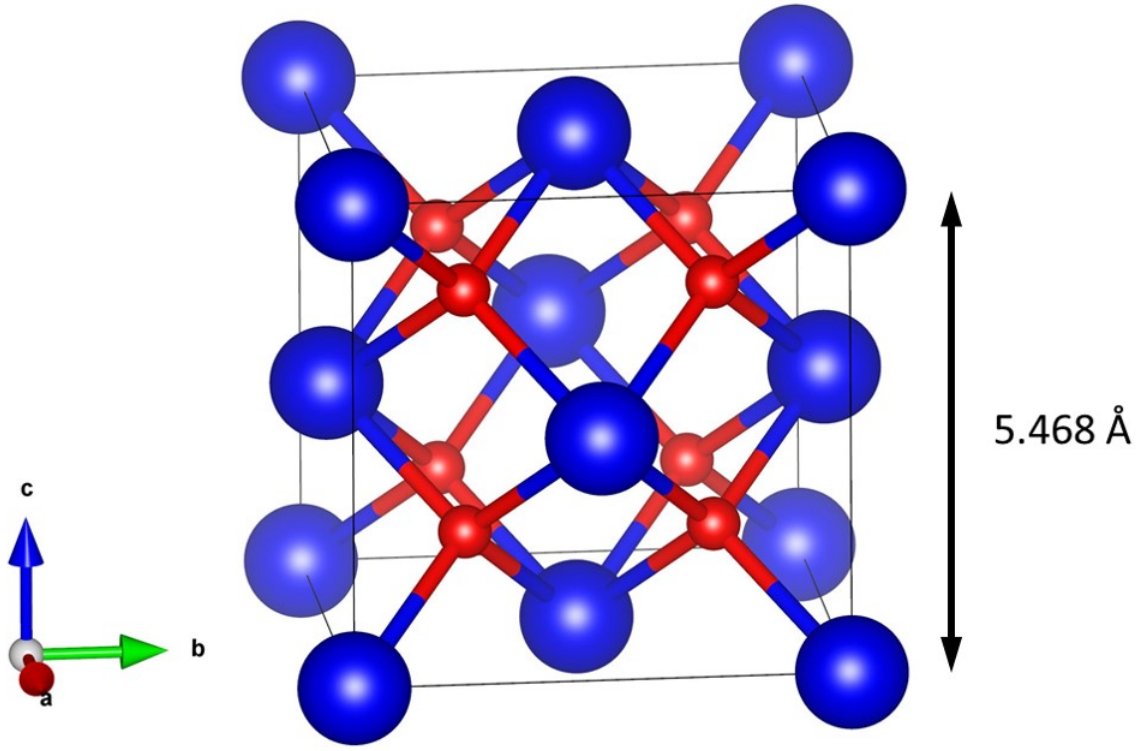

FIGURE 1.4. A diagrammatic representation of the cubic fcc structure of UO_2. Uranium atoms are represented in blue and oxygen atoms in red, arranged in the fluorite structure with lattice parameter 5.468 Å.

The electronic configuration of uranium dioxide is [Rn]$5f^2$, where uranium atoms are in the +4 oxidation state, bonded to two molecules of oxygen. UO_2 is thermodynamically stable, with a melting point at 2865°C. The density of this material is 10.97 g/cm^2 and the average molecular mass is 270.027 g/mol.

The fluorite structure of UO_2 allows it to tolerate a range of stoichiometry from hypostoichiometric to hyperstoichiometric compositions due to its empty octahedral sites which can be occupied by O_2^- ions forming the hyperstoichiometric UO_{2+x}. The lower limit for maintaining the fcc structure is $UO_{1.16}$ at 2447°C, while the upper limit is $UO_{2.25}$ at 1757°C [23].

1.2.1 Higher oxidation states

Uranium is strongly electropositive, therefore readily bounds with oxygen that is strongly electronegative. Oxidation of uranium metal was observed even under UHV conditions (10^{-10} mbar), where an oxide layer was formed within three minutes [24, 25]. Oxides of uranium apart of their application as a nuclear fuel, are also fascinating materials due to their dynamical properties [26], valence orbital configuration [27] and elementary excitations [28].

Uranium possesses multiple oxidation states as shown in Table 1.2. The +2 oxidation state is metastable, and the +3 oxidation state is possible but also very unstable and easily converts to +4. The wide range of the oxidation states of uranium, from +2 to +6, result in the largest number of oxides in the actinide series [23]. Here, only stoichiometric uranium oxide was discussed and hyper-stoichiometric up to U_3O_8 will be discussed, which is the subject of this thesis. The complexity of uranium - oxygen system, that have been studied for more than 60 years, can be seen on Fig 1.5.

Table 1.2: Oxidation states of uranium.

Oxsidation state:	+2	+4	+5	+4/+6	+5/+6	+6
Compound:	UO	UO_2	U_4O_9	U_3O_7	U_3O_8	UO_3

Uranium dioxide can undergo slow oxidation to its hyper-stoichiometric compound even in air at room temperature, over a period of several years [30]. Small changes to surface layer are observed after shorter period of time. Elevated temperature up to 300°C allows for faster incorporated of oxygen into the fluorite lattice [31]. Additional oxygen ions are accommodated at interstitial sites, which results in distortion to the original oxygen positions and creation of vacancies. The fluorite-type arrangement can incorporate oxygen up to $UO_{2.25}$, what is associated with a light volume reduction [31], and formation of U_4O_9.

U_4O_9 exhibits three different phases with temperature [32, 33]. The β phase, which is stable between 65 and 550 °C, of U_4O_9 [34] is shown on Fig. 1.6. The exact composition is actually $U_{128}O_{286}$ [35], but for simplicity and consistency with literature convention in this thesis it will be referred as U_4O_9. The β-U_4O_9 crystallizes in the I43d space group, with lattice parameter a = 21.76 Å. The conventional unit cell is built from a 4 x 4 x 4 repetition of the conventional unit cell of UO_2 [35]. The interstitial oxygens incorporated into this supercell form clusters. The shape

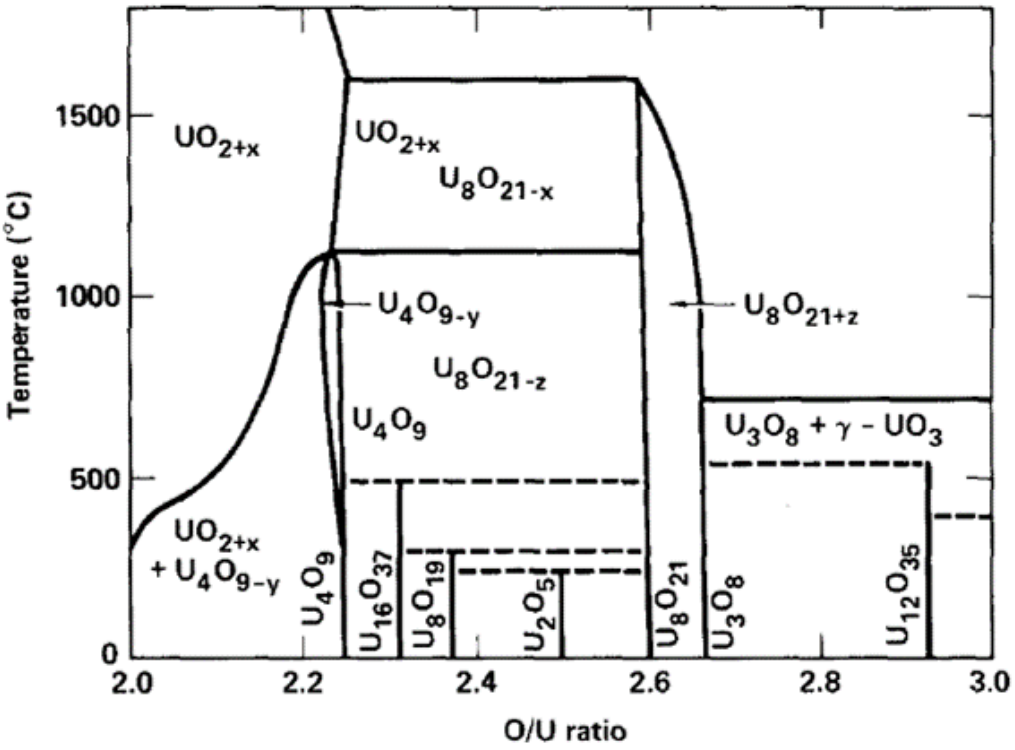

FIGURE 1.5. The phase diagram of UO_2-UO_3. Figure reproduced from [29].

of each cluster is cuboctahedral, composed of 12 oxygen atoms at its corners. The position of eight-atom oxygen cube in the fluorite-type structure is replaced by the cuboctahedron. Therefore structure of β-U_4O_9 is created by incorporating 12 clusters into the 4 x 4 x 4 UO_2 supercell [36]. The α-U_4O_9 structure exists in low temperatures and it is similar to the β phase, where a rhombohedral distortion reduces its space group from I43d to R3c [32]. The high-temperature phase of U_4O_9, γ, is isosymmetric to the described β, with changes in the volume and structure of the cuboctahedra [37].

Further incorporation of oxygen into the fluorite structure of $UO_{2.25}$ leads to creation of additional oxygen clusters and force a lattice distortion to tetragonal symmetry and formation of U_3O_7. The 7/3 ratio system has three polymorphs, the tetragonal α-, β-, and γ-U_3O_7. Polymorphs of U_3O_7 are called distorted phases, due to tetragonal distortions, where the relative changes

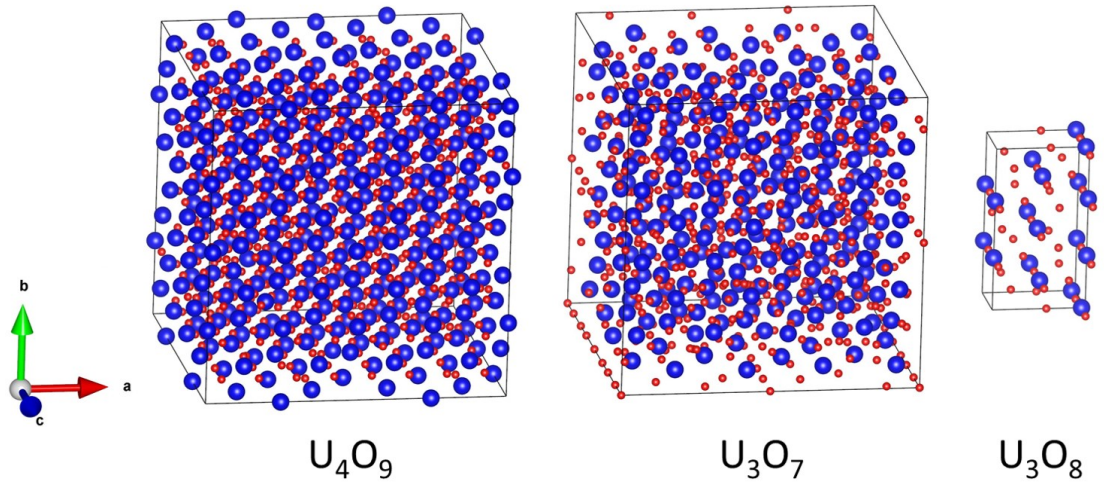

FIGURE 1.6. Crystal structures of the higher uranium oxides observed during oxidation from UO_2 to U_3O_8.From left to right: β-U_4O_9, β-U_3O_7 and α-U_3O_9. Uranium atoms are shown in blue, and oxygen atoms in red.

$|(a\text{-}a_0/a_0|$ and $|(c\text{-}a_0/a_0|$ do not exceed 2% [38]. There are still uncertainties about the structures of U_3O_7, and to classify their polymorphs the axial ratio c/a is used as the main parameter [39]. The structure showed on Fig. 1.6 is the structure of the most common β-U_3O_7 [40–42] [43] [44] [45–48] with c/a ratio 1.03. The lattice parameters a and b are 21.5898 Å, while c is 22,229 Å. The c/a ratio for α-U_3O_7 [39, 42–45] is reported to be close to 0.989, while for the phase γ-U_3O_7 the ratio is c/a = 1.016 [39]. Besides, intermediate U_3O_7 phases with c/a between 1.006 and 1.020 were reported [39, 41, 45, 49]. The phases of U_3O_7 are know to be very dependent on the preparation technique and parameters [39].

As one can see there is a lot of similarities between structures of U_4O_9 and U_3O_7, which makes them difficult to distinguish from one another [31, 39]. This aspect has been addressed in detail by several authors [31, 32, 39, 45, 50–54]. In this thesis, where distinction was not possible, the commonly used term U_3O_7/U_4O_9 will be applied.

The next stable structure formed when uranium binds to additional oxygen is U_3O_8. U_3O_8 exhibits an orthorhombic layered structure with two polymorphs α and β. The structure of α-U_3O_8, observed throughout work in this thesis, is shown on Fig 1.6. The space group of this structure is C2mm, with lattice parameters a= 6.716 Å, b= 11.96 Å, and c = 4.147 Å[55]. The

oxidation state of U_3O_8 is a mixed valence of U(V)/U(VI). The ratio between U(V) and U(VI) was suggested to be 1:2, but more recent studies [56] showed that opposite ratio, 2:1, which seems to be the correct valence state of U_3O_8 [57].

The highest oxidation state of uranium is 6+, observed as UO_3 structure. The UO_3 system has seven polymorphs, this structure will not be described here as only UO_2 - U_3O_8 range is in focus of this thesis. A detailed description can be found in the literature [58–61].

1.2.2 Oxidation mechanism

Understanding the oxidation process of uranium dioxide is very important, because of its relevance to the dry storage and the ultimate disposal of spent fuel [50, 62–67], as well as fuel-recycling processes [68] and UO_2 powder storage [69]. This process has been studied for at least 60 years, providing a lot of information about UO_2, to use it safely as nuclear fuel, but still some questions are unanswered and some uncertainty exists.

The first studies focused on kinetics of the oxidation of uranium dioxide conducted by Aronson et al. [41], showed that oxidation to U_3O_8 is a two step process. In the first step the tetragonal oxide with composition $UO_{2.34\pm0.03}$ is formed, followed by the second step where this structure transforms to orthorhombic U_3O_8. This can be be written as:

$$UO_2 \rightarrow U_3O_7/U_4O_9 \rightarrow U_3O_8 \tag{1.4}$$

The product of the first step is referring the intermediate phase U_3O_7/U_4O_9 where due to previously described reasons, distinction is very difficult. Some earlier studies suggest that metastable U_3O_7 is formed prior to stable U_4O_9 [45]. This was found to not be true by more recent synchrotron studies performed by Rousseau et al. [70] on UO_2 powder at 250°C, where formation of the cubic U_4O_9 phase was observed before β-U_3O_7 was formed. The updated version of Eg. 2.36 proposed by the authors is:

$$UO_2 \rightarrow U_4O_{9-y} \rightarrow \beta - U_3O_7 \rightarrow U_3O_8 \tag{1.5}$$

In addition, kinetics were also studied by Rousseau et al. [70] using a method based on increments of temperature or pressure to verify the assumption of a single-limiting rate. Therefore, if the oxidation rate is defined by:

$$\frac{d\alpha}{dt} = \Phi(T, P_i)E(t) \tag{1.6}$$

where α is a dimensionless fractional conversion function of time, Φ function is a rate per unit area ($m^{-2}s^{11}$) which depends on the nature of the rate-limiting step (diffusion, interface reaction). The function E(t) (m^2 mol^{-1}) corresponds to the extent of the reaction zone where the rate-limiting step is located [70]. The function Φ is time independent, but may be a function of thermodynamic chemical potential of the reacting gases P_i, and temperature T. Therefore, this equation can be verified using a method based on sudden changes of pressure or temperature.

Eq. 1.6 involves the fractional conversion (α) associated with a single reaction step. At least two reaction steps were reported for oxidation of UO_2, without possibility to deduce the fractional conversion of each one separately from the weight gain curves, what lead Rousseau et al. [70] to modify Eq. 1.6 to the variation of mass variation (Δm):

$$\frac{d\Delta m}{dt} = n_0\Phi(T, P_i)E(t) \tag{1.7}$$

where n_0 is a constant with the unity of a mass. This equation was tested by sudden increase of temperature from 250°C to 280°C at different times, t_i, during the oxidation of UO_2 to U_3O_8. Using Eq. 1.7, the rates before (R_1) and after temperature jump (R_r), where calculated at different time points t_i. For the single rate-limiting step assumption the ratio R_r/R_1 are equal to each other for any time t_i.

The data collected by Rousseau et al. [70] is shown on Fig. 1.7, and allowed to distinguish four kinetic domains during the oxidation process of UO_2 to U_3O_8. In the first domain, UO_2 is converted to U_4O_9 and the ratio R_r/R_1 is constant and equal to 1.3. This confirms the single rate -limiting assumption for this transformation. For the second domain, two reactions are occurring simultaneously: remained UO_2 is transformed into U_4O_9, while U_4O_9 is converted to U_3O_7. The ratio of R_r/R_1, due to the presence of three crystalline phases, is evolving from 1.7 to 6 within

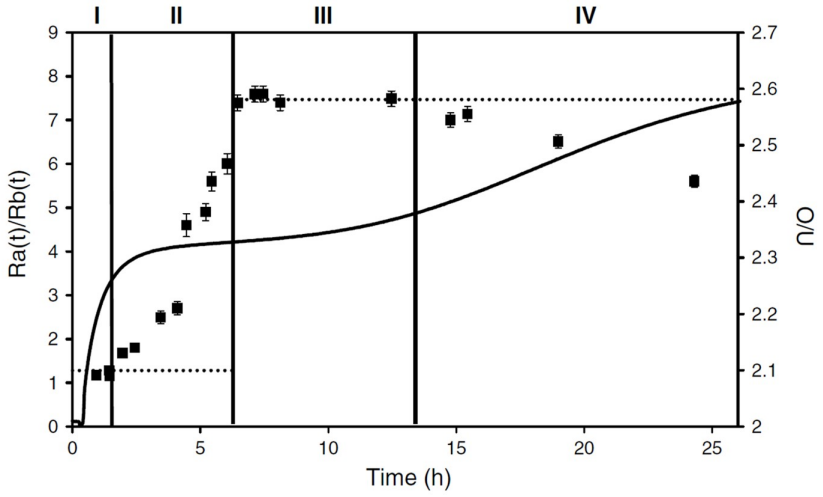

Kinetics domains	Crystalline phases
I	UO_2–U_4O_9
II	UO_2–U_4O_9–U_3O_7
III	U_3O_7–U_3O_8
IV	

FIGURE 1.7. Weight gain curve and Rr/Rl ratios plotted against time, with kinetic domains, related crystalline phases and chemical reactions. Figure reproduced from [70].

this domain. Single rate-limiting assumption is not valid anymore and formation of oxygen defect in U_4O_9, leading to formation of β-U_3O_7 is suggested.

The transformation to orthorhombic U_3O_8 from the tetragonal phase of U_3O_7 corresponds to the third and fourth domains. In the third domain R_r/R_1 is constant (7.6) verifying the rate-limiting step. Crystallite sizes of U_3O_8 stay the same, which can not be explained by a nucleation and growth mechanism. More studies are needed to fully understand what is happening in the third domain. The last, fourth domain, is also unclear as the R_r/R_1 decreases from 7.1 to 5.6, indicating that the rate-limiting step theory is not applicable during entire transformation of U_3O_7 to U_3O_8.

The dispute over which phase is formed first when UO_2 is oxidized, the mechanism of U_3O_8 formation, is still under discussion. Allen et al. [71, 72] suggested that a three-dimensional structural relationship exists between UO_2, and its oxidation product U_3O_8. This relation is between hexagonal arrays of uranium atoms parallel to the (111) planes of UO_2, and pseudohexagonal arrays parallel to the (001) planes of U_3O_8. In their model UO_2 is first transformed to U_3O_7 due to additional interstitial oxygen atoms. In the next step, extra oxygen in the lattice leads to the formation of monoclinic structures of U_2O_5. It is suggested that first β-U_2O_5 is formed followed

by α-U_2O_5, which has a similar structure to U_3O_8.

By studying the crystalline distortion of interstitial oxygen clusters, called cuboctahedra, Desgranges et al. [73] showed evidence of the possible transformation from α-U_4O_9 to U_3O_8, by stretching those cuboctahedra clusters of oxygen. Those interstitial oxygen clusters are present in both intermediate phases U_3O_7 and U_4O_9. In α-U_2O_5 these cuboctahedra sheets are considered crumpled, due to mechanical stress from the surrounding atoms which want to maintain their UO_2 positions. Therefore, under shear transformation, these sheets could become the regular sheets observed in layered U_3O_8 phase.

There are two conditions for the mechanism proposed by Desgranges et al. [73]. The first one is that the crumpled sheets are in the same plane in order to create large domain of U_3O_8 when the shear transformation occurs. The second one is that the energetic balance is in favour of formation of U_3O_8, indicating the existence of minimum concentration of crumpled sheets. Which one of these conditions is met, is considered to be influenced by parameters such as: grain size of the specimen, temperature of oxidation, and doping of the UO_2 compound [73]. Considering the grain size, limitation was found to be under 1 μm, where the grains are small enough that the disorientation of the crumpled sheets in U_4O_9 does not allow this shear transformation. Formation of U_3O_8 directly from UO_2 was suggested due to temperature effect on the cuboctahedra distortion. This was explained by the increase of thermal motion with temperature which rarefies the UO_2 layer, allowing the immediate shear transformation as an effect of formation of a cuboctahedron. When the temperature is lower than 400°C, the conversion to U_3O_8 occurs after formation of metastable U_3O_7 layer.

The metastable U_3O_7 layer is considered to be stabilised by tensile stress from mismatch between the smaller U_3O_7 unit cell than UO_2 [74]. In this scenario, the tensile stress in the U_3O_7 layer hinders the shear transformation of the cuboctahedra and more energy is required. The shear transformation to U_3O_8 therefore can only take place after the tensile stresses concentrated in the oxide layer is released by cracking of the U_3O_7 structure. Desgranges et al. stated that the cracking of the U_3O_7 oxide layer is key to the development of U_3O_8 [73, 74]. Macro-cracking of a sample surface associated with formation of U_3O_7 layer was also observed by Quemard et al. [75]. Their studies performed on a UO_2 single crystal linked this process with expansion

of the sample after incorporating enough oxygen to deform the fluorite structure causing their expansion. Studies of the expansion mechanism allow to offer a possible explanation of the typical sigmoidal kinetics associated with the UO_2 oxidation mechanism [75].

There are many parameters that affect oxidation rate of UO_2 such as temperature, moisture, and oxygen partial pressure [31]. Those conditions are given by the environment of the sample. Other parameters are sample related such as physical state of the sample: powder, pellet or a single crystal. When considering the influence of the sample structure, parameters such as particle size for powder have to be taken into consideration, while for pellets grain size and orientation can influence the rate [31].

The orientation effect was studied by Allen et al. [71, 72], using XPS, SEM and XRD. Single-crystal specimens with polished surfaces cut parallel to the [111], [110] or [100] faces and polycrystalline UO_2 disc were oxidised in 1.2 mbar of oxygen at 300°C. It was found that the reactivity follows the sequence [111] > [110] > [100] > [polycrystalline]. The rapid rate of oxidation in the UO_2 (111) was explained by previously mentioned epitaxial relationship with the U_3O_8 (001) direction. In contrast, for the [110] and [100] where there is no epitaxial relationship with the U_3O_8 and for the polycrystalline material, lattice expansion is not readily accommodated.

Recent studies conducted performed on (001) and (111)-oriented single-crystal UO_2 by Spurgeon et al. [76] utilizing STEM, EELS, and first-principles calculations showed an unprecedented large amount of interstitial oxygen distributed across gradient in the (001) surface. The stoichiometry of nearly $UO_{2.67}$, comparable with U_3O_8, was reported with maintained fluorite structure. Those studies were performed on thin films, therefore authors suggested substrate induced "clamping" that limits assosiated phase transition.

As shown, there is still a lot of uncertainty and discrepancies about the oxidation process of UO_2 to U_3O_8. In this thesis, a novel poly-epitaxial sample system was developed and used to study the oxidation rate of different UO_2 crystallographic orientations. The sample preparation and characterization will be discussed in Chapters 3 and Chapter 4. The in-situ oxidation studies on poly-epitaxial UO_2 system will be discussed in Chapter 5, while the oxidation process for (111), (110) and (001) single crystal in Chapter 6.

1.2.3 Thin films

One of the main challenges while studying uranium dioxide is the handling of the radioactive materials. This issue can be easily overcome by utilization of thin films as a low activity experimental surrogate for bulk systems. In addition to reduced radioactivity to a background level, thin films offer possibilities to engineer samples on a scale that is practically impossible in a bulk system. A thin film of UO_2 can have a thickness from several Angstroms to a few microns [77, 78] and can be single crystal or polycrystalline. Furthermore, it is possible to control stoichiometry and dopant levels, and even induce strains along specific directions. As UO_2 thin films are structurally and chemically comparable to bulk materials, they are excellent to study surface mechanisms of nuclear fuel such as oxidation and corrosion.

Thin films of uranium dioxide have been successfully produced using different physical and chemical methods. Polycrystalline UO_2 with a tower-like morphology were fabricated using an aqueous electrodeposition utilizing uranyl salt as a precursor [79]. Another technique used for the fabrication of uranium dioxide thin films is the sol-gel process, where uranyl acetate is dissolved in alcohol and acid before at eleveted temperatures before spreading over the substrate [80]. Single crystal thin films were reported to be deposited using electron beam evaporation on 4H-SiC substrates with Xe incorporated into the structure [81]. The best results in fabrication of a UO_2 single crystal thin films are reported by using a reactive DC magnetron sputtering [78, 82, 83].

In order to fabricate high quality UO_2 systems, a matching substrate is necessary. This compability allows to reduce lattice stretch and structural defects. A variety of substrates were tested [78, 81–83], with surprisingly good results reported for YSZ, were the lattice mismatch between UO_2 system and the substrate is 6.73 % [82, 83]. In this thesis, yttria-stabilized zirconia (YSZ) single crystals were used, also, an special process for the modification of ceramic YSZ was developed to fabricate poly-epitaxial thin films.

Recently, more interest in studies based on thin films is observed as they offer considerable potential in isolating individual parameters with single variable. Isolated effects provide excellent material for supporting theoretical models based on idealised systems, what is not possible when performing experiments on complex bulk oxide materials [83–87]. This approach allowed to investigate the role of crystal orientation in the dissolution of UO_2 system. It has been showed

by using engineered single crystal samples that the (001) and (110)-oriented films corrode at comparable rates, while the (111) film was significantly more corrosion resistant [83].

Here we push the application of epitaxial system of UO_2 even further by developing process of controlling the grain size, and producing unique poly-epitaxial system. This system possesses column structure of UO_2 grains, reducing the three dimensional problem to two dimensions.

1.3 Thesis Outline

This thesis will present research conducted on the fabrication and use of uranium dioxide thin films as a surrogate material for better understanding of UO_2 for nuclear energy applications. The techniques utilized during this experimental work are described in Chapter 2. Chapter 3 describes the method used for manufacturing uranium oxide thin films, together with a new method for fabricating poly-epitaxial thin films. This chapter also provides information on the construction of a DC magnetron sputtering system.

Chapter four focuses on the description of detailed post-deposition characterization of samples used within this thesis. While Chapter 5 will focus on in-situ oxidation studies performed on poly-epitaxial UO_2, where influence of the crystallographic orientation on oxidation mechanism is investigated. To even better understand the process of oxidation from UO_2 to U_3O_8, single crystal thin films are oxidised and characterized in-situ in Chapter 6 and a summary of the findings are concluded in Chapter 7.

CHAPTER 2

METHODS

This chapter describes the principles of techniques and their application for the characterization of uranium oxide thin films, used during this PhD. Those techniques were divided into three sections: X-ray related techniques, Electron and Ion imaging, and Scanning Probe Microscopy.

2.1 X-rays

X-rays are a form of electromagnetic radiation. They were discovered on 8th November 1895 [88] by Wilhelm Rontgen, after whom it is sometimes referred as Rontgen radiation. Although X-rays were observed before, as early as 1785 [89], by William Morgan, there were just a type of unidentified radiation.

The energies of X-rays are in the range of 100 eV to 100 keV, corresponding to a wavelength ranging from 0.1 Å to 100 Å. Within this energy X-rays can be divided into two groups: soft and hard X-rays. The soft X-rays have lower energies, below 5-10 keV and higher wavelength, above 1-2 Å. They find application in soft X-ray microscopes [90]. The hard X-rays have higher energy, therefore shorter wavelength, similar to the size of atoms. That makes them useful to study the structure of crystalline materials. They can be also used for elemental analysis and

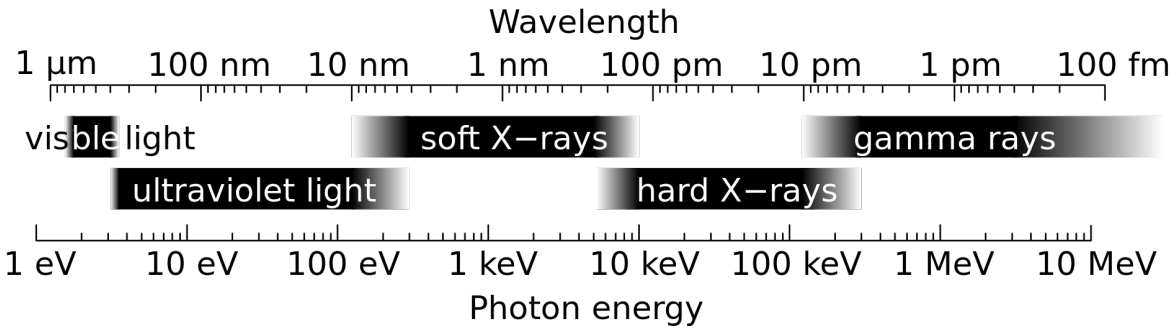

FIGURE 2.1. The Electromagnetic Spectrum of photons. Figure reproduced from [91].

chemical analysis employing techniques such as X-ray photoelectron spectroscopy (XPS) or X-ray fluorescence (XRF).

The relationship between energy and wavelength of a photon is represented by the following equation:

$$E = \frac{hc}{\lambda} \tag{2.1}$$

where E is photon energy, h is the Planck's constant, c is the speed of light in vacuum and λ is the photon's wavelength. This Eq. 2.1 can be expressed in electronvolts, when the wavelength is in micrometres as following:

$$E(eV) = \frac{1.2398}{\lambda(\mu m)} \tag{2.2}$$

2.1.1 Interaction with matter

When passing through matter X-ray may interact with it, resulting in change of intensity due to two mechanisms: scattering and absorption. Depending on the process different information can be extracted from the investigated material. Scattering involves two processes, namely: coherent scatter and incoherent scatter. In absorption three phenomena can be distinguished: photoelectric absorption, fluorescent x-ray emission and Auger electron emission.

The Fig. 2.2 shows two possible outcomes when an x-ray is scattered from an electron. Coherent scattering (Fig. 2.2 (a)), known also as Thomson scattering, is a form of an elastic

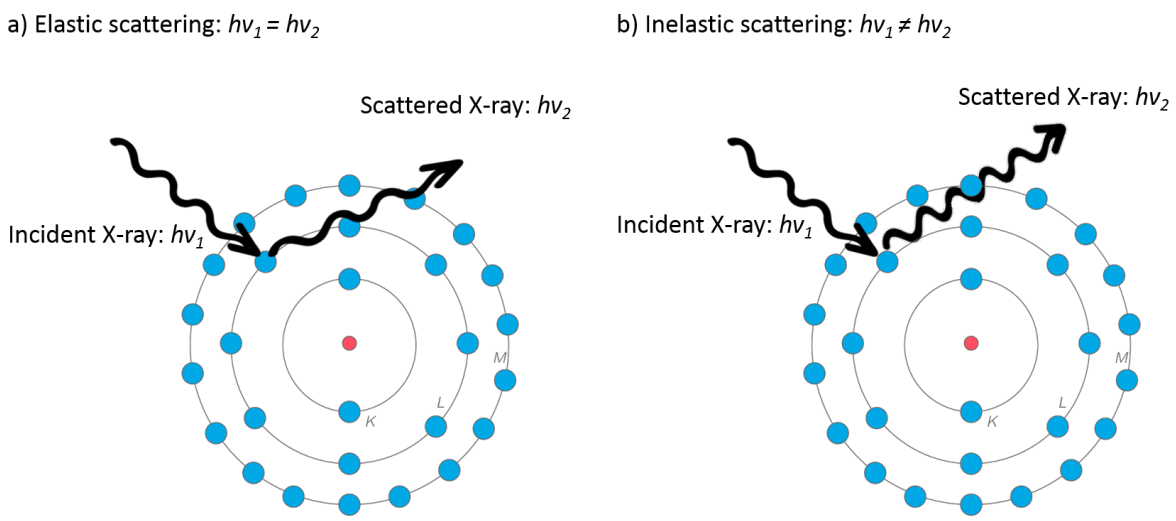

FIGURE 2.2. Schematic representation of X-ray scattering on an atom. (a) Coherent scattering, when the incident energy and phase of the photon is equal to the scattered photon. (b) Incoherent scattering, when energy was exchanged with an electron resulting with a different energy and or phase of the scattered photon.

scattering. It occurs when the x-rays are scattered and the energy and phase of the of the incident photon stay intact. This process was described by Sproull in 1946 [92] as follows "If the photon bounces off a firmly bounded electron, like the inner electrons of a heavy atom like lead, the recoil of the electron is not vigorous enough to shake it loose from the atom and it is unable to acquire kinetic energy from the photon. Hence the photon emerges with the same energy and hence the same wavelength as it had originally, and the scattering is coherent".

When the energy of the incident photon and or the phase is different to the scattered photo we are dealing with so called incoherent scattering (Fig. 2.2 (b). It is a type of inelastic scattering. If part of the energy is transferred the recoiling electron, the scattered photon energy is lower than incident photon and it is called the Compton effect. When part of a charged particle energy is transferred to a photon the inverse Compton scattering occurs. The change in wavelength (loss of energy) can be described as follows:

$$\Delta\lambda = \frac{h}{m_0 c}(1 - cos\phi) \tag{2.3}$$

where h is Planck's constant, m_0 is the mass of the electron at rest, c is the speed of light,

and ϕ is the scattering angle in degrees. After converting to nm and putting values of constants it can be expressed as:

$$\Delta\lambda = 0.243(1 - cos\phi) \tag{2.4}$$

The photoelectric effect occurs when an atom absorbs energy from an x-ray, and the excess of energy is transferred into an electron. This electron is ionized and expelled from an atom as shown on the Fig. 2.3 (a). The hole generated by the leaving electron can be filled in two processes. The first one is the fluorescent X-ray emission, shown on Fig. 2.3 (b). In this process characteristics lines K_α and K_β are created by electrons from outer shells filling the holes. In the example presented on the Fig. 2.3 (b) the lines are created by move of the electrons respectively from L shell and from M shell. An Auger electron is emitted when the atoms liberate this electron in order to relax to its ground energy state.

This processes find application in a wide range of analytical techniques used to investigate the structural, compositional and chemical properties of examined samples. The main techniques utilised throughout this thesis are X-ray Diffraction, X-ray reflectivity (XRR) and X-ray Photoelectron Spectroscopy (XPS) and will be covered in next sections.

2.1.2 Sources / Production of X-rays

X-rays are produced whenever charged particles such as electrons or ions, hit a material. The most popular source of x-ray for laboratory application is a x-ray tube source. As shown in Fig. 2.4, a typical tube source consists of cathode and anode.

The purpose of the cathode filament is to produce electrons. It is made out of a metal with high melting point. Filament is negatively charged, therefore electrons accumulate on it. The heat that is generated on the filaments causes thermionic emission. The rate of this process can be controlled by filament current, as more electrons will generate more x-rays. High voltage is used to create electric field that will accelerate electrons from cathode toward anode. To avoid obstructions to electrons such as air molecules, anode and cathode are enclosed in a vacuum chamber. Anode (target) is used to convert electron KE to X-ray photons. Anode usually consist of

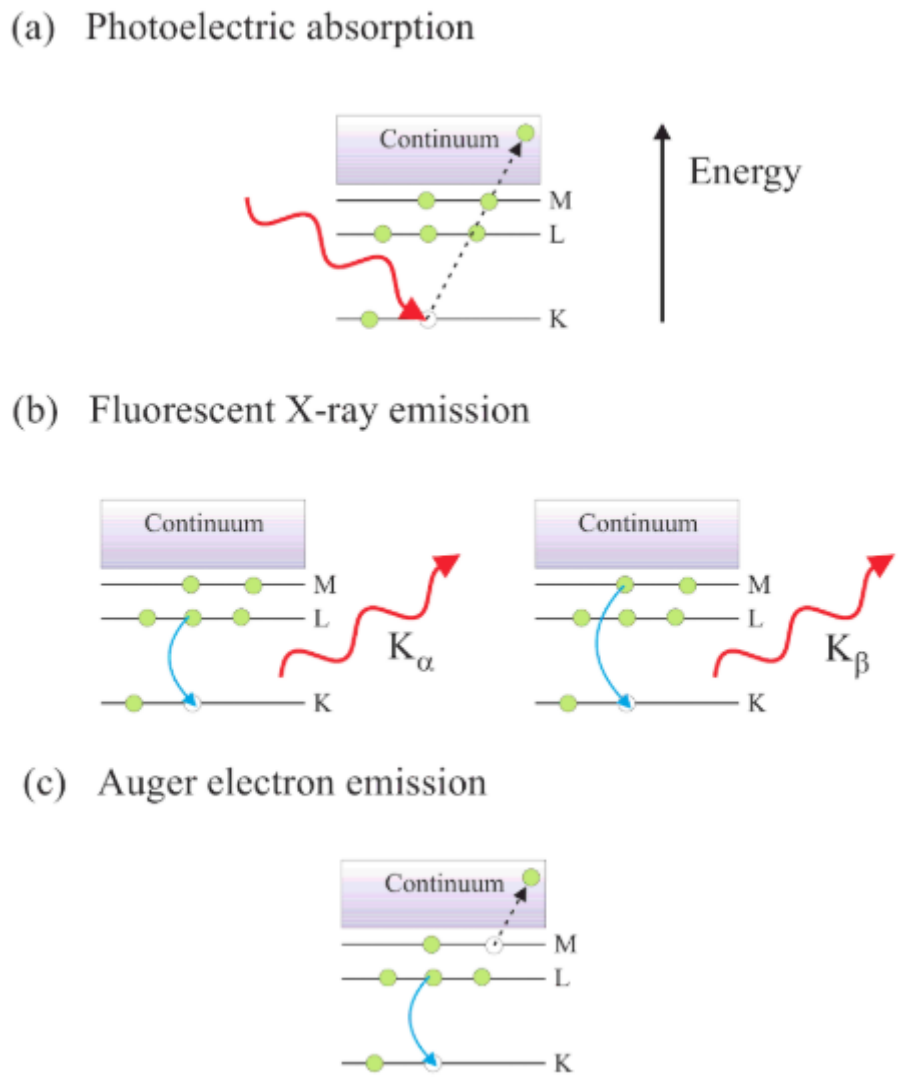

FIGURE 2.3. Schematic representation of absorption processes. The energy levels of three lowest shells are indicated, the rest are merged into the continuum. (a) The photoelectric absorption occurs when an X-ray photon is absorbed by an atom and the electron is ejected from the atom due to the transfer of excess energy to the electron. The hole created in this process can be filled in two ways: (b) Fluorescent X-ray emission when photon is created as a result of the electron from an outer shell filling the hole. In this example K_α line is formed when the electron travel from L shell and K_β for transfer of the electron from M shell. (c) Auger electron emission happens when the atom liberate an electron and relax to its ground state energy. Figure from [93].

a metal target, rotor, stator and a cooling system as most of the electrons energy is converted into a heat.

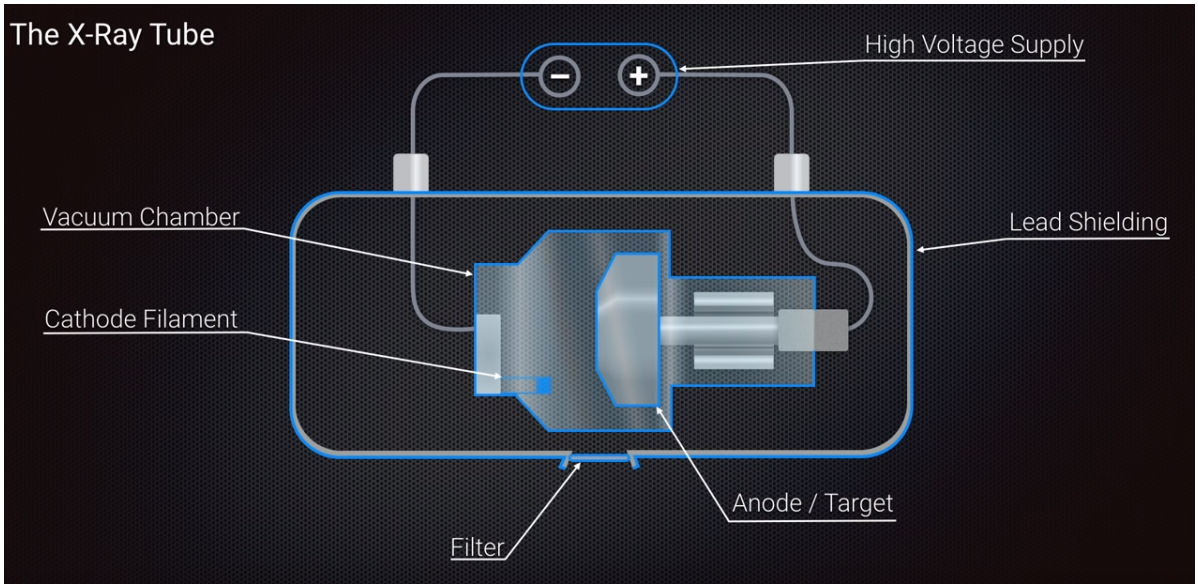

FIGURE 2.4. The schematic ilustration of the X-ray tube, including main components. Figure taken from [94].

X-rays are created by two different processes: Bremsstrahlung and characteristic emission. Bremsstrahlung is produced due to the loss of kinetic energy when an electron decelerate on the anode target. Bremsstrahlung has a continuous spectrum which can be seen on Fig. 2.5. The intensity increases starting from the minimum value for the wavelength that can be calculated using Eg. 2.3. The characteristic x-rays are associated with the atomic structure of targeted material. When high energy electrons hit the electrons on the two first shells, the holes created during this process are quickly filled by electrons from higher energy levels. Emission of characteristic x-ray photon is associated with this transition. When the transitioning ends on the K shell it is called K line. K_α corresponds to transition from 2p to 1s and is usually higher in intensity than K_β associated with transition from 3p to 1s. Therefore, K_β is typically blocked by a filter with a metal having one proton less than the target material of anode. As the characteristic emission is several orders of magnitude higher than the Bremsstrahlung, filters are used to also remove it from spectrum. In our PANalytical X'pert diffractometer at the University of Bristol a copper anode is used. The energy transition for copper from second to first level is equal to 8.04 KeV, what corresponds to a wavelength of K_α equal to 1.54 Å.

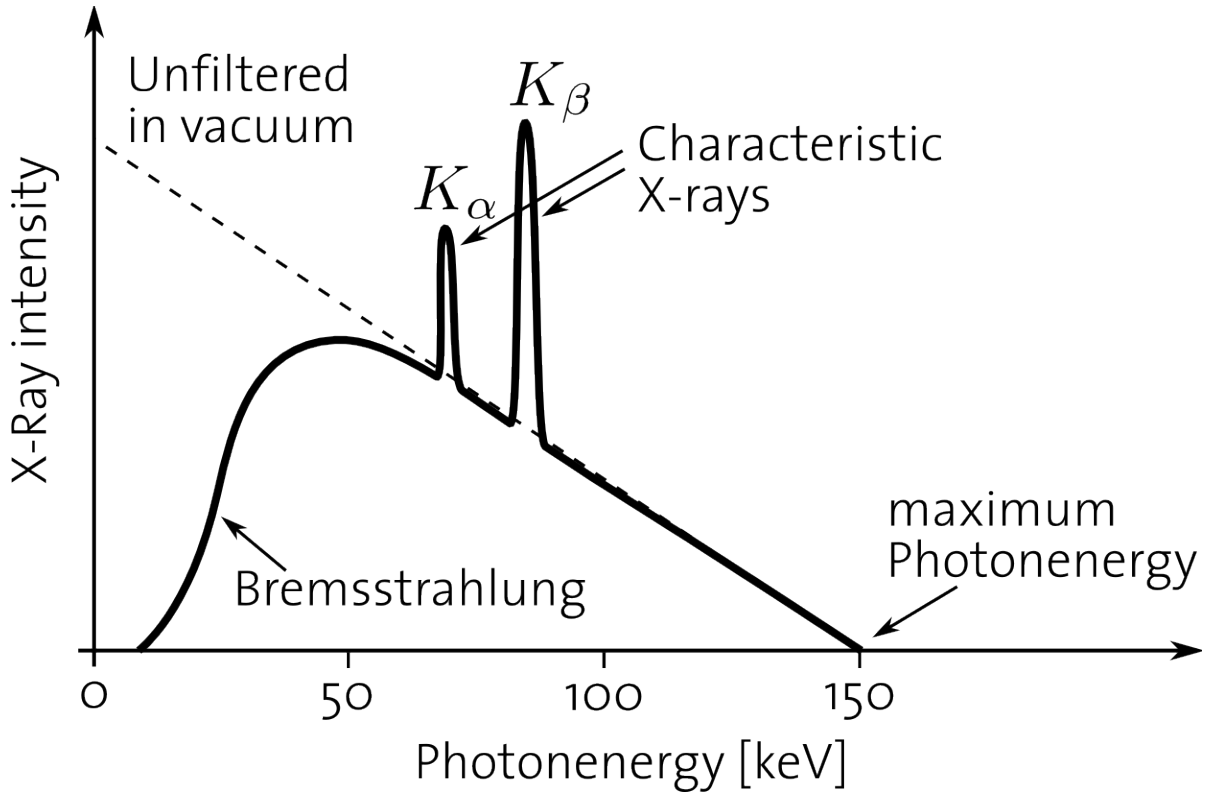

FIGURE 2.5. Spectrum of the x-rays with K_α and $_\beta$ characteristic radiation. The dashed line represents intensity of x-rays in UHV enviroment. Figure reproduced from [95].

$$\lambda_{\min} = \frac{c}{v_{\max}} = \frac{hc}{E} \tag{2.5}$$

The lab sources are limited in flux and wavelength, therefore special experimental equipment was developed. The synchrotron radiation has several advantages over laboratory sources. The wavelength can be optimized for a particular sample, and the radiation is extremely intense. Collimated beam in the vertical sense, allows for much higher 2θ resolution [96]. Those facilities offers also extensive experimental help from professional staff members.

The name of the synchrotron radiation comes from a specific type of particles accelerator. Nonetheless, nowadays it used to describe radiation that travels at relativistic speed along curved paths. To make that possible magnetic field is applied to force the trajectory of the beam. In a storage ring electrons or positrons are kept circulating at constant energy. The storage ring

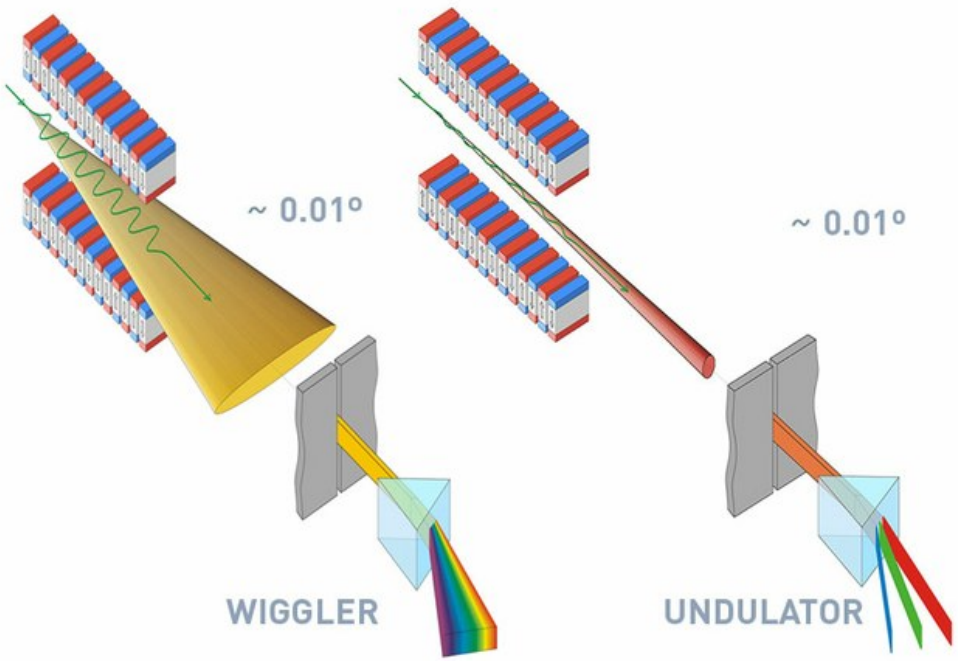

FIGURE 2.6. Two types of insertion-devices. On the left is a wiggler and on the right in an undulator. Figure reproduced from [97].

consists of curved and straight segments where particles are accelerated under ultra high vacuum (UHV) conditions. In the curved section of the storage ring, bended magnets force the electrons to stay in closed orbit, therefore, generating a continuous radiation spectrum. Insertion devices such as undulators and wigglers (Fig. 2.6) are located in a straight section. The radiation produced in those devices has different oscillation amplitude. In an undulator, electrons traversing a periodic structure of dipole magnets are forced to undergo oscillations and thus to radiate energy. The intensity of the radiation produced in an undulator is very hight and the amplitude of the oscillation is very small, whereas in wigglers the amplitude of the oscillation is large and the radiation from many wigglers add incoherently.

The term describing the quality of the X-ray beam is called the brilliance. It is a single quantity combining all the parameters for possibility to compare X-ray beam from different sources. Brilliance consist of amount of photons emitted per second, collimation of the beam (given in milli-radian for vertical and horizontal direction), size of the source area, and fixed relative energy bandwidth. Therefore, it can be expressed as follows:

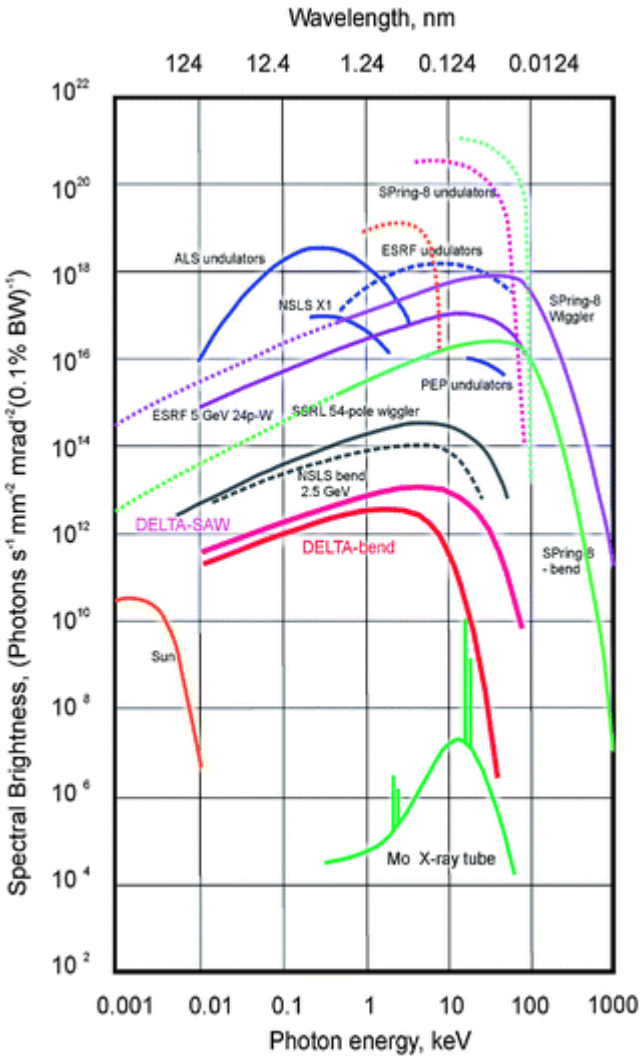

FIGURE 2.7. A comparison of brilliance produced by different sources. Figure reproduced from [98].

$$Brilliance = \frac{Photons/second}{(mrad)^2\,(mm^2\ source\ area)\,(0.1\%\,BW)} \tag{2.6}$$

The brilliance is a function of the photon energy, therefore, the brilliance produced by modern undulators can be 10 orders of magnitude higher than the one produced from a K_α laboratory source [98]. The Fig. 2.7 shows a comparison of the brilliance produced by different sources and synchrotron facilities.

2.1.3 X-ray Diffraction

X-ray diffraction (XRD) is a widely used, non-destructive scientific technique that provides crystallographic information about samples. The information that can be extracted includes: phase identification, crystal orientation, unit cell dimensions, crystallite size, strain characterisation, determining lattice mismatch between film and substrate and many other parameters.

2.1.3.1 Background

In this section, theory behind the scattering on different systems is described. The discussed system are: the electron, the atom, and the crystal. For the better understanding of X-ray diffraction, a good starting point is the scattering of X-rays on the smallest particle of matter capable to do so. In the case of X-rays, the scattering process occurs between an electrons surrounding the nuclei of an atom and the photon. X-ray as a electromagnetic wave posses an electric field which for a beam of monochromatic, polarised, plane radiation can be expressed as follow:

$$E = E_0 e^{i(\omega t - \phi)} \tag{2.7}$$

where E_0 is the amplitude of the wave, ω is the frequency, t is time and ϕ is the phase shift. The force exerted on a particle with charge q in the electric field E is given by $F = qE$. From the second Newton's law of motion we know that the forces F on an object is equal to the mass m of that object multiplied by the acceleration a of the object: $F = ma$. Using those equations to describe the acceleration that a wave of electric intensity E causes to the electron of mass m_e and charge q_e, can be expressed as follow:

$$a = \frac{q_e}{m_e} E_0 e^{i(\omega t - \phi)} \tag{2.8}$$

As this scattering is coherent, there is no change in the energy of the scattered wave, and the phase of the incident wave and scattered is the same. Therefore, the electromagnetic radiation emitted by accelerated charge will have the same frequency as that of the incident wave. In this

case the oscillating electron becomes a source of spherical X-rays radiation [99], by scattering the incident x-ray beam in all directions.

The electric field ε_r resulting from the acceleration a of a charge q at a point r far from that field, is given by:

$$\varepsilon_r = \frac{qa\sin\theta}{rc^2} \tag{2.9}$$

where θ is the angle between r and a, and c is the speed of light. If we consider a case where an electromagnetic wave is linearly polarized, monochromatic, and hits free stationary electron. Furthermore, if we consider that r is perpendicular to the oscillation direction and is in the equatorial plane through the the electron, where point r is outside of the charge distribution sphere, then the $\sin(\theta = 90°) = 1$ and Eq. 2.9 can be expressed as [99]:

$$\varepsilon_0 = \frac{qa_0}{rc^2} = \frac{q}{rc^2}\frac{q_e}{m_e}E_0 = -\left(\frac{q_e^2}{m_e c^2}\right)\left(\frac{E_0}{r}\right) \tag{2.10}$$

The negative sign on the right hand side of the Eq. 2.8 means that the angle of scattered radiation is 180°out of the phase with incident E

In the J. J. Thomson theory, so called Thomson's scattering length or the electron radius r_0 can be calculated from:

$$\frac{\varepsilon_0}{E_0} = -\left(\frac{q_e^2}{m_e c^2}\right)\left(\frac{1}{r}\right) = -\frac{r_0}{r} \tag{2.11}$$

It is one of the three related length scales, together with Bohr radius a_0 and the Compton wavelength of the electron λ_0.

Scattering from an Atom

When the X-ray is scattered from two electrons the phase difference ϕ between scattered waves is given by [93]:

$$\phi = (k - k') \cdot r = \boldsymbol{Q} \cdot r \tag{2.12}$$

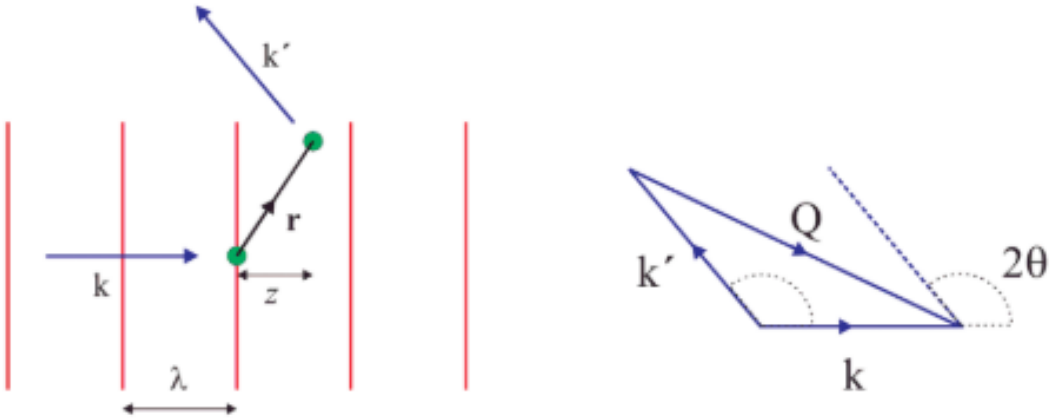

FIGURE 2.8. Scattering of an X-ray from two-electron system. The incident X-ray is represented by k wavevector, with wavefronts showed as vertical lines. The scatterd vector is represented by k'. As the scattering is elastic, the wavevector transfer, Q can be represented as the phase difference betrween scaterred and incident wavevectors. Figure reproduced from [93]

where k is incident wave, k' is scattered, and Q is the wavevector transfer, as shown on Fig. 2.8. In this case the phase lag is the ration of z to the wavelength λ times 2π. As the scattered wave retains its phase relationship to the incident wave and there is no change in the energy, the scattering is coherent, and $|k| = |k'|$. Therefore, the wavevector transfer is given by:

$$|Q| = 2k\sin\theta = \left(\frac{4\pi}{\lambda}\right)\sin\theta \tag{2.13}$$

The scattering form an atom is a superposition of scattering from all electrons in this atom. This can be described using electron density function $\rho(r)$. If we take a small volume dr, the number of electrons in this volume will be equal to $\rho(r)dr$. Assuming that at all scattering angels the full Thompson acceleration of the electrons is observed, the scattering amplitude from any assembly of n electrons can be written as [93]:

$$A(Q) = -r_0 \sum_n e^{iQ\cdot r_n} \tag{2.14}$$

where, r_n corresponds to the position of n-th electron. Therefore, total atomic scattering form factor $f^0(Q)$ can be obtained by integrating over r:

$$f^0(Q) = \int \rho(r) e^{iQ \cdot r} dr \tag{2.15}$$

When Q approaches 0 the situation is simple, the phase vector is close to unity and the integral over density of electron gives their total number: $f^0(Q) = Z$. On the other hand, with increase of Q, the wavelength of the radiation decreases compared to the atom, what leads to a case where the waves scattered from the different electrons interfere in a destructive way. Therefore, $f^0(Q) = 0$ for $Q \to \infty$.

The Eq. 2.15 is true when the energy of incident X-rays is higher than the electron binding energy. Otherwise, with the incident beam energy lower than the electron binding energy, the electron response is reduced thus the scattering is reduced. This phenomena is used in resonant scattering to probe the local electronic structure. Taking this into consideration, the atomic form factor can be written as [93]:

$$f(Q, \omega) = f^0(Q) + f'(\omega) + i f''(\omega) \tag{2.16}$$

where f' is the real part of the dispersion correction and f'' is the imaginary part of the dispersion correction.

Scattering from a crystal lattice

Scattering from a crystal can be considered as a scattering from regularly repeating array of atoms. Therefore, a crystal can be described as three-dimensional lattice with atoms at each point in the lattice. For that we can use a set of vectors R_n of the form:

$$R_n = n_1 a_1 + n_2 a_2 + n_3 a_3 \tag{2.17}$$

where n_i are integers, and a_i are the lattice vectors defining the unit cell. A family of lattice planes in crystal can be determined by three integers h, k, and l, which are called the Miller indices [99]. Two important features are that the density of lattice points within each family is

the same and that the planes are equally spaced. Therefore, the lattice spacing can be defined as d_{hkl}, and for the cubic crystal the lattice spacing is:

$$d_{hkl} = \frac{a}{\sqrt{h^2+k^2+l^2}} \tag{2.18}$$

where a is the lattice parameter [93]. If we consider R_n as the origin of the unit cell then the position of the atom in the crystal is $R_n + r_j$. Combining that with Eq. 2.14 the scattering factor for entire crystal will be [93]:

$$F^{crystal}(Q) = \sum_{r_j} F_j(Q) e^{iQ\cdot r_j} \sum_{R_n} e^{iQ\cdot R_n} \tag{2.19}$$

where the first sum is the unit cell structure factor and the second sum is the lattice sum. The unit cell structure factor is the scattering from the basis of atoms, therefore depends on the Miller. If this term as a combination of h, k, and l is equal to 0 then scatering from this family of planes are forbiden [99]. The second term, phase vector will be non-zero for:

$$Q \cdot R_n = 2\pi \times integer \tag{2.20}$$

To solve this we can use lattice basis vectors in reciprocal space, which can be defined as:

(2.21)
$$a_1^* = \frac{2\pi}{a_1 \cdot (a_2 \times a_3)} a_2 \times a_3 \qquad a_2^* = \frac{2\pi}{a_1 \cdot (a_2 \times a_3)} a_3 \times a_1 \qquad a_3^* = \frac{2\pi}{a_1 \cdot (a_2 \times a_3)} a_1 \times a_2$$

where the volume of the unit cell is $a_1\cdot(a_2 \times a_3)$. Now we can define the reciprocal lattice by set of vectors G:

$$G = ha_1^* + ka_2^* + la_3^* \tag{2.22}$$

The vector G_{hkl} will be perpendicular to the h, k, and l planes. Solution to the Eq. 2.20 is given by $G \cdot R_n$:

(2.23) $$Q = G$$

therefore, the scattering amplitude $F^{crystal}(Q)$ produce a non-zero value when this equation is fulfilled. This is known as the Laue condition for the observation of diffraction from crystalline material. This condition can be visualised in two dimensions using the Ewald circle, or Ewald sphere in reciprocal space [93], as shown on Fig. 2.9

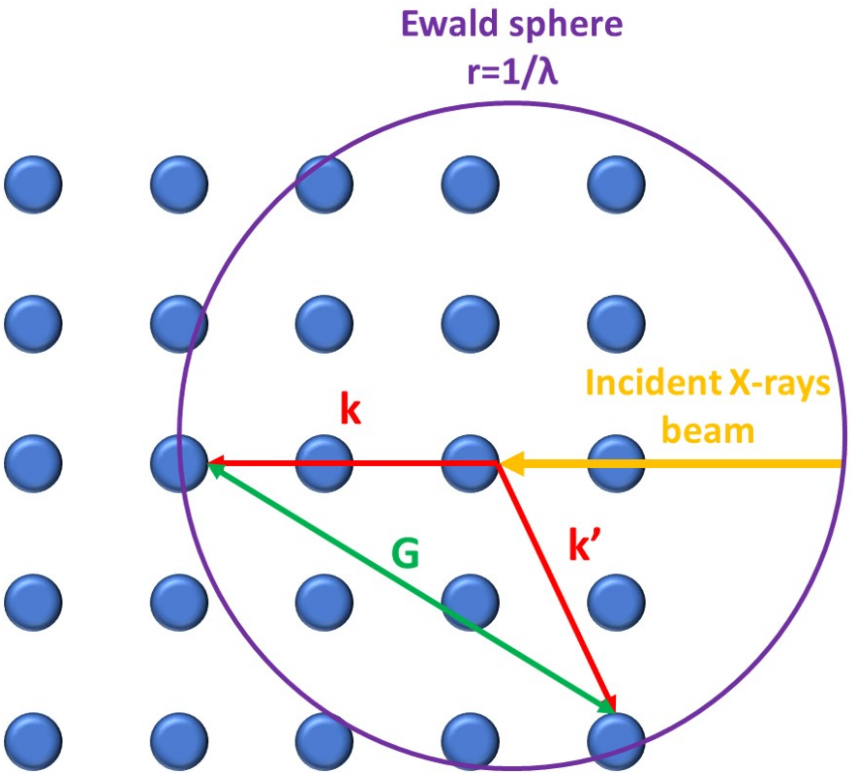

FIGURE 2.9. The Laue condition portrayed with the Ewald sphere construction.

Wulff-Bragg's condition

The Laue condition is exactly equivalent to the Bragg's law. The Bragg's (Wulff-Bragg's condition) law was proposed in 1913 by father and son [100], and rewarded the Nobel Prize in physics in 1915. To derive the Bragg's condition a schematic representation of monochromatic X-ray beam scattered at angle θ from an aligned planes of lattice separated by a length d, as shown on Fig. 2.10 can be used.

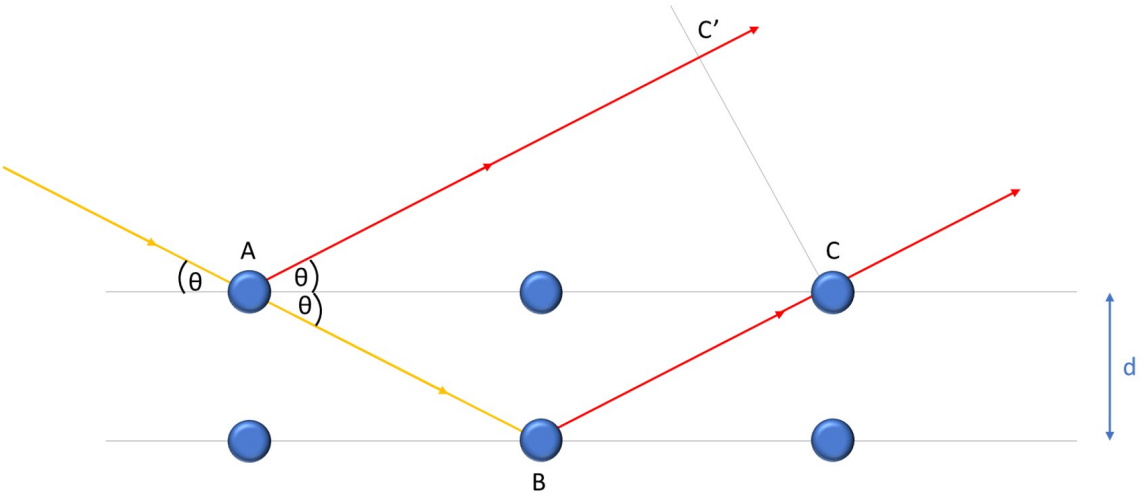

FIGURE 2.10. Schematic of Bragg's condition. The incident x-ray is labelled with yellow colour, and scattered with red. The blue circles represent atoms aligned on planes with separation d.

The path difference between the ray AC' and the ray transmitted to B and reflected from it can be expressed as $(AB+BC)-(AC')$. To get a constructive interference from those two waves, the path difference in between them have to be equal to an integer value of the wavelength:

$$(AB+BC)-(AC')=n\lambda \tag{2.24}$$

where n is a positive integer, and λ is the wavelength of the incident wave. Therefore, from basic trigonometry we can see that:

$$AB=BC=\frac{d}{\sin\theta} \qquad AC=\frac{2d}{\tan\theta} \qquad AC'=AC\cdot\cos\theta=\frac{2d}{\tan\theta}\cos\theta=\frac{2d}{\sin\theta}\cos^2\theta \tag{2.25}$$

Putting the Eq. 2.25 into the Eq. 2.24 we can rewrite it as:

$$n\lambda=\frac{2d}{\sin\theta}-\frac{2d}{\sin\theta}\cos^2\theta=\frac{2d}{\sin\theta}\sin^2\theta \tag{2.26}$$

what simplifies to famous Bragg's formula for observation of diffraction patterns:

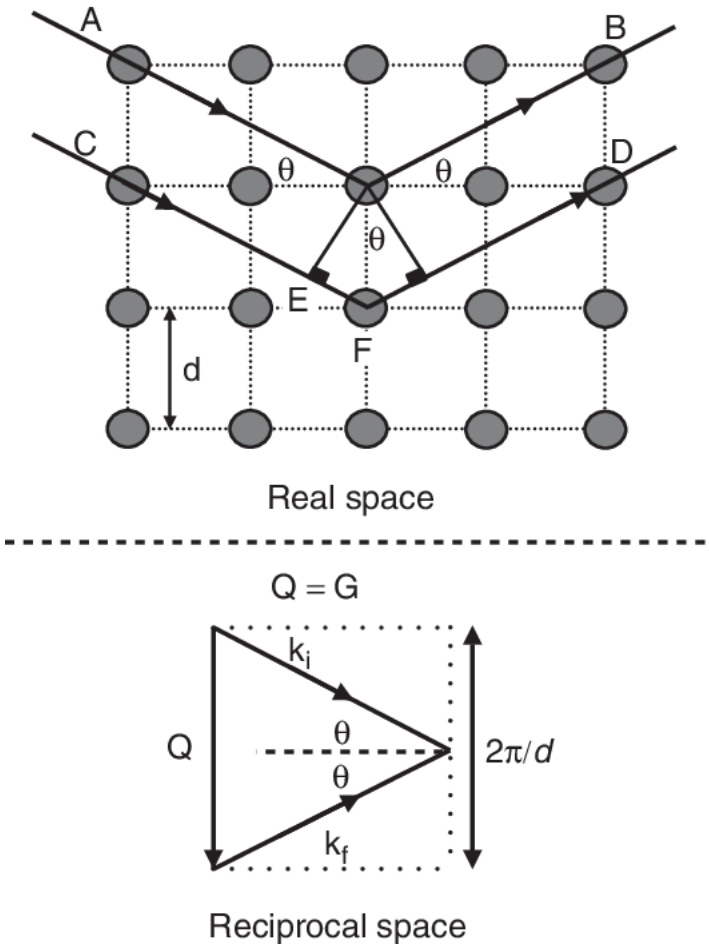

FIGURE 2.11. Schematic comparision of Bragg's condition to Laue condition. Figure reproduce from [101]

$$n\lambda = 2d\sin\theta \tag{2.27}$$

As mentioned before this condition in real space is equivalent to the Laue condition in reciprocal space what is shown on Fig. 2.11.

2.1.3.2 Instrumentation

The XRD data presented in this thesis was collected using both laboratory and synchrotron instruments. Most of the measurements, including $in-situ$ oxidation studies, were done on a PANalytical X'pert diffractometer at the School of Physics (IAC), University of Bristol.

The source of X-rays in the laboratory diffractometer is a rotation tube source with Cu anode. The characteristic wavelengths for copper are Cu K_{α_1}=1.54060 Å and K_{α_2}=1.54443 Å. The monochromator used in this equipment is a single crystal of Ge and the background of K_β is reduced by a Ni foil. To increase the resolution of the incident x-ray beam a set of divergence and soller slits are fitted. The divergence slits control the equatorial divergence of the incident beam, and thus, the area of the sample that is irradiated by the incident x-ray beam. The soller slits reduce the axial (vertical) divergence, improving peak shape and the resolution in 2θtype scans, especially at low scattering angles. Before the diffracted beam reaches the detector, an anti-scatter slit is applied to reduce the diffusely scattered x-rays, and an additional set of soller slits to further improve the resolution.

The schematic of the PANalytical X'pert diffractometer is shown on Fig. 2.12. The instrument uses the Bragg-Brentano configuration, where the diffraction vector is always normal to the surface of the sample, with an exchangeable sample stage in the middle of the diffractometer. Multiple stages can be mounted including the Open Eulerian Cradle and the Anton Paar HTK 1200 high temperature oven.

The Open Eulerian Cradle stage has two motors χ and ϕ that allows to manipulate the position of a sample. The first one can rotate the sample along the axis parallel to the beam direction, and the second one can spin sample on the stage allowing to measure off-specular diffraction peaks for single crystals.The second motor can be used also for adjustment of the height, and it can be done manually or by using the software. Although, as the change of height is associated with rotation of the sample, it has to be repositioned manually after using the height adjustment by software.

The Anton Paar HTK 1200 high temperature is an environment chamber with a temperature control. The chamber can operate in a pressure range from 10^{-4} mbar to 1 bar, although, to reach the low pressure a turbomolecular pump is required. The chamber has a inlet, therefore, an introduction of an ambient gas such as air, O_2, N_2, He, and other non-hazardous non-corrosive gases is possible. The temperature can be controlled from room temperature 25°C to 1200°C. This system allows to scan in 2θ range from 0 ° to 164 °.

The window foils in the hot stage are made of Kapton. Kapton is a polyimide mterial with high

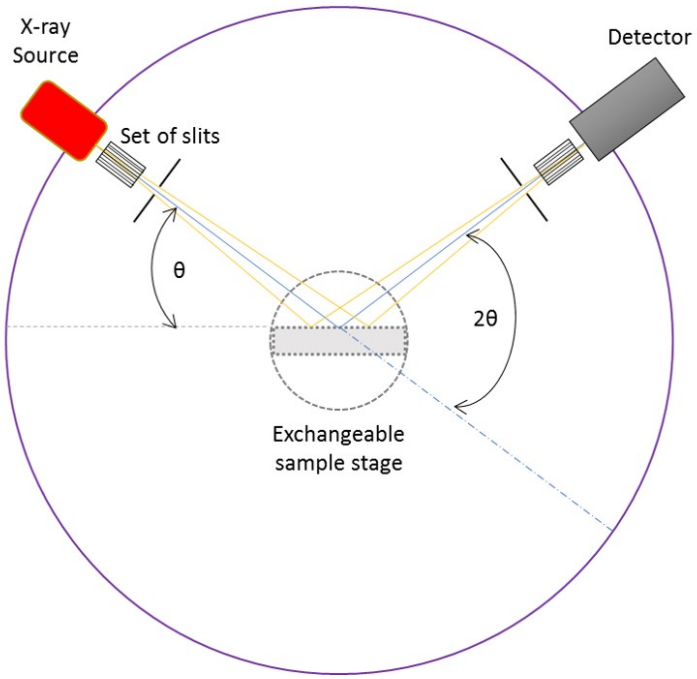

FIGURE 2.12. Schematic of the PANalytical X'pert diffractometer in the Bragg-Brentano configuration with an exchangeable sample stage.

mechanical and thermal stability, has extremaly low absorbtion of X-rays and is relatively insensitive to radiation damage [102]. Prior to any experimental work, old window was replaced with a graphite foil and non-coated Kapton foil. This combination allow to work with a temperatures higher than 1000°C, but the intensity of x-ray is decreased nearly by 15% due to the absorption by the graphite window foil. Afterwards, as the temperature during the experiment would not exceed 700°C, and visible cracks appeared on the graphite foil, the window was replaced with a aluminium coated Kapton foil. That solution guarantees minimum absorption, but is only suitable up to 1000°C.

The schematic of the experimental set-up developed for the XRD $in-situ$ oxidation studies is shown on Fig. 2.13. The evacuation of the chamber is performed through the KF vacuum flange and includes components from number 3 to number 15. Pressure inside the chamber can be measured using vacuum gauges (8). The gate valve (9) allows to isolate the set of the pumps from the chamber, what is necessary before gas insertion. The gate valve (4) can be used to lock small volume of a gas in between both gate valves (4 and 8), which then can be evacuated by opening

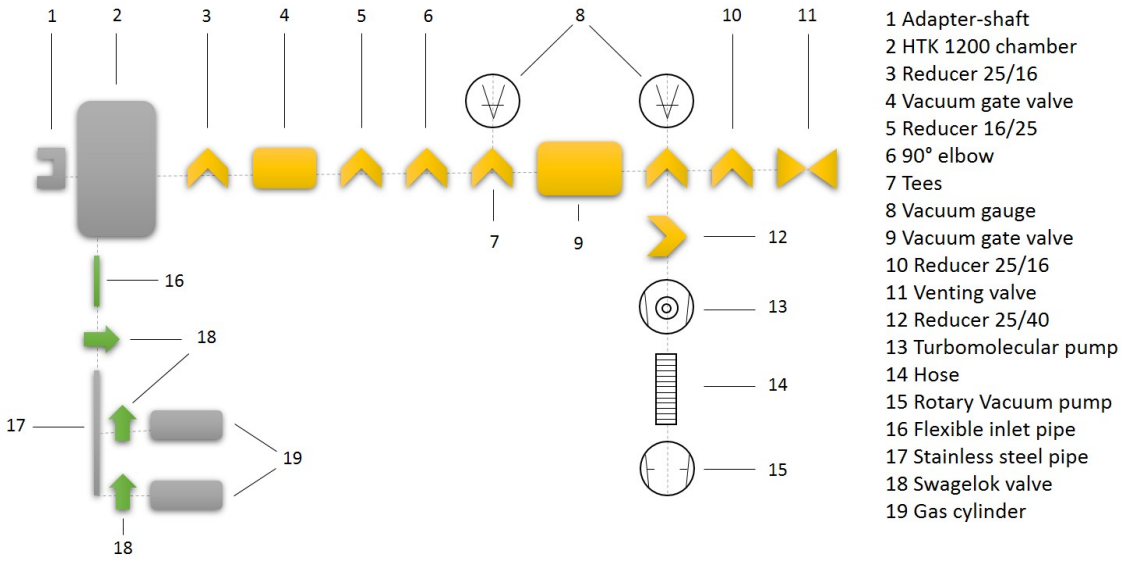

FIGURE 2.13. Schematic of the experimental setup used for in-situ oxidation experiments.

the valve (8) and keeping the valve (4) closed. This solution is particularly useful to lower the pressure inside the chamber in a controlled manner.

2.1.3.3 Measurement

The PANalytical X'pert diffractometer can conduct three types of diffraction scans: specular ω - 2θ scan, ω scan (rocking curve), and off-specular scans. Although, all three scans can be performed only on the Open Eulerian Cradle stage, as the Anton Paar HTK 1200 high temperature chamber can not read, nor record the ϕ rotation of the sample, therefore, off-specular scan is not possible on that stage.

Longitudinal ω - 2θ scan

The most practical scan providing information about the composition and quality of the sample is a specular high angle scan. This longitudinal, ω - 2θ scan in Bragg-Brentano configuration is performed by moving both the source and the detector at a constant rate around the sample. In this configuration the sample is stationary and the scattering vector Q, is perpendicular to the

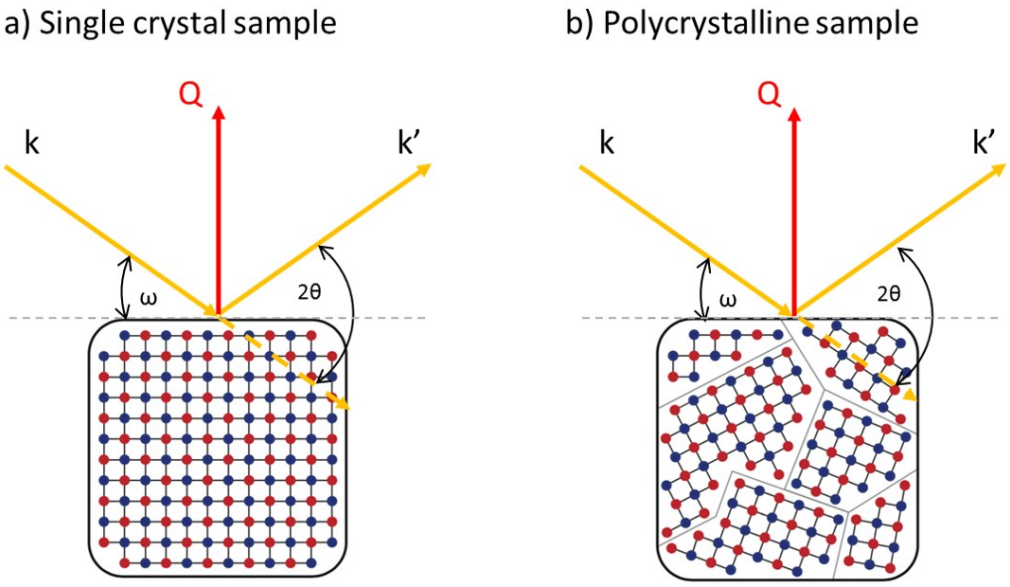

FIGURE 2.14. Schematic representation of x-ray scattering proses in a single crystal sample (a) and polycrystalline sample (b).

sample surface. Therefore, $\omega = \theta$ what means that only reflection from planes perpendicular to the scattering vector will be observed.

In case of a single crystal sample, X-ray diffraction scan will only have contribution from a single set of allowed (hkl) directions (Fig. 2.14(a)). Therefore, conducting a specular ω - 2θ scan on a single crystal material with a cubic structure, where the [001] direction is perpendicular to the sample surface, will shown only diffraction peaks within <001>. Although, presence of one direction can suggest single crystal structure it is not a confirmation, as preferred orientation might have very similar signal. In order to confirm if the structure is real single crystal, off-specular diffraction scan must be conducted.

In a polycrystalline system ,with a random alignment of the crystallites, a portion of the crystallites with each set of crystallographic planes will be perpendicular to the direction of the scattering vector Q, as shown on Fig X. Therefore, by performing ω - 2θ scan of a polycrystalline sample will give rise to all allowed crystallographic reflections. If a system has a statistically high number of crystallites without preferred orientation, then the ratio between peak intensities will correspond to the ratio between their structure factors. In that case the system is perfectly

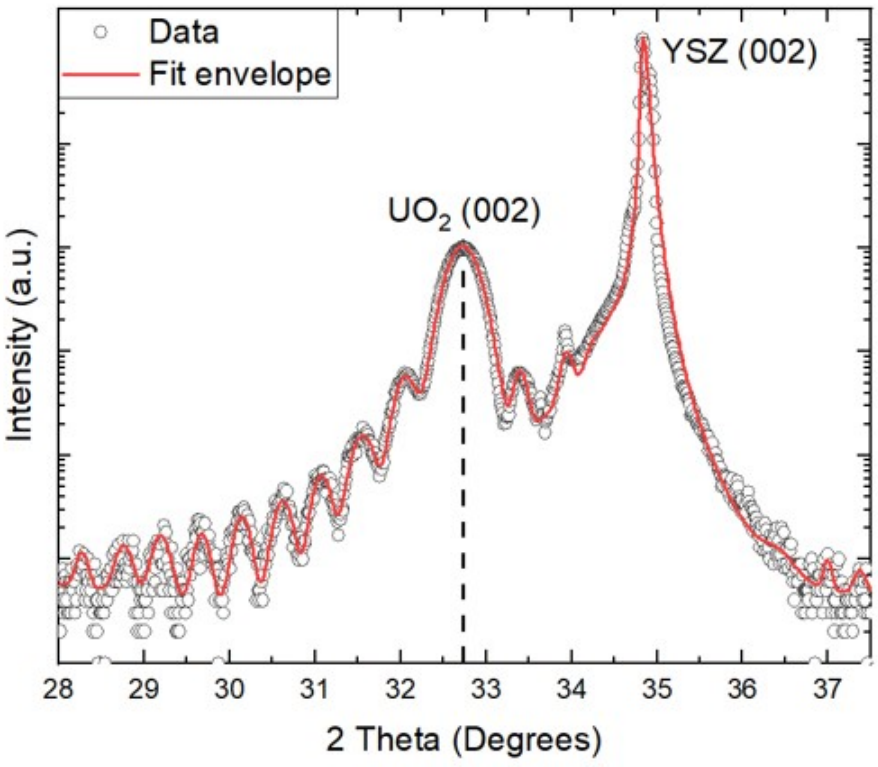

FIGURE 2.15. Example of an longitudinal ω - 2θ scan performed on 20 nm thick film of UO_2, showing Laue fringes.

polycrystalline. Additionally, for a polycrystalline sample it is possible to extract average grain size from the ω - 2θ scan, using the full width half maximum (FWHM) of the diffraction peak. A formula that relates FWHM with the mean size of the crystalline, τ, is called the Scherrer equation:

$$\tau = K\frac{\lambda}{\beta\cos(\theta)} \tag{2.28}$$

where K is a dimensionless shape factor, typically 0.9, λ is the X-ray wavelength, β is the (FWHM) of the Bragg peak, and θ is the Bragg angle. However, this equation applies only to the size of sub-micrometre crystallites.

Other information provided by ω - 2θ scan is thickness of a thin film. This is only possible for a very thin layer in a system with sharp interfaces. An example is shown on Fig. 2.15, where the scattered intensity extends far beyond normally expected from a Bragg peak. The visible oscillations are caused by constructive and destructive interference of the x-rays internally reflected from successive interfaces. These so called Laue fringes allow to determine the layer thickness of the thin film.

Off-Specular Scans

Off-Specular Scans are very useful in characterization of a single crystal sample, as they allow to distinguish between the truly single crystal nature and the preferred polycrystalline system. This scan is performed by setting 2θ to the position of chosen Bragg peak and adjusting an angular offset to ω in the way that the Q vector becomes perpendicular to the chosen crystallographic plane. In such a configuration, the symmetry of the off-specular diffraction peak can be measured by rotating sample 360°in ϕ. A schematic illustration of that process is shown on Fig. 2.16 (a).

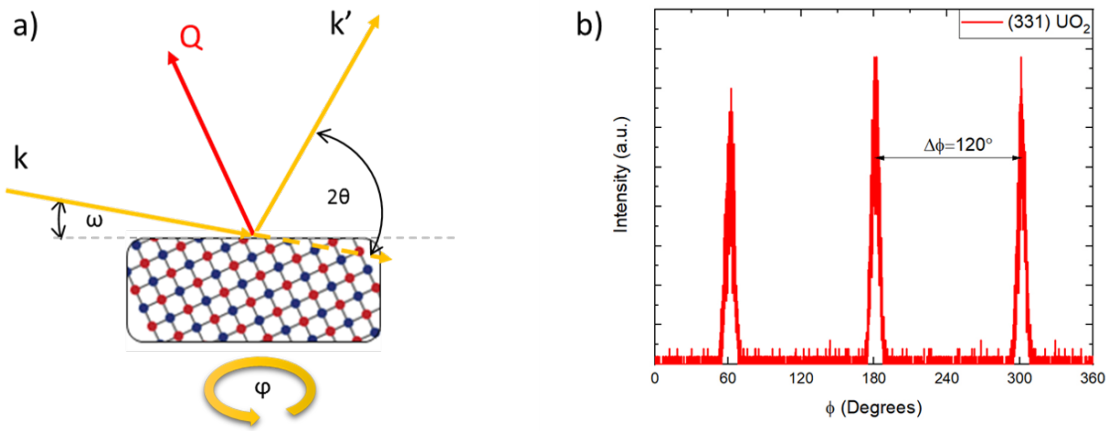

FIGURE 2.16. On the left (a) is shown schematic representation of the off-specular scattering geometry, where wave vectors k and k' are the incident and exit vectors respectively. The sample is aligned so the Q vector is perpendicular with the crystallographic planes, and the sample can be rotated in ϕ to measure the symmetry of the off-specular diffraction peak. Example of (331) off-specular scan performed on a (111) oriented thin film of uranium dioxide is shown on panel (b).

An example of an off-specular scan is shown on Fig. 2.16 (b). The sample is a (111) oriented single crystal thin film of uranium dioxide, and (331) off-specular scan was performed. To find the omega offset, the angle between the specular (111) vector and the off-specular (331) was calculated, which is 22 °. The expected 2θ position for (331) reflection in UO_2 is 75.76 °, therefore omega was set to half of the 2θ minus omega offset, which is 15.88°. By rotating the sample along ϕ in 360°, expected three fold symmetry with peaks separated by 120°was confirmed indicating a single crystal structure of the thin film sample.

Rocking Curve ω scan

To investigate the crystalline quality of the sample, a rocking scan can be performed. This scan is conducted by aligning 2θ position on chosen Bragg peak and rocking along ω direction. This configuration allows to scan for the misorientations in the crystallite alignment as the sample mosaic spread is related to the full width half maximum (FWHM) of the curve. Therefore, for an ideal perfect single crystal without any stain and defects, an extremely sharp peak for ω equal half of 2θ would be expected. This would indicate a perfect long range alignment along specific direction on which the rocking curve scan was performed.

In reality, materials are not free of defects or stains, especially epitaxial thin films. The imperfection in the structure of epitaxial thin films, due to the mismatch with substrate, will cause broadening of the measured rocking curve. An example of a rocking curve data collected for 20 nm thick (001) oriented single crystal of UO_2 thin will is shown on Fig. 2.17. Two components can be distinguished. The very sharp part exhibiting Gaussian distribution is associated with orientational order over very long range distances, usually provided by good match with substrate. The broad component that exhibits more of a Lorentzian distribution is related to the disorder within the structure on short length scales associated with misorientated crystal domains [103].

2.1.3.4 Data processing

The peak fitting for XRD data has been carried out using Line-Profile Analysis Software (LIPRAS) [104] software. LIPRAS allows for least-squares fitting of Bragg peaks in powder diffraction data using a graphical user interface. Full description of the errors for all profile parameters can be

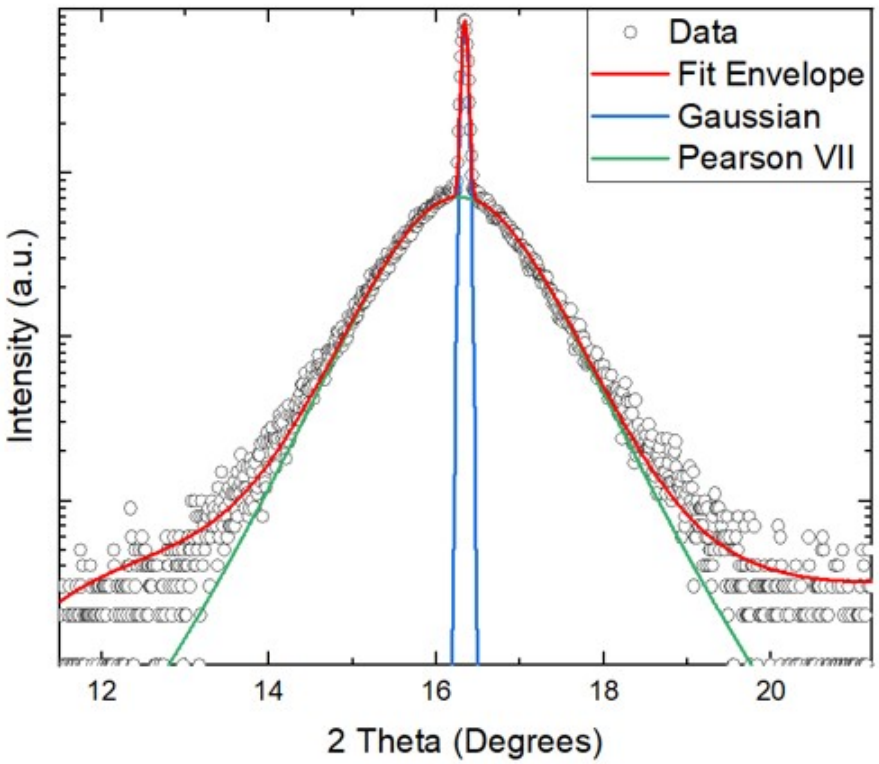

FIGURE 2.17. Example of a rocking curve data showing contribution from a narrow Gaussian component (blue) and broad Pearson VII (green) component. Overal fit is represented by the red line.

generated by conducting Bayesian inference analysis on least-squares results using a Markov Chain Monte Carlo algorithm. Information about the position, full width at half maximum (FWHM), area, and intensity of each peak can be extracted. During the fitting procedure multiple constrains can be applied to all parameters. Background can be fitted either separately using polynomial or spline function, or included in the least-squares routine as polynomial. The peak-shape functions offered by the software and used for fitting the data are:

Gaussian:

$$G(x) = \frac{C_G^{1/2}}{\sqrt{\pi} H} \exp(-C_G x^2) \tag{2.29}$$

where H is the full width at half maximum (FWHM),

$$x = 2\theta_i - 2\theta_k / H_k \tag{2.30}$$

$2\theta_i$ and $2\theta_k$ are the Bragg angle of the i^{th} point and the calculated Bragg angle of the k^{th} Bragg reflection, H_k is the FWHM of the k^{th} peak, and $C_G = 4\ln(2)$

Lorentzian:

$$L(x) = \frac{C_L^{1/2}}{\pi H}(1 + C_L x^2)^{-1} \tag{2.31}$$

where $C_L = 2$.

Pseudo-Voigt:

$$PV(x) = \eta G(x) + (1 - \eta)L(x) \tag{2.32}$$

is a linear combination of a Gaussian and a Lorentzian functions, where η is the pseudo-Voigt function mixing parameter defining the weighting between the two functions.

Pearson VII:

$$PVII(x) = \frac{\Gamma(\beta)}{\Gamma(\beta) - 1/2}\frac{C_P^{1/2}}{\sqrt{\pi}H}(1 + C_P x^2)^{-\beta} \tag{2.33}$$

where Γ is the gamma function, and β exponent describes the tails of the function: β= 1 is a Lorentz function and with increasing β the function resembles a Gauss function.

All of the functions presented are symmetrical and have their strengths and weaknesses in terms of thei intrinsic profiles. Gaussian distribution of the diffraction intensity is best fitted with the Gauss function, while for data with more pronounced tails the Lorentz function fits better. The most widely used line-profile is the pseudo-Voigt function compromising the Gauss and Lorentz function. The Pearson-VII function is similar to the Lorentz distribution with the possibility to adjust the tails by varying the β parameter [105].

To account of asymmetry in a peak, an asymmetric function can be used. The LIPRAS software offer a modification of the Pearson-VII function that allows for different integrated intensities on

both sides of the function. The asymmetric Pearson-VII is described by the following equation [106]:

$$\begin{aligned} &\text{for } x < x_0 \qquad aPVII_L(x) = \frac{N_L}{H_L\sqrt{\pi}} \frac{\Gamma(\beta_L)}{\Gamma(\beta_L) - 1/2}(1 + C_P x^2)^{-\beta_L} \\ &\text{for } x \geq x_0 \qquad aPVII_R(x) = \frac{N_R}{H_R\sqrt{\pi}} \frac{\Gamma(\beta_R)}{\Gamma(\beta_R) - 1/2}(1 + C_P x^2)^{-\beta_R} \end{aligned} \tag{2.34}$$

where N_L and N_R are the integrated intensities of the left and right side of the line-profile, therefore, for $x = x_0$ both equations will be equal.

After optimising the fit parameters in LIPRAS, the outcome was exported into Origin software, which was used to produce graphs. The data was compared with diffraction patterns calculated using VESTA software.

2.1.4 X-ray Reflectivity

X-ray reflectivity is a common analytical technique used to study thin films. The electron density perpendicular to the surface of the samples can be probed using x-rays to obtain detailed information about the thin film thickness, surface roughness and density.

2.1.4.1 Background

X-rays as electromagnetic waves experience refraction at interfaces between different media, similar to propagating light. For the visible light Snell's law is used to describe this phenomenon, with the refractive index n in the range between 1.2 and 2 for transparent materials (glass ranging from 1.5 to 1.8). In the case of electromagnetic waves, the index of refraction exhibits resonant behaviour at frequencies corresponding to electronic transitions. Normal dispersion were n increases with ω occurs on the low frequency side of a resonance[93]. Decay of n is immediately observed above resonant frequency. Transition frequencies are usually lower than x-ray frequencies, therefore, in the x-ray region the refractive index $n < 1$. Hence, the phenomena of total external reflection occurs for glancing angles lower than the critical angle α_c in accordance with Snell's law:

$$\cos\alpha = n\cos\alpha' \tag{2.35}$$

where α is the incident grazing angle and α' is the refracted grazing angle.

To derive the refractive index for x-rays, lets start just with the scattering contribution. The equation can be expressed as:

$$n = 1-\delta, \qquad \text{with } \delta = \frac{2\pi\rho_e r_0}{k^2} \tag{2.36}$$

where ρ_e is the electron density, r_0 is the scattering amplitude, and k is the wavevector related to the wavelength of the radiation by $k = 2\pi/\lambda$. Therefore, combining the Eqs. 2.35 and 2.36, the critical angle α_c can be calculated for total external reflection $\alpha' = 0°$:

$$\alpha_c = \sqrt{2\delta} = \frac{\sqrt{4\pi\rho_e r_0}}{k} \tag{2.37}$$

X-rays are also absorbed by the material. Attenuation of the x-rays in the medium follows the characteristic $1/e = \mu^{-1}$ length,where μ is the absorption coefficient. Therefore, the intensity attenuation after travelling a distance z is $e^{-\mu z}$, and the amplitude is attenuated by a factor of $e^{-\mu z/2}$.

If we now account the absorption process, the Eq. 2.36 can be rewritten as:

$$n = 1-\delta+i\beta, \qquad \text{with } \beta = \frac{\mu}{2k} \tag{2.38}$$

By replacing the electron density ρ_e with the product of the atomic density ρ_{at} and the atomic scattering length $f(Q)$ from the Eq. 2.16, the refractive index becomes [93]:

$$n = 1-\frac{2\pi\rho_{at}r_0}{k^2}\left\{f_0(0)+f_0(0)'+f_0(0)''\right\} \qquad \text{with } \beta = -f''\left(\frac{2\pi\rho_{at}r_0}{k^2}\right) \tag{2.39}$$

The Fresnel equations and Snell's law in the X-ray wavelength region can be delivered using Fig. 2.18. For that, the wave and its derivative at the interface $z = 0$ must be continuous. Then, the amplitudes are related in the following way:

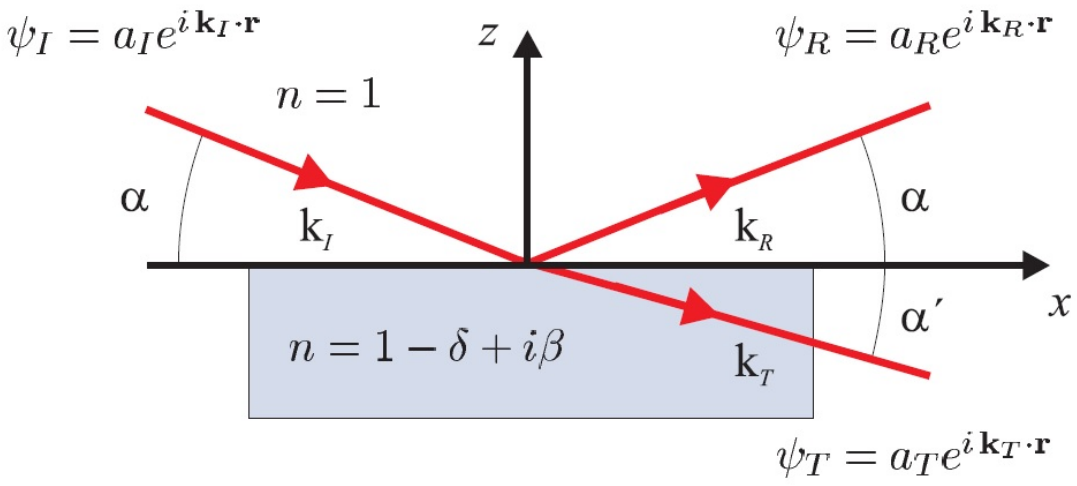

FIGURE 2.18. Schematic illustration used for deriving the Fresnel equations and Snell's law by requiring continuity at the interface of the wave and its derivative. Figure taken from [93].

$$a_I + a_R = a_T \tag{2.40}$$

and

$$a_I k_I + a_R k_R = a_T k_T \tag{2.41}$$

where a_I, a_R *and* a_T are the incident, the reflected and the transmitted amplitudes respectively, and k_I, k_R *and* k_T are similarly the wavevectors. In the vacuum the wavenumber can be denoted as $k = |k_I| = |k_R|$, and for the material as $nk = |k_T|$ [93]. The incident angle α_I is equal to the reflected angle α_R, therefore: $\alpha = \alpha_I = \alpha_R$. Whereas, the transmitted angle α_T will be denoted as α'. Taking into account the components of k parallel and perpendicular to the interface we get respectively:

$$a_I k \cos\alpha + a_R k \cos\alpha = a_T (nk) \cos\alpha' \tag{2.42}$$

$$-(a_I - a_R)k\sin\alpha = -a_T(nk)\sin\alpha' \tag{2.43}$$

By combining together equations 2.40 and 2.42, Snell's law (Eq. 2.35) can be delivered. Additionally, by considering Eq 2.40) and the perpendicular projection of k (Eq. 2.43 it follows that:

$$\frac{a_I - a_R}{a_I + a_R} = n\frac{\sin\alpha'}{\sin\alpha} \approxeq \frac{\alpha'}{\alpha} \tag{2.44}$$

This can be transformed into the Fresnel equations for the amplitude reflectivity, r, and amplitude transmissivity, t:

$$r \equiv \frac{a_R}{a_I} = \frac{\alpha - \alpha'}{\alpha + \alpha'} \qquad t \equiv \frac{a_T}{a_I} = \frac{2\alpha}{\alpha + \alpha'} \tag{2.45}$$

The intensity reflectivity, R, and the intensity transmissivity, T, are related to the amplitudes as $R = r^2$ and $T = t^2$ respectively. Using Eq. 2.44 α' can be decomposed into its real and imaginary parts [93]:

$$\alpha' \equiv Re(\alpha') + iIm(\alpha') \tag{2.46}$$

from which the attenuation with increasing depth follows:

$$a_T e^{i(k\alpha')z} = a_T e^{ikRe(\alpha')z} e^{-kIm(\alpha')z} \tag{2.47}$$

The fall of the intensity with a $1/e$ penetration depth Λ can be written as:

$$\Lambda = \frac{1}{2kIm(\alpha')} \tag{2.48}$$

For the X-ray diffraction and reflection phenomena, the wavevector transfers can be given as:

$$Q \equiv 2k\sin\alpha \approxeq 2k\alpha \qquad Q_c \equiv 2k\sin\alpha_c \approxeq 2k\alpha_c \tag{2.49}$$

with their dimensionless counterparts:

$$q \equiv \frac{Q}{Q_c} \approxeq \left(\frac{2k}{Q_c}\right)\alpha \qquad q' \equiv \frac{Q'}{Q_c} \approxeq \left(\frac{2k}{Q_c}\right)\alpha' \tag{2.50}$$

For the small α and α' the Snell's law (Eq. 2.35) can be rewritten after multiplying both sides by $(2k/Q_c)^2$, as:

$$q^2 = q'^2 + 1 - 2ib_\mu, \qquad \text{with } b_\mu = \left(\frac{2k}{Q_c}\right)\beta = \frac{2k}{Q_c^2}\mu \tag{2.51}$$

For the critical angle α_c the wavevector Q_c will take the following form:

$$Q_c = 2k\alpha_c = 2k\sqrt{2\delta} = 4\sqrt{\pi\rho r_0\left(1+\frac{f'}{Z}\right)} \tag{2.52}$$

Taking into consideration the wavevector form of Eq. 2.51, and the Fresnel equations for the amplitude reflectivity and transmittivity from Eq. 2.45, in conjunction with the condition that $\frac{2k}{Q_c^2}\mu \ll 1$, three different cases can be considered:

$q \ll 1$ On these terms q' is almost completely imaginary, with $r(q) \approxeq -1$ and $Im(q') \approxeq 1$. As the reflected wave is out of phase with the incident wave, which translates into a very weak transmitted wave, called an evanescent wave. The penetration depth is minimal $(1/Q_c)$ and independent of α for $\alpha \ll \alpha_c$

$q = 1$ Eg. 2.51 simplifies to $q' = \sqrt{b_\mu}(1+i)$. The incident and the reflected waves are in the same phase. The penetration is $b_\mu^{-1/2}$ times deeper.

$q \gg 1$ In this case Eg. 2.51 becomes $Re(q') \approxeq q$ and $Im(q') \approxeq b_{mu}/q$. The phases for the incident and the reflected waves are the same. The attenuation of the intensity reflectivity is $R(q) \approxeq (2q)^{-4}$, with the penetration depth, $\alpha\mu^{-1}$, therefore, there is almost complete transmission.

The behavior in those three scenarios is shown on Fig. X, where R is plot against Q. The total external reflection of x-rays for $q \ll 1$, where $Q < Q_c$. The critical angle $Q_c = \sqrt{2\delta}$ for $q = 1$, and a q^{-4} dependence above it for $q \gg 1$ (Add The description of infinitely thick layer + graph for it)

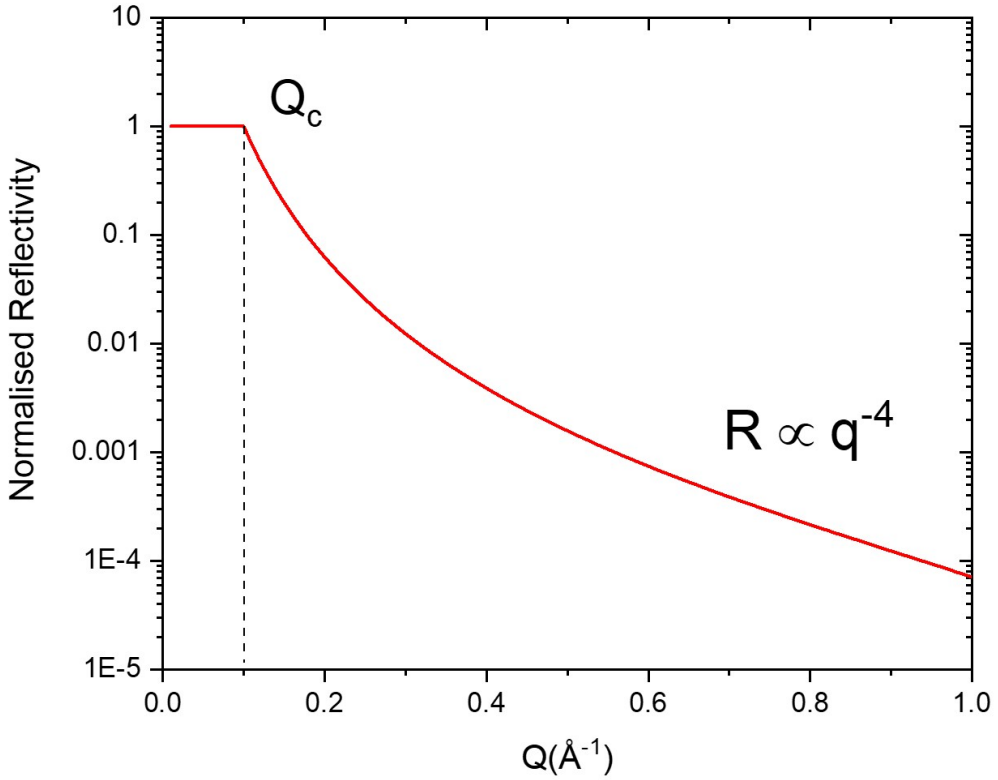

FIGURE 2.19. XRR for an infinitely thick sample, showing the reflectivity profile below the critical angle Q_c and decrease of the intensity equal to q^{-4}

Reflectivity from a single layer

For a single layer of finite thickness deposited on an infinite substrate, X-rays interact with three different media: the air, the sample and the substrate. Those regions are shown on Fig. 2.20 and are numbered 0, 1 and 2 respectively. The beam will be infinitely reflected in the medium 1 from the interface r_{12} and r_{10}. The outcome of that will be an infinite sum starting from reflection at interface 0 to 1 with amplitude r_{01}. The next contribution will be from a wave transmitted from medium 0 to 1, t_{01}, reflected at the interface 1 to 2, r_{12}, and then transmitted from 1 to 0, t_{10}, with a phase factor $p^2 = e^{iQ\Delta}$. Each next reflection will have transmission through the layer in both directions combined with more reflections in the sample and higher phase factor. The total

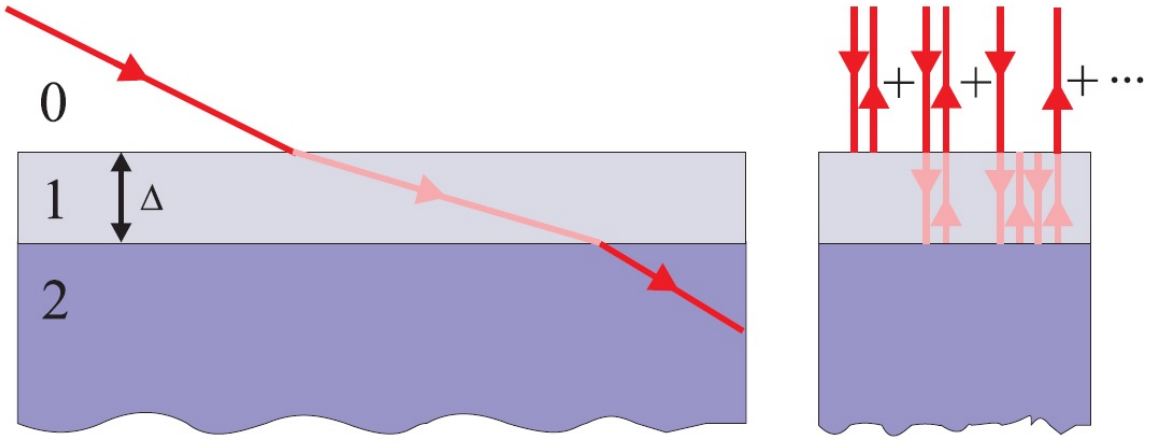

FIGURE 2.20. Schematic of the reflection and transmission in a finite layer of a material. Total reflectivity as can be seen on panel (b) is the the sum of the infinite number of reflections

amplitude reflectivity is given as following sum:

$$r_{sample} = r_{01} + t_{01}t_{10}r_{12}p^2 \sum_{n=0}^{\infty} (r_{10}r_{12}p^2)^n \tag{2.53}$$

This can be simplified as a geometric series $\sum_{n=0}^{\infty} x^n = \frac{1}{1-x}$ to produce:

$$r_{sample} = r_{01} + t_{01}t_{10}r_{12}p^2 \frac{1}{1 - r_{10}r_{12}p^2} \tag{2.54}$$

Using the relationships from Fresnel equation (Eq. 2.45), that: $r_{01} = -r_{10}$ and $r_{01}^2 + t_{01}t_{10} = 1$, this equation can be further simplified to give:

$$r_{sample} = \frac{r_{01} + r_{12}p^2}{1 + r_{10}r_{12}p^2} \tag{2.55}$$

The outcome of this equation is plotted in Fig. 2.21, and displays a periodic oscillation known as Kiessig fringes [107]. The peaks and dips correspond to the interference of the waves scattered in phase and out of phase respectively. The separation of the fringes is directly related to the thickness of the sample, d(Å), by:

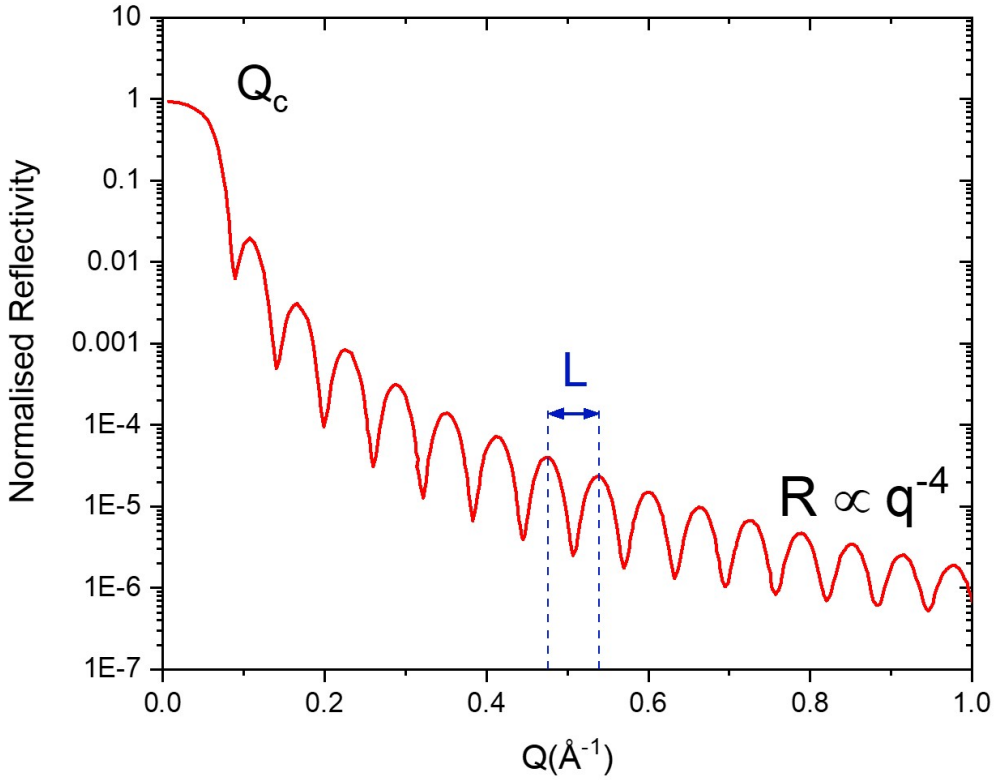

FIGURE 2.21. Example of a single layer on infinitely thick substrate, showing oscillations caused by interference between the reflected waves, known as Kiessig fringes.

$$d = \frac{2\pi}{L} \tag{2.56}$$

where L is the period of the fringes given in Å^{-1}.

Reflectivity from multilayers

To calculate the reflected intensity from multilayered systems on top of an infinitely thick substrate a number of methods can be used. The general approach is to expand the single layer model to account for multiple reflections and refraction. Although, an assumption that these

effects are sufficiently small at angles far away from the critical angle has to be made. Therefore, the multiple reflection and refraction can be considered in the region near α_c.

A recursive method based on the single layer model (Eq. 2.55) was developed in 1954 by Parratt [108]. This method accounts for a medium composed from N layers on an infinitely thick substrate, where the first layer is the top layer and the N^{th} layer is the bottom layer (the one closest to the substrate). To each layer, j, the refractive index $n_j = 1 - \delta_j + i\beta_j$ and the thickness d_j, can be assigned. The wavevector perpendicular to the surface, $k_{z,j}$, which is determined from the total wavevector for the j slab, $k_j = n_j k$. Moreover, the x component, $k_{x,j}$ dose not change throughout all layers, what means that $k_{x,j} = k_x$ for all j. Therefore, the $k_{z,j}$ can be calculated from [93]:

$$k_{z,j}^2 = (n_j k)^2 - k_x^2 \tag{2.57}$$

taking into consideration Eq. 2.49, that $Q_j = 2k_j \sin\alpha_j = 2k_{z,j}$ the wavevector transfer for each layer is:

$$Q_j = \sqrt{Q^2 - 8k^2\delta_j + i8k^2\beta_j} \tag{2.58}$$

The reflectivity at the interface between the layer j and $j+1$ can be calculated from the Fresnel relation, without including multiple reflections as:

$$r'_{j,j+1} = \frac{Q_j - Q_{j+1}}{Q_j + Q_{j+1}} \tag{2.59}$$

This equation can be used to calculate the reflectivity from infinitely thick substrate and the bottom layer N, labeled as $r'_{N,\infty}$, where $'$ stands for no multiple reflections. Above the substrate the reflectivity between layer N and $N+1$ can be summarized by using model of a single layer, with $p_j^2 = e^{id_j Q_j}$, as[93]:

$$r_{N_{x-1},N_x} = \frac{r'_{N_{x-1},N_x} + r_{N_x,N_{x+1}} p_{N_x}^2}{1 + r'_{N_{x-1},N_x} r_{N_x,N_{x+1}} p_{N_x}^2} \tag{2.60}$$

The reflectivity intensity for a multilayer sample on a infinitely thick substrate can be calculated using this equation recursively for every layer from the bottom to the surface.

Rough interfaces

The reflectivity described previously for single and multi layer systems, was based on the assumption that interfaces are sharp and flat. In real materials this assumption does not apply, as usually inter-diffusion of atoms occurs on interface due to the energetics of the deposition process and the relative difference in atoms size. Additionally, the finishing of a layer is not perfectly flat in most cases and a vertical fluctuations in the layer thickness is present, that can be interpreted as an interfacial roughness.

To account for those imperfections, the reflectivity from a multilayer with non ideal interface is the product of the intensity from an ideal multilayer, $R_I(Q)$ and a factor associated with an electron density gradient across the interface. Those changes can be modelled by summation of the contributions of infinitesimally thin layers and the incorporation of a function, $f(z)$ used to describe the electron density profile, with allowed any induced phase changes. This gives the reflectivity intensity for a graded interface as:

$$R(Q) = R_I(Q)\left|\int_0^\infty \left(\frac{df(z)}{dz}e^{iQ_z}dz\right)\right|^2 \tag{2.61}$$

This equation is also known as the *master formula* for the intensity reflectivity of a graded interface [93], where the modulus squared term is the Fourier transform of the electron density gradient. This term allows for the incorporation of an error function to describe the electron density profile across the non ideal interface. The derivative of this function is a Gaussian and the result of the Fourier transform of a Gaussian gives another Gaussian, therefore this formula can be modified to:

$$R(Q) = R_I(Q)e^{-Q^2\sigma^2} \tag{2.62}$$

where σ represents the thickness of the interfacial region.

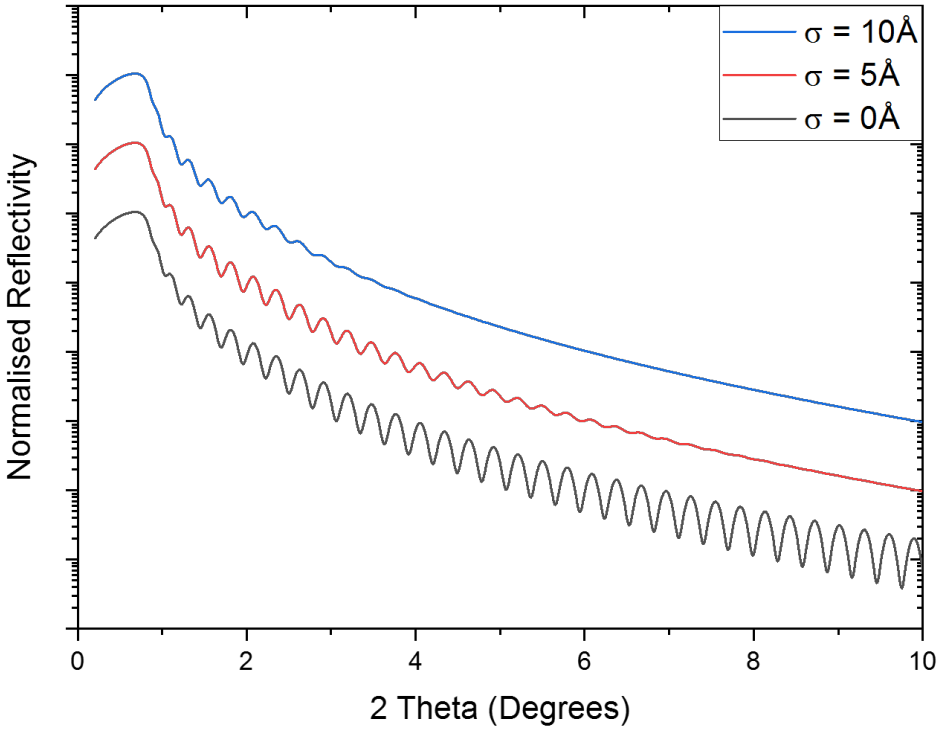

FIGURE 2.22. The effect of introducing a roughness to a model of 30nm UO_2 layer on a YSZ substrate. The black line shows ideal flat interface with no grading, the red line represents model with roughness of 5 Å, while the blue line is model with 10 Å of roughness. The reflectivity intensity decay faster with increased roughness.

By modelling the variation in the height of each layer it is also possible to account for the roughness of an individual layer. Based on the Parratt's recursive method [108] and method proposed by Nevot and Croce [109] it was possible to implement an uncorrelated roughness by varying the refractive index [110–112]:

$$n_j(z) = n_j + (n_{j+1} - n_j)F(z,\sigma_j) \tag{2.63}$$

where the Fourier transform, $F(z,\sigma_j)$ is defined as:

$$F(z,\sigma_j) = \frac{1}{\sigma_j\sqrt{2\pi}}\int_{-\infty}^{z} e^{(-z^2/2\sigma_j^2)}dz \tag{2.64}$$

By introducing a factor describing an uncorrelated roughness to the the reflectivity from an ideal multilayer, an expression for reflectivity with rough interface is given as:

$$R(Q) = R_I(Q)e^{-Q^2\sigma_j^2} \tag{2.65}$$

where σ_j is the root mean square (rms) roughness. The contribution of the roughness given by Eq. 2.65, is therefore identical to the contribution from the graded interfaces given by Eq. 2.62, what is the source of the difficulty in distinguishing whether the effect is caused by a surface roughness or a graded interface.

The influence of roughness in the interface on reflectivity profile is shown on Fig. 2.22. To show that, a 30 nm layer of UO_2 on YSZ substrates was modelled with three different roughness parameters. The example with perfect flat interface without grading is represented by the black line. As it can be seen with increase of the RMS from ideal scenario (black) to 5 Å(red) and then to 10 Å(blue), causes the reflectivity intensity to decay faster.

2.1.4.2 Data processing

For processing the XRR data Gen X software was used [113]. This software uses the differential evolution algorithm for fitting reflectivity data, and can be also used for analysing x-ray diffraction data. GenX utilises Parratt recursion method as an in-built function for fitting specular x-ray reflectivity data. To model the roughness of an interface a Gaussian distribution is used [109]. Furthermore, this software allows parameters such as instrument resolution and beam footprint to be taken into account.

A model of the sample is crated using a layered structure. Each layer is described using four parameters: layer composition, density, thickness and the interfacial RMS roughness. The density used in Gen X is recalculated from g/cm^3 to units per $Å^3$

$$dens = \frac{\rho(kg/m^3}{1.66054x10^3 x u_{scatt}} \tag{2.66}$$

where u_{scatt} is the total atomic mass of the elements defined in layer composition. The first layer of a model is the substrate, with thickness set to be infinite. The starting parameter

of substrate roughness is taken from the supplier information, and allowed to be fitted. The structure of the thin film deposited on the substrate might be formed from a single layer or be represented as a series of layers. The initial thickness of the layer is estimated based on the calibration for deposition rate. All that information is then used to calculate and optimize the modelled reflectivity intensity.

The optimisation is performed by varying the starting parameters of the model to minimize the difference between the calculated model and the data. This method is highly effective and allows to avoid local minima. To measure the difference between the calculated model and raw data a figure of merit (FOM) function is used. The FOM is also used to calculate the error on each fitted parameter, by finding the range of the parameter within 5% increase of the FOM.

2.2 XPS and UPS

X-ray photoelectron spectroscopy is a powerful technique for precise characterization of a sample surface, known also as Electron Spectroscopy for Chemical Analysis (ESCA). It is a surface-sensitive method for investigating the elemental composition of the outer 1-10nm of the sample. This technique is very useful for studying oxide materials as in addition to information about the chemical composition, it is also sensitive to element bonding environment, which allows to determine the sample stoichiometry. XPS measurements of uranium dioxide polycrystalline thin films have been conducted to probe the dependence of oxidation rate based on the crystallographic orientation, as well to confirm the oxidation state of the samples. Therefore, in this section, the basics of the operation and instrumentation will be described.

Introduction

X-ray photoelectron spectroscopy utilises the photoelectric effect to extract information about the material and its bonding environment. This occurs when a sample surface is irradiated with x-rays, and enough energy is transferred for photoelectrons to be emitted from the exposed material. By analysing the energy of the released photoelectrons, information about the chemical state of the sample is obtained.

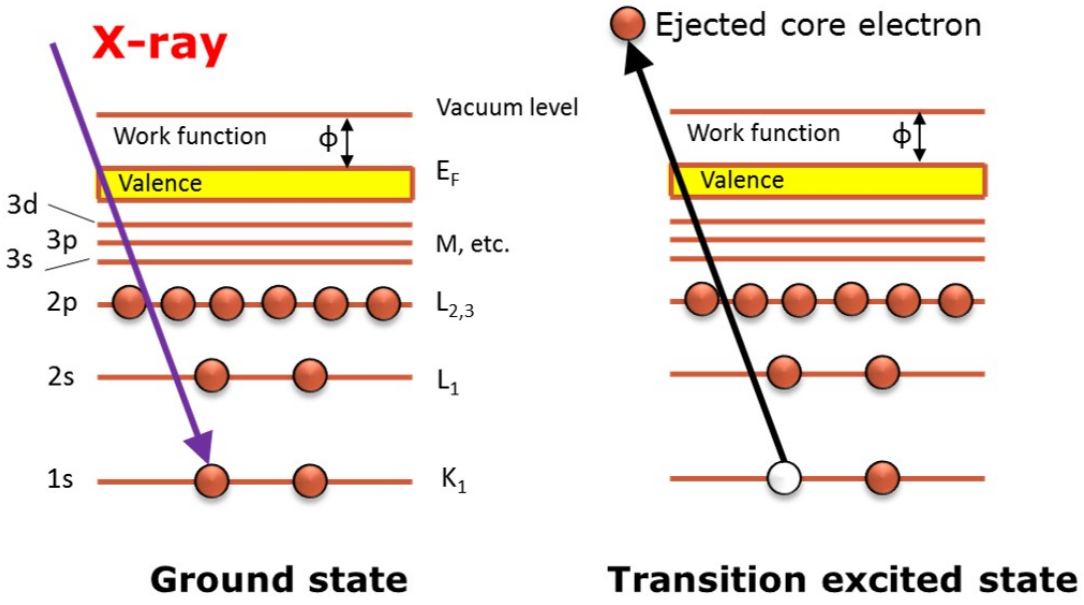

FIGURE 2.23. Schematic illustration of the photoelectric effect utilised in XPS.

Schematic of this process is shown on Fig. 2.23. If the incident x-ray posses energy higher than the binding energy (BE) of the core electron, then this electron will be ejected from the material when colliding with the x-ray. The kinetic energy (KE) of the released electron is related to the binding energy and can be calculated using following equation:

$$E_{KE} = h\upsilon - \phi - E_{BE} \tag{2.67}$$

where h is Planck's constant, υ is the frequency of the electromagnetic radiation, and ϕ is the work function of the material. The work-function is defined as the minimum energy needed to remove an electron from a solid surface to the position far from the surface on the atomic scale but still too close to the solid to be influenced by ambient electric fields in the vacuum.

This measurement is conducted in an ultra high vacuum environment (UHV) in order to minimise the collision between the electrons that escaped from the sample and the gas molecules, resulting in increased read out on the detector. The mean path of photoelectrons within the material is also very limited due to inelastic collisions, recombination, excitation of the sample, recapture or trapping in various excited states within the material. Therefore, most of the

signal will come from the surface and the signal will be weaker exponentially with the depth, disappearing after around 10 nm based on the source of x-rays and the investigated material.

Electronic structure

Each electron in a material can by described using a set of quantum numbers: n, l, and j. The first number n, is the principal quantum number that describes the electron shell, or its energy level. The values of n are natural numbers starting from 1, making it a discrete variable. The second number, l, is the orbital quantum number (or angular quantum number), and defines the electron sub-shell. The values of l are also discrete variable, and for l = 0, 1, 2, and 3, sub-shells are labeled as s, p ,d, and f, respectively from their historical names sharp, principal, diffuse, and fundamental. Orbitals can hold two electrons with the values $s = \pm$ 1/2. Therefore, the amount of electrons that each sub-shell can hold is $2(2l + 1)$, and each electron shell can hold $2n^2$ electrons. The last value, j, is the total angular momentum quantum number. This spin-orbit splitting of different energy levels is defined as $j = l+s$. The graphic representation of the electronic configuration is shown on Fig. 2.24

Consequently, j will have two values for l equal and above 1, while for l = 0, there will be only one value of j. In case of uranium with $4f$ configuration, the spin-orbit values will be j = 7/2 and j = 5/2, as the principal quantum number n = 4 and the orbital quantum number l = 3. This can be denoted as $4f_{7/2}$ and $4f_{5/2}$, and the area ratio between those peaks will be 4:3, as they have 8 and 6 electrons respectively.

Instrumentation

The main components of a typical XPS systems are: an ultra-high vacuum (UHV) chamber made of stainless steel with a set of pumps, an x-ray source and an electron energy analyzer. More about the UHV chambers and pumping system can be found in Chapter 5, and x-ray sources were described previous in this chapter. The most common type of electron energy analyzer is the concentric hemispherical analyser (CHA).

A schematic diagram of system with the concentric hemispherical analyser configuration is shown on Fig. 2.25. The passage of electrons with specific energy to be counted is possible by

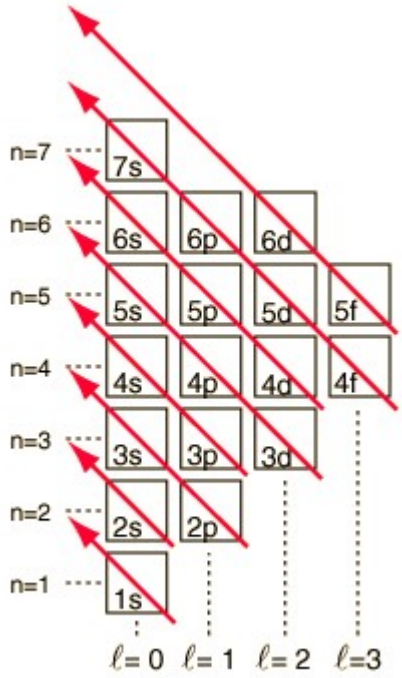

FIGURE 2.24. Schematic representation of the order of filling of electron states, witch marked principal quantum number n, and orbital angular momentum quantum number l. Figure taken from [114]

utilizing two metal hemispheres. Potentials are applied to both of them allowing to generate an electric field between them. Consequently, the kinetic energy of the electrons will decide if they can travel through this potential and reach the detector, as the electrons with too high energy will impinge on the outer hemisphere and with too low energy will be attracted to the inner hemisphere.. By adjusting the electric field created between the concave, and the convex hemispheres it is possible to scan for desired kinetic energies of electrons.

Before electrons ejected from the sample surface enter the CHA detector, they are focused using a series of magnetic lenses. Two type of lenses can be distinguished, Constant Retard Ratio (CRR) and Constant Analysis Energy (CAE), the second one is also known as Fixed Analyser Transmission (FAT). In the first one, the initial kinetic energy of the electrons is reduced to a set percentage by slowing them down and a scan is conducted by changing the voltage difference between the hemispheres. In the second mode, the voltage applied to hemispheres is fixed and a scan is performed by varying the retardation of the electrons. Constant energy resolution is

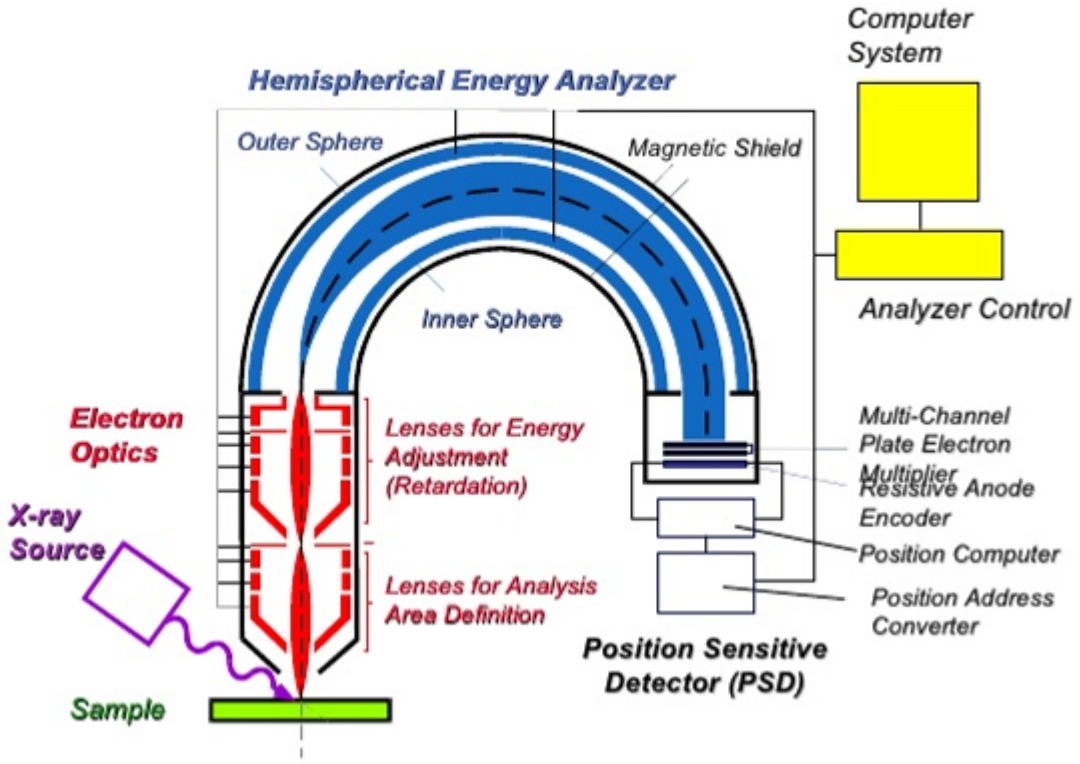

FIGURE 2.25. Diagram of a system with a concentric hemispherical analyser used in XPS measurements. Figure taken from [115]

achieved by using CAE mode, while constant resolving power is obtained with CRR.

Measurements conducted for this thesis were performed on three different systems. the first one is the Bristol NanoESCA facility which uses an Al x-ray tube source with a ScientaOmicron XPS Argus analyser. The other two systems are based at Diamond Light Source, and are Kratos Axis Ultra DLD and Thermo Fisher Scientific NEXSA. Both systems are equipped with monochromatic Al x-ray sources and are capable to performing XPS mapping of the sample surface with an image resolution close to 3 μm. All mentioned systems operate at UHV.

Software and data analysis

X-ray photoelectron spectroscopy data in this thesis was analyzed using CasaXPS peak fitting software. This software offers the possibility for both spectral and imaging data processing. Before

performing the fitting operation, data was calibrated as specified in each data section, due to the difference in the work function ϕ of the electron spectroscopy analyser.

From the numerous backgrounds offered in CasaXPS, to fit the background of the data presented in this thesis, the Shirley method [116] was used due to the nature of the uranium peaks. The essential feature of the Shirley algorithm is the use of the integrated areas of the peaks, A_n, to calculate the background intensity [117]

$$I_{BG} = I_{min} + \kappa \frac{A_2}{A_1 + A_2} \tag{2.68}$$

where κ is the step in the background. The peaks regions were fitted using Gaussian/Lorentzian peakshapes, typically with mixing ratio of 30:70, respectively.

Ultraviolet Photoelectron Spectroscopy (UPS)

Ultraviolet Photoelectron Spectroscopy (UPS) is based on the same principle as XPS. The difference between those two techniques is the energy of the ionising radiation. While in XPS high energy photons (higher than 1keV) are used to induce the photoelectric effect, UPS utilises photons with energies of 10s of eV. To produce ultraviolet photons gas discharge lamps are used, usually filled with helium gas that have photon energies of 21.2eV and 40.8eV for He I and He II respectively.

UPS is sensitive to the valence band region as most core level photoemissions are inaccessible due to lower energy of the photons. Two types of experiments can be conducted using UPS: electronic workfunction measurement and valence band acquisition.

The molecular orbitals from which valence band photoelectron are ejected posses a high degree of hybridisation. This causes the shifts in peak binding energy more varied and subtle compared to the core level photoemission peaks. Therefore, those spectra are not used for quantification, but mostly for material characterisation. Collection of of both XPS and UPS valence bad spectra is extremely useful as the ionisation cross section of an orbital is dependent on the incident photon energy. UPS is also more surface sensitive, as lower incident photon energy results in lower kinetic energy of emitted photoelectrons, therefore information in UPS measurements comes from approximately 2-3 nm from the sample surface.

Another surface property that can be examined using UPS is workfunction. The workfunction is extremely sensitive to any variation in the composition and structure at the surface, including atmospheric contamination. The workfunction is obtained by measuring the difference between the Fermi Level and the end of the spectrum on the low kinetic energy. Typically a small bias of 5-10 V is applied to the sample surface to deconvolute the workfunction of the material from the internal workfunction of the spectrometer.

The UPS measurements of uranium dioxide thin films were performed at the Bristol NanoESCA facility and the data was analyzed using IgroPro and Fiji software.

2.3 Electron Microscopy

Electrons are subatomic particles with negative electric charge. They were discovered in 1897 by J. J. Thomson and his team of physicists [118]. With a much shorter wavelength than visible light, electrons are perfect candidates for microscopy techniques. Through this PhD, multiple electron microscopes and imaging techniques were used to study uranium dioxide thin films. In this section basics of the electron generation, their interaction with matter and microscopes will be described.

2.3.1 Electron emission sources

Electrons can be emitted from a solid cathode via two processes: thermionic emission and field emission [119]. In the first process, a filament material is energized by resistive heated, so electrons have enough energy to overcome the material work function barrier and be emitted from the surface of the filament. In the second process, field emission is based on reducing the work function barrier so electrons can tunnel through the potential barrier.

A typical material used in the fabrication of thermionic emission filaments is tungsten as it has the highest melting point and lowest vapour pressure of all metals, moreover its price is very low. Schematic of thermionic source with tungsten filament is shown Fig. 2.26. The disadvantage of this solution is short lifetime compared to other sources due to gradually loss of mass caused by evaporation. Also, it has lower image resolution as in high operating temperature

their beam spread is broader with lower brightness. Therefore, when the higher special resolution is required, a single crystal of lanthanum hexaboride (LaB_6) and cesium hexaboride (CeB_6) are used as sources, as shown on Fig. 2.26. They need lower temperatures to emit electrons, what improves beam spread and provides higher brightness. Their lifetime is significantly higher as those materials are less volatile than tungsten. The current of thermionically emitted electrons is described by Richardson's equation:

$$J = A(1-\overline{r})T^2 e^{(-\frac{e\varphi}{kT})} \tag{2.69}$$

where J is the current density, A is the Richardson constant, $\overline{r}$ is the zero-field reflection coefficient for incident electrons, T is the absolute temperature and φ is the work function. T = absolute temperature

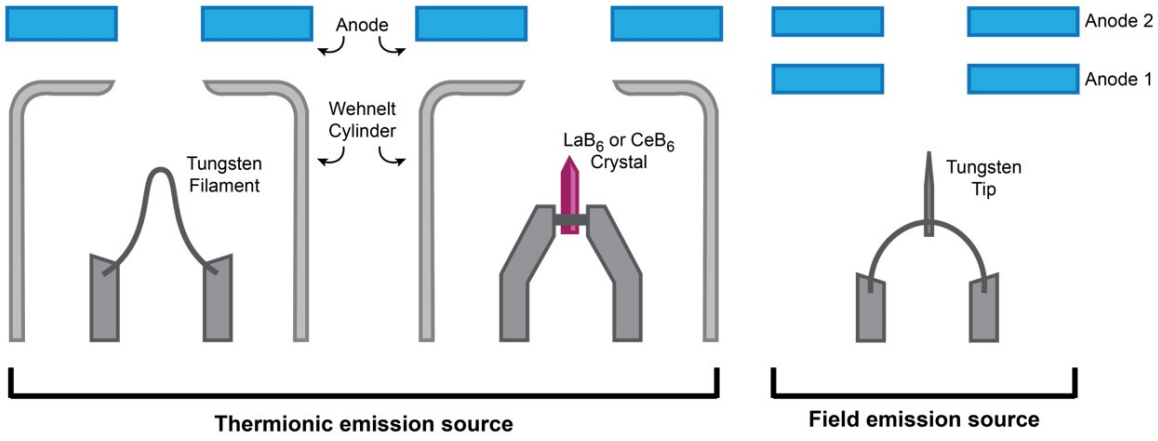

FIGURE 2.26. Illustration comparing the various electron emission sources. For thermionic sources the Wehnelt cylinder focuses the electrons as they flow toward the anode. In a field emission source, the first anode accelerates the electrons whereas the second anode focuses them. Figure taken from [120].

Field emission sources (FEGs) use a strong electrostatic field to induce electron emission[120]. This solution requires an extremely sharp tip, with a radius lower than 50 nm, fashioned from a source material, where high-energy electrons can escape due quantum mechanical tunneling. The image quality is enhanced, as brightness is much better due to the emission area which

is in nanometers rather than in micrometers as in thermionic source. The lifetime of FEG is the highest from all the sources, the only disadvantage of this source is its price, as it requires ultra-high vacuum environment to sustain an electrostatic fields. The current in field emission sources can be calculated from the following Fowler-Nordheim-type equations equation [121]

$$J = \Big(\frac{1.55x10^{-6}E^2}{\varphi}\Big)exp\Big(\frac{-6.86x10^{7}\varphi^{\frac{3}{2}}\Theta(z)}{E}\Big) \tag{2.70}$$

where E is the field strength and $\Theta(z)$ is the Nordheim elliptic function:

$$\Theta(z) = 3.62x10^{-4}\frac{E^{\frac{1}{2}}}{\varphi} \tag{2.71}$$

Amongst FEG sources, two types can be distinguished cold sources (cFEG) and Schottky FEG. In the second type, the field emission is thermally enhanced combining advantages of thermionic and field emission sources. This is achieved by coating a sharp tip of tungsten with zirconium oxide, the potential barrier is lower and less thermal heating is required to start emission. Although, generally the Schottky emitter offers higher brightness, they have shorter lifetime than cFEG and at lower voltages the resolution is also lower due to a larger energy spread.

2.3.2 Electron beam - sample interaction

When a focused beam from a thermal field emission gun or FEG hits the surface of a specimen a variety of physical processes occur. Those scattering events transfer energy from the electron beam to the sample atoms. The path they can travel within the solid is therefore limited as well as alternation of the direction. This interaction produces the backscattered electrons (BSE), secondary electrons (SE), and X-rays [122]. By collecting and processing those signals, information about the sample topography, composition, crystal structure or even local magnetic and electric fields can be extracted. Those processes can be generally divided into two subgroups similarly to the x-rays: inelastic and elastic scattering.

2.3.3 Inelastic scattering

In inelastic interaction a variety of processes change the energy of the incident electron beam. The energy transfer between the sample atoms and the beam produces a multitude of signals that can provide useful information about the material. The detailed explanation can be found in [122]. Here only brief description is provided:

Secondary electrons: Those electrons are primary located in outer-shell therefore are weakly bounded and easy to eject and form secondary electrons. Due to low binding energy of few eV, only signal from the top layers of atoms (10 nm) can be detected. The observation of those electrons allows to create a topographical image of the sample in high resolution, allowing detection of surface features.

X-rays: When electrons that are tightly bound in inner shell are ejected, their vacancy is filled by the relaxation of an electron from a higher orbital, which subsequently results in emission of characteristic X-rays.

Auger Electrons: X-ray emitted from the sample can further interact with electrons. If energy from the x-ray is transferred to another electron causing its ejection, this ejected electron is called an Auger electron.

Breaking Radiation: The deceleration of the beam electron in the electrical field of the atoms leads to production of a broad continuum of X-ray energies called Bremsstrahlung radiation.

Plasmons: When incident electrons interact with conducting metallic solids, the energy transferred can induce collective oscillations in the free electron gas. These oscillations are called plasmons.

Phonons: The electron-sample interaction can cause heating of the specimen. The increase in the vibrational energy can be transmitted throughout the sample, what is referred to as phonons.

Cathodoluminescence: In case of a semiconductor, incident electrons can promote electron from valence band in to the conduction band. The relaxation from this configuration

will emit a photon with an energy equal to the semiconducting band gap.

2.3.4 Elastic scattering

Simultaneously with inelastic scattering, elastic scattering occurs. In this event there is no transference of energy between the specimen atoms and the incident beam. Due to interaction of the electron beam with the positively charged atomic nucleus a Coulomb repulsion occurs, so the electron beam is deflected by the electrical field of an atom. Result of this is the change of the original trajectory on to a new path[122].

The probability of elastic scattering strongly depends on the atomic number Z of a specimen material and on the energy of the electron. Higher nuclear charge has bigger cross-section, thus probability of scattering incoming electrons is greater. For this reason heavier materials with high Z appear brighter when imaged. Apart of using elastically scattered electrons to probe the topography of the sample, they can be used for diffraction studies similar to x-rays. Adjustment of the incident electron energy allows to tune its wavelength into inter-atomic region. Those electrons can then be used to produce electron diffraction patterns, providing crystallographic information.

2.3.5 SEM

Scanning Electron Microscope is an excellent tool to investigate surface, composition, crystallographic orientation, and other physical and chemical properties of thin films. This instrument creates magnified images of a specimen using a beam of high-energy electrons (1-30keV) and rastering across the specimen surface. Schematic of a typical SEM is shown on Fig 2.27. After an electron being ejected from an electron source and accelerated to high energy, the beam is reduced successively when passing through apertures, electrostatic and.or magnetic lenses, and electromagnetic coils. This focused beam of electrons scan sequentially discrete locations on the specimen creating an image.

Two main signals are used for investigation of the sample surface are backscattered electrons (BSEs), which were deflected by the atoms in the sample, and secondary electrons (SEs) that escaped from the sample surface after bombardment from incident beam electrons. The majority

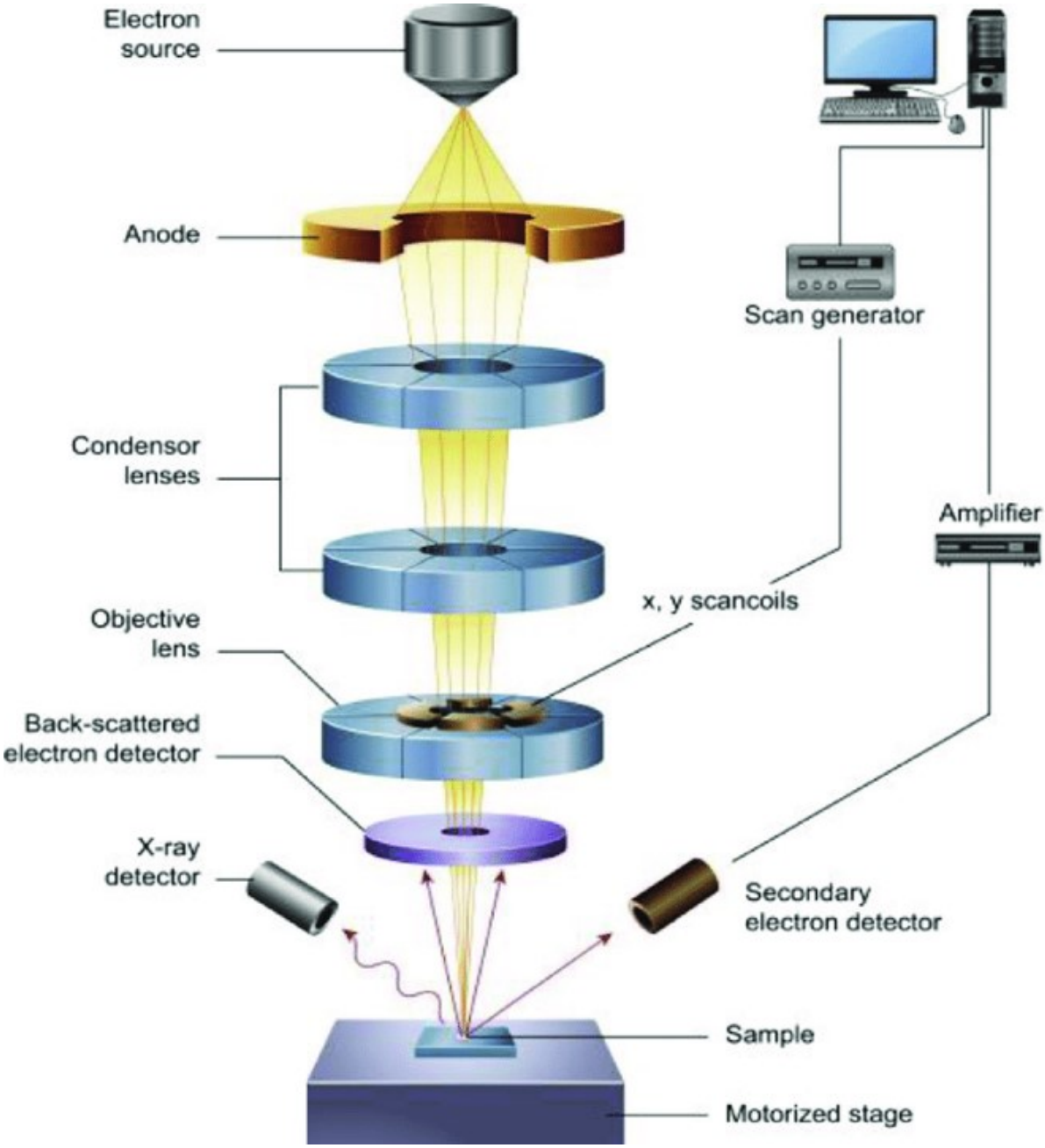

FIGURE 2.27. Schematic of an SEM. Figure taken from [123].

of the secondary electrons are ejected from the specimen surface with energies below 5 eV. To measure those signals one or more detectors can be used. The most popular is the Everhart-Thornley (ET) detector [124], that can detect both the secondary electron and the back-scattered electron. However, the ET detector is mostly used for the secondary electron, and a separate

detector, insensitive to SEs, is dedicated for backscattered electrons.

Energy dispersive X-ray analysis (EDX)

Characteristic x-rays emitted upon interaction of the electron beam with the sample atoms can be measured to provide information on the elemental composition of a sample. This technique is called Energy dispersive X-ray analysis (EDX). The unique atomic structure of each element allows to easily identify it. However, due to the materials used in the construction of the detector, analysis of elements with masses typically greater than sodium might not be possible.

The lithium-drifted silicon [Si(Li)-EDS] detector was the original type of EDS [125]. This detector has a layer of p-type silicon crystal covered with uniform thin layer of gold, which acts as an electric contact to the semi-conductor. To reduce the migration of indium and lithium dopant in silicon, cooling with liquid nitrogen during operation is required. When an x-ray photon is absorbed in the active volume of Si, an electron from inner atomic shell is ejected. The ejected photo-electron undergoes inelastic scattering within the Si crystal. This generates an electron-hole pairs, and by applying potential between the entrance surface electrode and the back surface electrode it is possible to produce a charge. This process requires around 3.6 eV energy per electron hole pair, therefore for a Mn K-L_3 photon (5.895 keV) 1638 electron-hole pairs are created, generating a charge of 2.6 x 10^{-16} coulombs [122].

Although it might be possible to detect atoms with a mass grater than lithium, the crystals are held in high vacuum shielded with an 8 μm thick window of beryllium. This window stops any x-rays with energies lower than 0.8 keV, therefore quantification is accurate for mass higher than sodium. A newer construction, the silicon drift detector design (SDD-EDS), is based on the same detection physics, the difference is in the rear surface electrode. Collection channel created out of the nested ring electrodes with a small central anode, allows to bring free electrons deposited anywhere in the detector volume to the central anode for collection.

The system used for EDS measurement in this work was Zeiss Sigma HD VP Field Emission SEM with EDAX EDS detector, and data was analysed using software provided with the equipment (APEX^{TM} Software for EDS).

Electron backscatter diffraction (EBSD)

Electron backscatter diffraction (EBSD) was developed for orientation determination and phase identification purposes.The diffraction patterns are obtained by illuminating a highly tilted specimen with an electron beam. The backscatter electrons are produced due to inelastic interaction of the incident electron beam with the sample atoms. In conventional EBSD system backscattered electrons are detected from a sample volume, while in transmission-EBSD (TKD) the patterns are formed by the transmitted electrons through a very thin sample.

In both cases, part of the electrons scatters inelastically losing a small amount of the original energy satisfying the diffraction condition of the sample crystalline planes. Electrons that escaped from the region closer to the sample surface, create the EBSD pattern. The first to describe these patterns was Kikuchi, after whom they are called Kikuchi patterns [122]. The Bragg conditions for diffraction will be satisfied for some of the backscattered electrons. The accelerating voltages used in the SEM (10-30 kV) will produce electrons with short wavelength, resulting in a small Bragg angle (below 2°). The typical Kikuchi patterns with effect of the acceleration voltage are shown on Fig. 2.28. The Kikuchi bands appear as nearly straight lines, and with increase of the acceleration voltage the Kikuchi bands are narrower due to decrease in the Bragg angle.

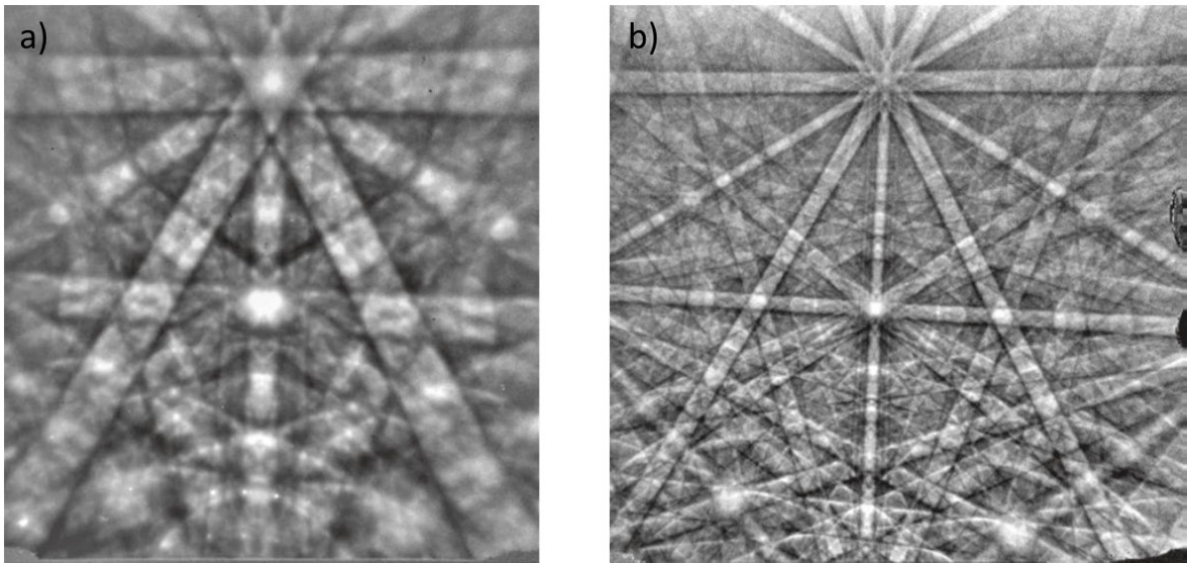

FIGURE 2.28. Example of Kikuchi patterns recoreded at different acceleration voltage, (a) 5 keV and (b) 40 keV. Figure reproduced from [122].

The EBSD measurement were conducted at acceleration voltage of 30 keV and aperture of 120 μm using Zeiss Sigma HD VP Field Emission SEM with EDAX EBSD detector. To analyse the data OIM Analysis^{TM} software was used.

Variable Pressure Scanning Electron Microscopy (VP-SEM)

The regular SEM must operate in high vacuum environment, therefore typically the sample chamber pressure is around 10^{-6} mbar. This is necessary to sustain stable operation of the electron source, which has to operate in high vacuum otherwise the gas molecules will diffuse to the gun and the increase of pressure might cause an unstable operation and lead to gun failure. Most of the conventional SEM is equipped with a separate pumping system for the gun to prevent this event. Another reason for operating in low pressure is the integrity of the beam, as the electron beam will scatter elastically and change trajectory while encountering gas atoms, deviating out of the focused beam. The Everhart-Thornley secondary electron detector can not operate also above $10^{-}3$ mbar, due to bias of +10 000 volts or more applied to the scintillator. In higher pressure gas will ionize between the scintillator and the Faraday cage (+250 V), and electrical arcing might damage the detector.

The study of insulating materials requires deposition of conductive coating to provide discharging patch for the electrical charge that develops on the surface after interaction with the electron beam. Not all materials can be covered, especially if the specimen will be used for further studies or fabrication processes. This case applied to annealed and polished ceramic YSZ substrates, where putting a conductive layer of different materials was impossible as the substrate was later used for growth of epitaxial uranium dioxide thin films. Imaging of this and similar materials without need of coating become possible due to the development of the variable pressure scanning electron microscope (VPSEM).

The VPSEM uses a differential pumping system that allows to increase the pressure in specimen chamber even up to 25 mbar, maintaining high level of imaging [122]. The ionized gas atoms allow discharging of uncoated insulating sample. Multiple gases such as oxygen, nitrogen, and argon or even water vapor can be used, not only to allow insulating sample characterization, but also to conduct in-situ experiment watching changes of the sample in "real time".

The microscopes with such capabilities used throughout this thesis were the Zeiss Sigma HD VP Field Emission SEM located within the School of Physics (IAC) at the University of Bristol and the High Temperature - Environmental Scanning Electron Microscope FEI Quanta 200 FEG ESEM at the Institut de Chimie Separative de Marcoule (ICSM) in Marcoule, France.

High Temperature Environmental Scanning Electron Microscope (HT-ESEM)

Working at elevated temperatures with ambient pressure under SEM has been a long lasting goal for many researchers and remains to this day a difficult technique to operate efficiently [126]. From two detectors used in a conventional SEM, the ET and the backscattered electron detector, only the first one can be used in high temperatures. The second one due its sensitivity to light illumination has no use because of the black body emission associated with temperature. Furthermore, in closer distance to heat it semiconductor properties would disappear. Due to those reason only the ET detector is linked with the furnace inside an SEM system.

Generally two ways are used to heat the sample in the SEM chamber, leaser heating (LASEM) [127] and resistive heating. The first one is useful if local heating of the sample is required to study specimen response to thermal shocks. Special care have to be taken to protect the detector from extreme thermal electron emission and gas emission from the specimen [126]. Laser can be also used to heat an entire sample holder providing simultaneously heating for the entire sample [128]. The maximum reported temperature achieved by this solution is 1700°C [129]. The second solution, resistive heating, usually compromise of heating element made out of refractory metal. This type of heating provides heating to the entire sample, and a temperature of even 2500°C can be achieved [130].

Another issue while operating at high temperatures is emission of thermal electrons, which intensity can be calculated using equation 2.69. The challenge is to separate the thermo-ionic emission, that can be higher than the signal coming from the interaction of incident beam with the sample, from the secondary electron emission. The best solution is to use a suppression grid or a shielding system for filtering the electrons energy. Biased applied to the suppression grid allows to stop thermionically emitted electrons and let pass higher energies possessed by secondary electrons. The shielding system protects also the detectors from light emission [126].

The microscope used for in-situ oxidation studies presented in this thesis was High Temperature - Environmental Scanning Electron Microscope FEI Quanta 200 FEG ESEM at the Institut de Chimie Separative de Marcoule (ICSM) in Marcoule, France, operated by Renaud Podor.

Transmission Electron Microscope (TEM)

Transmission Electron Microscopy (TEM) uses information from high-energy electrons that are transmitted through ultrathin specimens, rather than electrons scattered from sample surface as in SEM. The same sources of electrons can be utilised in TEM, including lanthanum hexaboride (LaB_6) crystals and FEGs. However, the acceleration voltage is much higher than SEM, and typically its range 80-300 kV. The energy of the electron beam limits the thickness of the sample that can be investigated, based on the material the upper thickness is around 100 nm [131].

Construction of a Transmission Electron Microscope is similar to a beam set-up in SEM, a schematic is shown on Fig. 2.29. The key components of the system are the electron gun, electrostatic lenses to focus the electrons before and after the specimen, and a transmitted electron detection system [132].

In TEM, the two mainly used imaging modes are: bright-field (BF) and dark-field (DF). In the first mode the incident beam, after passing through a sediment, is filtered by aperture placed in the back focal plane of the objective lens, therefore only direct beams are recorded. In areas with lower diffraction the resulting image will be brighter. Therefore areas which are thicker, have heavier atoms or a crystalline area have denser packing will appear darker. In the second mode, dark-field (DF), the direct beam is blocked by the aperture and the diffracted beams are let through to create the image. As the diffracted beam strongly interacted with the sample, information about particle size, stacking faults and planar defects can be extracted.

Due to high energy of the electrons used in TEM their wavelength is extremely short, around hundred times smaller than the spacing between atoms in a solid. This allows to observe diffraction of electrons as some of them will be scattered under angles determined by the crystal structure of the sample, and rest will pass without deflection. This measurement is performed by changing the objective aperture to the diffraction aperture. The diffraction apertures have different sizes allowing to choose the area of the sample to record the diffraction pattern. This

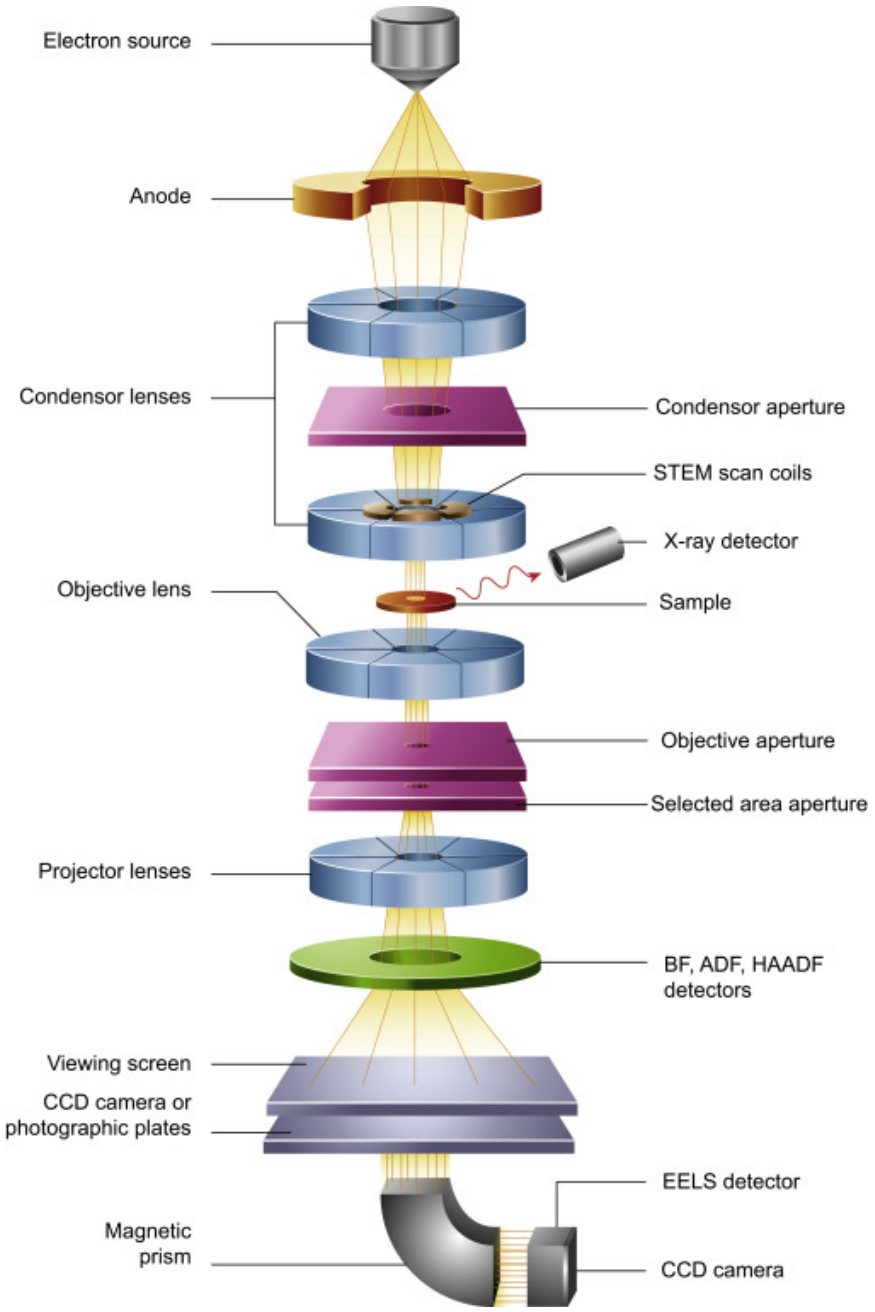

FIGURE 2.29. Schematic of components in a Transmission Electron Microscope. Figure taken from [132].

technique is therefore called Selected Area Diffraction (SAD) [in some literature refereed as Selected Area Electron Diffraction (SAED)].

Generally three types of the selected area diffraction pattern (SADP) are observed, based on the crystal structure of the specimen. For a polycrystalline system with randomly distributed

grains, signal visible as rings formed from spots will be observed. If the specimen is amorphous then halos will be visible. In case of a single crystal material, sharp spots arranged according to the symmetry of and the d spacing of the crystal will be recorded. Similar to x-ray diffraction, Bragg's law can be use for determining the d spacing of the analysed area of the sample.

Another feature offered by the transmission electron microscope is high-resolution imaging (HRTEM). The HRTEM is an extremely powerful technique allowing for direct imaging of the atomic structure of the sample with point resolution of around 0.5 Å, from which the d spacing of the lattice can easily be extracted. Images are obtained by using a large objective aperture allowing a direct beam and some diffracted beams to pass through. Multiple images taken at different angles for the sample sample allow to create a 3D map what is called electron crystallography.

The TEMs used in this thesis was a Jeol 1400 TEM placed at School at Chemistry, university of Bristol, operated by Dr Sean Davis. The software used for data analysis was Gatan Digital Micrograph.

Scanning Transmission Electron Microscopy (STEM)

Basic transmission studies of a specimen can be also performed in a SEM microscope (STEM). A scanning transmission electron microscope, has additional detectors usually a passive scintillator-photomultiplier placed below the sample that can collect signal that passed through the specimen. Same as in TEM, bright-field and dark-field images can be created. The detector in this microscope will produce images only from inelastically scattered electrons as elastically scattered electrons will not reach the detector. Therefore, Rutherford scattered electrons are collected and there is a direct correlation between the local contrast and the atomic number Z. This technique is known as high-angle annular dark-field imaging (HAADF) or Z-contrast imaging.

Possibilities of conducting STEM mesurments are offered and were used on FEI Helios NanoLab 600; Dualbeam microscope with three-axis micromanipulator upgraded with Kleindiek Nanomanipulator, EDX system Oxford Instruments (XMax-50), platinum deposition and selective carbon mill.

2.3.6 Focused ion beam (FIB)

Focused ion beam (FIB) system offers possibilities of imaging samples similar to SEM, but instead of the focused beam of electrons, a beam of focused ions is used. Bombarding the sample surface with ions will produce secondary electrons and secondary ions which can be used for creating an image. Destructive properties of ions can be also used for patterning the surface or preparing thin foils for further studies. Apart of imaging and sputtering, a precise sputtering deposition of various materials from their gas form such as platinum is possible.

Ion source

Most of the FIB instrumentation uses gallium as a metal source of ions. Gallium has low melting temperature, low volatility and low vapour pressure what makes it perfect to use as an ion source. In gallium liquid metal ion source (LMIS), gallium is flowed to the tip of a tungsten needle. The tip of the needle is extremely small with a radius lower than 5 nm. By application of high voltage between the tip of the needle and an extraction plate causes ionization of the gallium atoms and field emission.

The acceleration voltage applied to the LMIS is typically in range from 1 to 50 kV, and ions are focused on the sample surface by use of electrostatic lenses. Higher ion energy increases the sputtering rate of atoms from the sample surface. Modern sources, equipped with Xenon plasma beams have much grater sputtering rates.

Ion Interactions

Ions have greater mass than electrons which results in increased destructive capabilities. When an energetic ion from the incident beam is injected into a sample it can be deflected due to the interaction with the electron charges and the atomic nuclei. Due to its high energy, ion can knock atoms off their position within the lattice. The knocked off atoms can posses enough energy to knock another atoms off from their positions. The atoms that have been knocked from their atomic positions can reoccupy a lattice position or interstitial position. If the lattice site after losing an atom is not reoccupied, vacancies are created. Both defects are considered as damage to the crystalline structure of the specimen.

As the cascades collision continue it will reach the surface of the sample where atoms might be knocked into the vacuum. Due to loss of material in this process its called sputtering. Part of the incident ions will end up within the sample structure. This phenomena is called ion implantation. When ions enter or leave the specimen, secondary electrons are generated and can be utilised for producing an image of the sample surface. The range that gallium ions can travel within sample is extremely limited due to its very heavy weight. Typically when acceleration voltage of 30 kV is used, the maximum distance is lower than 50 nm and it depends on the atomic number of the target material.

Deposition with FIB

Another possible process utilizing FIB is chemical vapour deposition (CVD). The ion beam induced deposition takes place when a gas, such as cyclopentadienyl trimethyl platinum (IV) $[C_5H_5Pt(CH_3)_3$ or tungsten hexacarbonyl $[W(CO)_6]$ is injected into the vacuum chamber and allowed to chemisorb onto the sample. This gas can be decomposed to volatile and non-volatile components by scanning an area of the sample with the beam of ions. The non-volatile part will remain on the sample surface. Small contamination from implantation of gallium ions, carbon deposition from the gas or oxygen if the vacuum level is no ideal, is possible.

Dual beam microscope

Modern microscopes with focused ion beams, like the one one used in the course of this thesis FEI Helios NanoLab 600, comprises of two-column systems. Both SEM column and FIB column are placed on one chamber as a configuration that their beams are focused precisely on the sample spot on the sample. This solution allows to image sample without damage using SEM as well as observed the milling process performed by the FIB. Another advantage is the capability of producing 3D images by sequential SEM imaging combained with FIB milling.

The construction of a FIB system is very similar to the SEM. The main difference are the lenses, as the mass of the ions is much higher than the mass of the electrons. The magnetic lenses used in SEM are not strong enough, therefore are replaced with electrostatic lenses which are

supplied with high voltages to focus energetic ions due to their relatively large mass to charge ratio [122].

The dual beam system FEI Helios NanoLab 600 used in this thesis for STEM was also used for patterning areas on the polycrystalline uranium dioxide sample prior to the EBSD mapping. In case of the sample used for XPS mapping, in addition to marks made on the sample surface, platinum was deposited in those regions as an extra indication of the position on the sample during XPS scanning.

CHAPTER 3

MATERIAL AND SAMPLE PREPARATION

This chapter will focus on materials and processes used for the fabrication of uranium dioxide thin films. Firstly, two ultra high vacuum equipment are described. The existing DC magnetron sputtering system, and construction of a new instrument for the purpose of this research. The second part focuses on the material and a choice of substrate, as well as the substrate preparation process to produce poly-epitaxial systems.

3.1 Reactive DC magnetron sputtering

The Reactive Direct-Current Magnetron Sputtering systems used in this research are located at School of Physics (IAC), University of Bristol. DC or Direct Current Sputtering is a Thin Film Physical Vapor Deposition (PVD) method of coating surfaces. In this approach, a target material is bombarded with ionized gas molecules ejecting sputtered atoms to form the plasma. Such vaporized atoms are deposited then on the substrate (and other areas of equipment) as a thin film.

A schematic of the reactive DC magnetron sputtering system is shown on Fig 3.1. Prior to the deposition process, an Ultra High Vacuum environment inside the chamber is required to minimize sample contamination and allow the sputtering gas to reach the target. Usually argon

gas is used due to its relative mass and ability of converting the kinetic energy upon collisions with the target material. Typically a negative potential of several hundred volts is applied to the target material using a high impedance DC power source. Plasma is formed by the electrically neutral atoms of argon gas that is ionized as a result of the collision with the negative bias of the target surface. The sputtering cycle is maintained by the secondary electrons created during the ejection of the target material, and further ionization of the neutral argon ions. In the meantime, the ejected particles from the target are deposited on the substrate to produce a thin layer from the sputtered target material.

The sputtering deposition rate is defined as the number of particles deposited on cm^2 per second. This rate is mainly controlled by the pressure of the sputtering gas, as well as the power supplied to the gun cathode. The relation between the power supplied to the system and the increase of the deposition rate is linear. Manipulation of the rate by a change of argon pressure is a more complex process a higher the gas pressure means that more ions hitting the target and more sputtered particles are created. On the other hand, increasing the amount of molecules, increases the back-scattering process, causing less particles to be deposited on the substrate. Therefore, these two effects have to be considered to find the optimum parameters, while the changes to the deposition rate are easier to adjust by the power supply settings.

A faster deposition rate can be achieved by placing magnets behind the negative cathode. In that way the electrons are trapped over the negatively charged target material, increasing the access of the sputtering gas to the target materials. As the result of that, the deposition rate can be increased approximately hundred times and lower ignition pressure is required. This technique is called as magnetron sputtering.

To grow multi-layers or alloys, one of the possible approaches is a system with multiple guns. This solution allows to deposit materials one after another to form layer over layer, or to co-sputter at the same time to form an alloy material. An alternative solution, not suitable for multi-layers, is to use a pre-fabricated alloy material as a target. The disadvantage of such solution is the poor control over the stoichiometry of the growth sample. Another possibility especially useful to growth oxides and nitrides is to use a reactive sputtering.

In reactive sputtering process, in addition to the pure argon acting as a sputtering gas, an

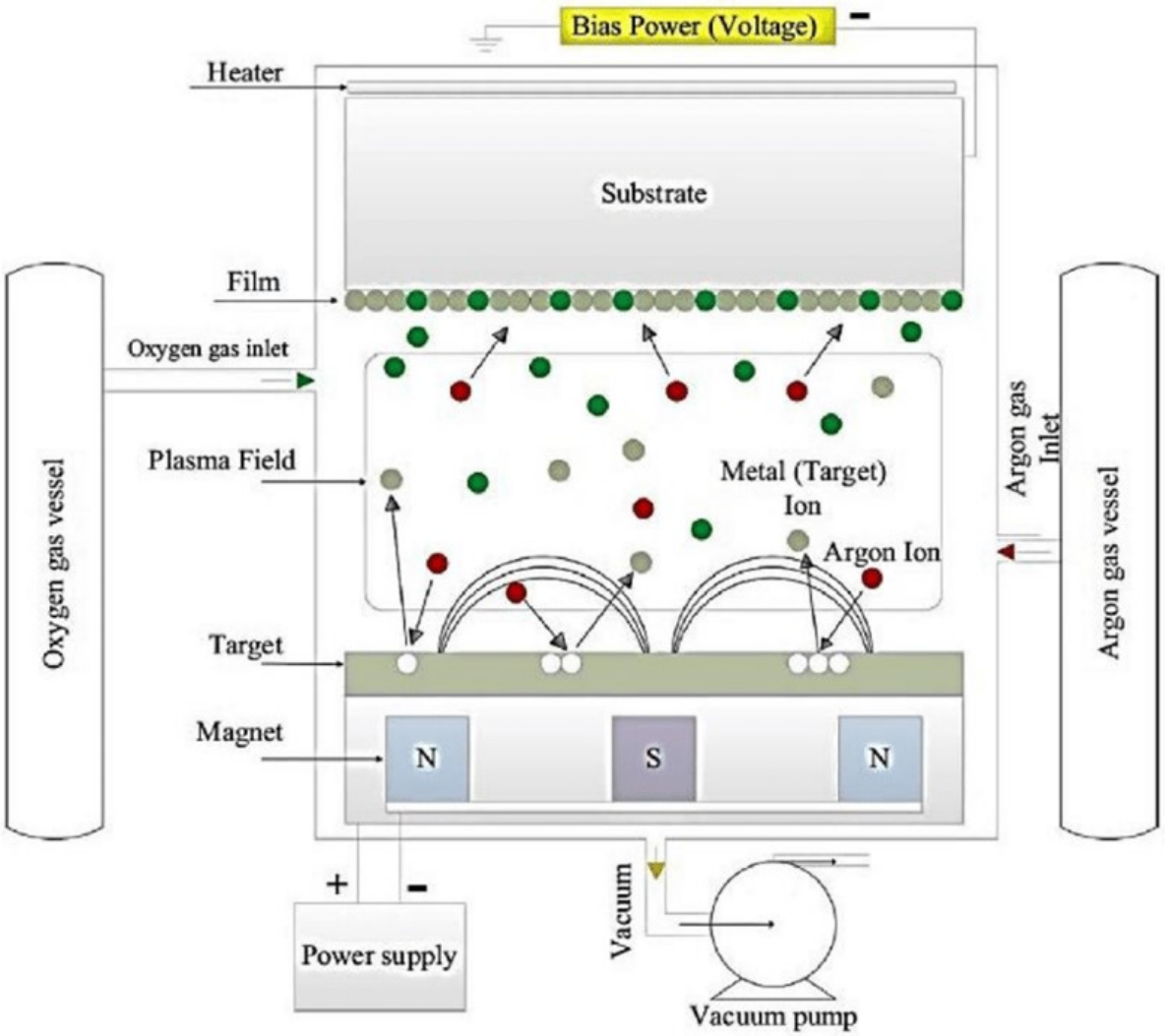

FIGURE 3.1. Schematic diagram of reactive magnetron sputtering. Magnets are confining plasma above the surface, what increase the probability of gron ions to collide with the target and eject sputtered material. The ejected atoms are deposited the on heated substrate. Figure from [133].

additional gas is injected/fed into the system, in this case the reactive gas is oxygen to allow the formation of uranium dioxide. The advantage of this solution is its possibility of controlling the partial pressure of oxygen, what allows to react with the metal atoms and control the final thin film stoichiometry.

3.1.1 Existing DC magnetron sputtering system

The existing reactive DC magnetron sputtering set-up at the University of Bristol, School of Physics (IAC) is shown on Fig 3.2. This system was used to grow thin films samples for the work presented in this thesis. The kit operates at ultra high vacuum environment with the base pressure in the order of 10^{-10} mbar. To maintain this level of vacuum without the need of performing bake-out often, and avoid contamination, this system uses a loading chamber attached to the main chamber. In between chambers there is a manual vacuum gate valve, that is open during the tranfer of a substrate from the loading chamber to the main chamber, and then to take out the sample with a thin film back to the loading chamber. The typical pressure of the loading chamber, before opening the separation valve, is in the order of 10^{-8} mbar. To generate this level of vacuum both chambers are first evacuated using lubricant free scroll pumps to achieve pressure of 10^{-2} mbar. Then turbomolecular pumps are used, with the scroll pumps backing them up.

To avoid water vapor building on the walls of the chambers, and other contamination from air, chambers are vent using nitrogen gas. Substrates are mounted on a recess area in a molybdenum holder using clips made out of the same material. Those holders are then transferred into the loading chamber, upside down, so the gravity force works against the possible contamination. The loading chamber can host up to four molybdenum plates with substrate at the same time, this solution reduces the risk of contamination, the time needed to grow multiple sample and helps to save the venting gas, by reducing the amount of time that chamber is exposed to atmospheric pressure.

Substrates located inside the loading chamber, can be moved into the main chamber after reaching the required vacuum level (10^{-7} mbar - 10^{-8} mbar). In order to do that, a magnetic arm with three pin ending is used. This arm is suitable to operate inside an ultra high vacuum system. The construction of the arm head consists of three pins in triangle configuration, preventing the substrates plates from falling down during the transfer. Substrates are moved into the main chamber using this arm and the picked up by the holder inside the main chamber, then arm is pulled back, and the valve between the main chamber and the loading chamber is closed.

This system is also equipped with a Reflection high-energy electron diffraction (RHEED)

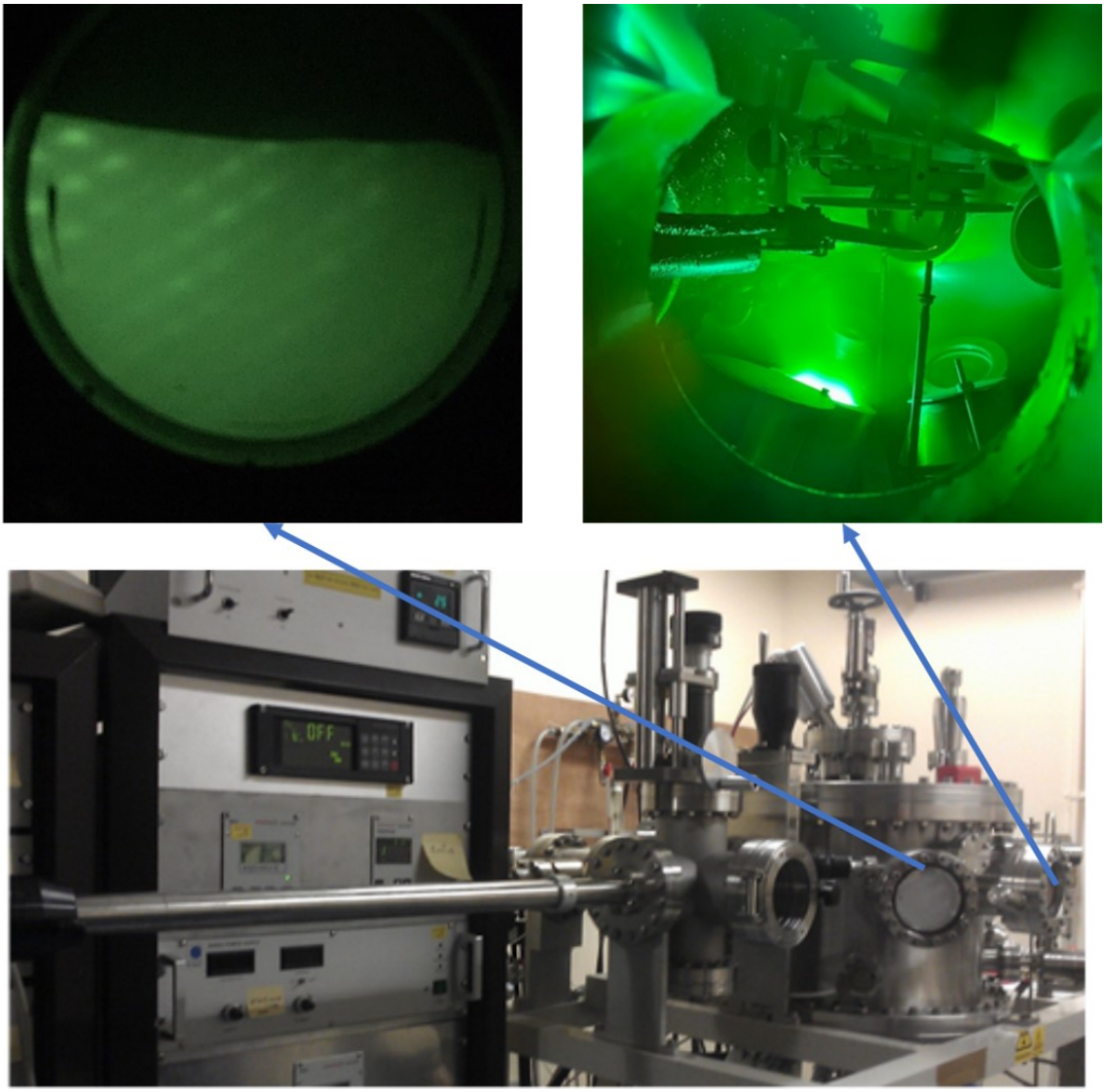

FIGURE 3.2. Photo of the reactive DC magnetron sputter deposition kit located at the University of Bristol, within the School of Physics. The top left shows the RHEED reading of a single crystal substrate. The plasma crated during the deposition process of ytterbium is shown on top right photo.

set-up as shown on Fig 3.2. A typical RHEED system consists of an electron gun (source) and fluorescence screen, and requires a pressure lower than 10^{-5} mbar [134, 135]. As it can be seen on Fig 3.2 the fluorescence screen is mounted in the front of the sputtering system, and the source is on the opposite site. The RHEED system is used to characterize the surface of crystalline materials by striking beam of electrons at it at a very small angle. As electrons interfere with the

position of atoms, a pattern will be visible only for crystalline surfaces.

The RHEED is very useful for the growth of thin films as it is sensitive only to the atoms at the sample surface [136]. Although, this system was not used for qualitative assessment of the sample crystallinity, it is an excellent tool to verify if the material is a single crystal. In the case of single crystals, nice spots will be visible, such spots will change their position while the sample is rotated. Therefore, for the growth of epitaxial single crystal thin films, RHEED was used prior and after the deposition, that allow to check if the substrate is a single crystal and later to verify if the growth film is also a single crystal.

Inside the main chamber, the substrate is located under the home-made heating system. The heater has a resistive heating wire made out of 0.5 mm thick niobium wire, bent into an spiral shape inside an alumina tubing. The temperature of the heater was calibrated using using infrared thermography (IRT) for a multiple setting of the current applied to the heating element. The temperature was measured at the sample spot not directly on the heater, to know the actual temperature that helps with the nucleation of the deposited material. This heater construction allows to reach temperatures of up to 1000°C, what is more than enough for growing UO_2 structures, which is usually in the range of 500-700°C. The possibility of heating substrates to previously mentioned temperatures allows for growth of high quality epitaxial single crystal thin films.

Once the substrate is heated to the required temperature, a reactive and an sputtering gas can be introduced to the main chamber. As the system operates at ultra high vacuum, those gases have to be dosed in a very small quantities. In order to do that, leak valves are used. A typical leak valve consists of a movable piston with a flat sapphire that forms a seal with the captured metal gasket. Movement of the sapphire is controlled using a threaded shaft-and-lever mechanism, that allows to dose the pressure in range from atmosphere to below 10^{-11} mbar.

Based on the material to be grown, different reactive gases can be used. In the case of uranium oxides, pure oxygen gas was used. The typical pressure to manufacture UO_2 was around 2 x 10^{-5} mbar, and was adjusted prior to the introduction of the sputtering gas. Then, argon, the sputtering gas, was dosed to obtain a pressure around 7.3 x 10^{-3} mbar.

The sputter deposition rate is calibrated by depositing a target material in known conditions

for fixed amount of time, usually 300 seconds. From the economical point of view, a glass substrate is used. The thickness of the calibration sample is accurately measured using x-ray reflectivity, from which the rate is extracted. The value of the sputtering rate is usually in the range of 1 - 2 $Ås^{-1}$, where metals are close to the lower end and oxides rates are higher.

Once the required sample thickness was deposited, the sample was left to cool down and in case of single crystals a RHEED measurement was conducted. Then using the magnetic arm sample was transferred back into the loading chamber. When all samples were ready in the loading chamber, it was vented using nitrogen gas, and samples were placed in individual membrane boxes.

Vacuum generation

For many scientific instruments, including characterization and deposition equipments, a very clean and ultra high vacuum is required for proper operation. In the deposition system the degree or quality of vacuum is not only important from the operation point of view, a lower pressure environment helps to minimize the contamination providing a better control over the sample composition. Vacuum in science can be sub-divided into five arbitrary categories with different pressure ranges as shown in Table 3.1.

Vacuum	**Pressure range (mbar)**
Low/Rough	1 - Atmospheric
Medium/Fine	10^{-3} - 1
High Vacuum (HV)	10^{-7} - 10^{-3}
Ultra-high vacuum (UHV)	10^{-12} - 10^{-7}
Extreme High Vacuum (XHV)	lower than 10^{-12}

Table 3.1: Five pressure ranges

To generate a low/medium vacuum multiple pumps can be used. To avoid contamination and reduce maintenance, as those pumps have to work 24/7, dry solutions are used in our laboratories. The most common pump is a dry scroll pump. As the name says, that pump uses two interleaving scrolls to pump out gases as shown on Fig 3.3. A common solution is to fix one of the scroll, while the other orbits eccentrically without rotating. Another possibility is to co-rotating the scrolls in synchronous motion and with offset centers of rotation. This technology allows to create a

vacuum up to 1 x 10^{-2} mbar, what is enough to start up a turbomolecular pump [137].

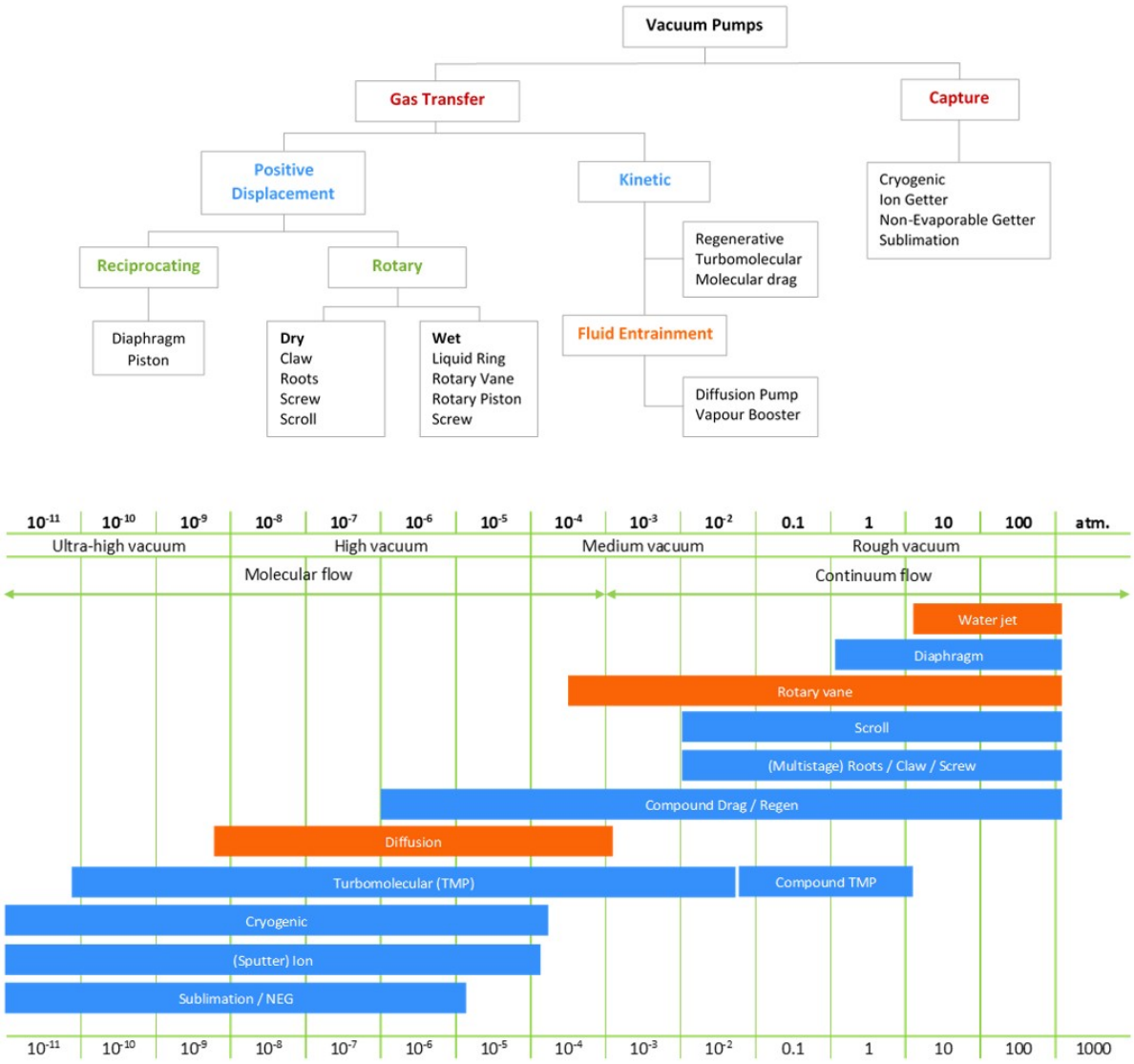

FIGURE 3.3. Graph presenting pump classification used to generate vacuum, together with their pressure working range. Figure reproduced from [138]

A turbomolecular pump is used to provide and maintain high vacuum [137]. The principle behind these pumps is that momentum can be given to the gas molecule in a desired direction, using rotating solid blades. A typical turbomolecular pump consists of stacks of multiple pairs of quickly rotating rotor blades and stationary stator blades, as shown on Fig 3.3. Rather than

taking the gas out, this pump increases energy of the gas molecules. The upper stage captures the gas and successively pushes it into the lower levels until it reach the backing pump. To increase the efficiency of this process, blades need be thin and robust at the same time.

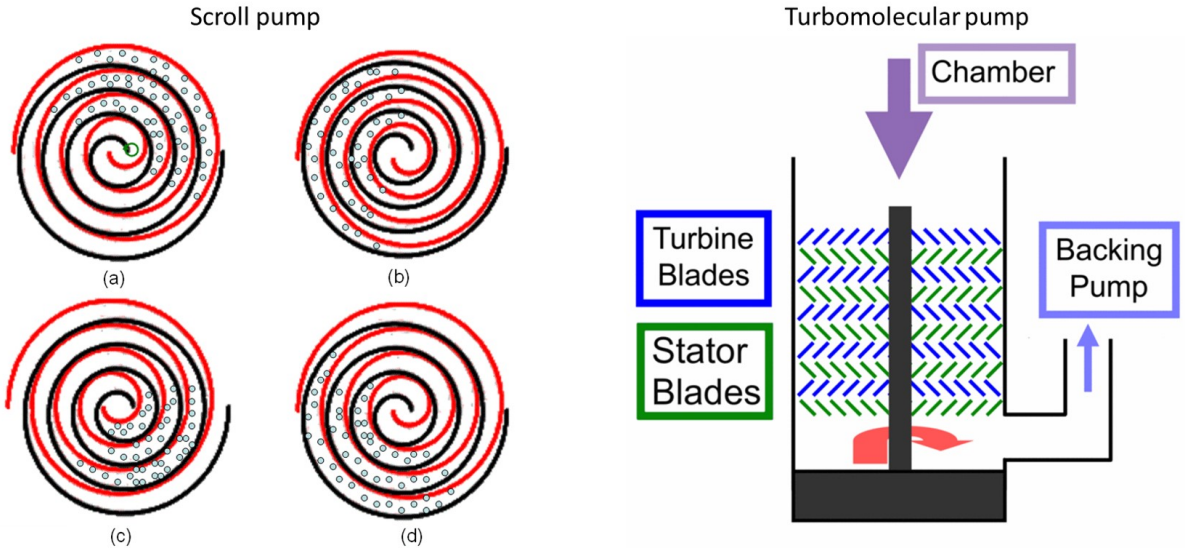

FIGURE 3.4. Schematic of a scroll pump on the left, showing the process of pumping out gases. On the right schematic of a turbomolecular pump. Figure from [139]

Modern turbomolecular pumps use magnetic bearings. This solves the problem of oil contamination and reduces friction, but also have a disadvantage. The limited clearance between rotor and stator combined with magnetic bearing is very intolerant due to material expansion with temperature, therefore an efficient cooling system is required. Turbo pumps operate at very high speed, hundreds of rpm, providing a vacuum down to 10^{-7} mbar, with possibility to improve it by couple orders of magnitude.

A desktop solution allowing to pump straight from the atmospheric pressure, down to the UHV is available on the market, and were used during the work done in this PhD. Such set consist of a turbomolecular pump supported with a diaphragm pump. The working principle of the diaphragm pump is similar to the cylinder in a combustion engine. When the diaphragm moves up, the volume of the chamber increases, the pressure decreases and the gas is drawn into the pump. Then the volume decreases, increasing the pressure and forcing out previously trapped gas. Diaphragm pumps are also lubricant free, but they can only provide a low level

vacuum, therefore there are combined with specific turbomolecular pump.

In order to achieve even lower pressure inside the deposition chamber, a bake-out process can be applied. During the bake-out the temperature of the equipment is increased to evaporate gases absorbed on the walls inside the chamber. This can be done using bake-out tapes in combination with high current filament light bulb located inside the chamber. This procedure is extremely useful, if the main chamber was exposed to the air i.e for a maintenance. Typically bake-out takes from one to three days, and the evaporated gases are continuously pumped out using turbomolecular pump to further increase the vacuum from 10^{-7} mbar to 10^{-10} mbar.

Measuring the pressure

Multiple solutions are used to measure the level of the vacuum inside the equipment. As some of them work only for specific range of the vacuum, it is important to understand the physics behind them and the way they operate in order to avoid damage the the gauge. Often the measured range of the vacuum overlaps for certain gauges, what allows to combine them in order to build a so called full-range gauge. The examples of gauges and the range of the vacuum they can operate/measure is shown on Fig 3.5. Here we will only focus on the gauges used within the work associated with this thesis.

The most common gauge is using thermal conductivity to measure the pressure in the vacuum system, and was named after his inventor Marcello Pirani [140]. The Pirani gauge consists of a metal filament (usually gold plated tungsten or platinum). This filament is suspended in the gas and kept at constant temperature. The heat can be transferred to the surrounding in four ways: gas conduction at high pressure ($E \propto dT/dr$, r is the distance from the wire), gas transport at low pressure ($E \propto P(T_1 - T_0/\sqrt{T_0}$), thermal radiation ($E \propto (T_1^4 - T_0^4)$, and due to end losses associated with the support structure. Therefore, reduce of the gas pressure will reduce the number of molecules responsible for heat transfer and wire will lose hear slower. Measuring the voltage needed to keep the sensor at constant temperature will give indirect indication of pressure. In this case, the thermal radiation losses and the end losses are constant [141].

Two additional approaches are also possible, both are based on measuring the change in resistance as a function of pressure. The first one operates with the constant voltage on the

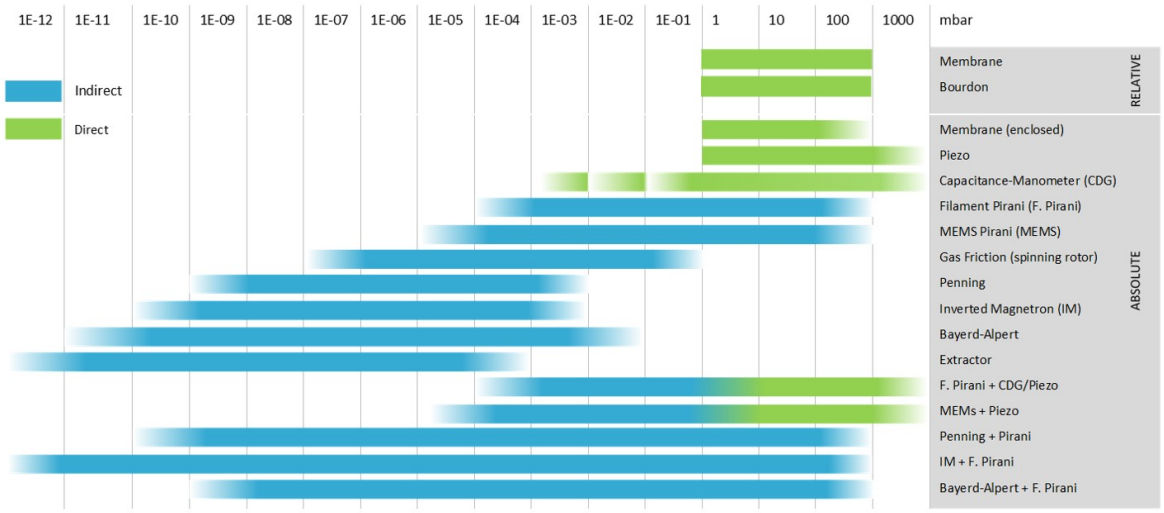

FIGURE 3.5. Graph presenting different technologies and their measuring ranges of the vacuum. Figure reproduced from [138]

bridge, while the other one keeps the current constant. The measurement range for the Pirani gauge is between 5 x 10^{-4} mbar to 1 000 mbar. Although, the reading below 1 x 10^{-3} and above 100 mbar is associated with lower accuracy ± 50% of the reading.

To measure accurately the pressure below 1 x 10^{-3} mbar, a Cold Cathode gauge (CCG) can be used. The cold cathode ionization vacuum gauges consist of a cathode and an anode. It uses a crossed electric and magnetic field to trap the electrons. The typical values for the high voltage are from 2 - 6 kV, and for the magnetic field 1 - 2 kG. Due to field emission, negatively charged electrons leave the cathode and move towards the anode with high velocity; on their way, neutral gas molecules are ionized, which ignites a gas discharge. By measuring the gas discharge current, the pressure can be indirectly investigated. The cold cathode can measure pressure from 5 x 10^{-9} to 1 x 10^{-2} mbar, and the gauge should not be activated above 0.1 mbar as it might get damaged.

A common way out is to mount both, the Pirani and the cold cathode gauges in the same device, therefore a wide spectra of the pressure can be measured. This solution benefits also from only one housing required, allowing to mount another vacuum equipment if the space is limited. In this work PKR 251 and PKR 261 FullRange gauges from Pfeiffer Vacuum company were used.

When the pressure level is below 5 x 10^{-9}, another method to measure the vacuum is required. Similar approach to the CCG is used in hot cathode gauge (HCG). The main difference is the way of ionization, while in the CCG electron plasma circulated in crossed magnetic and electric fields is responsible for this process, in the HCG ionizing electrons are accelerated, by suitable electrodes into an ionizing space, from a thermionic cathode. For example, in a Bayard-Alpert configuration electrons are boiled off from a hot filament and accelerated towards a cylindrical grid cage. On their way, the electrons ionize some of the gas molecules, and resulting cations are collected by a wire located at the center of the ionization volume. The collector current is lineary releted to the gas pressure, at a constant temperature, what makes it easy for the calibration process. Modern designs allow to measure pressure in range from 10^{-11} mbar to 0.1 mbar.

3.2 Chamber construction

Fabrication of metallic samples and oxides samples in the same system is not optimal and requires additional steps, especially when switching from the oxides growth to metals. To overcome this issue and limit oxygen exposure to the main sputtering system, a new system was designed and built by myself as a part of this PhD. This allows to have designated systems, one for the fabrication of oxides thin films and one for the deposition of metallic layers. Another benefit is the increased amount of samples that can be fabricated. This sub-chapter describes the design and construction process, which took two years, and includes information about the material choices.

A crucial part of each deposition equipment is the main chamber, where the process of sample growth will take place. Chambers are usually made of stainless steel as it does not impede the desired degree of vacuum pressure in the vacuum system. Multiple variation of austenitic stainless steels can be used for vacuum applications such as 304, 304L, 304LN 316, 316L and 316LN. Other benefits of using stainless steel are: corrosion resistance, ease of machining and manufacturing, mechanical strength, temperature tolerance and long life.

Vacuum chambers can be manufactured in different shapes including box shape, spherical and cylindrical. An important feature is also the amount and location of the port, to allow the installation of the necessary components for providing and measuring vacuum, deposition and

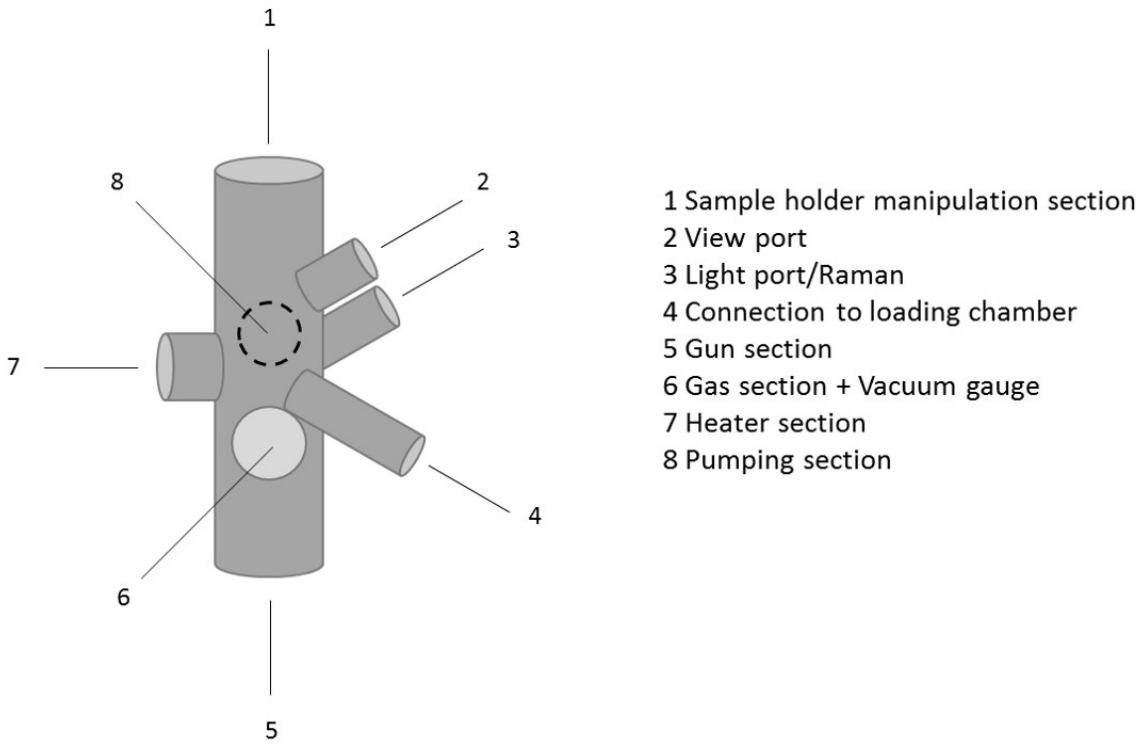

FIGURE 3.6. The schematic of the stainless steel main chamber used for the construction of a new deposition system. This system has eight connection, which are designated for different applications.

characterization of the material. From economical reasons, due to very limited budget, in this project old / second hand component were used where possible. As the main chamber a cylindrical vessels made of stainless steel, with unknown history was used. Inside of the chamber was cleaned using acetone and quality of the knife edges on the connection was verified.

The schematic of the new DC magnetron sputtering system is shown on Fig. 3.6. As shown, the main chamber has eight connections which will be described in this chapter. The first section is designated for a sample holder, the second section allows to see what is happening inside the chamber. The third section at this moment is blank, with a possibility for further installation. Transport of substrate/sample from/to main chamber is done using section four. The gun used for sputtering is attached in section 5. The sixth section is used for measuring vacuum level and insertion of gases. The heating system is attached in section 7. The last section (8) is used for chamber evacuation.

To design the components for the new sputtering chamber Fusion 360 software on a free education license was used. The Fusion 360 is a 3D Computer-Aided Design and Drafting (CADD) software with a Computer Aided Engineering (CAE) and Computer Aided Machining (CAM) tools. At the design stage, prototype parts designed with this software were usually exported to the FlasPrint software, and printed using a plastic 3D printer (name company of the printer). Final parts were manufactured by the Mechanical Workshop, Faculty of Science at University of Bristol.

As a sample carrier a commercially available flag style holder was used. The outline of the holder is shown on Fig. 3.7. This sample plate is made out of molybdenum, which makes it suitable to work in extremely hight temperature and under ultra hight vacuum condition. Molybdenum (Mo) is a silvery-grey metal with atomic number 42. The widespread use and popularity of molybdenum in vacuum applications is due to its wide range of properties. The high melting point at 2620°C and low thermal expansion 4.8 μm/(m x K) (at 25 °C) combined with low vapor pressure makes it perfect where high temperatures in UHV are present. Furthermore, this material has high thermal conductivity and is highly resistant to corrosion. High elastic modulus allow to machine it to required form and shape. In this project, commercially available, high piurity (99.9%) Mo was purchased from Goodfellow Cambridge Ltd. (UK).

The design of the sample holder is shown on Fig. 3.8. The most limiting factor in design of the sample holder is the diameter of ConFlat (CF) 40 flange through which it must pass. The internal diameter of such a flange is 35mm, therefore, the sample holder has to be smaller than that. To meet this requirement a 3mm thick and 34mm in diameter disc was used. At the middle of the disc a space to hold flag type sample holder, and a part of the edge for loading and unloading the sample, were cut out. This holder was then welded to a U shape narrow plate, in a way to match the position of the loading arm, and allow for smooth sample transportation. In order to achieve that, the disc was rotated 30 degrees relative to the U shape. The top middle point of the U plate have a 6mm hole for a road. The M6 road is 20cm long ending with a 4cm of a thread which combined with two nuts and washers allow for height adjustment. All those components were made out of 316 stainless steel.

Stainless steel 316 is a corrosion resistance steel alloy, with a maximum of 1.2% carbon

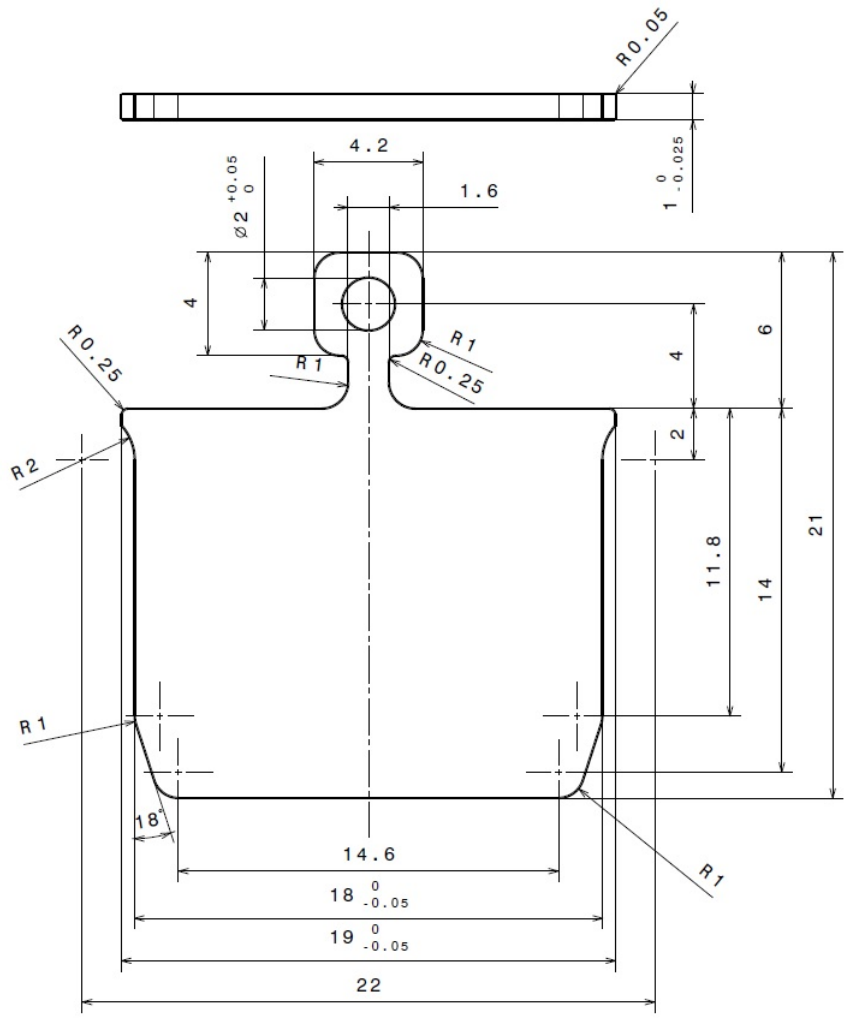

FIGURE 3.7. The drawing of commercially available molybdenum flag type holder used in the construction of the new deposition system. Reproduce from [142].

by mass and a minimum of 10.5% chromium. The minimum of 10.5% chromium provides a temperature resistance to 700°C. The 300 series of austenitic stainless steel contains chromium and nickel, and it is the largest group and the most widely used. The 316 steel in addition contains 2-3% of molybdenum, what increases corrosion resistance, improves resistance to acids, and increases strength at high temperature. The resistance at high temperature is very important in case of the sample holder, as temperature during the deposition process can reach up to 750°C. Type 304 and 316 can withstand temperatures up to 920°C, what is perfect for application in this chamber.

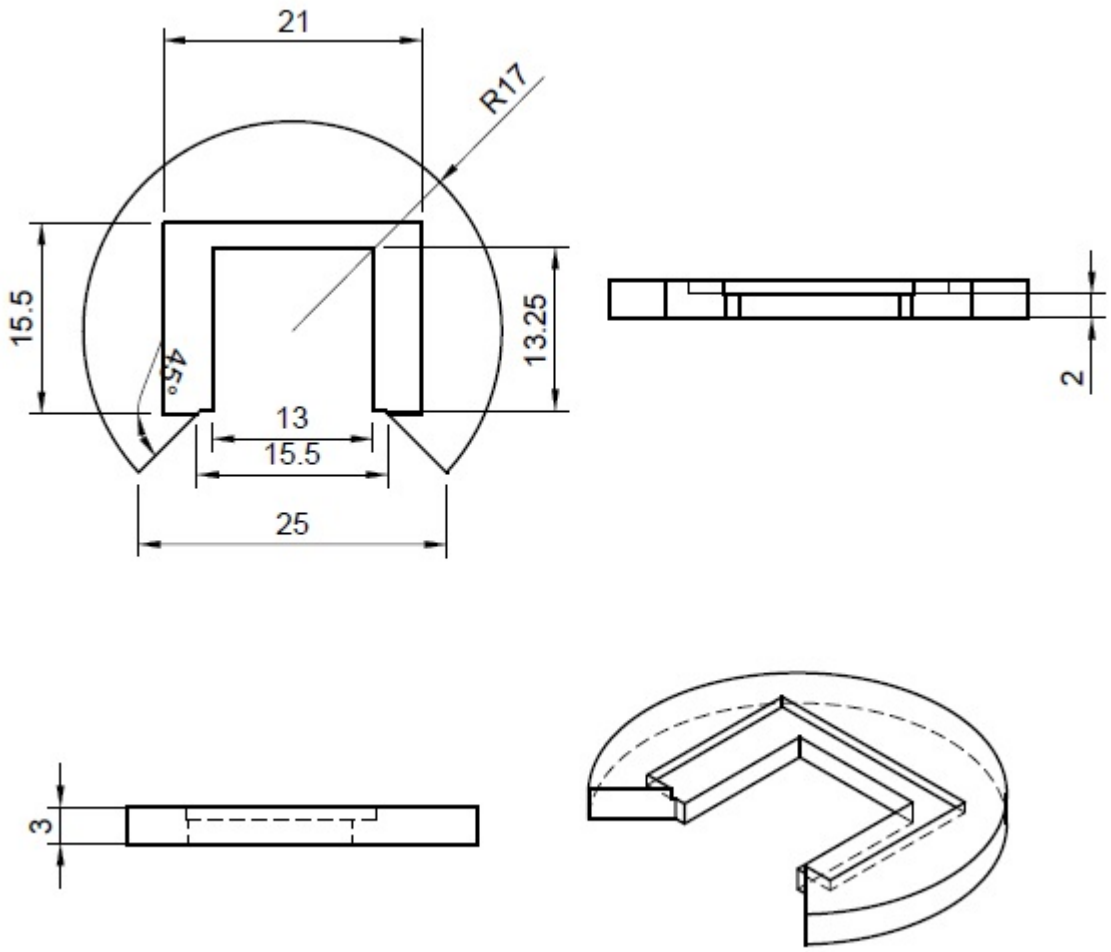

FIGURE 3.8. The drawing of a sample holder. It is a 3mm thick and 34mm in diameter disc with a spacing at the middle to fit the flag type sample holder. The material used to make this holder is 316 stainless steel.

When the sample holder was welded to U shape plate and attached to a M6 rod, it was mounted on a rotary motion CF40 feedthrough allowing for a 360°rotation. All that was then attached to a bakeable Linear Shift Mechanisms, allowing for a movement along 2cm, what was necessary for picking up a substrate from the loading arm, and later for returning the sample on the arm. All those component were made out of stainless steel.

Section two is located above all the other connections (excluding the top connection, number one), providing a perfect view on the meeting point of the remaining sections. This connection therefore was used as a viewpoint. To make it possible while maintaining an ultra high vacuum

environment inside the chamber, a CF63 vacuum viewport was mounted. It is a standard bakeble viewport made of borosilicate and fused silica. The view provided by this port is necessary for sample manipulation, during the loading and unloading process. In addition, visual inspection of the processes occurring inside the chamber is possible. Currently, there is no viewport shutters to prevent deposition of the material on the glass, what gradually will contribute to the decreasing of the transparency of this viewport. (But it will be mounted in the nearest future).

The section 3 is located below the view port, around 30°to the right and it is perpendicular to the main chamber. In the current configuration an electrical CF 40 feedthrough with two molybdenum pins (LewVac UK, FHM-2-28-40KF), able to conduct current of 28 A per pin, is mounted. The length of those pins was adjusted in order to mount a halogen light bulb at the end of them, and to provide light inside the chamber with limiting exposure of the light bulb to the deposited material. This source of light can also produce a lot of heat what is very useful during the equipment bake outs.

The future plans for this connection assume additional use of it for the in-situ Raman spectroscopy. That requires an optical feedthrough, that can transfer laser into the sample surface and bring signal back to the external Raman system. In this case, the feedthrough would have to be under the sample in order to collect signal from the substrate/deposited material, and remove during the deposition process to not block the patch of the ejected molecules.

The transfer of the substrate/sample takes place through section 4. This section is located at the same hight as sections 3, 6 and 7 and the size is CF 40. At the end of this section is a loading chamber, separated from the main chamber by a ultra high vacuum manual gate.

Loading chamber

The schematic of the loading chamber is shown on Fig 3.9. The Mini UHV gate valve (2), allows to vent the loading chamber to atmospheric pressure, while maintaining ultra high vacuum environment inside the main chamber. The main bit of the loading chamber is the 6-way stainless steel CF 40 cross. To the bottom of this cross a O-ring seal PKR 251 (Pfeiffer Vacuum) full range gauge is connected, allowing to read pressure level from 5 x 10^{-9} mbar to 1 x 10^{3} mbar.

The vacuum inside the loading chamber is generated using Pfeiffer HiCube 80 connected to

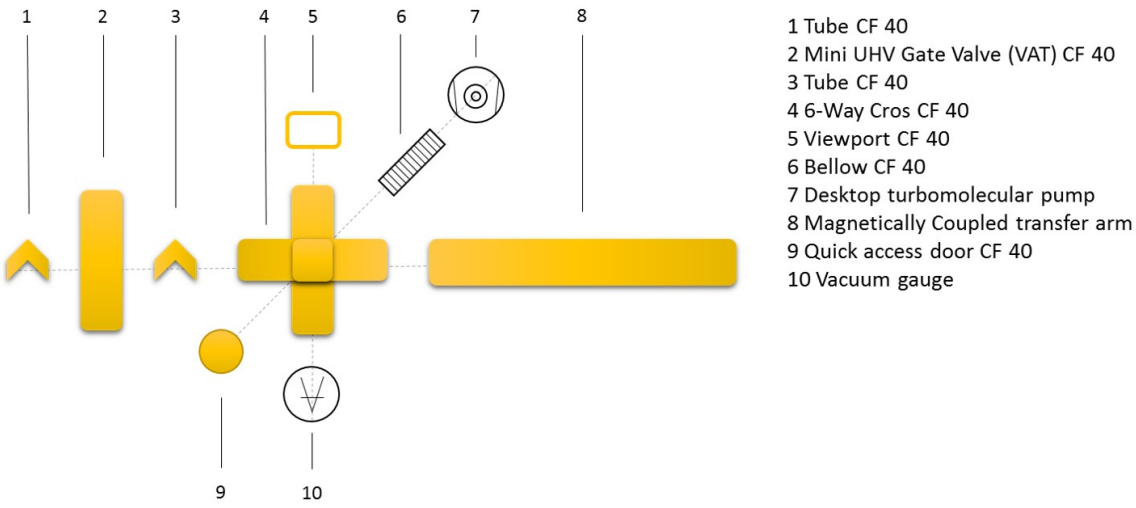

FIGURE 3.9. The schematic of the loading chamber for the new DC magnetron sputtering system.

the 6-way cross by a CF40 bellow. The HiCube 80 is a turbo pumping stations using an integrated diaphragm pump as a backing pump for the turbomolecular pump. This combination allow to reach a vacuum pressure of low 10^{-8} mbar, what is sufficient for a loading chamber to be open to the main chamber.

Transfer of the sample is done using a quick accesses CF 40 door with O-ring sealing. A flag type sample holder is mounted on a specially designed arm head. The view inside the chamber for this operation is provided by the view port mounted on the top of the 6-way cross.

The section 5 which is located at the bottom of the main chamber is used for a deposition source, which in this case can be a DC magnetron gun or an evaporator source.

The section 6 is used from gas inlets and measuring the vacuum level inside the main chamber. To read the pressure level a full range gauge PKR 261 (Pfeiffer Vacuum) with metal seal is used. Same as the PKR 251 model, allows to read pressure level from 5 x 10^{-9} mbar to 1 x 10^{3} mbar, with the difference in the sealing component what makes is suitable to use even for lower pressure that can not be measure with it. An additional gauge installation is planned, and it will be an ion gauge allow to read pressure values below the PRK 261 limits.

Two types of gases can be distributed into the chamber using mounted sapphire leak valves.

The first one is connected to the source of the sputtering gas, which is argon. The gas is provided by BOC company, it is a research grade N5.5 (99.9995% purity) argon in a 2L cylinder with a 0.3m^3 content. Cylinder has a BS3 valve into which a regulator is connected. The connection between the regulator on the cylinder and the leak valve is made using a Swagelock stainless steel 4mm pipe, with two Swagelocks, one behind the regulator, and one in front of the leak valve. The second valve has no gas connected right now, but can be used for any gas desired during the sample deposition.

The limitation that applies to the heating element is size of the elements holding the sample holder, which is 32 mm. Therefore, the with of the heater is only 30 mm as shown on Fig 3.10. To compensate this limitation and allow for more heating wire, the length of the heater was deigned to be 50 mm. Furthermore, price and availability of the materials from which heaters is made also limits the size to 50 mm. In this rectangle configuration 30 x 50 mm as spiral 1 mm wide and 1.5 mm deep tranches were made to fit a total of more than 50 cm of niobium wire.

The thickness of the main part of the heater is 6 mm, what allowed not only for comfortable mounting of the heating wire but also provides enough space to mount a thermocouple inside. In order to be able to measure the temperature a 25 mm deep hole with 2 mm diameter was drilled on the side of the heater for the K type thermocouple. The material used to make is part of the heater is MACOR.

MACOR was developed by Corning Inc. and it is a white ceramic which can be machined with ordinary steel or carbide tools [143]. The typical composition for MACOR is 46% silica (SiO_2), 17% magnesium oxide (MgO), 16% aluminium oxide (Al_2O_3), 10% potassium oxide (K_2O), 7% boron trioxide (B_2O_3), 4% fluorine (F), with a density of 2.52 g/cm^3. The tight-tolerance capabilities of this material allows to use it with complicated shape design, in this case the trenches for the heating wire. MACOR is stable up to 1000°, and can be used continuously up to 800°what meets the requirements for growing uranium oxides. It is a good thermal insulator, therefore, perfect to use a material for the back of the heater. This ceramic is an electric insulator, what is required form a material to be a body for a resistive heater. The low outgassing, and possibility of degassing before use, together with non-wetting properties make it perfect for ultra high vacuum plication [144]. All MACOR material used in this thesis was bought from GoodFellow Inc.

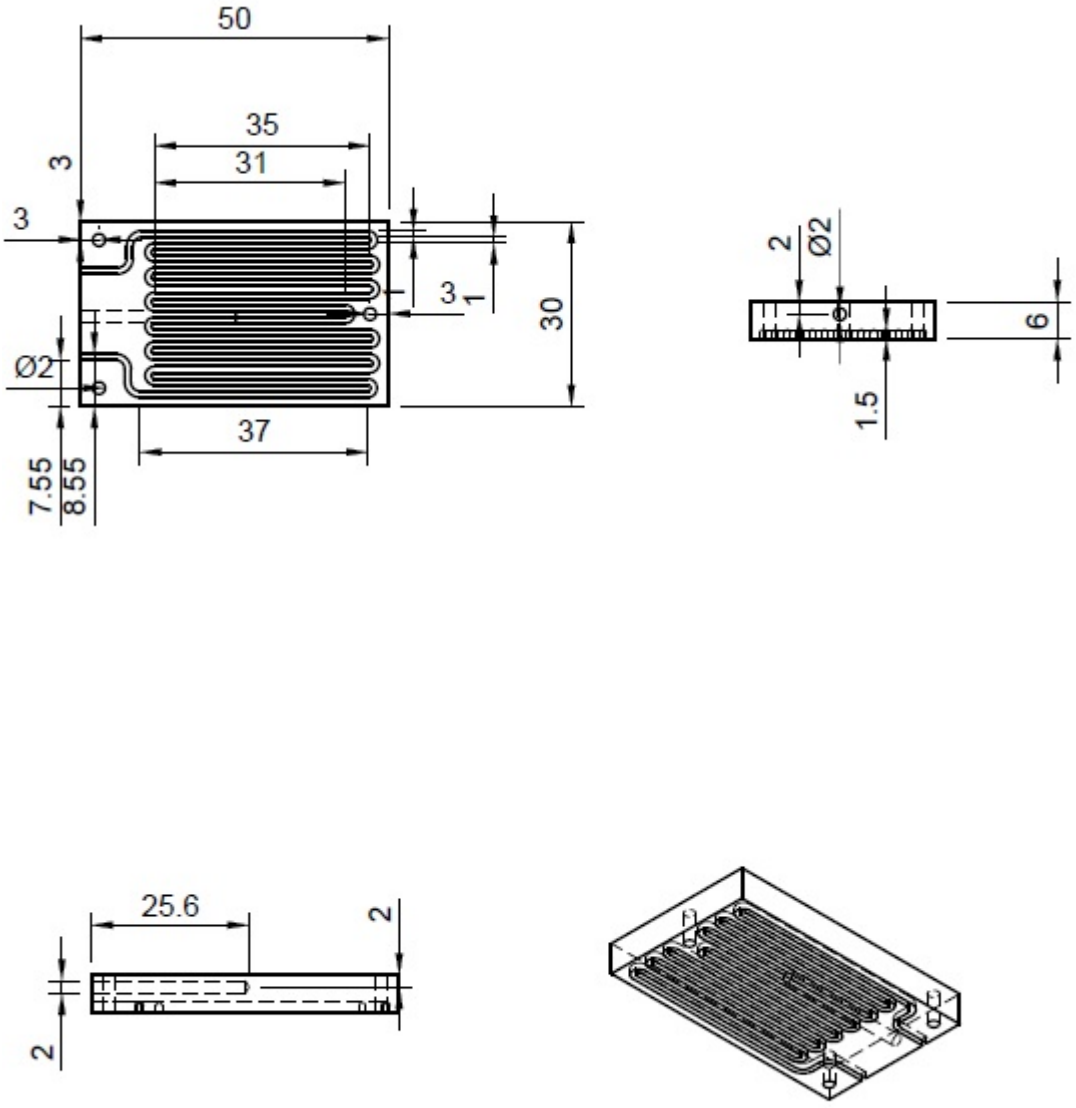

FIGURE 3.10. The drawing of the heater main body. This part is made of 6mm thick MACOR. The trenches for niobium heating wire are 1mm wide,1.5mm deep, with a length of 31-35mm. The spacing in-between lines for Nb wire is 1mm. The body has three holes with 2mm diameter, used to asseble the main body with a bottom plate, and attach to heater arm. On the side of the heater is a 25mm deep hole with 2 mm diameter for a K type thermocouple.

The design of the bottom plate of the heater is shown on Fig. 3.11. The dimensions of the plate and the positions of the holes for screws match with the main body of the heater. This plate is

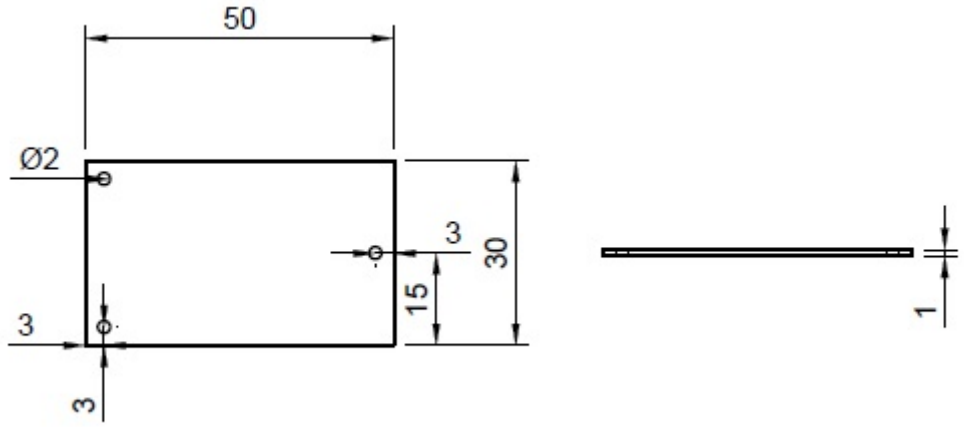

FIGURE 3.11. The heater bottom plate is a simple rectangle 30x50mm with a three holes 2mm in diameter to match the heater main body for an easy assembly.

directly in-between the heating element and the substrate, therefore, high thermal conductivity and possibility to machine are required from a material for this part. MARCOR due to low thermal conductivity can not be used, and another material was found to be suitable.

Shapal is a combination of two different traditional ceramics: aluminium nitride and boron nitride, unlike MACOR a glassy ceramic material. Although, it can be machined into a variety of shapes using ordinary tools, whilst retaining many of the advantages of traditional aluminium nitride. Shapal has much higher thermal conductivity 92 W/mK, compare to MACOR 1.46 W/mK, at room temperature. The material used to fabricate the bottom plate was Shapal Hi-M soft from GoodFellow Inc, which is a new improved version of Shapal-M soft released in 2012.

Prior to mounting heaters component into the holding arm shown on Fig. 3.13 , those component should be assembled together. Niobium wire should be placed inside the tranches in the main body, and then covered with the bottom plate. To fix those part together M2 molybdenum screws were used, due to properties of this material.

The U shape part of the holding arm shown on Fig 3.13 is made of 3mm thick MACOR sheet. This component has 2mm diameter hole to match those on the bottom plate and main part of the heater. Additional two holes of the same diameter were made for a possible connection between power supply wire and the heating wire. The 4 mm hole at the central part allows to adjust the height of the heater by changing the position of the nuts used to couple the U shape arm head

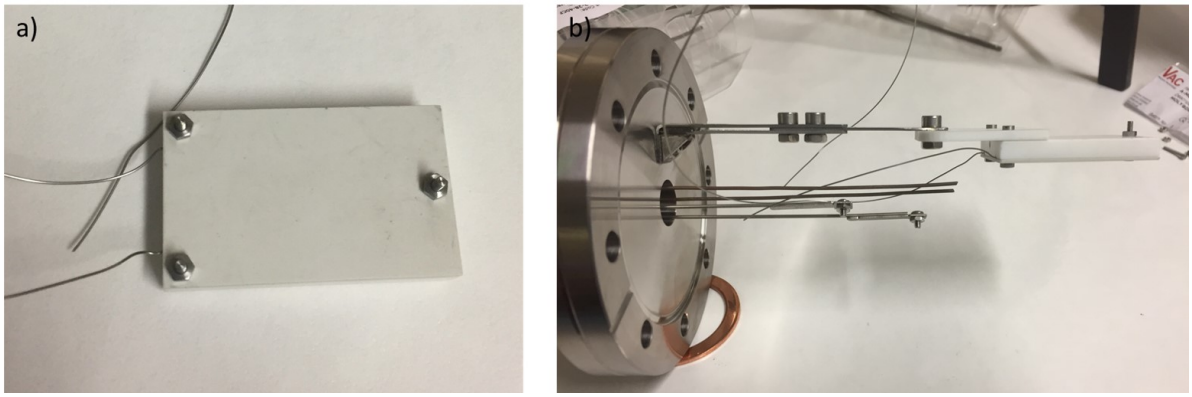

FIGURE 3.12. The left image (a) shows assembly of the main heater part and bottom plate with niobium wire inside. On the right image, the heater is mounted on the U shaped part of the arm holder.

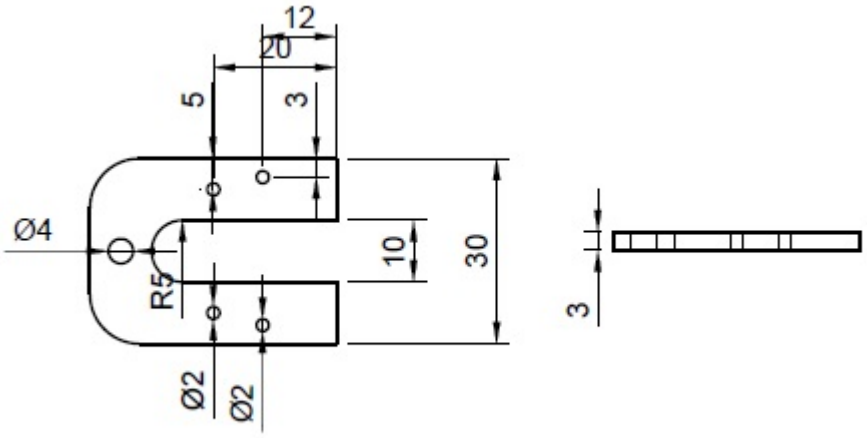

FIGURE 3.13. Drawing of the U shaped component responsible for connecting the main heater parts to the heater arm. This component is made of 3 mm thick MACOR, and has a set of 2mm diameter holes for the heater attachment, and a 4 mm wide hole for an adjustable mounting to the heater arm.

with the adjustable part shown on Fig 3.14.

The component shown of Fig 3.14 and Fig 3.15, are made of stainless steel, as there is no need for use of MACOR. MACOR was used for other components due to its good isolating and thermal properties. Those two component are assembled together using two M4 bolts and nuts. The first component can move in the space between two plates in the second component. This

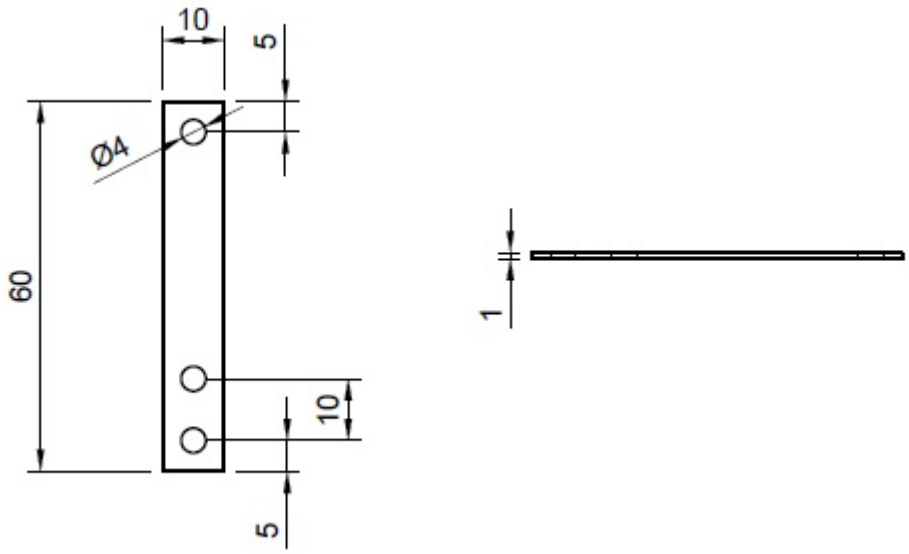

FIGURE 3.14. Drawing of the rectangular stainless steel 316 plate with 10x60x1mm detentions. The top 4mm hole is used to mount the U shaped part responsible for holding the main heater part. After adjusting the length, this part is fixed with two M4 nuts and bolts to the part shown on Fig. 3.15

solution allows to adjust the length that the heater is inserted into the main chamber, what is necessary for any adjustments.

The left part of the component visible on Fig 3.15 was mounted on to a CF63 to CF16 zero - length reducer flange made out of stainless steel, using a stainless steel vented screw. Such a type of screw is also known as a Vacuum Screw, due to their application in vacuum systems. They prevent from creating virtual leaks, which cannot be found using lead detection method. A virtual leak corresponds to a trapped volume of gas at the base or below the tip of a blind-tapped hole. To eliminate possibility of creating virtual leaks, the vented crews features a hollow core and/or cut on the sides of the screw. This solution is applied also to the washers.

Mounting the arm to the reducer using the vented screw allows for tilting adjustment if needed, or to dismount and mount another component into the flange what would not be possible with welded parts. To supply the power into the heating wire and measure the temperature inside the heater an CF16 electrical feedthrough is used. This feedthrough has two copper pins allowing to provide enough heating power, and a chromel pin with a alumen pin to collect readout from the K type thermocouple inside the heater.

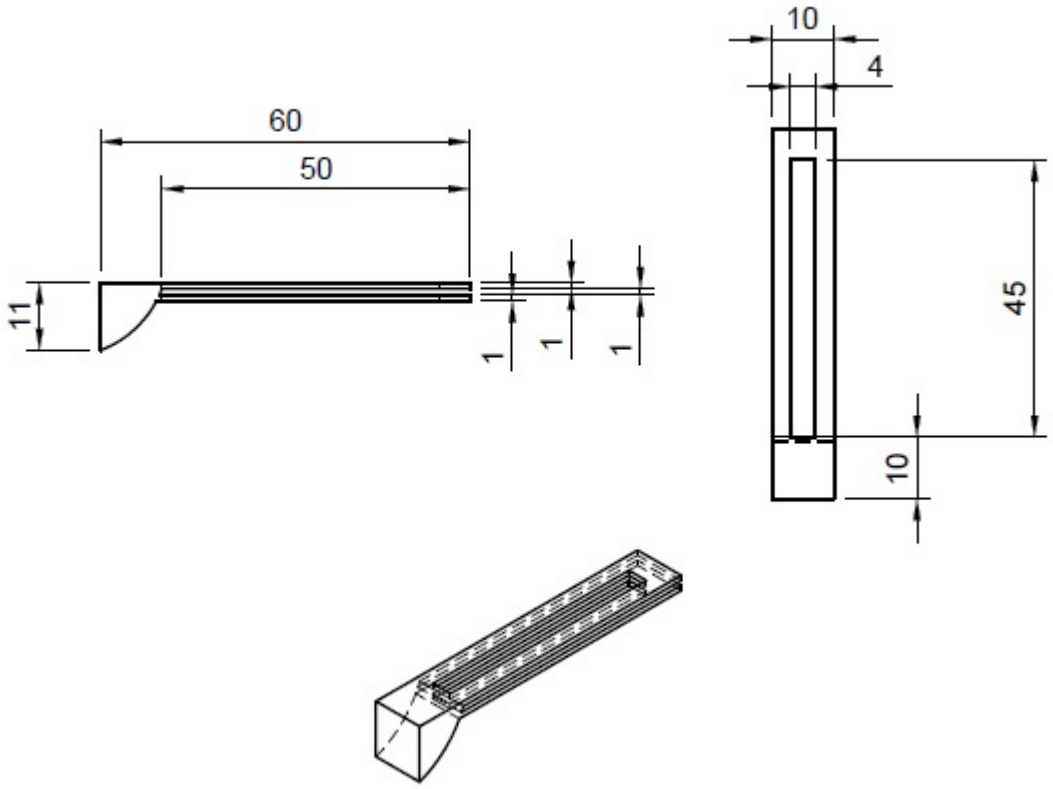

FIGURE 3.15. Drawing of the arm part attached to the flange. This part is made out of SS316. The length of adjustable part is 50 mm and thickens of the plates is 1mm with a 1 mm gap in between them for insertion of the part shown on Fig. 3.14.

The fully assembled heater can be seen on Fig. 3.16. The left photo (a) shows the heater in actual orientation that will be placed above the sample holder inside the main chamber. All the wires were isolated using alumina tubing, and connected either by placing wire in-between the nut and the screw (for the thermocouple), or by using inline barrel connectors (power for the heating wire). The up-side-down view on the heater is shown on Fig. 3.16 (b).

The power source for the heater is the RS PRO 1 Phase 2.4 kVA Variac (890-2872) providing adjustable current from 0 to 10 A. The heat generated by the resistance of the niobium wire can be measure by mounted K type thermocouple. To read the temperature the handheld RS PRO RS41 Digital Thermometer with 1 K type input is used.

A thermocouple consists of two dissimilar electrical conductors welded together to form an electrical junction. Due to the thermoelectric effect a temperature-dependent voltage will

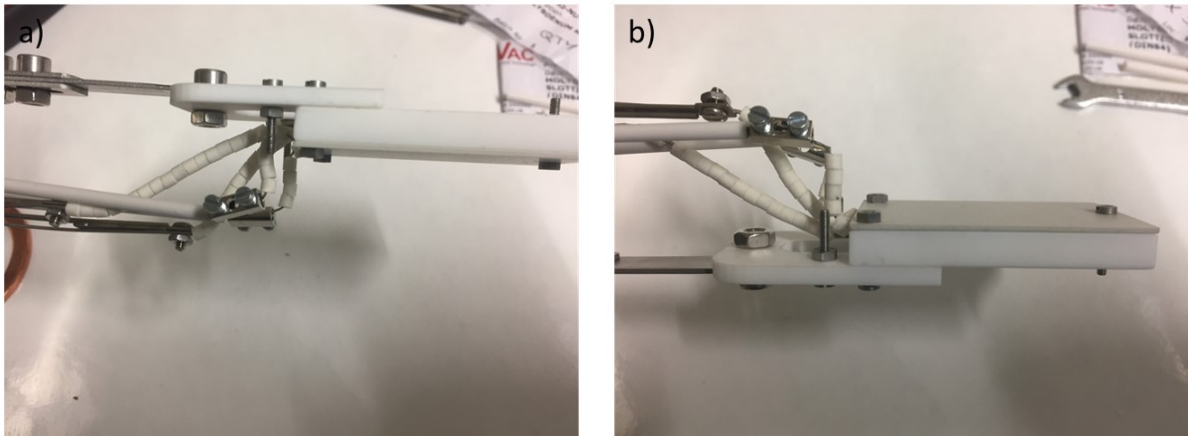

FIGURE 3.16. The fully assembled heater is visible on panel (a). Both set of wires, for the heating and for the thermocouple are covered/isolated using alumina components. The figure (b) shows the heater in up-side-down position.

be created, and this voltage can be translated into the temperature reading. One of the most common type of the thermocouples is called K type. This tape of thermocouple is made of a chromel (approximately 90% nickel and 10% chromium) and alumel (approximately 95% nickel, 2% aluminum, 2% manganese, and 1% silicon) wires. This inexpensive construction allows to measure in a wide range from -200 °C to + 1350 °C. Another advantage of this solution for growth of oxides is its their ability to operate very well in oxidizing atmospheres.

The vacuum inside the main chamber is generated and maintained using bigger CF100? 120? connection placed at the other side of the chamber, opposite to the connection 6. Prior to starting the turbomolecular pump the chamber is evacuated to $^{-2}$ mbar base pressure using a dry pump. The pump used in the main chamber of this equipment is nXDS Scroll Pump (Edward) model 10i. The benefit of using such a pump, is that it does not require any lubricant preventing cross contamination and providing clean and dry vacuum. Furthermore, the maintenance of the pump is reduced to a minimum, as for example it does not require change/refill of oil, the parts that wear-off are tip seals. The nXDS10i model can pump 10 $\frac{m^3}{h}$, with a continues inlet pressure of 200 mbar. The nominal rotation speed is 1800 rpm, what generates a noise level of 52 dB(A). The pump can be remotley controled using a RS232 or RS485.

Once the turbomolecular pump is switched on, the main roll of the scroll pump is backing the

turbomolecular pump. The outlet of the pump is connected using a flexible hose to the exhaust line on the wall. The exhaust line terminate outside the building, therefore, the laboratory air is not contaminated by any gasses used during the operation of the sputtering equipment. Currently the equipment operates at vacuum level lower than 5 x 10^{-9} mbar. Although, the correct value can not be measured due to limitation of the full range gauge.

In order to achieved such a UHV environment a bake-out of the equipment is conducted. That involve use of a baking tape set to 120 °C combined with the halogen light bulb mounted in section 3. The sputtering system is left for couple hours, until there is no visible change in pressure, and the allowed to cool down to room temperature.

Turbomolecular pumps generate heat as they compress gasses, and therefore must be cooled. Based on the pump, different cooling methods can be used, in this case, a water cooling is required. Cooling block was fixed to the turbomolecular pump using a thermal conductive paste and screws. The inlet and outlet of the cooling block was connected to the 18 °C water circuit. The flow rate is adjusted using a acrylic flow meter FL-2051 (Omega) to be around 0.5L/m.

The sections previously indicated on schematic drawing on Fig. 3.6, are now shown on photos (a) and (b) Fig. 3.17. The first section (1) allows for sample rotation and hight adjustment. The viewpoint (2) is covered with aluminium foil for bake-out and to prevent dust deposition. Connection to the loading chamber (4) can be seen on the right side of the main chamber. The gun/evaporator connection (5) goes through the top of the trolley to the lower part (Fig. 3.17 (c)). The bottom part of the trolley hold desktop turbo pump used for the loading chamber and the primary scroll pump for the main chamber. Also, the Argon cylinder is attached to one of the support and rest on the bottom part. The deposition gas is connected to section (6), where also a vacuum gauge is mounted. The turbomolecular pump (8) used to provide UHV in main chamber is visible on Fig. 3.17 (b). The heater section (7) is placed on the left side of the main chamber. The view inside the chamber with switched on heater, without light, is shown on Fig. 3.17 (c).

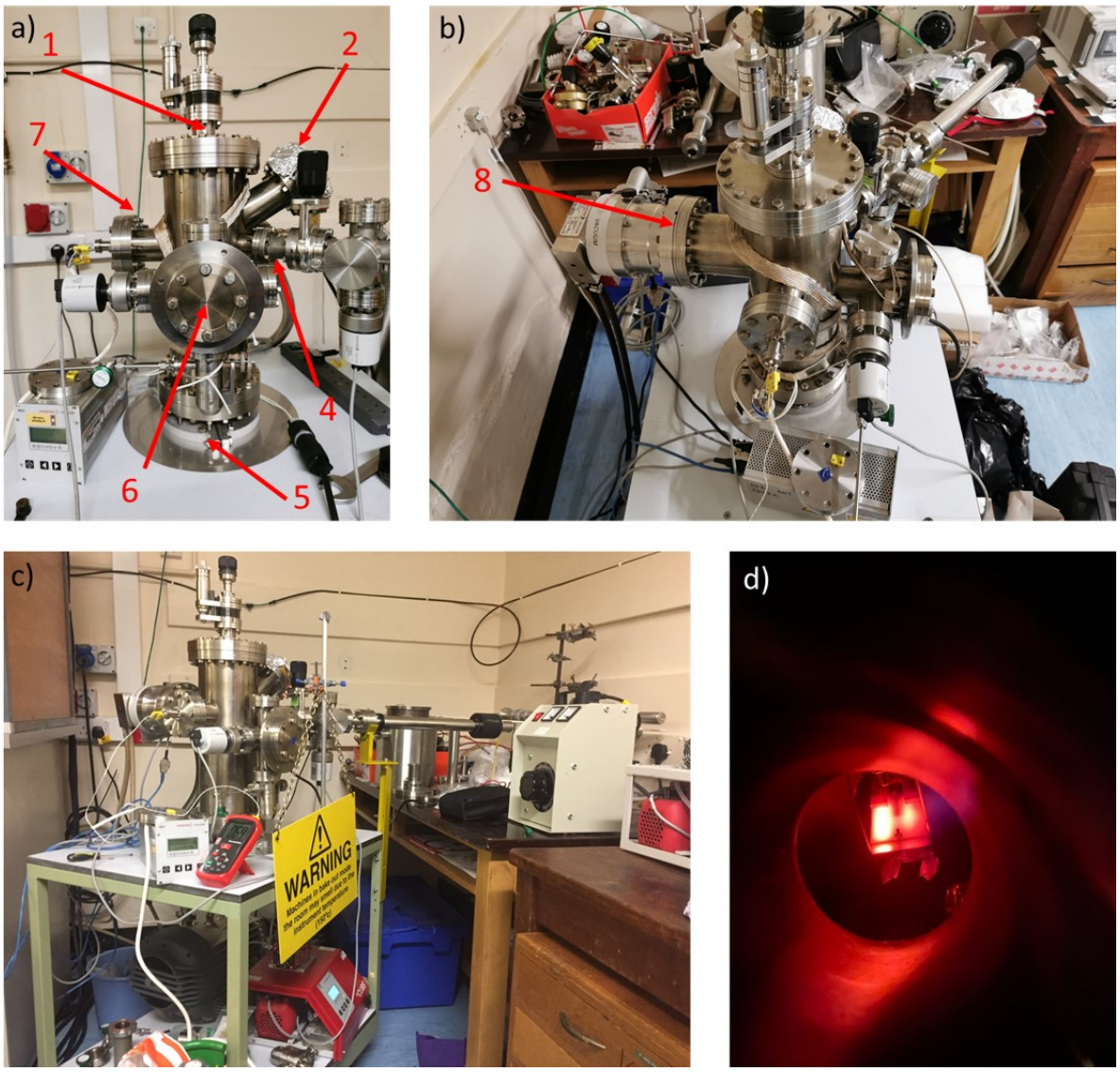

FIGURE 3.17. Photos of the new sputtering system (a-c) with numbered sections. Panel (d) shows heating element during operation at hight temperatures.

3.3 Depleted uranium

Uranium used for the fabrication of sample for the purpose of this thesis is the depleted uranium (DU) metal. Depleted uranium has a lower content of the fissile isotope U-235 than natural uranium. The amount of this fissile isotope in DU is lower than 0.3%, while natural uranium contains about 0.72%. As most radioactivity comes from the U-235 isotope, use of the DU allows

to decrease the level of radiation to around half of its value. This makes it easier and safer to work with, and to transport to external facilities. As thin films already have extremely low activity, this concern mostly the bulk starting material.

The starting material used as the depleted uranium metal target is a disc 2 inches in diameter and 6 mm thick, purchased from Goodfellow company. Prior to mounting the sputtering target on the gun, a cleaning process is required. If the surface of the target has a lot of contamination or is tarnished from prolonged use, a good solution is to polish the surface. Based on the starting quality of the surface, different silicon carbide grade of polishing paper can be used. Usually starting from P180, and systematically reducing to P1200 as a final step.

Before the target is placed inside the main chamber under ultra high vacuum conditions, exposure to the air is unavoidable. This can lead to oxidation of the uranium metal and formation of an oxide layer on its surface. To remover this contamination, as it can influence the quality and the stoichiometry of a sample, guns are sputter cleaned for around 30 minutes before proceeding with any sample deposition process. The sputter cleaning takes place also each time when the chamber has been vented.

3.4 Substrate choice and preparation

The structure of uranium dioxide is well known and was studied using both x-rays and neutron techniques. It is a cubic fluorite structure (cF12 in Pearson notation), where each uranium is surrounded by eight oxygen atoms. The coordination geometry of U^{IV} is cubic, with oxygen O^{2-} atoms in tetrahedral geometry. Therefore, UO_2 space group is Fm3m, No. 225. The lattice constant at room temperature for a stoichiometric cubic uranium dioxide is 5.47 Å.

To grow high quality samples of UO_2, using a DC magnetron sputtering system, a matching substrate is required. A good match between the thin film and the substrate helps to reduce lattice stretch and structural defects. Based on the experience from the research grumps using a reactive DC magnetron sputtering system at the University of Bristol, at the University of Illinois, and at the Institute of Transuranic Elements, suitable substrates were identified. In the work of Bao et al. [78] match between (001) oriented thin film of UO_2 and the (001) oriented substrates

of calcium fluoride (CaF_2) and lanthanum aluminate (LAO) was reported. The yttria-stabilized zirconia (YSZ) substrate to growth a (001) single crystal of UO_2 was reported by Strehle et al. [82]. Later all three orientations (111), (110) and (001) of YSZ were used by Rennie et al. [83] to produce single crystals of UO_2 for corrosion studies.

Yttrium Stabilised Zirconia (YSZ)

Yttria-stabilized zirconia (YSZ) is a ceramic material in which the crystal structure of zirconium dioxide is stabilized at room temperature by an addition of yttrium oxide. The name of this compound related to the oxides it consists of, zirconia (ZrO_2) and yttria (Y_2O_3). Pure zirconia has monoclinic crystal structure at room temperature. The phase transition to cubic structure is observed above 2370°C, after the formation of tetragonal structure at around 1173°C. The melting point for zirconium dioxide is 2715°C.

Making a cubic zirconium dioxide stable at room temperature is therefore challenging, as each phase transition is associated with a large volume change. To achieve stability of the cubic structure over wide range of temperatures, the Zr^{4+} ions are replaced with with slightly larger ions. In this case the ions of zirconium with ionic radius of 0.82 Å, are substituted with 17 % larger ions of Y^{3+}, hence the name.

Different effect are obtained, based on the amount of the stabilizing material. The system ZrO_2 - Y_2O_3 has been extensively studied for more than 60 years. Mostly YSZ with less than 7 mol% Y_2O_3 was used in the early publications. The amount of yttria in the range of 2-6 mol% produce the partially stabilized zirconia. A fully stabilized cubic YSZ is possible with a Y_2O_3-content of >7 mol%.

Substrates used to grow samples in this thesis were 8 mol% - Y_2O_3 stabilized YSZ from MTI company. The lattice constant provided by the supplier is 5.125 Å. Therefore the lattice mismatch between the UO_2 and YSZ substrate in this case is 6.73 %. The epitaxy relation in this system is shown on Fig 3.18, for each three principle orientation (111), (110) and (001).

Apart of providing an epitaxial match for the three principle orientation, YSZ can be also used as a scaffolding for a polycrystalline UO_2 with a controlled grain size. This is a very important property, as the UO_2 nuclear fuel is polycrystalline. The size of the grains is in range of tens of

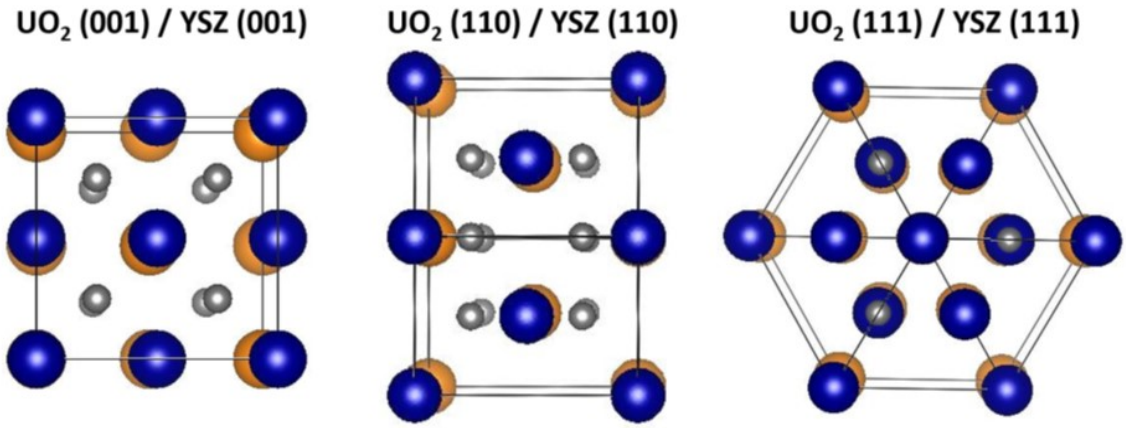

FIGURE 3.18. Schematic of the three principle cubic orientations (100), (110) and (111) and the epitaxial match between UO_2 and YSZ substrate. Oxygen atoms are shown in gray, uranium atoms in blue and YSZ atoms in orange. The lattice mismatch is the same in each case at 6.3 %. Figure from [83]

micrometers, while the thickness of a film is measured in nanometers, which allows to create columns of UO_2 that will exactly match the structure of the ceramic YSZ substrate.The example of this application is shown on Fig 3.19

Using the columnar approach to fabricate samples allows to reduce the three-dimensional problem into a two-dimensional one. This opens new possibilities to study the influence of the grain orientation, and grain boundaries on the mechanical, electrical and other properties of the UO_2. In this scenario, the total length and concentration (area) of the grain boundaries can be easily measured using a SEM, as all the grain boundaries are visible on the surface. In a 3D approach that would not be possible, as often the grain boundaries inside the material can't be measured without destroying the sample, and even then it would not be as precise as in the columnar case.

Grain size of the epitaxial UO_2 can be controlled by modifying the YSZ substrate. In a columnar system, if spot measurements such as XPS or Raman are conducted on a specific grain, the signal will contain only information for this specific crystal orientation, as there are no other grains below to contribute to the signal. Combining EBSD mapping with other techniques allows to precisely measure the difference in the behaviour of the grains, based on their orientation .

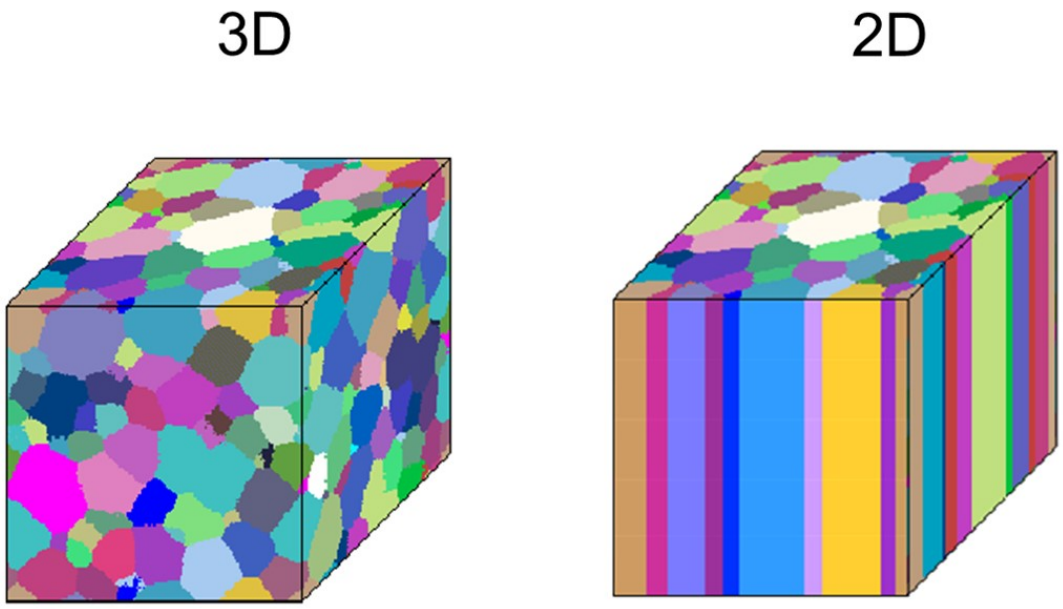

FIGURE 3.19. Schematic of a polycrystalline sample as a three-dimensional material (on the left), where the contribution to the measurement comes from all the grains and grain boundary. On the right a columnar approach, allowing precise measurement of the grain boundaries, and signal coming only from specific orientation of the grain.

Another unique property of the YSZ/UO_2 is previously mentioned latices mismatch, where the YSZ unit cell is smaller than UO_2. The importance of that fact is in behaviour of the UO_2 while oxidising to U_4O_9. The lattice constant shrinks due to incorporation of oxygen from 5.47 Åto 5.44 Å, and the increase of oxygen to $UO_{2.25}$ happen even at room temperature and air atmosphere. Therefore, the UO_{2+x} structure relaxes while oxidizing, and this process is energetically favourable.

3.4.1 Annealing, polishing, cleaning (Substrate modification)

Intense temperatures and radiation fields present within a nuclear reactor induce substantial differences in crystallinity across the uranium dioxide fuel pin [145]. The resultant large grain size distribution as a function of position within a fuel pin, teamed with a poor thermal conductivity and large temperature gradients requires full understanding of the heat transfer mechanism in

the predominant fuel worldwide. Additionally, variations in grain boundary density influence rates of corrosion, an important consideration for the safe storage of spent nuclear fuel [146].

To investigate these effects, polycrystalline yttria stabilised zirconia substrates, that provides a cube-on-cube epitaxial match for UO_2 for all crystal, can be annealed to mimic the size of the grains within a nuclear fuel prior, during and after operation.

Annealing is a heat treatment process, where the material is exposed to high temperature during prolonged time. Atoms are able to migrate, due to increased energy, in the crystal lattice and the number of dislocations decreases. The material progresses towards its equilibrium state, as heat allows to break bonds by providing the needed energy. This process in metallurgy can be divided into three steps [147]. The first step, recovery, happens at the lower temperatures and reduce the amount of dislocation within material, not affecting the grain size and shape. The next stage is recrystallization, where nucleation of grains occurs. Once this process is finished and the sample is still exposed to high temperatures, the third stage, grain growth take place.

Lateral grain sizes of the YSZ substrates was increased by annealing them in tube furnace. This process was carried out in air atmosphere, at 1600 °C. The heating ramp rate was set to 15 °C/min, and the same rate was used for cooling down process after annealing at 1600 was finished. While there was no difference between set point and actual temperature during the heating stage and annealing stage, a noticeable difference of 10-100 °C was observed during cooling down at temperatures below 300 °C. At lower temperatures, the furnace was unable to lose temperature quickly enough to follow the set point. The substrate was left in the oven until room temperature was reached. Due to changes in the grain size and shape, roughness of the material increased, and it was necessary to minimize this effect. In order to obtain a smooth and clean surface, required for sputtering of high quality polycrystalline thin film of UO_2 using DC magnetron sputtering system, polishing and cleaning processes were applied.

Resin encapsulation

Before the polishing process, the sample has to be encapsulated in resin. In our laboratories two types of resins are available, hard (hot) and soft (cold). The hard one has better conductivity which makes it more suitable if the sample will be characterized by electron microscopy, however

due to its process (as the process involve pressure and temperature) it is not recommended to use with YSZ substrates as it causes cracks, and material is no longer suitable to be used for deposition at the DC magnetron sputtering system at University of Bristol.

Two soft resins from Struters are accessible in our laboratory: ClaroCit and EpoFix. ClaroCit is an acrylic resin with short curing time (20 min.), EpoFix is a epoxy resin with much longer curing time (12h), and better shrinkage properties. For the YSZ substrate the recommended mounting is ClaroCit systems, which consists of two components: a hardener (curing agent) and a resin.

All the operation should be handle using gloves or tweezers. Prior to the mounting of the sample in resin, both the sample and the mounting cup have to be clean and dry. Each surface must be free from grease, moisture and any other contaminants for the best possible adhesion.

To mount the sample following items are needed: ClaroCit powder, ClaroCit Liquid, two mixing cups, wooden stick and mounting cup. The ratio of powder to liquid is 20:12 by weight or 5:2 by volume, as the density of powder is 0.66 g/ml and liquid is 0.95 g/ml. To obtain the best results using weighting method is recommended. For mixing amounts smaller than 20g of powder it may be necessary to add a few drops of the liquid. Mounting procedure is following:

- Place the sample facing down in the centre of the mounting cup
- Weight the required amount of the ClaroCit powder in mixing cup
- Weight the required amount of the ClaroCit liquid in mixing cup
- Pour the powder into the liquid while stirring
- Stir for around 90 seconds (without introducing air into mixture)
- Immediately pour the mixture to the mounting cup
- Leave at room temperature for at least 20 minutes (more time might be required for bigger mounting cups)

Three stages from this process are shown on Fig 3.20. On the first picture 20 mm moulds were cleaned using isopropanol and dried out, then samples were placed in the center. In the

second step, resin was pure and sample were left to set (Fig 3.20 (b). Mould with removed lids and visible encapsulated substrates are visible on Fig 3.20 (c).

Alternatively, it is possible to use just one mixing cup and add liquid to the powder while measuring it weight on the scale. However, adding powder to the liquid is recommended for better homogeneity of the resin mixture.

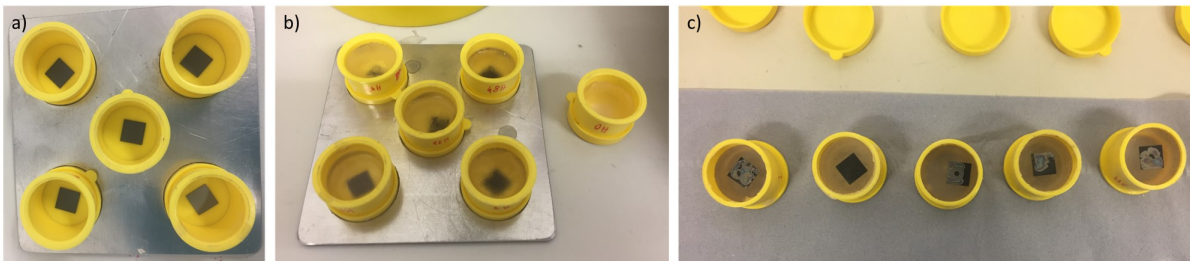

FIGURE 3.20. Different stages of substrate encapsulation. Panel (a) substrates loaded into clean forms. In the next stage (b) resin is pure into the form and felt overnight. Encapsulated substrates, ready for polishing process, are shown on panel (c).

Good practice is to add additional for on the top of the substrate, so it adheres better to the bottom of the mould. This can be achieved by simply placing a stainless steel nut over it. That would prevent resin getting under the sample, and forming additional layer that needs to be removed prior to grinding/polishing the area of interest. Additionally, it will prevent substrate from moving while resin is pure and is setting. If the sample has possibility to move, it can end up being tilted in the fixed resin, making polishing process much more difficult and final product having a gradient of thickness. Alternatively, the sample can be fixed to the bottom using a SEM carbon stick, as the glue leftovers from this process will be removed/polished anyway.

Grinding/Polishing

As some stages of the grinding and polishing process requires to rotate the sample by 90°, or keep it at the same position, it is important to have a reverence points on the sample. Good practice is to engrave a compass rose on the back of the sample as shown on Fig 3.21 (a) with red colour.

Another difficulty faced during grinding and polishing, especially when holding sample by hands, is to evenly apply force during those processes. This might cause again gradient to the

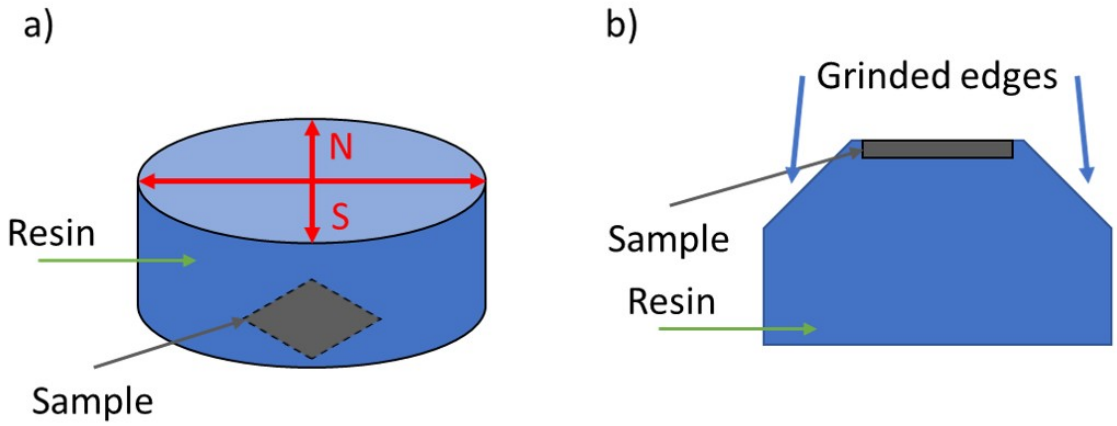

FIGURE 3.21. Schematic of two very useful steps applied to a sample encapsulated in the resin. On the left (a) schematic of up-side down sample, where compass rose is engraved on resin, allowing to control sample rotation during the polishing grinding process. Before grinding/polishing of the substrates it is beneficial to remove softer resin from around the top edges (next to the sample) as shown on (b).

thickness of the sample, but what is more important the surface will not be homogeneous. The entire polishing process is done in steps, therefore, if some area of the sample was not exposed to the same conditions (force applied), the next steps will be only beneficial to the part of the sample. To help with this obstacle, the top edge of the soft resin should be grinded, so the area of the sample is mostly exposed to the grinding/polishing material, as shown on Fig 3.21 (b). It is important not to damage the sample during this process. The best is to use for this step sandpaper grade P600. The same procedure of creating bevels can be applied to the opposite side of the sample to remove any resin imperfections (the meniscus) making it more comfortable to grab with fingers.

After creating bevels sample should be thoroughly cleaned using detergent and finger-scrubbing to remove any adherent debris created during this process. The cleaning process have to be done every time when the sample is to be polished by a finer paper grade. Otherwise, the coarse debris can be transfer between grinding platters, contaminating them. As a result, sample surface will be damaged, and it will be necessary to go back to previous grades and repeat polishing process.

The only way to know what is happening with the sample surface during the grinding/polishing

process is to look at it with naked eye and under optical microscope. This should be done regularly, especially before going to a finer paper grade. To make this process easier, a good practice is to rotate sample 90 °each time the paper grade is changes, and only by 180 °while using the same paper. In this way, line/tranches done by the SiC grains digging only in one direction, will be orthogonal to the previous steps. Therefore, if marks from the previous process are still visible, more grinding/polishing is required. In that case it is important to not increase pressure, what will only increase the depth of smear, but to increase the polishing time. Sometimes , based on the material and paper grade it might be necessary to repeat this process few times, each time slightly reducing pressure to improve surface finishing. Furthermore, peripheral and central area should not be used for polishing.

Based on the polishing process applied to the YSZ substrates by supplier MTI Corporation (USA), different SiC grades of paper were used as a starting point. Two possible finishing are available from supplier, one side polished (can be used straight for deposition) and fine ground. In both cases, if substrates were annealed in order to increase grain size, their roughness changed as well and polishing is required. For the fine ground polished substrate a P800 Silicon Carbide grinding paper was used, followed by P1200, P2500 and P4000. The first stage of polishing process for one side polished YSZ was P1200, fallowed by P2500 and P4000. Time needed for each step was usually between 3 minutes to 20 minutes. The polishers used during this stage are shown on Fig 3.22 (a).

In order to further reduce the roughness of the sample, the surface can be polished using diamond polishers. The ECOMETs polishers are shown on Fig 3.22 (b). Each of them use diamond paste with different size starting from the left the grade of diamond paste are 3um, 1 um, 0.25 um and 0.1 um. The three polishers with higher grades, use MasterTex polishing cloths fitted to wheel, while the last one is fitted with MicroCloth.

Cleanliness plays extremely important role during the process of polishing with diamond pastes. Prior to polishing, the sample should be clean thoroughly to remove possible SiC contamination and other debris from previous stage. Then it has to be cleaned after each step of polishing when changing to the finer-grade polisher to avoid transfer of coarser diamond grains. The sample has to be dried after each cleaning, as water is not good for diamond polishing.

To clean the sample, surface should be first sprayed with lubricant (oil), and then rubbed with a finger (using gloves during entire process) to mobilise debris into the oil. Then a drop or two of washing-up liquid should be applied to form an emulsion with the dirty oil. Diamond is hydrophobic, and will be carried away in the emulsified oil droplets, when rinsed well under the tap water. To help drying, and avoid deposition of minerals for the water, surface should be rinsed using isopropyl alcohol. The use of acetone is not recommended, as it would soften the resin used for encapsulation.

The polishing process using diamond polishers is almost identical to the one for coarse grinding on SiC papers. Although, the force applied to the sample can be lower to allow lubricant oil under the sample. The best results are obtained by moving sample inwards and outwards. To polish the YSZ substrates, a bit of paste (1 cm long for syringe) was added on the cloth together with oil, and then the sample was polished for 5-10 minutes, adding lubricant when required.

FIGURE 3.22. Pictures of the grinders/polishers at the School of Physics (IAC), University of Bristol. From the left (a) grinder/polisher Buehler Metaserv with two rotors with exchangeable coarsest papers. ECOMETs polishers using a diamond paste are shown on picture (b). From left to right the grade of Diamond paste are 3um, 1 um, 0.25 um and 0.1 um. Vibro-Polisher used for the final polishing step of the sample, with colloidal silica (20 nm diam.) is shown on picture (c).

The last step of the polishing process involves use of a Vibro-Polisher. Vibratory Polisher is a machine designed to provide a high quality polished surface, suitable for surface sensible techniques such as AFM or EBSD. This procedure can be applied also as a final step for preparation of the substrate for the DC magnetron sputtering deposition.

The device consists of a bowl containing the polishing cloth with colloidal silica suspension, mounted on a triad of springy angled beams. During operation, an electro-magnet bends the

beams, what causes the bowl to lift and rotate slightly. The inertia of the ground and the encapsulated sample (with extra weight added on top) increases the contact-pressure between the sample and the cloth, increasing the abrasive effect of colloidal silica. When the magnetic field disappears, the bowl is pulled down by the mounting beams faster then gravity. The sample moves, as it is thrown in the air with a tiny rotation and then it lands slightly further forward on the cloth. The polishing happens always at the same relative direction, as the imparted rotary action causes sample to orbit in the Vibro-polisher with a constant radial orientation.

To prepare the Vibro-Polisher, first 75 ml of Milli-Q water are added into the the bowl to wet the cloth. In the next step, 50 ml of Colloidal Silica are added and mixed with water inside the polisher. This result in a homogeneous 0.5 mm thick film of cloudy liquid over the cloth. Samples are mounted into Buehler pucks of different diameter, depending on the resin pot size used for encapsulation, available puck sizes are: 25, 30, 40 and 50 mm. Resin with the sample must have their edges still bevelled as shown on Fig 3.21 (b), otherwise the efficiency of this process will be lower and the file time of the polishing cloth will be reduced. The pucks have a grab screws on the sides to fix the sample. The top point of the sample surface should be around 3 mm from the pucks in order to prevent abrading the puck and lifting suspension into them. The final step before placing puck with a sample inside the Vibro-polisher is to add weight on top of it.

YSZ substrates for this studied were polished using the method described in this section on the Vibro-Polisher shown on Fig 3.22 (c). The magnitude of vibration was kept constant for all the substrates, by setting always the amplitude to 50 %. The total polishing time using Vibro-Polisher was longer than 24 h in each case, resulting in high quality polished surfaces.

Cleaning

A clean surface of the substrates is indispensable for the fabrication of high-quality thin films using PVD on substrates. Contamination might adversely affect the thin film growth, causing reduced adhesion strength to the substrate, defects and dislocation or lead to undesired chemical reactions with either the substrate material or the deposited film. Contamination can occur in various forms e.g. : as particles, absorbed gases and closed films [148].

Prior to the film deposition, different cleaning procedures can be applied to remove contami-

nants. Most of the cleaning procedures established and optimized of several decades [148, 149], focus on effective cleaning of silicon but can be applied to other materials as well. For the microelectronics application, the standard cleaning procedure of Si substrates was developed by Kern and Puotinen in 1970, and named RCA (after the Radio Cooperation of America) [150]. Another possibility to clean substrates surface is use of UV-ozone treatment, this method was developed by Vig in 1985 [151]. On the other hand, this method might cause an increase of the thickness of oxide layer on a silicon surface [152]. Another more efficient way of eliminating organic contaminant [153] than UV-ozone treatment, is oxygen plasma cleaning [154].

The methods mentioned above involve the use of acids (RCA) or special devices. Even though, new contaminants can be introduced from the cleaning equipment, used chemicals and even ambient conditions in laboratory, during the cleaning process itself. Furthermore, handling and transporting the substrates after cleaning have to be done very carefully in order to maintain a very clean surface.

Taking into consideration all of the above information, a method developed by Menon et al. [155] was modified and used to clean the YSZ substrates. This method involves using the common laboratory solvents (acetone and ethanol), an ultrasonic bath, and is easy to handle as no acids are required. Once the polishing is finished, the substrate is still encapsulated into a resin. To soften the resin and be able to remove the sample, entire specimen should be immersed in acetone and left in an ultrasonic bath for one hour. After that time, the resin should be soft enough to scalpel out the substrate. Leftovers of the resin should be disposed to designated bins, as pouring it down the sink will block it.

The sample in addition to the debris from polishing process, will also have some remainings of the resin. Those contamination will prevent from the epitaxial growth of the UO_2 on the YSZ, therefore it is necessary to make this surface as clean as possible. The first stage is to ultrasonicate substrate in acetone for 1 hour to remove bigger resin contamination of the sample. During this time, it is important to check on the process as the temperature will increase and the solvent will evaporate. As the rise of the temperature help the process, evaporation should be avoided as results of that will be re-setting of the resin. Once this step is finished, sample should be rinsed with acetone, and again ultrasonicate for additional 45 minutes in clean acetone.

In the next step to further remove organic contaminants, substrates were submerged in ethanol and left in an ultrasonic bath for one hour, then rinsed with ethanol. The same steps were followed with isopropanol. Once the substrate was subsequently cleaned using those three solvents, the surface was dried using flow of clean warm air to prevent build up of residues.

3.5 Sample Growth

For the growth of samples all substrates have been purchased from MTI Corporation (USA). Prior to shipment substrates undergo sophisticated polishing and cleaning processes resulting in extremely smooth and clean surface on an atomic level. Each substrate is individually packed in protective atmosphere. Therefore, no additional cleaning process is required if the substrates are not annealed, and can be used straight for deposition. Otherwise the substrate undergo the processes described in the previous section. To avoid any additional contamination during substrate handling, gloves and tweezers cleaned with isopropyl alcohol are used. Final samples are stored separately in membrane boxes from Agars Cientific (UK).

Samples in this thesis were fabricated using the existing reactive DC magnetron sputtering system. Substrates were mounted on special molybdenum holders and loaded into the loading chamber. First, in order to be able to open this chamber, the pumping system was switched off and the chamber was vented using nitrogen gas, to prevent any contamination from air. The stage inside the loading chamber allows placement of four molybdenum holders at once, reducing the amount of times that the chamber has to undergo the venting/pumping process.

Before moving to the main chamber for deposition process, a couple of preparation steps were done. Firstly, to achieve an ultra-high vacuum environment, thereby reducing the final sample contamination, the chamber was baked out as described in section 3.1 . Secondly, an out-gassing process was applied to the heater, by increasing it temperature 100 °C above the temperature used for sample deposition. A higher temperature is kept for an hour to allow desorption of the contaminants built up on the heater elements.

Another step undertaken before deposition to minimise any contamination is gun cleaning. Although the target material, which in this case is uranium metal, is polished prior to mounting

inside the chamber, it is exposed briefly to air. Due to the high reactivity of uranium metal, an oxide layer is formed on the top, and there is a chance for another contamination during the target change process. To overcome this issue, the gun was sputter cleaned for 45 minutes prior to sample growth.

Once all the steps and measures were taken to prevent any sample contamination, samples were fabricated. In order to do that, substrates were transferred using magnetic arm from the loading chamber to the main chamber, after opening the manual gate valve in-between those chambers. In case of single crystal substrates a RHEED measurement was taken at this step of the process. Then substrates were gradually preheated to the required temperatures and left for 45 minutes to let the temperature stabilise. A partial pressure of oxygen (usually 2 x 10^{-5} mbar) was introduced into the chamber. In the next step, argon sputtering gas, was let inside and the pressure of argon was adjusted using a leak valve to be around 7.3 x 10^{-3}. Then 50 W power was applied to gun to start the deposition process for required amount of time. Detailed parameters for each sample are listed in Table 3.2.

In case of single crystal growth a RHEED measurement was done once the growth sample reached the room temperature again. The sample was taken out of the main chamber to the loading chamber using the magnetic arm. From the loading chamber samples were transferred into the membrane boxes.

Sample Number	Composition	Sputter Time (s)	Temperature (°)	Argon Pressure (mbar)	Oxygen Pressure(mbar)	Chapter Ref
SN1191	UO_2 / YSZ	1000	600	7.2 x 10-3	2 x 10-5	5
SN1498	UO_2 / YSZ	565	600	7.3 x 10-3	2 x 10-5	5
SN1545	UO_2 / 12h annealed YSZ	950	700	7.3 x 10-3	2 x 10-5	5
SN1493	UO_2 (111) / YSZ (111)	565	600	7.3 x 10-3	2 x 10-5	6
SN1494	UO_2 (110) / YSZ (110)	565	600	7.3 x 10-3	2 x 10-5	6
SN1495	UO_2 (001) / YSZ (001)	565	600	7.3 x 10-3	2 x 10-5	6
SN1535	UO_2 (001) / YSZ (001)	630	600	7.3 x 10-3	2 x 10-5	6
SN1614	UO_2 (001) / YSZ (001)	117	700	7.3 x 10-3	2 x 10-5	6
SN1627	UO_2 (001) / YSZ (001)	293	700	7.3 x 10-3	2 x 10-5	6

Table 3.2: List of samples grown for the studies presented within this thesis, including their composition, growth parameters and to which chapter of this thesis they are related.

CHAPTER 4

POST-DEPOSITION SAMPLE CHARACTERISATION

Based on the deposition parameters and substrates it is possible to grow uranium dioxide samples with different crystal structures. That includes polycrystalline structure with grain sizes from nanometers to tens of microns, and single crystals of specific orientations. This chapter will focus on the characterisation of UO_2 thin films grown using DC magnetron sputtering. XRD characterisation has been conducted on all samples to determine the structural properties of the fabricated films. Where possible, thickness of the sample was measured using XRR, grains and their orientation were characterised with EBSD for polycrystalline samples, and off-specular diffraction was conducted for single crystal samples.

4.1 Growth mechanisms

The first studies on thin film formation processes are dated to at least the 1920s [156]. The concept of formation of nuclei that grow and coalesce was presented from research at the Cavendish Laboratories by Lewis at. al.[157]. Interest in thin-film growth led to the development of new techniques that allowed for the fabrication of materials in a new way, pushing forward in the study of functional complex oxide materials [158], such as UO_2.

The three major thin film growth mechanisms are shown on Fig 4.1, those are (a) Volmer-

Weber (or island growth), (b) Frank-Van der Merwe (or layer-by-layer growth), and (c) Stranski-Krastanov growth.

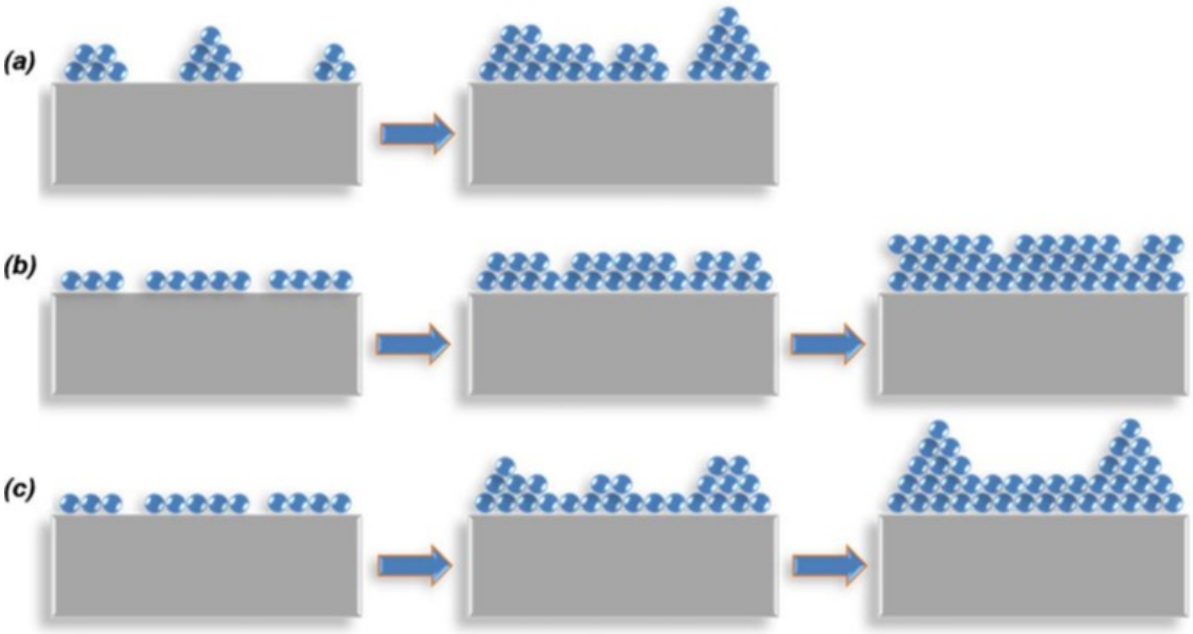

FIGURE 4.1. Illustrations of the three basic growth processes (a) Volmer-Weber (island), (b) Frank-Van der Merwe (layer-by-layer), and (c) Stranski-Krastanov growth. Frigure taken from [159].

The first of the illustrated processes on Fig 4.1 (a) is Volmer-Weber, island growth occurs when the smallest stable clusters nucleate on the substrate and grow in three dimensions forming islands. This happens in systems where the bonding energy between atoms in the deposit is much higher than between the deposited atom and the substrate material. This behaviour is typically observed in the fabrication of metals on insulators, and is rarely observed in the growth of oxide films.

The opposite characteristics are exhibited in in Frank-Van der Merwe. Here the growth of the smallest stable nucleus take place overwhelmingly in two dimensions resulting in the formation of planar sheets. The bonding energy of the atoms to the substrate is much stronger than the bond to each other. Once the first monolayer is completed it is covered with a second layer, which is less strongly bonded. The decrease in the bonding energy progresses with every layer until the bulk bonding strength is reached. This layer-by-layer process involves single-crystal epitaxial

growth of oxide thin film. The recent development around the ability to control deposition through this and other similar growth modes, allows for unprecedented control of oxide materials down to the single (or even half-) unit cell level [159].

The Stranski-Krastanov growth mechanism is an intermediate combination of the aforementioned modes. In this layer-plus-island model, after initial formation of one or more monolayers, subsequent layer growth can transition from two- to three-dimensional growth and islands are formed. This transition is associated with a decrease in binding energy, characteristic of layer growth, which can be caused by film-substrate lattice mismatch, as the lattice strain decreases with each layer. This sort of growth is very common and has been observed in multiple metal-metal and metal-semiconductor systems.

A more detailed description of the aforementioned growth models, including thermodynamic models can be found in the book: Materials Science of Thin Films [156]. In the end, during the deposition of the material on the substrate, nucleation and growth can occur in a number of ways based on the kinetics of the system. Therefore, parameters such as growth temperature, deposition rate, pressure, etc., can be used to control the thin films.

Epitaxial growth

Epitaxial growth refers to the formation of a single crystal film on top of a single crystal substrate. The name comes from Greek *epi* - placed or resting upon and *taxis* - arrangement, as the deposited material adopts the crystallographic structure of the substrate. Two types of epitaxy can be distinguished: homoepitaxy and heteroepitaxy. In the first case a substrate is made out of the same material that will be used for deposition. The films fabricated in this way have very high quality and are free of defects.

Heteroepitaxy is the second type of the epitaxy, where the substrate and the film are different materials, but there is a relation between their structure allowing them to coexist in their forms. One of the simplest examples in show on Fig 4.2, (a) it is a direct cube on a cube, while (b) is also a cubic match, but with a 45 $\pm$ rotation.

The difference between homoepitaxy and heteroepitaxy is demonstrated on Fig. 4.3. The very

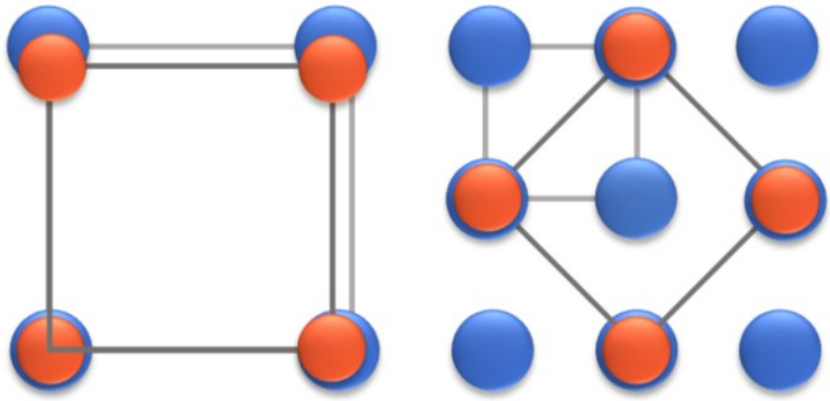

FIGURE 4.2. Epitaxial relation, (a) shows a direct cube on cube match and (b) shows a cubic match with a 45 °rotation.

good match between the substrate and the films results in a nearly perfect lattice match, which is characteristic for the first type of epitaxy as shown on Fig. 4.3 (a). A more complex scenario is achieved when the film and substrate materials are different and the lattice parameters have a slight mismatch. The strained-layer epitaxy is shown on Fig. 4.3 (b). This scenario occurs when very thin films have the same crystal structure regardless of substrate mismatch. The relaxed epitaxy is illustrated on Fig. 4.3 (c). The materials might have different crystal structures, and the lattice mismatch is larger than in the previous example.

Epitaxy has crucial importance not only in the laboratory for growth of single crystal samples for better understanding of the material properties, but also in industrial applications such as solid-state device processing. Therefore, a perfect epitaxy is an extremely desired system and a lot of work has been conducted in this field [156].

Defects

A perfect crystal, where all the atoms are at rest on their correct lattice position in the crystal are extremely rare. Real systems have some interruptions of regular patterns. These imperfections have a thermodynamic origin, as the material will try to reach the minimum of

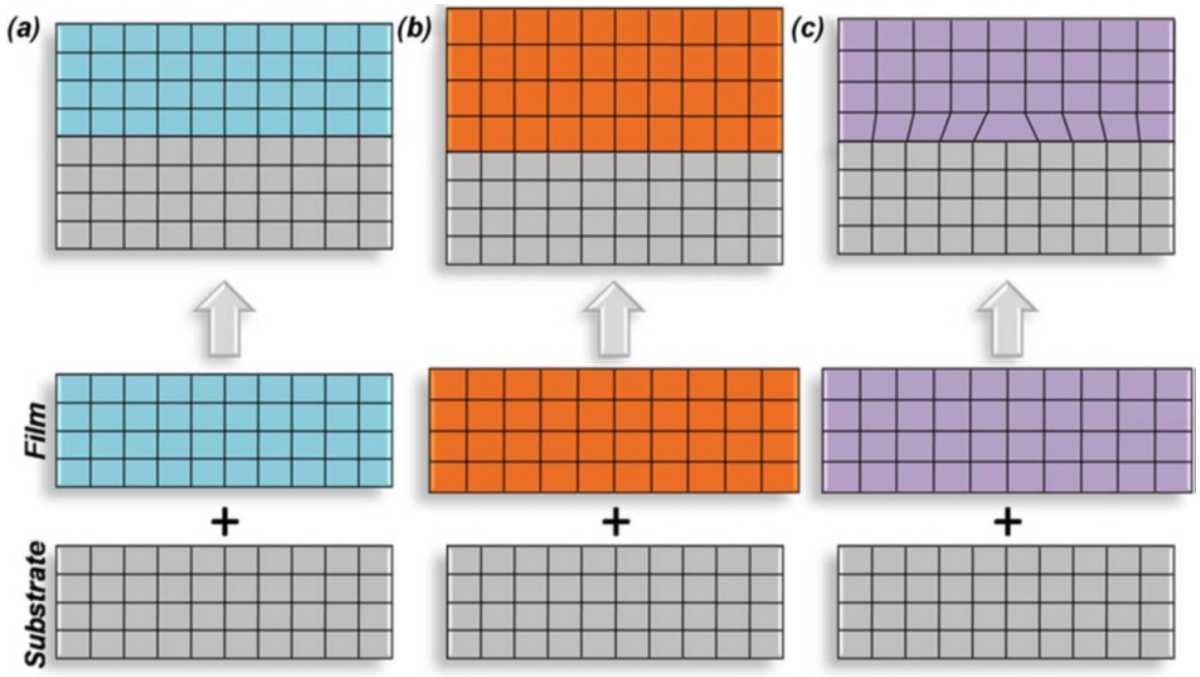

FIGURE 4.3. Different types of epitaxy, (a) homoepitaxy with excellent substrate-thin film match (b) strained-layer epitaxy (c) heteroepitaxy.

Gibbs free energy [160]. Generally those defects are categorised based on their dimensionality: point defects (0-dimensional), line defects (1-dimensional), surface defects (2-dimensional) and volume defects (3-dimensional).

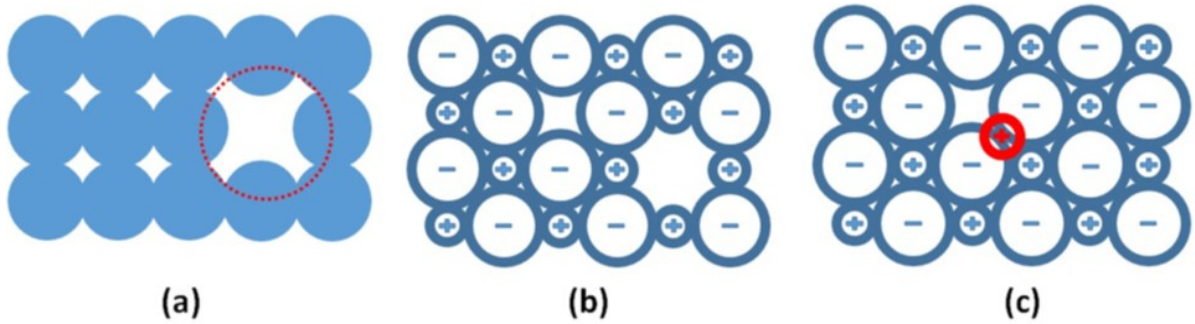

FIGURE 4.4. Three types of the point defects:(a) vacancies created in a lattice, (b) a Schottky defect and (c) a Frenkel defect. Figure taken from [161].

In the 0-dimensional defects an unoccupied atom position within a crystal lattice creates a vacancy or vacant site. This imperfection exists only or around a single lattice point and is

not extended in space in any dimension. Three types of these defects are shown in Fig 4.4, (a) vacancies in a lattice, (b) a Schottky defect and (c) a Frenkel defect. They may occur as a result of imperfections in the original crystal growth or they may be formed from thermal vibrations at higher temperatures as the increase in thermal energy increases the probability of individual atoms to move from their original position to a lower energy position. In this case a distortion to the lattice planes is observed, as atoms surrounding the vacancy tend to be closer to each other. If there are two or more of vacancies they may condense into di-vacancy or tri-vacancy states [161].

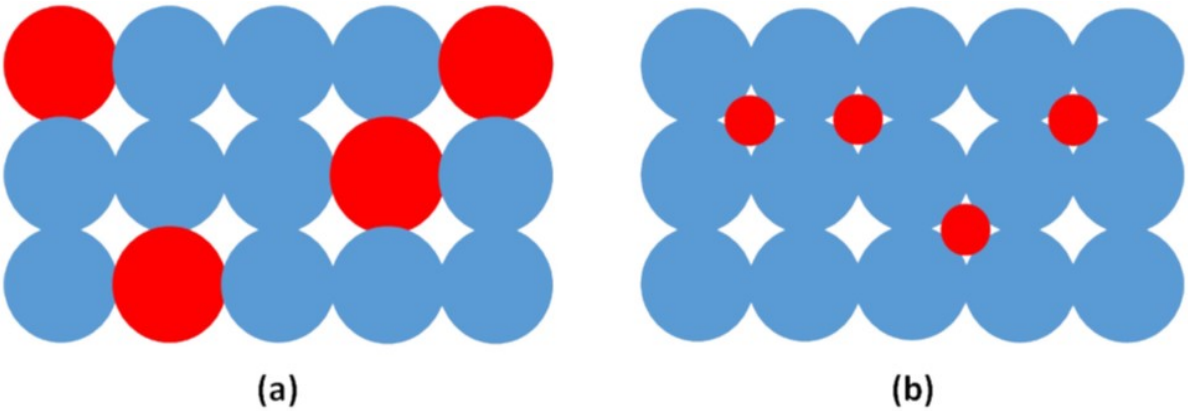

FIGURE 4.5. Examples of the (a) substitutional and (b) interstitial atoms. Figure taken from [161].

Closely related to vacancies are the Schottky defect and the Frenkel defect, shown on Fig. 4.4 (b) and (c). In the first case, an anion-cation pair is displaced from its position in an ionic compound creating a vacancy of the charged pair. In the second case, the smaller in size cation can migrate to another lattice position creating a vacant an interstitial defect. In both cases the overall electrical neutrality is maintained.

An interstitial defect can be created by atoms occupying positions between the atoms of the ideal crystal, as shown on Fig 4.4 (b). This defect can also cause distortion to the lattice planes, as interstitial atom tends to push the surrounding atoms farther apart, what is usually the case in self-interstitial. If the interstitial atom is an impurity and is smaller than the original atoms, distortion to the lattice plane might not occur.

Impurities may not only take interstitial place in a crystal structure, but also substitute

an atom on original position, as shown on Fig 4.4 (a). Foreign atoms usually act as centres of distortion due to their different atomic radii and different electronic structure. Therefore, those impurities may considerably distort the lattice.

In the one-dimensional defect, the most important are dislocations. A dislocation is a disturbance between two substantially perfect parts of a crystal, usually caused by stress or strain being applied to a material. The two basic types of dislocations, which typically coexist in the structure are: edge dislocation and screw dislocation.

The lattice distortion resulting from an edge dislocation, shown on Fig. 4.6 (a), can be described using the Burgers vector. This vector informs about the magnitude and direction of the defect. In this case the Burgers vector lies perpendicular to an edge dislocation. An edge dislocation consist of an extra row of atoms above or below the slip plane, so called positive edge dislocation and negative edge dislocation respectively. This defect causes a distortion in the adjacent lattice planes, and can change the position. When a shear stress a negative dislocation moves to the left and positive to the right, therefore the movement is in the direction of the Burgers vector.

A screw dislocation is parallel to its Burgers vector,as shown on 4.6 (b) , and the movement happens in the perpendicular direction to its Burgers vector [161]. The distortion has a helical shape, as the name suggest, with both paths possible: right-hand and left-hand. It continues as a helical arrangement of atoms around the core, rather than a series of parallel planes.

While the edge defect originates from the mismatch between the film and substrate lattice parameters and slight mismatch in the orientation of the adjacent atoms row in the epitaxial crystal growth, the screw dislocation might be created during crystallization if there is a twisting in the stacking sequences of atoms. Edge dislocations are very common in epitaxial thin films of UO_2 deposited on YSZ due to 6.3% of lattice mismatch between those structures as they reduce the surface energy. The highest amount of the defect will therefore be at the interface area, and will decrease with the film thickness. The stain will follow the same relation, as the energy gain from dislocation will become less favourable.

Two-dimentional defects are regions between homogeneous crystal areas with a distinct interface and include grain boundaries, tilt boundaries, twin boundaries, stacking faults, coherent and incoherent precipitate interfaces [161].

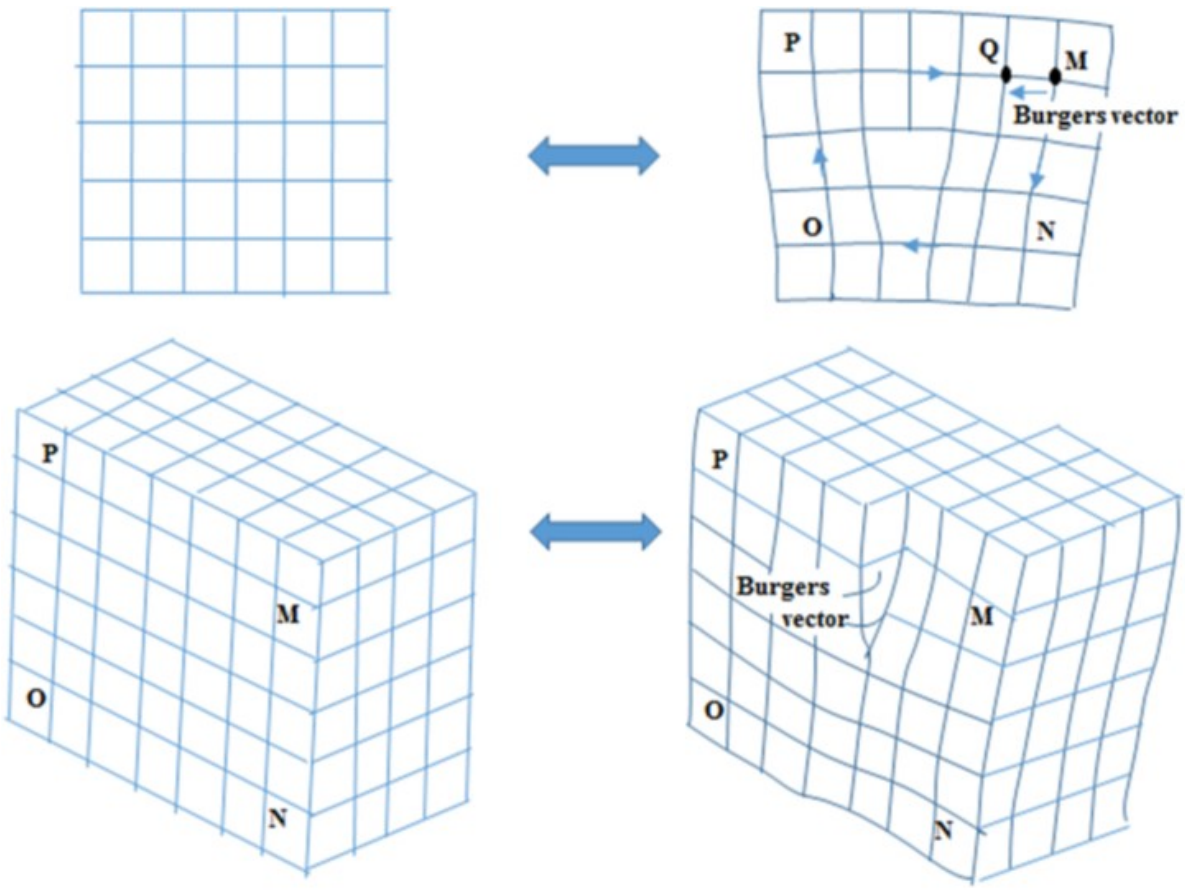

FIGURE 4.6. Schematic ilustration of Burgers vectors used to ilustrate (a) an edge dislocation and (b) a screw dislocation. Figure taken from [161].

Grain boundaries are a part of polycrystalline samples as those planar imperfections separate crystals of different orientation. They are created at the area where two or more growing grains meet, and their structures are imperfect with a transition zone not aligned with any grain. Atoms at the grain boundaries have higher free energy and are in highly distorted and strained position compared to undisturbed atoms inside the crystal.

Other surface imperfections are tilt boundary and twist boundaries that might be regarded as a set of edge dislocations and screw dislocations respectively. When a surface imperfection separates two parts of a crystal with the same orientation and the angel between them is very low, they are called twin boundaries.

The crystal morphology, mechanical strength and catalytic properties can be also significantly

affected by the surface finishing [162]. For any ionic or even partly ionic crystal, the surface can be classified into one of three categories shown on Fig. 4.7.

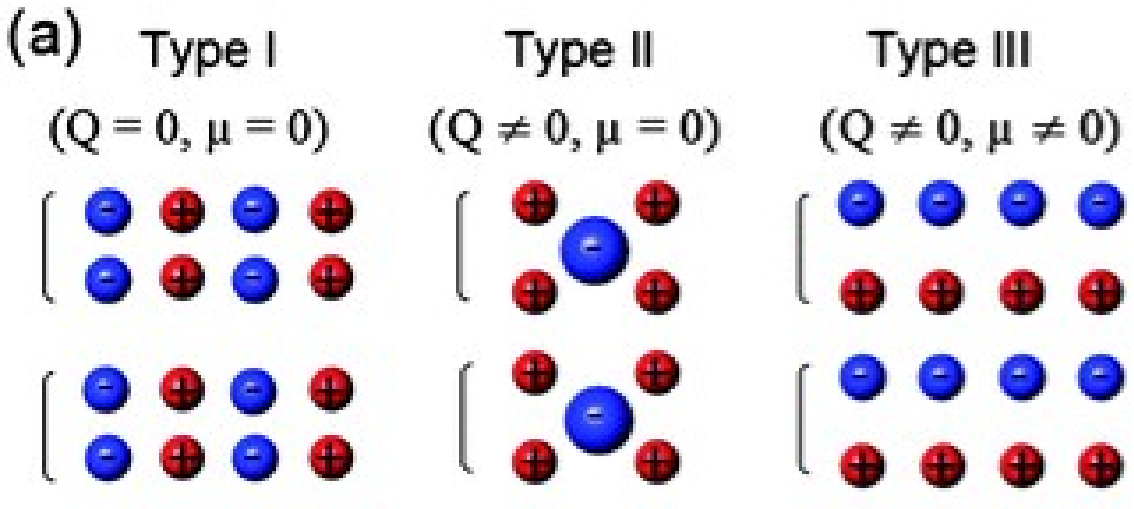

FIGURE 4.7. Schematic illustration of Tasker's classification of ionic crystal surfaces.

Type 1 is a neutral surface due to stoichiometric proportion of cations and ions in each plane.

Type 2 overall charge of the system, is neutral due to symmetrical arrangement of charged planes.

Type 3 a dipole moment is present in the repeat unit perpendicular to the surface due to a charged surface.

This plays an important role in thin epitaxial films where the most of the material is its surface. It makes the thin film the perfect candidate for conducting surface studies.

The last type of the defects is very rare for thin film materials and is more common for bulk materials. Those three-dimensional imperfections are volume defects formed by aggregates of atoms or vacancies. The volume defects are precipitates, inclusions and pores/voids. More information about them can be found in [161].

As shown in this subsection, the structure of the final thin film can be complex, with a different combination of defects. In general thin films can have the following structures [159]:

Perfect Epitaxial, usually homoepitaxy where a single crystal film grown on the substrate made of the same material.

Nearly Perfect Epitaxial, only limited imperfections are present at the interface of the substrate and the film single crystals.

Textured Epitaxial, mosaic structure of epitaxial material deposited on a single crystal substrate.

Perfect Polycrystalline, crystalline grains are randomly oriented in all directions.

Textured Polycrystalline: crystalline grains have preferred orientation in a specific direction.

Amorphous: no long range order is observed within the structure.

Therefore it is important to characterise deposited thin films prior to conducting any experiments, which will be described in the rest of this chapter.

4.2 RHEED

Reflection high-energy electron diffraction (RHEED) system described in Chapter 4 was used in-situ during the growth of the films. In the case of a single crystal material the RHEED pattern will consist of sharp spots, which will undergo systematic variations upon the sample rotation, consistent with the crystalline symmetry. Signal can be also observed in the form of rings for a sample with preferred orientation, whereas due to the sensitivity there is no visible signal for a polycrystalline structure. Furthermore, for an amorphous thin film no pattern will be observed.

Therefore, RHEED measurement was conducted only while growing single crystal structures. Signal from the substrate and from the film was observed for samples: SN1493, SN1494, SN1495, SN1535, SN1614 and SN1627. As this method does not provide any specific information with higher precision than x-ray characterisation, it was used only as an indication. An example of the observed pattern is shown on Fig 4.8. The panel (a) on the left shows the signal obtained from the YSZ (001) substrate prior to deposition. Measurement of the substrate is not only conducted

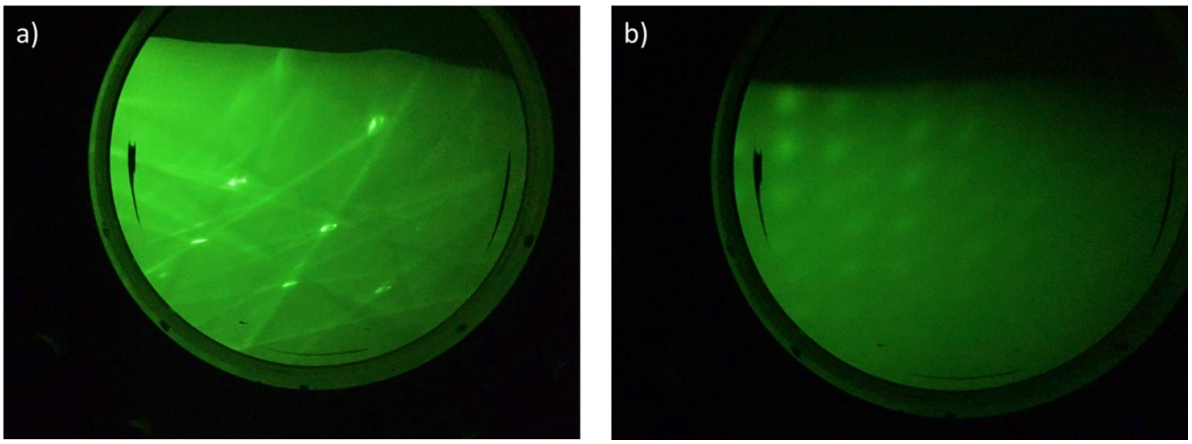

FIGURE 4.8. Example of the RHEED measurment conducted on YSZ (001) substrate (a), and (b) on the thin film of uranium dioxide grown on this substrate.

to verify its structure but also to assure that the system is fully operational prior to sample investigation. The signal from the thin film of uranium dioxide grown on this substrate is shown on Fig 4.8 (b). Those measurements performed at S_h = 8 mm and at the power setting 27kV and 1.44A.

4.3 Sample characterisation

X-ray characterisation

Post-deposition characterisation of the samples used in this thesis was done using PANalytical X'pert diffractometer at the School of Physics (IAC), University of Bristol. This equipment was previously described in Chapter 3. Unless stated otherwise, the open eulerian cradle stage was used for the measurement as it provides higher precision of sample alignment than any other available stage in our laboratory. Prior to any measurement, the x-ray tube source was bred using the software provided with the equipment which ramps up voltage in steps up to 70 kV. All the diffraction measurements were taken at a generator operating at 40 kV and 40 mA. Whereas, to prevent the detector from damaging with a high intensity x-ray beam, for the reflectivity measurement at very low angle (usually below 1.2 °) the power was reduced to 30 kV and 10 mA,

or a copper absorber 0.1 mm was placed in front of the source.

The same alignment procedure was used for all samples. In order to be sure that sample is placed at the middle of the beam, and signal comes actually for the sample not the stage a half cut procedure was conducted. Firstly, the position of the source and the detector is placed to 0 (θ = 0°), and copper absorber is placed in front of the x-ray source. Then, the intensity of the full beam, without sample, is measured. Sample height is then adjusted until the intensity is half of its initial value.

In the next step the omega offset was found by setting 2θ to 0.2°and scanning along ω for the maximum of intensity. Once this was done, and the omega offset was applied, the chi motor was varied to make sure sample is not tilted with respect to the source and the detector, and the maximum intensity again was found. As those alignment might influence each other, those set of steps were repeated until there was no changes observed to the position of maximum of the intensity.

Electron microscopy

Since the demonstration of SEM principle by Knoll in 1935 [163], and the construction of the first true SEM in 1938 by von Ardenne [164], a huge development have been made in the field of electron microscopy [122]. Modern microscopes allow to create magnified images which provide microscopic-scale information on the size, shape, composition, crystallography, and other physical and chemical properties of a sample.

Proper sample preparation plays an important role in obtaining the required information when using scanning electron microscopy (SEM). the surface of the sample should be as clean as possible, therefore to maintain that, samples were stored in special separate boxes and were handled with tweezers and gloves. Another important feature to consider are conductive properties of the specimen. If the sample surface is not well conductive a conductive film coating can be used. Although uranium dioxide is a ceramic, its conductive properties are good enough to perform electron imaging without a conductive layer on top of it. To mitigate sample charging, as the YSZ substrate is not a good conductor, a bridge using a silver paste between the surface of

the thin film and the aluminium SEM stub was made prior to imaging all the samples. Also the sample was fixed to the stub using silver dug.

A variety of electron microscopes are available at the University of Bristol. At this stage of sample characterisation two of the microscopes placed at the School of Physics (IAC) were used. The first one is a dual beam system FEI Helios NanoLab 600 with three-axis micromanipulator, equipped with a Field Emmission Gun (FEG) as an electron source, and Focused Ion Beam (FIB) of the Ga+ ions. This microscope was used for marking the region of interest on the sample surface.

The second system is Zeiss Sigma HD VP Field Emission SEM with EDAX and EBSD (AMETEK-EDAX). This system was used for mapping the grain orientation of previously marked areas. All the maps were taken at accelerating voltage of 30 kV and aperture open to 120 μm to provide enough signal for the EBSD. The acquisition step varied depending on the sample. The diffraction data acquired from EBSD was processed using OIM^{TM} software, to produce crystallographic orientation and phase maps from predefined surface areas using an automated mapping routine.

4.3.1 Single crystal samples

X-ray studies of a single crystal material allow to extract additional information in comparison to polycrystalline systems. For a single crystal sample only rise to the allowed diffraction peaks will be observed in the longitudinal $\omega - 2\theta$, that allows for an alignment of the sample to the actual lattice planes if there is even a small parallel mismatch between those planes and the sample surface. Furthermore, rocking curves on a specific Bragg's peak can be conducted to investigate the texture (mosaic) of the sample.

The single crystal nature of a sample can be truly confirmed by conducting perpendicular scans to the sample surface, in addition the the in-plane diffraction. Those scans were performed by aligning 2θ on a specific Bragg peak and then setting an angular offset to ω, in the way to make the Q vector perpendicular to the off-specular peak. After the alignment, the sample off-specular symmetry was measured by rotating it 360°in ϕ.

Sample SN1493: (111) UO_2 / (111) YSZ

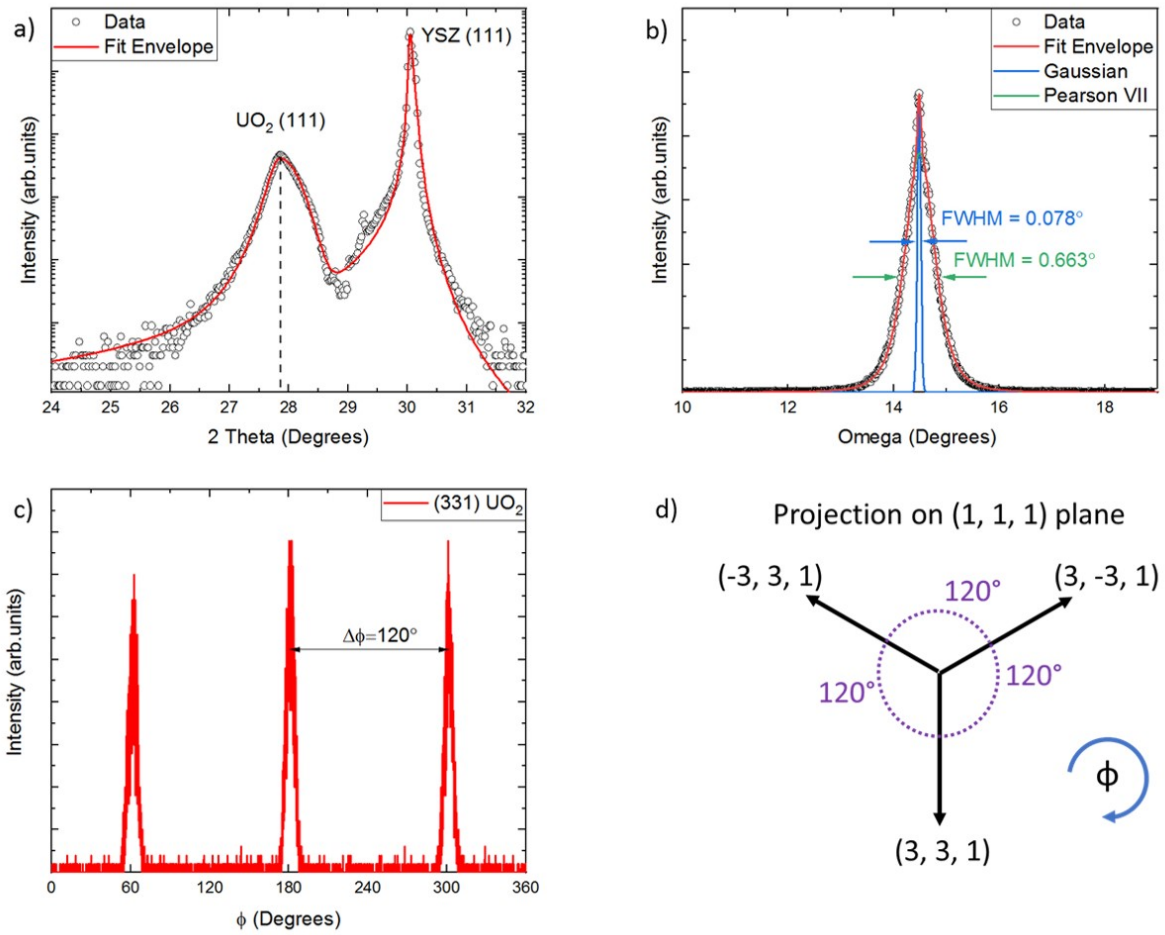

FIGURE 4.9. X-ray measurements of sample SN1493 (111) single crystal of UO_2. Panel (a) shown the longitudinal $\omega - 2\theta$ scan with visible (111) Bragg peak. Associated rocking curve is shown on panel (b). The off-specular (311) scan with three fold symmetry is presented on panel (c). The projection of the off-specular vectors onto (111) plane is displayed on panel (d).

The data collected for a single crystal of (111)-oriented UO_2 thin film (SN1493) is shown on Fig 4.9. The first plot (Fig 4.9 (a) is a high-angle diffraction pattern showing reflections only from two single crystal structures, the YSZ substrate and the UO_2 film. This profile was modeled using two asymmetric Pearson VII function for the (111) Bragg peak of the UO_2, and the peak arising from the (111) YSZ substrate. The central positions of the Bragg peaks were extracted to

calculate the (111) inter-planar distances which are 3.20 ± 0.03Å and 2.97 ± 0.02Å for the UO_2 and YSZ respectively.

The corresponding rocking curve to the (111) Bragg peak is shown on Fig. 4.9 (b). The profile was fitted using two functions. The long range order expressed as the middle sharp peak was fitted using a Gaussian function, while the broad part was fitted by Pearson VII component. The FWHM for the sharp component is $0.078 \pm 0.005°$, and for the Pearson VII the m=2.16 and the FWHM is $0.663 \pm 0.005°$. The (331) off-specular reflection measurement is presented on Fig. 4.9 (c) showing expected three fold symmetry from the projection of the off-specular vectors onto the specular plane Fig. 4.9 (d), indicative of a single crystal thin film.

Sample SN1494: (110) UO_2 / (110) YSZ

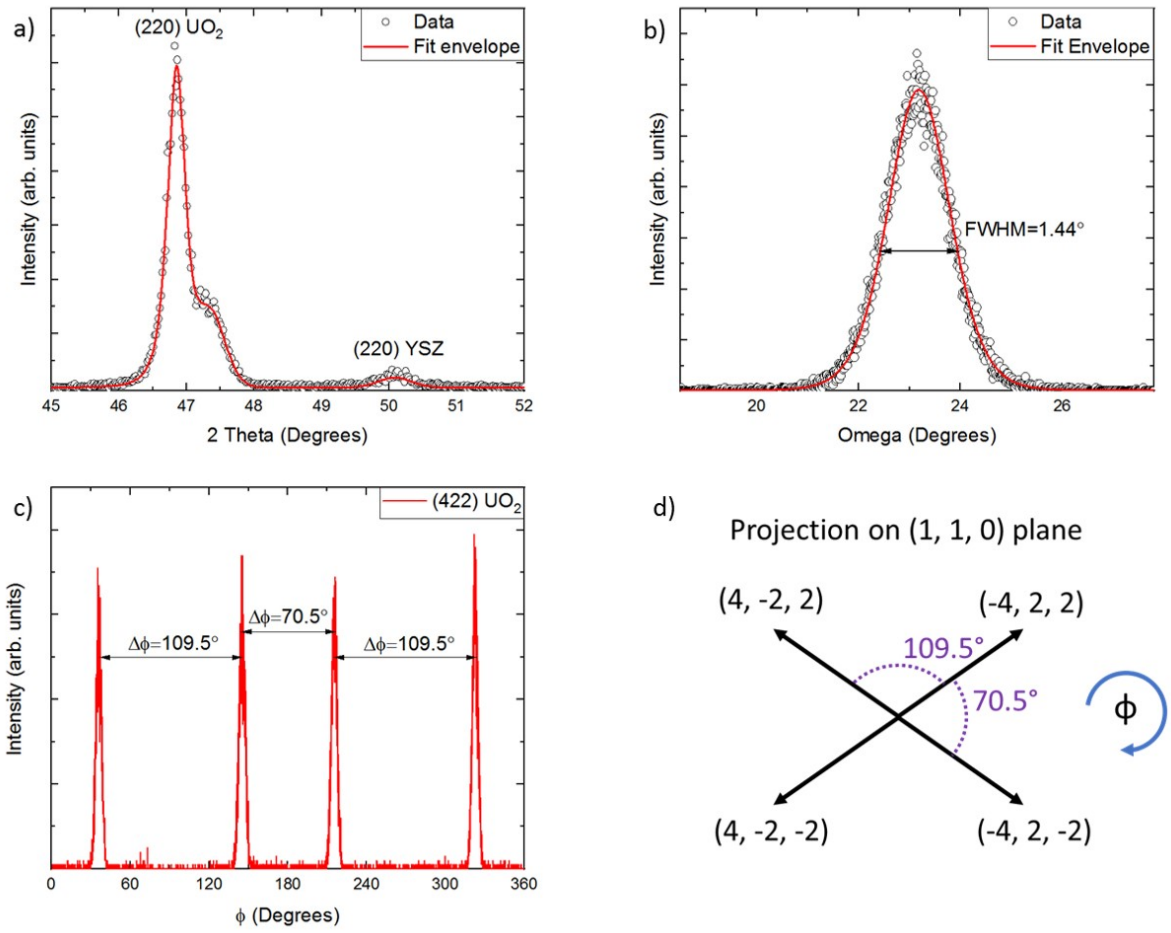

FIGURE 4.10. X-ray measurements taken for sample SN1494. The longitudinal $\omega - 2\theta$ scan is shown on panel (a). The associated rocking curve with the (220) UO_2 Bragg peak is presented on panel (b). The confirmation of a single crystal structure by taking (422) off-specular scan is shown on the panel (c). The projection of the off-specular vectors onto (110) plane is displayed on panel (d).

The next sample SN1494: (110)-oriented single crystal thin film of UO_2 was characterised in the same way, and the collected data is presented on Fig 4.10. The longitudinal $\omega - 2\theta$ scan of (220) Bragg peaks for uranium dioxide and yttria-stabilized zirconia are shown on Fig 4.10 (a). The data is represented by black circles and the fit by the red line. To fit this data a Gaussian function an an asymmetric Pearson VII were used. The lattice spacing of (110) planes was calculated from extracted central Bragg peak positions, and was found to be 1.94 ± 0.03Å and 1.82 ± 0.02Å for the

sample and substrate respectively.

Fig 4.10 (b) presents the corresponding rocking curve pattern of sample SN1494 , measured at the (220) Bragg peak for UO_2. To fit the rocking curve profile Pearson VII function was used, and the FWHM was found to be $1.44 \pm 0.01°$. The lack of the strong narrower Gaussian component indicates worst long range alignment of the crystal structure, and a significant amount of stress and defects. The measurement of the (422) off-specular reflection for UO_2 structure is shown on Fig. 4.10 (c). The theoretical calculation (Fig. 4.10(d)) matches very well with the obtained data and confirms a single crystal structure.

Sample SN1495: (001) UO_2 / (001) YSZ

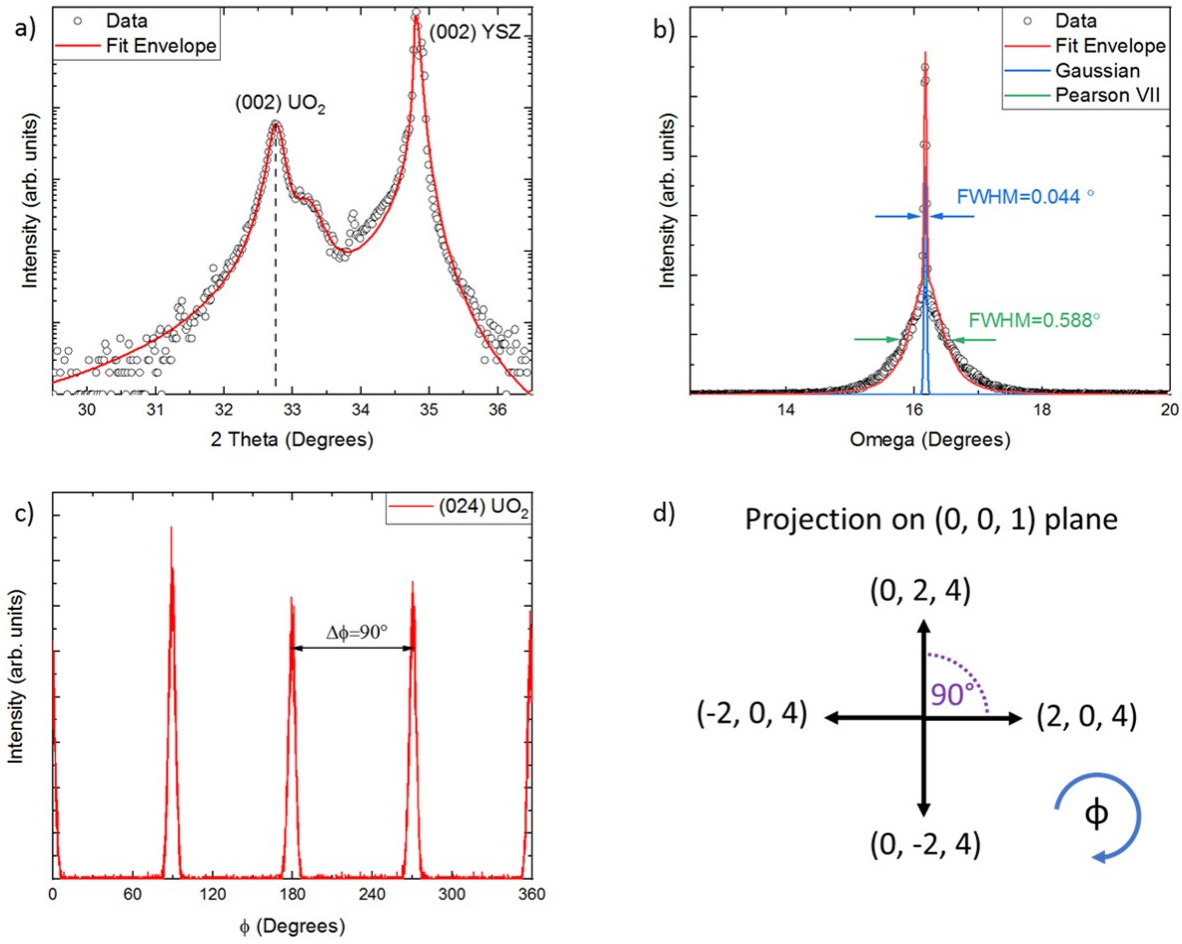

FIGURE 4.11. X-ray characterisation of sample SN1495. Panel (a) shown the high angle with the (002) Bragg peaks of UO_2 nad YSZ. The rocking curve associated with the (002) Bragg peak for UO_2 is shown on panel (b). The (024) off-specular scan with a four fold symmetry is presented on panel (c). The projection of the off-specular vectors onto (001) plane is displayed on panel (d).

Measurements taken for the sample SN1495, which is a 100 nm thin film of uranium dioxide (001)-oriented single crystal, are shown on Fig 4.11. The high angle scan showing reflection only from (002) Bragg peaks of UO_2 and substrate is shown on Fig 4.11. Data was fitted using a Gaussian function and an asymmetric Pearson VII function, and central Bragg peaks positions were extracted. The calculated lattice distance for UO_2 and YSZ, was found to be 5.46 ± 0.02Å

and 5.15 ± 0.02Å respectively.

The rocking curve measurement corresponding to the (002) Bragg peak of UO_2 from sample SN1495 is shown on Fig 4.10 (b). To fit the data, two functions were used a Gaussian and a Pearson VII. The FWHM of the sharp component fitted with Gaussian function is equal $0.044 \pm 0.005°$, and the broad Pearson VII FWHM was found to be $0.588 \pm 0.005°$. The off-specular measurement of (024) is shown on Fig 4.10 (c) showing four fold symmetry with a peak distance of 90 °as expected from the off=specular vectors (Fig 4.10 (d)), once again indicating a single crystal material.

Sample SN1535: (001) UO_2

The specular and off-specular XRD scans taken for sample a 100 nm thin film of (001)-oriented uranium dioxide (SN1535) are shown on Fig. 4.12. The longitudinal measurement demonstrates the presence of a single crystallographic (001) orientation of both the thin film and the substrate. To fit those peaks a Pearson VII and an asymmetric version of this function were used, respectively. Based on the fit, the central Bragg positions were extracted and the lattice parameter was calculated for the UO_2 5.45 ± 0.01Å and the YSZ substrate = 5.16 ± 0.02Å. To confirm that SN1535 is a single crystal an off specular scan, indicative of a single crystal material, of (024) plane was conducted for the substrate and the thin film as shown on Fig 4.12 (b). The distance between peaks is 90 ± 1 °and its a four fold symmetry as expected (d). The position relative to each other between thin film and the substrate indicates that it is a cube to cube match.

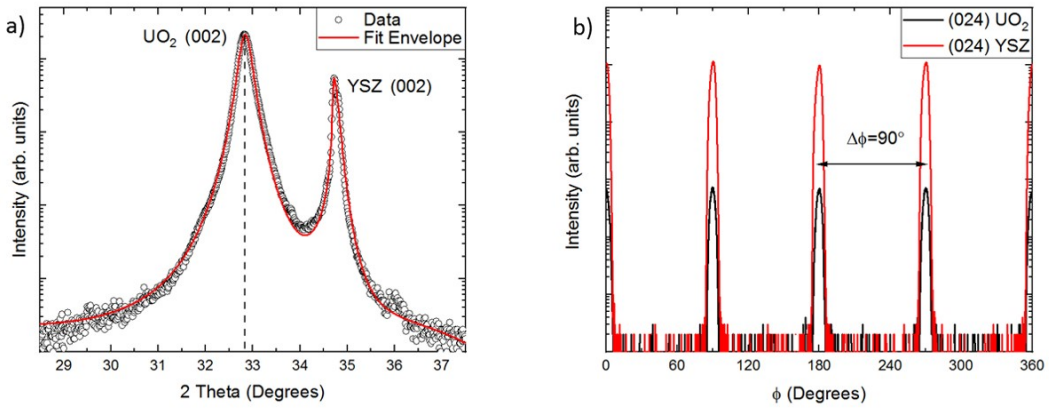

FIGURE 4.12. X-ray characterisation of 100nm thick sample SN1535. On the left (a) is a longitudinal $\omega - 2\theta$ that showed only expected (002) Bragg peaks assigned to cubic structure of UO_2 and YSZ. On the right (b) are (024) off-specular scan of of the thin film and the substrate, indicating a single crystal structure of both, with expected four fold symmetry. Furthermore, the UO_2 fluorite structure sits exactly at the YSZ cubic structure.

Sample SN1614: (001) UO_2 / (001) YSZ

In order to determine the parameters of the SN1614 sample, XRR measurements were performed,. Fig 4.13 (a) shows a longitudinal $\omega - 2\theta$ scan with visible Kiessig fringes, evidence of a smooth interface between the substrate and the thin layer of uranium dioxide film. This XRD profile was modeled using a series of Gaussian function, and an asymmetrical Pearson VII was used to fit the sharp Bragg peak arising from the (002) YSZ substrate.The central Bragg peak positions were extracted from those fits, which allowed to calculate specular lattice parameters for the thin film and substrate, which are 5.47 ± 0.03Å and 5.15 ± 0.02Å respectively.

Rocking curve corresponding to the (002) UO_2 Bragg peak is shown on Fig 4.13 (b). To fit the profile of the rocking curve two functions were used. The middle sharp part associated with long range order was modeled using a narrow Gaussian fit, where the FWHM is $0.083 \pm 0.005°$. An asymmetrical Pearson VII component was used to fit the broad part of the rocking curve, where the $m = 4.11$ and the FWHM is $1.503 \pm 0.005°$.

The starting thickness and roughness of the SN1614 sample was determined by conducting x-ray reflectivity measurement and fitting data using GenX software. The data is shown on Fig 4.13 (c) as open black circles and the fitting model is represented by the red solid line. The thickness of the SN1614 UO_2 thin film was extracted from the fit as 192.3 ± 0.3Å with a surface roughness of 4 ± 1Å, and YSZ substrate roughness is 2 ± 1Å.

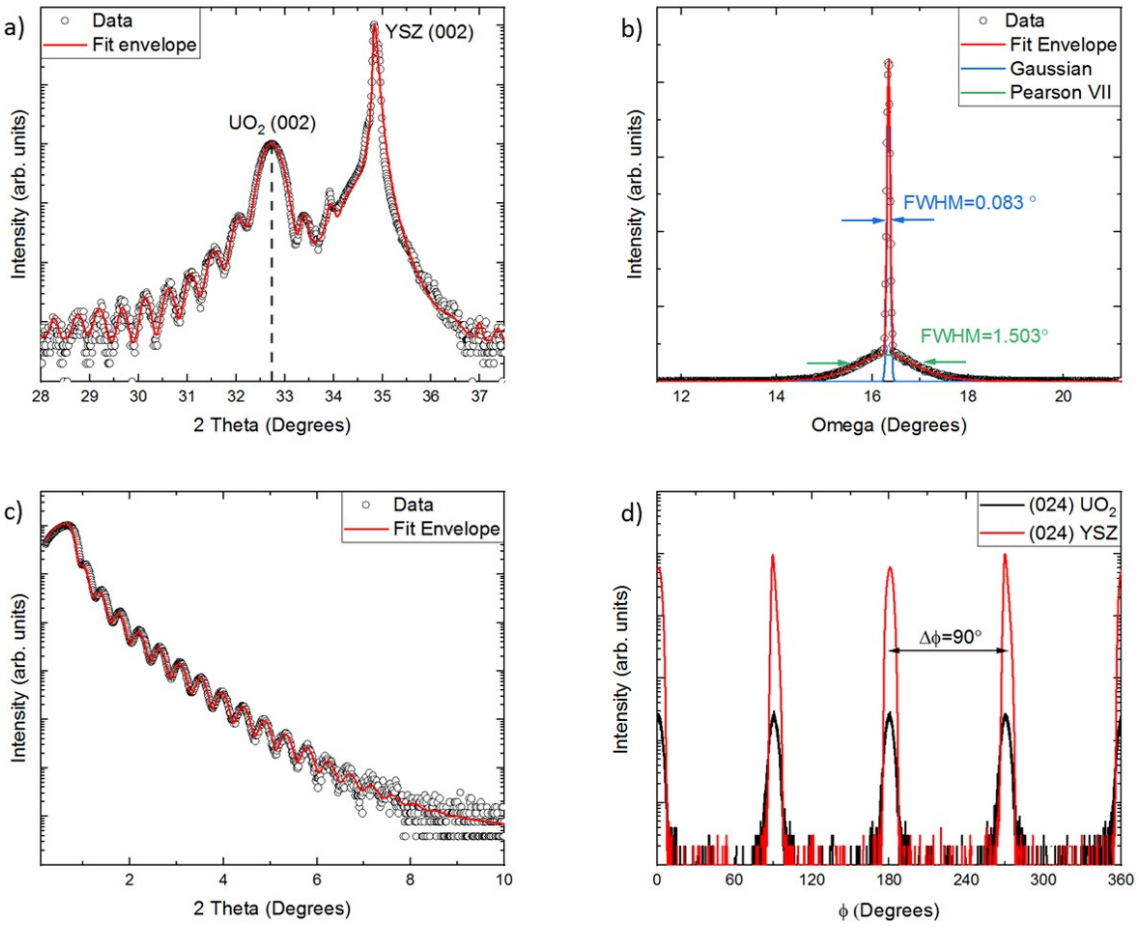

FIGURE 4.13. X-ray measurements of sample SN1614 prior to the oxidation experiment. Panel (a) shows the longitudinal scan of the (002) UO_2 Bragg peak, (b) shows the corresponding rocking curve measurement taken at the (002) Bragg peak. Panel (c) shows the x-ray reflectivity measurement of the SN1614 sample, and (d) shows off-specular rotational phi scans for the (420) crystal plane of the UO_2 thin film and the (420) crystal plane of the YSZ substrate. Open black circles represent the data points and the solid lines shows the fits.

Sample SN1627: (001) UO_2 / (001) YSZ

Sample SN1627, thin film of UO_2 on YSZ substrate, was characterised prior to the oxidation experiment using x-rays, in order to determine the starting parameters of the sample. Fig 4.14 (a) shows a longitudinal $\omega - 2\theta$ scan. This XRD profile was modelled using two asymmetric Pearson VII functions to fit the Bragg peak arising from the (002) UO_2 thin film and (002) YSZ substrate. The central Bragg peak positions were extracted from those fits, what allowed to calculate specular lattice parameters for the thin film and substrate, which are 5.44 ± 0.03Å and 5.15 ± 0.02Å respectively.

The rocking curve profile of the (002) Bragg peak for the sample SN1627 is plotted on 4.14 (b). To fit the data two functions were used, Gaussian with FWHM of 0.061 ± 0.005°for the sharp part related to long order of the structure, and Pearson VII with FWHM of 1.518 ± 0.005°for the broad part associated with defects and stress within the thin film.

The XRR data was fitted using GenX software to find the thickness of the UO_2 thin film, as well as the roughens on the substrate-thin film interface and thin film-air interface. The thickness of the sample was found to be 47.5 ± 0.3 nm with sample-substrate roughness of 4.3 ± 0.8 Å, and the roughness of the UO_2 layer was 14 ± 4 Å.

The truly single crystal nature of the sample was confirmed again by performing scan of (024) off-specular reflection for both the thin film of UO_2 and YSZ, shown on 4.14 (d).

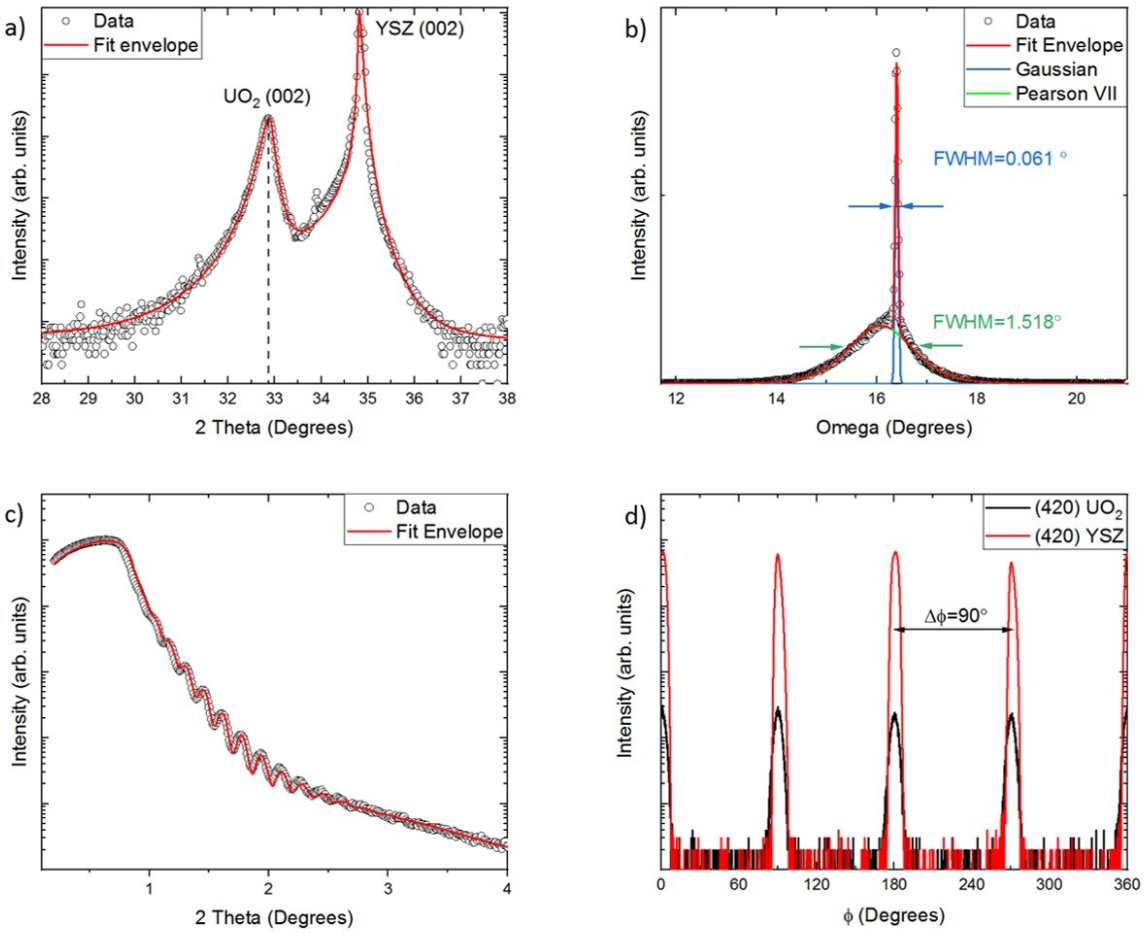

FIGURE 4.14. X-ray measurements of sample SN1627 prior to the oxidation experiment. Panel (a) shows the longitudinal scan of the (002) UO_2 Bragg peak, (b) shows the corresponding rocking curve measurement taken at the (002) Bragg peak. Panel (c) shows the x-ray reflectivity measurement of the SN1614 sample, and (d) shows off-specular rotational phi scans for the (420) crystal plane of the UO_2 thin film and the (420) crystal plane of the YSZ substrate. Open black circles represent the data points and the solid lines shows the fits.

EBSD assessment of single crystals

Although, EBSD can be used to complement the XRD analysis of the single crystal [165] material and has shown a good correlation for assessment of UO_2 thin films [166], it does not provide extra information to that obtained from XRD. Another disadvantage of EBSD for characterisation of single crystals compared to XRD, is the volume of the sample that is examinable. In the first case a small surface area of the sample is investigated, while x-ray diffraction of thin film allows to access almost entire volume of the sample, when investigating very thin films.

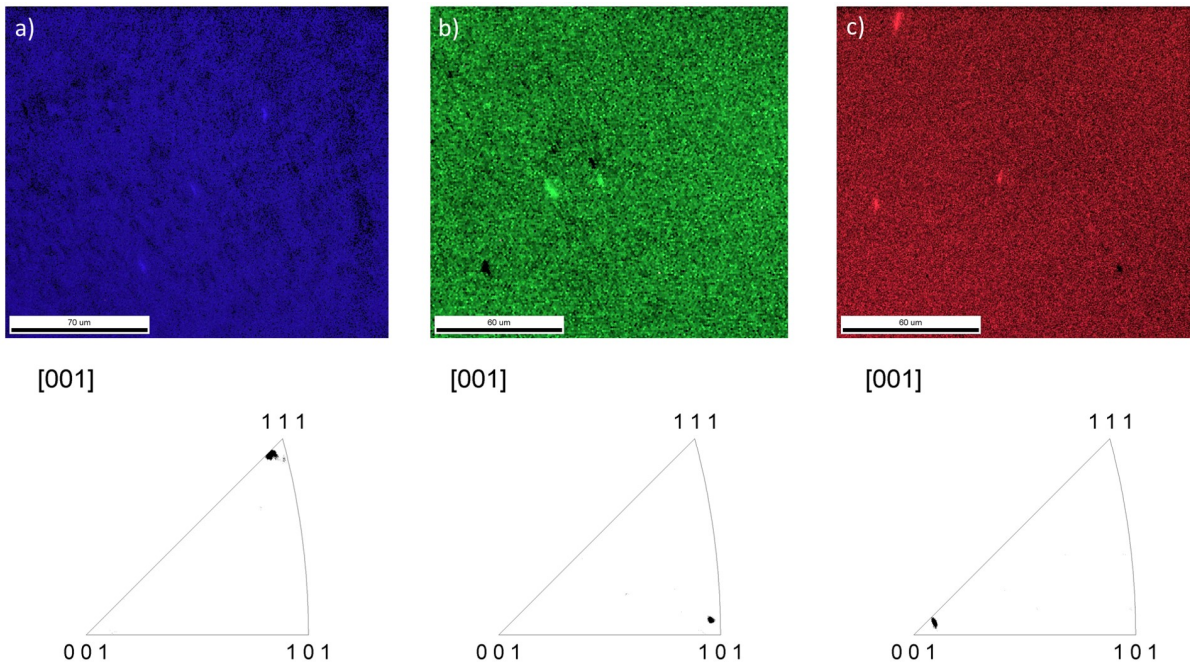

FIGURE 4.15. The inverse pole figure maps of sample (a) SN1493 , (b) SN1494 and (c) SN1495, which are respectively (111), (110), and (001) oriented single crystals of UO_2, including triangular IPF diagrams.

An example of an EBSD data collected for a single crystal UO_2 thin film is shown on Fig. 4.15. Areas of three samples representing the main orientations of fluorite structure of uranium dioxide (111), (110), and (001) were scanned and their triangular Inverse Pole Figure (IPF) diagrams are shown below. As expected in each sample signal only from one orientation is present, within the

	Structure factor intensity	Integrated measured intensity	Theoretical lattice spacing (Å)	Calculated lattice spacing (Å)
(111)	100%	100%	3.16	3.18(±0.03)
(002)	35.81%	34(±3)%	2.73	2.73(±0.04)
(220)	46.97%	48(±4)%	1.93	1.93(±0.02)

Table 4.1: Comparison between theoretical structural form factor intensities and lattice spacing to values obtained from the measurement.

entire area. This shows that the ROI is has a single crystal nature, what was previously observed in XRD data.

4.3.2 Polycrystalline samples

The polycrystalline character of a sample can be assessed using x-ray diffraction, it gives a good estimation about the volume composition of the sample. For samples with a grains at nano-scale it is also possible to calculate the average size of crystallites using the Scherrer equation. This equation is no longer valid when the grain size becomes larger than sub-micrometre, and alternative techniques to measure the grain size are required. The perfect tool to use for that is the Electron Backscatter Diffraction in the Scanning Electron Microscope (SEM).

A typical XRD specular scan for a poly-epitaxial UO_2 thin film deposited on YSZ substrate using DC magnetron sputtering system is shown of Fig. 4.16. The first three observed peaks in UO_2 fcc structure (111), (002), and (220) were calculated using Vesta software and are labelled with green color. The reflection associated with the substrate and the sample stage are in blue and pink respectively.

The observed intensity was compared against theoretical values in table 4.1. Very good agreement between the calculated and the theoretical data indicates a good distribution of poly-epitaxial grains, without any preferred orientation. Furthermore, the positions of the peaks were used to calculate the spacing between the close-packed planes of U atoms for (111), (002), and (220). Those values are also in very good agreement with the literature values.

The EBSD in polycrystalline material not only allows for assessing the grain size but also to determinate the grains orientation. In comparison to XRD, here a specific area on a sample surface can be mapped, so the orientation of the grain in ROI is known. That allows to study the influence

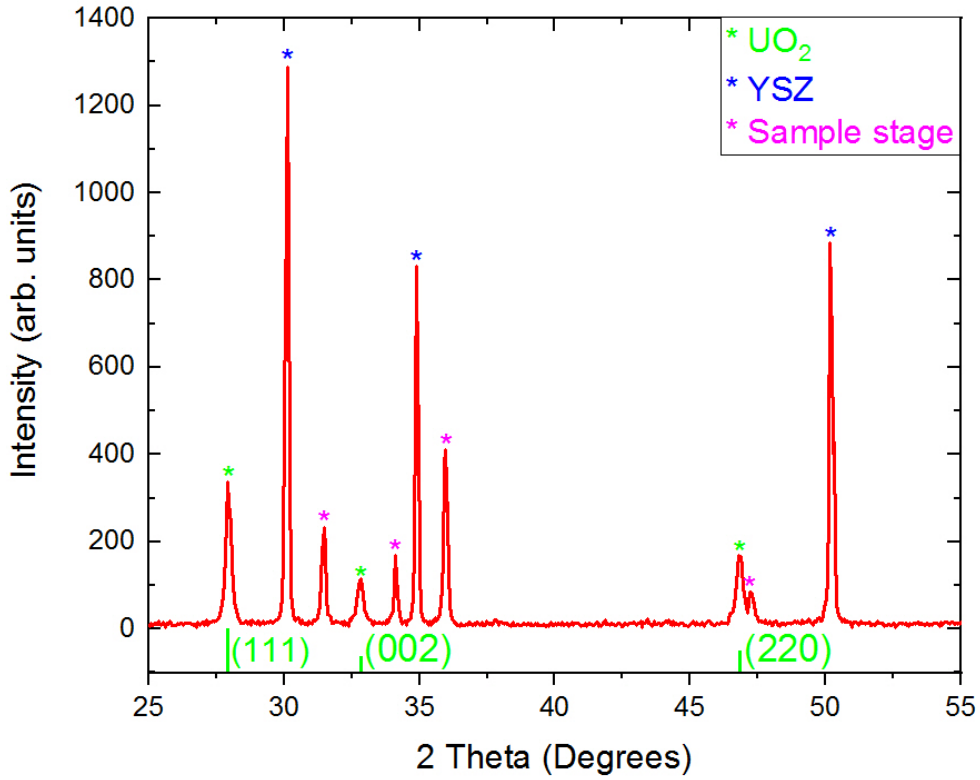

FIGURE 4.16. The longitudinal measurement of a poly-epitaxial UO_2 deposited on YSZ substrate. The calculated data for ideal polycrystalline UO_2 using Vesta software is shown in green, with reflections labelled. The reflection from YSZ substrate are in blue, while peaks from the sample stage are in pink.

of the crystallographic orientation of grains in the material properties within polycrystalline systems. By marking the region the EBSD, maps can be linked with other techniques providing additional information, as well as assessing resistance to corrosion and oxidation based on the orientation of the specific grains.

Sample SN1191: UO_2 / $YSZ_{ceramic}$

A thin film of uranium dioxide was deposited on a pristine ceramic YSZ substrate, forming a 160 nm thick layer of polycrystalline UO_2 SN1191. To investigate the influence of the grain

orientation on the oxidation properties, an area of 200 x 200 μm^2 with a good representation of all possible orientations in a cubic system was chosen. In order to examine the exact same area prior and after the oxidation experiment, a dual-beam microscope was used for marking. The crosses visible in corners of Fig. 4.17 (a) were used to mark the area, while dots made next to them were used to find the orientation of the sample.

After preparing the region of interest the sample SN1191 was transferred back to the FEG-SEM for further investigation. Previously created markings allowed to easily find the ROI and conduct mapping using the EBSD detector. Very precise map against the cubic structure of stoichiometric UO_2 was made. The inverse pole figure (IPF) map showing the orientation of the grain is shown on Fig. 4.17 (a), where red color is associated with [001] orientation, green with [110] and blue with [111].

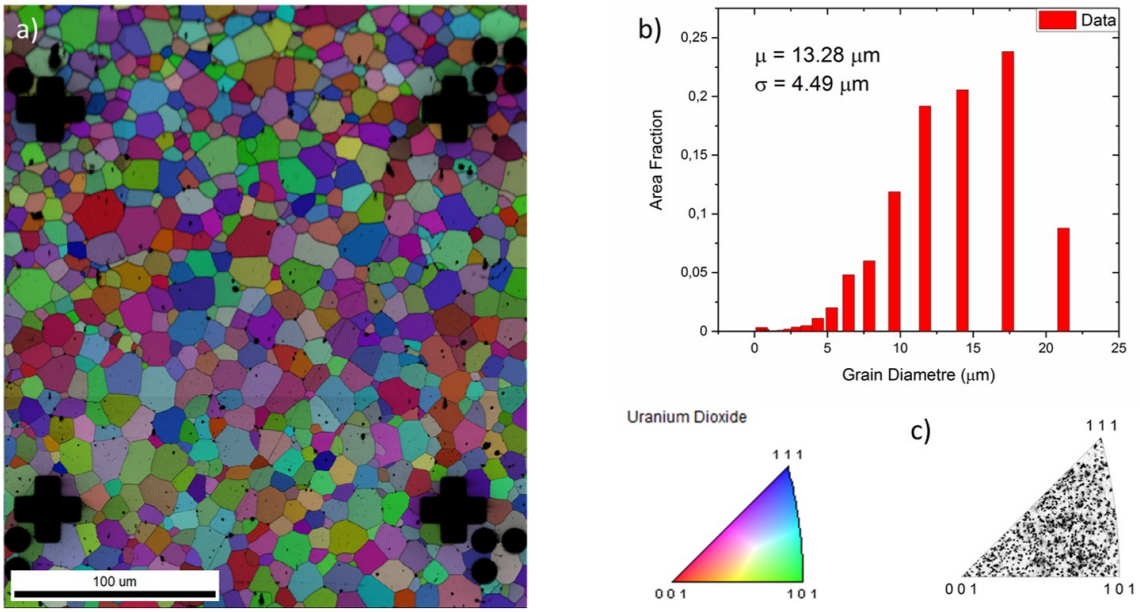

FIGURE 4.17. EBSD data collected for sample SN1191. On panel (a) is a inverse pole figure map of the grains. Graph (b) shows the grain size distribution with an average grain diameter of 13.28μm and standard deviation of 4.49μm. The distribution of the grain orientation is shown on panel (c), which exhibit random distribution expected from a polycrystalline material.

The distribution of grain orientations is shown on Fig. 4.17 (c), and it exhibits properties of a very good polycrystalline material with random distribution, as all orientations are present

without any preferred orientation. The grain size distribution is shown on Fig. 4.17 (b). The mode value for the grain size is 17.4 μm, while the average grain size was found to be 13.28 μm with the standard deviation of 4.49 μm.

Grain boundaries were found using the same software, and skeletonized image is shown on Fig. 4.18. The grain boundaries are considered any pair of points with misorientation exceeding 1°, and was divided into three groups. The first group , red, is formed by boundaries with misorientation higher than 1°but lower than 5°. Green colour was used to mark boundaries within the range of 5°- 15°, and the blue colour cover grain boundaries above 15°.

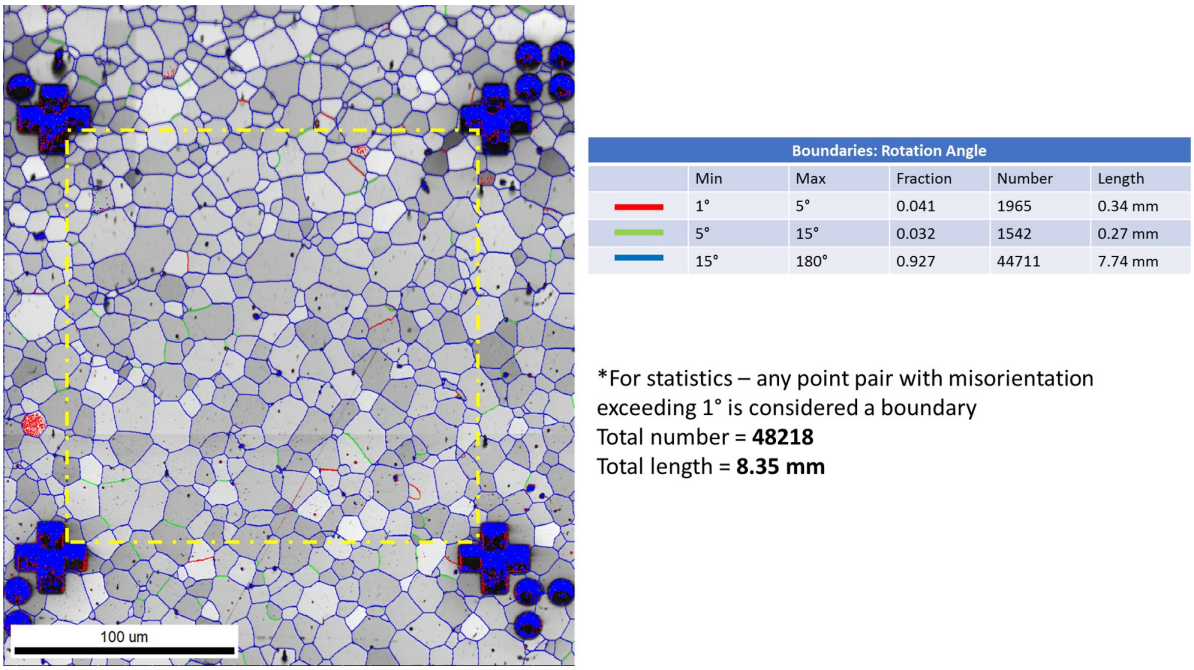

FIGURE 4.18. Skeletonized version of Fig. 4.17 (a) showing grain boundaries of ROI on sample SN1191. Low angled boundaries (1°- 5°) are marked with red colour, green is used for misorientation is range 5°- 15°, and blue for high angled boundaries (15°- 180°). Total length of grain boundaries is 8.35 mm.

The misorientation of the vast majority of the grain boundaries (93%) exceeds 15°. The length of those boundaries was found to be 7.74 mm. The second most common boundaries are in range from 1°to 5°, contributing 0.34 mm to the total length, which is about 4%. The rarest grain boundaries in sample SN1191, representing only around 3% are classified between 5°- 15°, with 0.27 mm length. The total length of all boundaries is 8.35 mm.

Sample SN1498: UO_2 / $YSZ_{ceramic}$

Electron Backscatter Diffraction is know to damage soft materials [167]. Although, uranium dioxide is a ceramic material, prolonged exposure to highly energetic electron beam focused on small area leads to permanent damage of the sample surface. Another side effect is the deposition of carbon in the scanned area, which also was observed through this thesis during XPS mapping of the sample surface. Accelerating voltage is an important parameter for damage in the sample structure, while acquiring high quality EBSD patterns, along with other parameters such as beam current, dwell time, step size, and vacuum level.

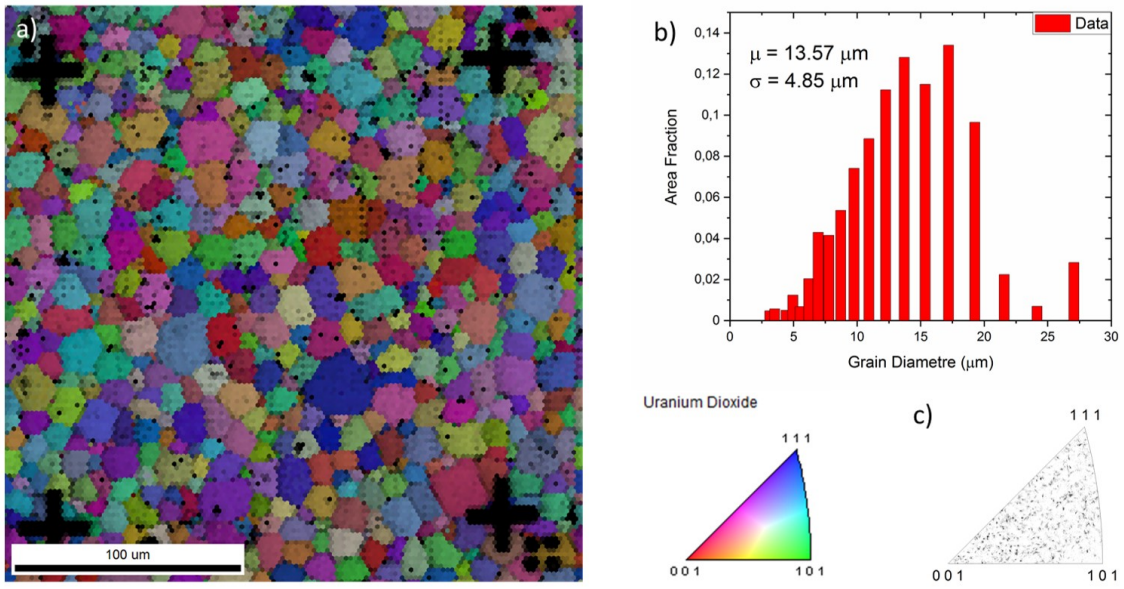

FIGURE 4.19. EBSD data collected for sample SN1498. On panel (a) is a inverse pole figure map of the grains in selected area measured in lower resolution to limit exposure time in order to reduce damage and contamination to the sample surface. Graph (b) shows the grain size distribution with an average grain diameter of $13.57\mu m$ and standard deviation of $4.85\mu m$. The distribution of the grain orientation is shown on panel (c), which exhibit random distribution expected from a polycrystalline material.

In order to maintain a good quality pattern and minimize any damage and contamination that might occur during surface mapping, the step size and the exposure time for the sample SN1498 was significantly reduced, while keeping the same acceleration voltage of 30 keV. The

IPF map of the marked area on sample SN1498 is shown on Fig. 4.19. The average grain size was found to be 13.57 μm with a standard deviation of 4.85 μm (Fig. 4.19 (b)), which is very similar to the size of the grain in sample SN1191, as both samples were grown on unannealed YSZ substrate. The truly polycrystalline character of the sample is indicated by the triangular IPF diagrams shown on Fig. 4.19 (c).

Due to limited resolution it was not possible to produce a good quality skeletonized version of SN1498 EBSD map. Therefore, because of similarities in the average grain size and distribution to sample SN1191 it was assumed that the grain boundaries density was also very similar.

Sample SN1545: UO_2 / $YSZ_{ceramic}$

Sample SN1545 was grown on re-polished YSZ substrate from the sample SN1184 in order to obtain bigger grains of uranium dioxide. This substrate was annealed at 1600°C for 12h. The thickness of the UO_2 layer is estimated to be around 100nm. Dual-beam microscope system was used to mark an area of 200 x 200 μm^2, using crosses and dots for orientation which is visible on Fig. 4.20 (a).

The inverse pole figure map with grains orientation is presented on Fig. 4.20 (a), from which the grain size was extracted. The average grain diameter is 41.7 μm with standard deviation of 13.5 μm, which is expected as the sample was grown on the same substrate as SN1184 with 45 μm grain size. The distribution of the grains size is plotted on Fig 4.20 (b). The representation of the grains orientation is shown on Fig 4.20 (b), as only a limited amount of the grain is inside the ROI, it is possible to see the reflection of that on the triangular IPF diagram.

To find the grain boundaries, the EBSD map recorded for the SN1545 was skeletonized, as shown on Fig. 4.21. The total length of the grain boundaries was found to be 2.43 cm, and within this length the 2.43 mm (89%) are boundaries with misorientation higher than 15°. The contribution of boundaries marked with green colour to the total length, is around 7% which makes its length equal to 0.2 mm. The smallest fractions are boundaries with misorientation is range from 5°- 15°, which length is 0.1 mm.

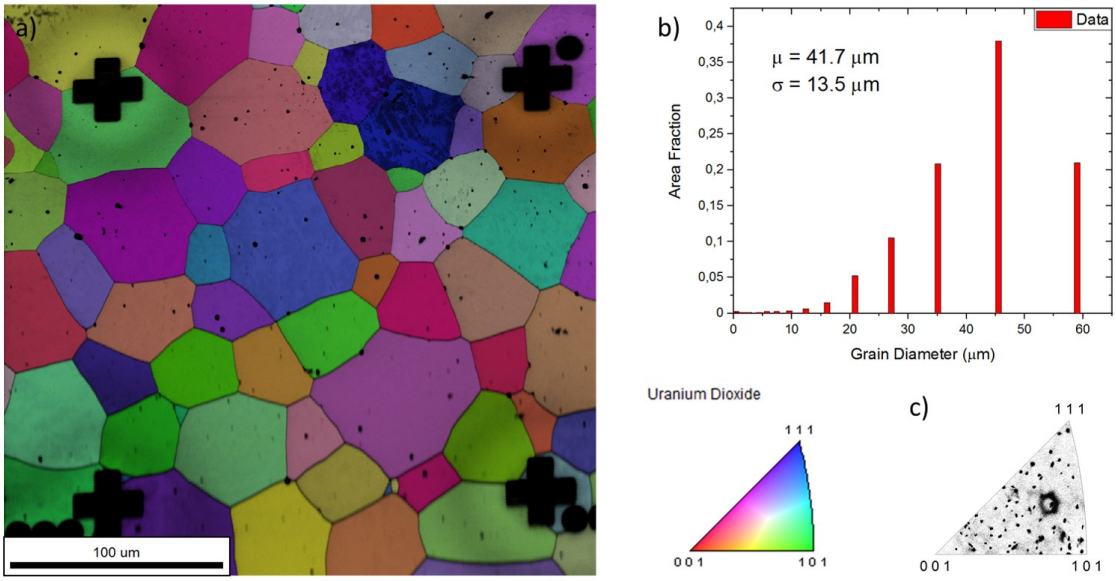

FIGURE 4.20. EBSD data collected for sample SN1545. On panel (a) is a inverse pole figure map of the grains in selected area. Graph (b) shows the grain size distribution with an average grain diameter of 41.7μm and standard deviation of 13.5μm. The distribution of the grain orientation is shown on panel (c), which exhibit random distribution expected from a polycrystalline material.

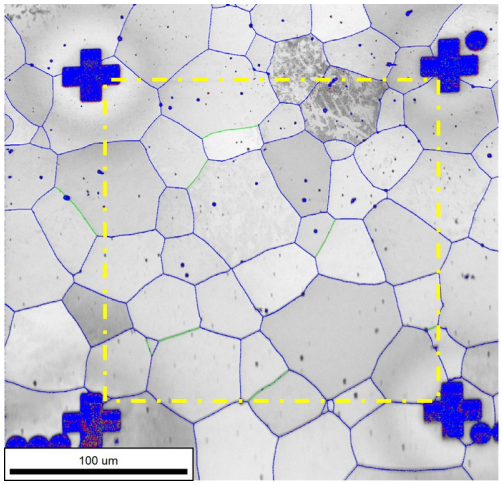

Boundaries: Rotation Angle					
	Min	Max	Fraction	Number	Length
	1°	5°	0.038	724	0.1 mm
	5°	15°	0.073	1387	0.2 mm
	15°	180°	0.889	16853	2.43 mm

*For statistics – any point pair with misorientation exceeding 1° is considered a boundary
Total number = **18964**
Total length = **2.74 mm**

FIGURE 4.21. Skeletonized version of Fig. 4.20 (a) showing grain boundaries of ROI on sample SN1545. Low angled boundaries (1°- 5°) are marked with red colour, green is used for misorientation is range 5°- 15°, and blue for high angled boundaries (15°- 180°). Total length of grain boundaries is 2.74 mm.

4.4 Summary

Structural analysis of samples performed in this Chapter has shown that reactive DC magnetron sputtering deposition technique combined with correct choice of a substrate material results in high quality epitaxial and poly-epitaxial thin film. The fabricated single crystal thin films of UO_2 on single crystal YSZ substrate, showed that the (001) oriented films have the best mosaic, based on the rocking curve profiles. The single crystal nature of all the single crystal sample was confirmed by performing off-specular scans.

The rocking curve scans of the UO_2 single crystal thin films, centred on their peak and normalized, are plotted on Fig. 4.22. From the data collected for the films with the thickness of 100 nm, SN1493, SN1494, SN1495, the best long range order is observed for the (001) orientation, where the narrow FWHM is most pronounced indicating less stress and defects, followed by wider FWHM of (111) and (110). Furthermore, while the thickness of the film decreases from 100 nm (SN1495), to 50 nm (SN1627), and finally to 20 nm (SN1614), the ration between the narrow Gaussian component to broad Pearson VII component increases.

The XRR measurement of thinner (001) oriented single crystals of UO_2, SN1614 and SN1627, showed that the sample surface is extremely smooth. The thinner sample with thickens of 19 nm had roughness around 0.5 nm, while the 47 nm sample had roughness below <2nm. Furthermore, a very smooth interface was observed for sample SN1614, giving rise to Kiessig fringes.

While the single crystals were mainly investigated using x-rays, for the poly-epitaxial system XRD was used to show the distribution of the different grains. Due to fcc structure of the UO_2, the most preferred orientation should be (111) . This is not valid for the poly-epitaxial system used in this thesis, where the truly polycrystalline system is observed.

As due to the columnar character of the grains, and their size bigger than few microns, the average grain size characterisation based on Scherrer formula was not possible. To access the size and orientation of grains in region of interest, EBSD mapping was performed. The table 4.2 shows the average grain size collected for samples with different substrate annealing time.

The size of the poly-epitaxial grain of UO_2 can be controlled from around 13 μm, for an unannealed substrate, up to 42 μm for substrate annealed for 12 h at 1600°C. Possibly the grains

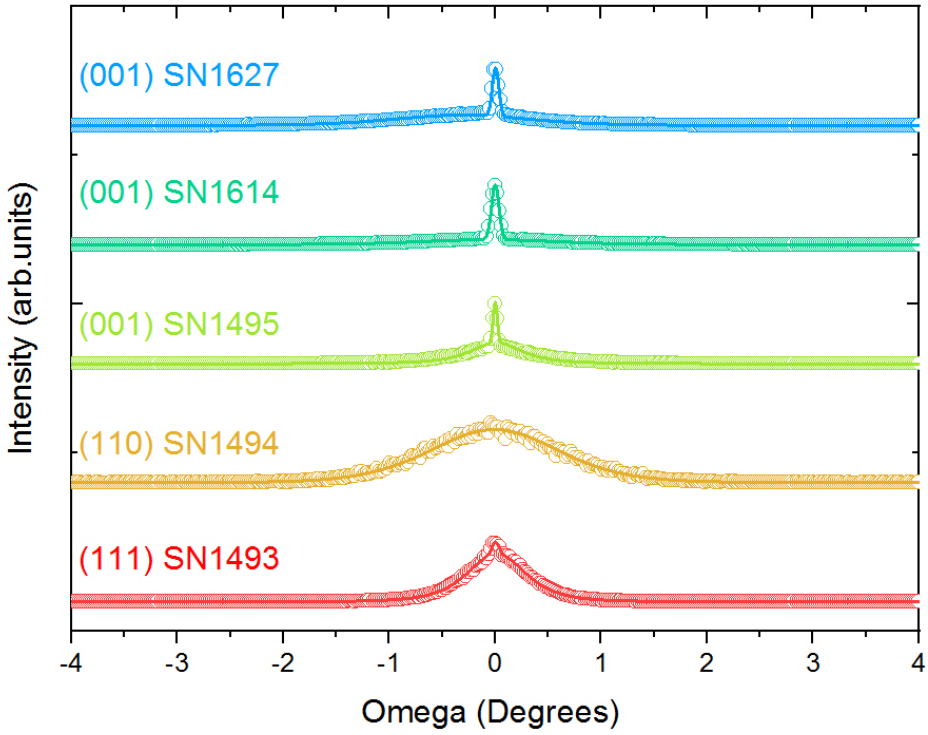

FIGURE 4.22. Normalized rocking curve profile for single crystal samples. Data is represented by circles, and fitting by a straight line. For clarity offset was applied, and each second measurement point is shown.

Annealing time	0h	2h	12h
Average grain size (μm)	13.3	31.6	41.7
Standard deviation (μm)	4.5	12.8	13.5

Table 4.2: Average grain size of UO_2 thin film deposited of YSZ substrate annealed at 1600°C for given amount of time.

could be even bigger after longer treatment. By controlling the average grain size, the density of the grain boundaries can be also controlled from 68.5 mm per mm^2 to 208.75 mm per mm^2. It was also found that the majority of the grain boundaries (around 90%) are high angled boundaries with angles in range 15°- 180°. The ability of controlling the average grain size, therefore the density of the grain boundaries, provides excellent opportunities to study its influence on the oxidation or corrosion properties of UO_2.

This chapter has shown that DC magnetron sputtering is perfect for growth of UO_2 epitaxial and poly-epitaxial system on YSZ substrates. High quality single crystals with all three orientations were successfully fabricated, along with poly-epitaxial UO_2 columns with controlled grain size. Properties of each sample are shown in table 4.3.

Sample Number	Orientation	Thickness	Roughness	Grain size	Grain boundary misorientation (fraction)		
		(nm)	(Å)	(μm)	1-5°	5-15°	15-180°
SN1191	Poly-epitaxial	160*	n/a	13.28	0.041	0.032	0.927
SN1498	Poly-epitaxial	100*	n/a	13.57		n/a**	
SN1545	Poly-epitaxial	100*	n/a	41.7	0.038	0.073	0.889
SN1493	(111)	100*	n/a	n/a		n/a	
SN1494	(110)	100*	n/a	n/a		n/a	
SN1495	(001)	100*	n/a	n/a		n/a	
SN1535	(001)	100*	n/a	n/a		n/a	
SN1614	(001)	19.2	4	n/a		n/a	
SN1627	(001)	47.5	4.3	n/a		n/a	

Table 4.3: Summary of the samples an their parameters characterised in this chapter and used for the oxidation studies. (*) thickness estimated based on the sputtering rate (**) low resolution scan to avoid carbon contamination.

CHAPTER 5

OXIDATION OF POLY-EPITAXIAL UO2 THIN FILMS

This chapter describes a series of experiments to measure the effect of the crystal orientation on the oxidation rate in UO_2. Specially developed poly-epitaxial samples were utilised to reduce the three dimensional problem into two dimensions. Samples were oxidised in-situ using x-ray diffraction, scanning electron microscopy and x-ray photoelectron spectroscopy.

5.1 Introduction

Parameters that affect the rate of UO_2 oxidation can be divided into two groups, ambient conditions such as temperature, moisture, oxygen partial pressure etc. and the physical parameters, including grain size (or particle size in case of powders), density of the pellet, and orientation effects that will be further investigated in this thesis.

The temperature at which oxidation of UO_2 is performed not only influences the rate of reaction, but also affects the final stoichiometry of the material. It has been shown that due to the extremely low activation energy, chemisorption of oxygen onto UO_2 occurs rapidly even at temperatures as low as -183°C [168]. Oxidation at low temperatures, below 50°C, gives results similar to those obtained at high temperatures but changes are only observed at thin surface

layers, due to extremely slow bulk diffusion of oxygen ions in such lower temperatures. For fine powder, 50 nm grains, a 5 nm layer with final stoichiometry of $UO_{2.16}$ to $UO_{2.18}$ corresponding to an oxidised U_4O_9 was found [169]. At higher temperatures, above about 100°C and below 250°C, the rate of oxygen diffusion is high enough to cause bulk oxidation to U_3O_7/U_4O_9 [31]. Above 250°C, bulk formation of the orthorhombic U_3O_8 is observed.

The first study that focused on the effect of grain size on the rate of oxidation were conducted on sintered UO_2 pellets and gave ambiguous results [170, 171]. Uncertainty arose from the correlation between the sample density and grain size, therefore it was not clear whether the observed effect was due to grain size or sample density. Generally a negative correlation between grain size and the initial oxidation rate was observed. It was reported that for samples with grain sizes below 5 μm the oxidation rate increases with decreasing grain size, and above that size and for single crystals the reaction rate is the same [31]. In contradiction, in oxidation of used fuel performed by Thomas et al. [50] they show a similar behaviour for all samples regardless of the fuel type, burnup, grain size, fuel particle size or air moisture. From those unexpected findings, it was later suggested [31] that due to the big grain sizes of examined samples, (up to 30 μm) the effect of grain size may have been obscured by sample-to-sample variations in the oxidation rate.

To investigate further the effect of grain size, single crystals were studied, as those samples can be considered equivalent to material having only a single grain. Studies on small single crystals showed similar behaviour to sintered pellets [172]. Experiments performed on single crystals by Wang [173], showed very slow rates of oxidation for [111] oriented slice of UO_2 in comparison to a sintered polycrystalline UO_2. In contrast, Allen et al. [71, 72] showed different oxidation rates between all three main orientation of cubic UO_2 and a polycrystalline sample [111]>[110]>[100]>[polycrystalline].

The evidence of preferred-orientation effects on oxidation of UO_2, was shown also by Taylor et al. [49], their XRD data suggests that UO_2 grains with the (100) plane parallel to the sample surface form rather U_3O_7 with [100] parallel to the surface, not the [001]. The effect was related to the minimization of stress in the oxidised surface layer. This is in agreement with evidences published by Teixeira and Imakuma [65], where they found that the activation energy for the formation of U_4O_9 on UO_2 was significantly lower in the [100] direction than in [311], 90 kJ/mol

and 117 kJ/mol respectively. The data was later re-analysed by McEachern and Taylor using thin film model, and they reported no significant differences between the activation energy for oxidation in the two crystallographic directions [174].

There is still uncertainty and inconclusive models in the literature about the preferential oxidation in specific orientations for UO_2, and many of them are contradictory. One of the factors influencing the data and what might lead to inaccurate conclusions is the quality of the investigated sample.

Apart from the studies related to the influence of the crystallographic orientation on the oxidation of uranium dioxide, the impact of the orientation on the dissolution of analogous fluorite structures [175–178] as well on the dissolution of UO_2 [83] was reported in the literature.

The simulation and experiments performed by Maldonado et al. [175] have shown that the relation between the surface energy of any Miller-indexed plane and the surface energy of those reference planes, is dependent on the fluorite surface structure only. Those studies were conducted on CeO_2 and CaF_2, which showed a correlation between the trends of dry surface energies and surface stabilities during dissolution, apart from having different chemical dissolution processes. The effect of surface orientation on dissolution rates in CaF_2 was studied by Godinho et al. [176], and has revealed that the (111) is the most stable plane, while (112) is the least stable plane and dissolves 33 times faster. It was stated that the surfaces that expose both Ca and F atoms in the same plane dissolve faster.

Dissolution of polished fluorite surfaces with different orientations has been directly observed utilizing atomic force microscopy [177]. A new model of dissolution was proposed that highlights the importance of considering surface defects and crystal orientation during dissolution. High densities of defects are observed at the grain boundaries, and it has been shown by Corkhill et al. [178], that preferential dissolution occurs at grain boundaries. Furthermore, from utilizing CeO_2 and ThO_2, it has been demonstrated that the boundaries with high misorientation angles are dissolving faster than those with low misorientation angles. More recent studies performed on single crystal thin films, allowed to investigate the role of crystal orientation in the dissolution of UO_2 system. It has been revealed that the (001) and (110)-oriented films corrode at comparable rates, while the (111) film was significantly more corrosion resistant [83].

For the studies performed in this chapter, high quality thin films of UO_2 were fabricated using DC magnetron sputtering. A poly-epitaxial match between YSZ and UO_2 was utilized to bring the three dimensional problem into two dimensions by growing columns of UO_2 on YSZ grains. Sample were accessed using x-rays and electrons and in-situ oxidation experiment were performed.

5.2 In-situ XRD

The main aim of the in-situ XRD oxidation experiment was to investigate the influence of the crystallographic orientation of UO_2 on the oxidation process, and to find the time and parameters such as temperature and oxygen pressure at which UO_{2+x} undergoes a phase transition from fluorite structure (fcc) to tetragonal structure (U_3O_7). Then, if possible, further transformation into orthorhombic U_3O_8. In order to investigate this, in-situ oxidation in HTK 1200 chamber inside a Philips X'pert pro diffractometer was conducted. Prior to performing this experiment, an specially engineered poly-epitaxial sample of UO_2 (SN1191) was characterised, and EBSD map on marked area was performed as described in Chapter 5. The estimated thickness of the uranium dioxide layer was 160 nm.

The uranium oxide thin film was mounted on a sample stage using thermally conductive paste. After sealing the sample stage in the chamber, the chamber was pumped out first using an scroll pump and then using a turbomolecular pump overnight, to reach 1.2 x 10^{-4} mbar. The experiment was conducted in two steps. In the first step the sample was exposed to 100 mbar of oxygen at 150°C, posteriorly the temperature was increased to 250°C and left under the vacuum. The experimental set-up at that time did not allowed to refill oxygen without braking the vacuum. The second step involved increasing oxygen pressure to 200 mbar and was conducted at two temperatures: 150°C and 300°C.

During the first part of the experiment, before the sample was exposed to oxygen, the temperature was increased slowly in steps to stabilise both the temperature and the pressure. Once the 150°C point was reached, the sample was left under the vacuum to check if under those conditions any changes will be visible. After 3h no changes were observed and oxygen

was introduced to the system. The sample was first exposed to oxygen for 5 min, then oxygen was pumped out, and a scan was conducted. Fig. 5.1 shows the changes to the crystallographic structure over total exposure time. Further exposure of the sample to oxygen, for additional 40min and 80min, did not show any changes. The sample was then left at 100mbar of oxygen atmosphere overnight (18h) with continuous hour long scans, nevertheless changes were not observed.

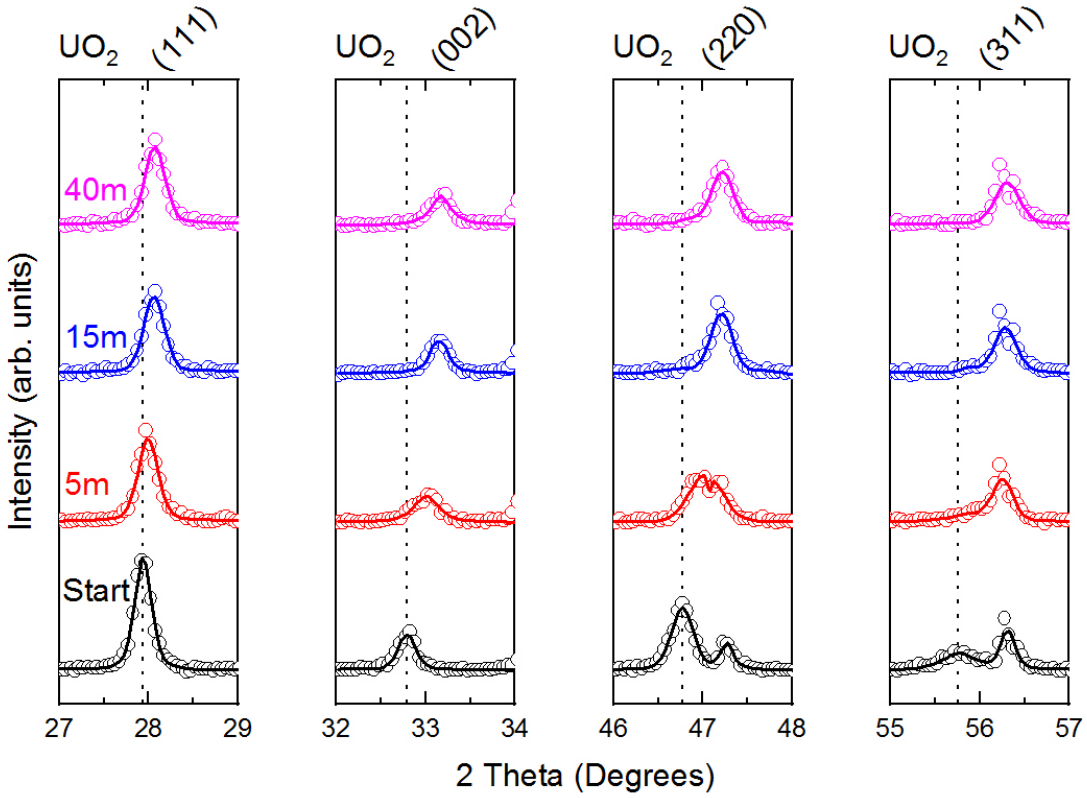

Figure 5.1: XRD patterns of SN1191 sample showing oxidation at 150°C in atmosphere of 100 mbar of Oxygen. Time shown on the graph is total exposure time to O. Data points are represented by circle, while strait line shows fitting envelope. Vertical dotted lines shows centres of the UO_2 peaks at the beginning of the oxidation. Additional peak at higher angles in columns for (220) and (311) comes from the sample stage.

Data collected during this part of the experiment are displayed on Fig. 5.1 as open circles. To fit this data LIPRAS [104] software was used utilizing pseudo-Voigt function, and the fit is represented by the straight line. Different colours were used to show changes after exposing the

sample to 100 mbar of O_2 at 150°C, where black is the starting point, red, blue and pink show data collected after 5 min, 15 min and 40 min respectively. For clarity, data for (111), (002), (220) and (311) Bragg peaks of UO_2 were separated to columns. The vertical dotted lines were added showing the center of the peak before oxidation to exhibit the changes within time.

Tracking changes to both (220) and (311) reflections was more challenging due to overlap with the sample stage reflection while oxidised. General shift in the peaks towards higher 2θ can be observed for all peaks as the degree of non-stoichiometry increases, being particularly remarkable for the (200) reflection. This phenomena is associated with shrinking of the lattices parameter, which is well reported in literature [43, 179–183]. It should follow the Vegard's law in the hyperstoichiometric range, and expression:

$$a_0 = 5.4696 - 0.1495x \tag{5.1}$$

was proposed by Alekseyev et al.[184] for homogeneous UO_{2+x} powder for x<0.38. This was later found not to hold in region of x from 0.17 to 0.22 [179], and will be discussed later in this chapter.

The presence of additional peaks near the (200) and (311) reflections has been attributed in literature to both the U_3O_7 tetragonal phase and to the U_4O_9 cubic superlattice [40, 185, 186], and related to the formation of cuboctahedral oxygen clusters [39] due to the difference in spatial arrangements between U_4O_9 and U_3O_7 polytypes clusters and their subsequent lattice distortion. With increasing of the oxygen amount x in the system their contributions became more relevant. This phenomena is not observed here and the presence of additional peaks is attributed to presence of additional material (the sample stage). The lack of those satellites peaks might be connected with the nature of the material. Here a thin film sample of UO_2 is oxidised, allowing for the entire volume of the sample to reach the same stoichiometry, while in data presented in literature, powder samples might have oxides only on the outer shell, thus signal from both structures can be present at the same time, visible as a satellite peaks.

No further changes to the sample structures were observed in 100 mbar of oxygen at 150°C after 40 minutes, what suggests that this time was enough to oxidise 160 nm of UO_2 to U_4O_9/U_3O_7.

Even after 18 hours the position of the peaks remained unchanged. To allow further oxidation, the temperature was increased to 250°C, and the system was left for an hour to let the temperature stabilise. As system did not allow for replacement of the empty oxygen source, without cooling the chamber to room temperature and breaking the vacuum, the sample was kept overnight at 250°C at vacuum pressure of 4 x10^{-4} mbar. Fig 5.2 shows the scans taken at the starting point and after 1h, 2h, 4h, 8h and 16h respectively.

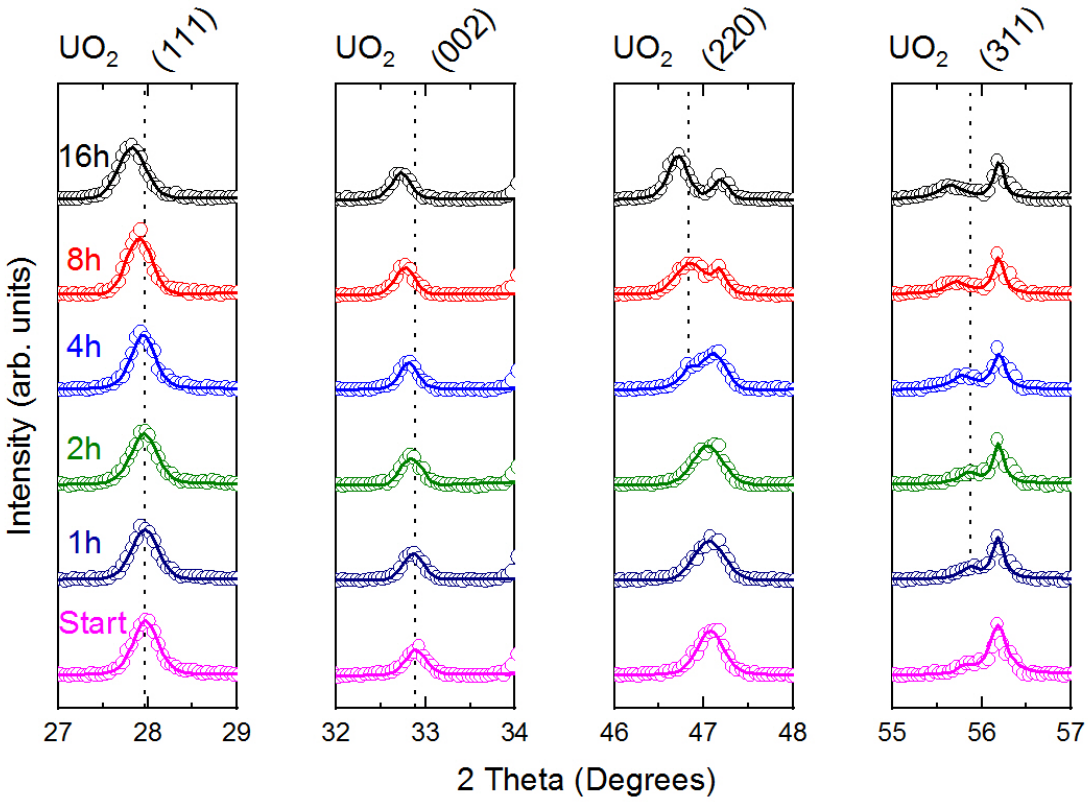

Figure 5.2: Changes in structure of SN1191 sample after increasing temperature to 250°C and keeping under vacuum of 4 x 10^{-4} mbar. Reduction of the structure is observed. For the (220) and (311) vertical dotted lines were added, when deconvolution of the UO_2 signal from the sample stage peak became possible.

The same procedure was applied to fit the data. The vertical dotted lines indicating center of the starting point for the (200) and (311) reflections were added after 4h and 1h respectively, as only after that time deconvolution of the peaks become possible. The opposite trend is observed at at 250°C and vacuum 4 x 10^{-4} mbar, the peaks are shifting back to lower angles indicating

reduction of the U_4O_9/U_3O_7 back to UO_2.

The center of the Bragg peaks position was extracted from fittings of both data sets, and used to calculate the lattice parameter, using an x-ray wavelength of 1.5406 Å associated with Cu K_{alpha_1}. The left panel on Fig. 5.3 shows changes to the lattice parameters for (111), (002), (220) and (311) over time given in minutes. The data in red circles might not represent the real position of the Bragg peak associated with UO_{2+x} structure as it overlaps with reflection from the sample stage and the deconvolution of the peaks was not possible, instead lattice parameters were calculated based on the central position of one combined peak.

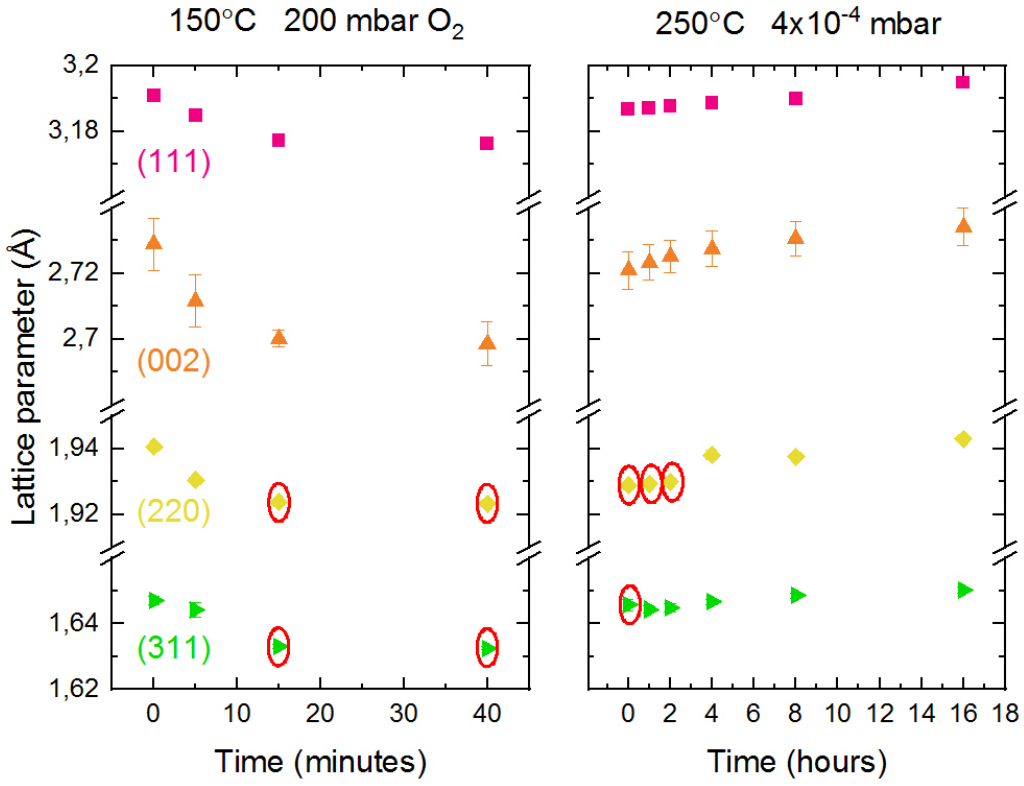

FIGURE 5.3. Changes in lattice parameter as a function of time for (111), (002), (220) and (311) planes of UO_{2+x} during (left) oxidation at 150°C in 200 mbar of O_2, and (right) reduction at 250°C and vacuum 4 x 10^{-4} mbar. Data points in red circles are not measured from de convoluted peak of UO_{2+x}, but from overlapping peak of sample stage and the thin film.

The shrinking of the lattice parameter is observed for all the grains while the oxidation

proceeds. No significant changes are observed after 15 minutes, indicating that at 100 mbar of O_2 at 150°C, this time is enough for the 160 nm of UO_{2+x} thin film to absorbed maximum amount of oxygen into its structure. The decrease expressed in Å and % of the lattice parameter for each of the measured Bragg reflection is presented in table 5.1. The most significant changes to the lattice parameters are observed for the (002) reflection, which is 1.21%, followed by (220) and (311), and the smallest change of 0.54 % is observed for the (111) reflection.

	(111)	**(002)**	**(220)***	**(311)***
Contraction in Å	0.015	0.03	0.017	0.014
Contraction in %	0.54	1.21	0.89	0.88

Table 5.1: Changes to lattice parameter of UO_2 in measured reflections, expressed in Å and percent during oxidation of thin film at 150°C. The most remarkable changes are observed for (002) orientation. * were due to the presence of the sample stage reflection, precise analysis was not possible.

The decrease of the lattice parameter is related to formation of U_4O_9 and U_3O_7, but due to the similarities between those two structures [187] and uncertainties about their crystal structure [31, 41, 45, 73], combined with limited resolution of the equipment, distinguishing between those two phases was impossible. One of the possibilities, based on recent work by Rousseau et al. [70] where it was shown that the the cubic U_4O_9 phase occurs prior to the formation of tetragonal U_3O_7, could suggest oxidation of the thin film to the tetragonal structure. Findings of Rousseau et al. [70] are in contradiction to the previously published data [41, 46, 172], where formation of U_4O_9/U_3O_7 was assumed to happen at the same time. In spite of that, the shift of the peaks (Fig. 5.1) to the higher angle, indicate a decrease of the lattice parameter (Fig. 5.3), reported in literature as the first step of the oxidation from UO_2 to U_3O_8, where U_4O_9/U_3O_7 is formed [70]. The change of the lattice constant for the powder sample of UO_2 after oxidising to UO_9/U_3O_7 reported by Rousseau et al. [70] is 0.7%, is consistent with data shown in Tab. 5.1.

Exposure of the sample to a vacuum of 4 x 10^{-4} mbar at 250°C resulted in reduction of the sample oxidation state. The associated changes to the lattice parameters are shown on the right panel on Fig. 5.3. The same issue with overlapping peaks was encountered for the (220) and (311), which translates into a greater analytical error indicated with * in Tab. 5.2. As it

is hard to conclude changes observed in the (220) and (311) reflections, due to the previously mentioned issue, changes along (111) and (002) point out a significant difference in oxidation and reduction based on the crystallographic orientation of the grains. In both cases changes to the lattice parameter for (002) are doubled.

	(111)	**(002)**	**(220)***	**(311)***
Expansion in Å	0.008	0.013	0.0142	0.045
Expansion in %	0.25	0.48	0.73	0.28

Table 5.2: Changes to lattice parameter of UO_2 during reduction performed under high vacuum at 250°C. The most remarkable changes are observed again for (002) orientation. * were due to the presence of the sample stage reflection, precise analysis was not possible.

The difference between the time needed to oxidise and reduce a thin film of UO_2 is significant. Full transition from UO_2 to U_4O_9/U_3O_7 is observed in less than 40 minutes , while exposing the sample to 100 mbar of oxygen at 150°C. This suggest much faster kinetics of oxidation under the given conditions when compared to reduction process observed in vacuum pressure of 4 x10^{-4} mbar at 250°C which took more than 16 hours. Therefore, if sample with specific stoichiometry is required, the reduction process would give more control and more accurate result.

The EBSD maps of the ROI on the investigated sample (a) before and (b) after oxidation are shown on Fig 5.4. The difference in the resolution between these two maps is caused by the acquisition time. The first scan was taken overnight for 14h, while the second scan due to the equipment availability and to limit oxidation of the sample in atmospheric condition, was captured within 2h. The structural changes associated with oxidation of cubic UO_2 to smaller cubic U_4O_9 and tetragonal U_3O_7 should negatively influenced the accuracy of measured data which is expressed by a confidence index (CI). As during this experiment due to lack of oxygen while the sample was exposed to 250°C, reduction was observed resulting in very similar stoichiometry compared to starting stoichiometry of the sample, no changes to CI were observed as expected.

This XRD and EBSD data show that oxidation of poly-epitaxial thin films of UO_2 to U_4O_9/U_3O_7 is a reversible process, without any damage to the sample structure. The reduction process from even higher oxide such as U_3O_8 has been extensively studied in many investigations [188–195].

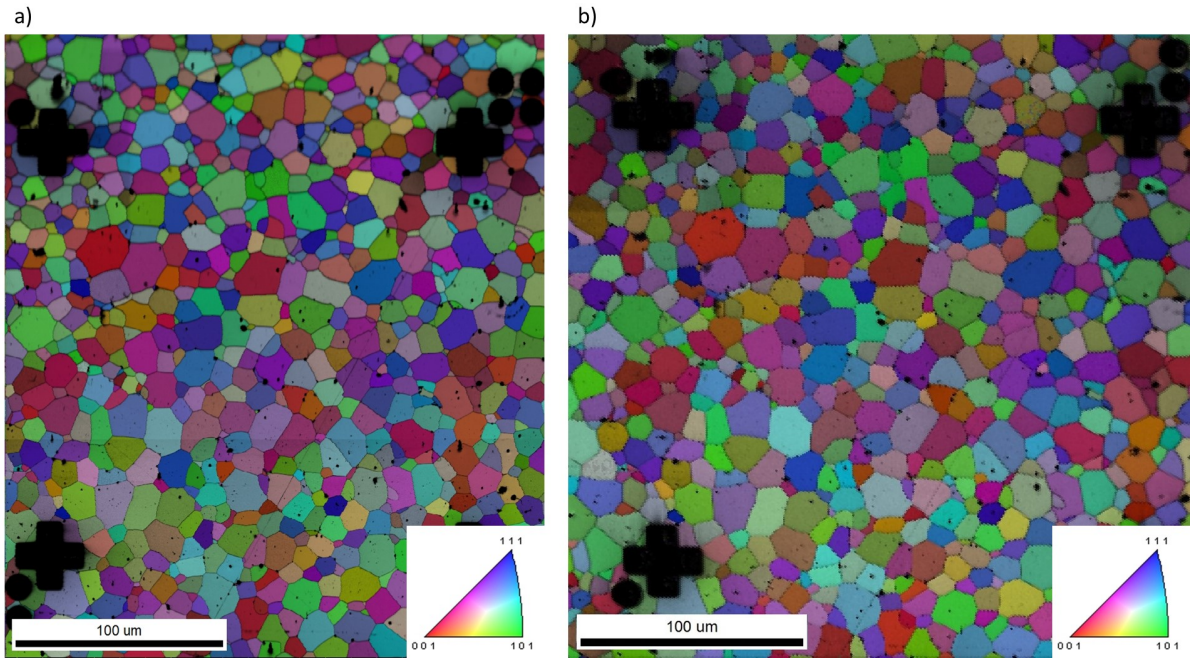

Figure 5.4: EBSD inverse pole figure map of the poly-epitaxial uranium dioxide thin film sample SN1191, (a) before the in-situ oxidation, and (b) after the oxidation. The difference in quality is purely related to the scanning time, which was much shorter after oxidation as no changes were expected.

Studies were mostly conducted on powder and pelletized U_3O_8 material, by thermal treatment in a reducing atmosphere. Many of the researches have been made in the hydrogen or hydrogen-containing gas atmospheres [188–191], while others studied this process in Ar and CO_2. Here is shown that reduction of thin films is also possible to almost stoichiometric UO_2 just under vacuum condition at elevated temperatures. The data obtained for the thin film agrees with literature, demonstrating that uranium oxide thin films can be used as a surrogate material for its bulk equivalent.

Studies conducted by Quemard et al. [75] show that when UO_2 (111) single crystal is oxidised at 300°C in air for 10h to form U_3/O_7, cracking of the sample is observed. Here, where very similar conditions are used, no cracking is observed for any grains, including the ones near the (111) orientation. The difference is probably in the physical state of the sample, where a bulk single crystal have the oxide layer of U_3O_7 with a thickness of 1 μm. This layer is almost a magnitude greater that the thickness of the thin film used in this experiment (0.16 μm). Another

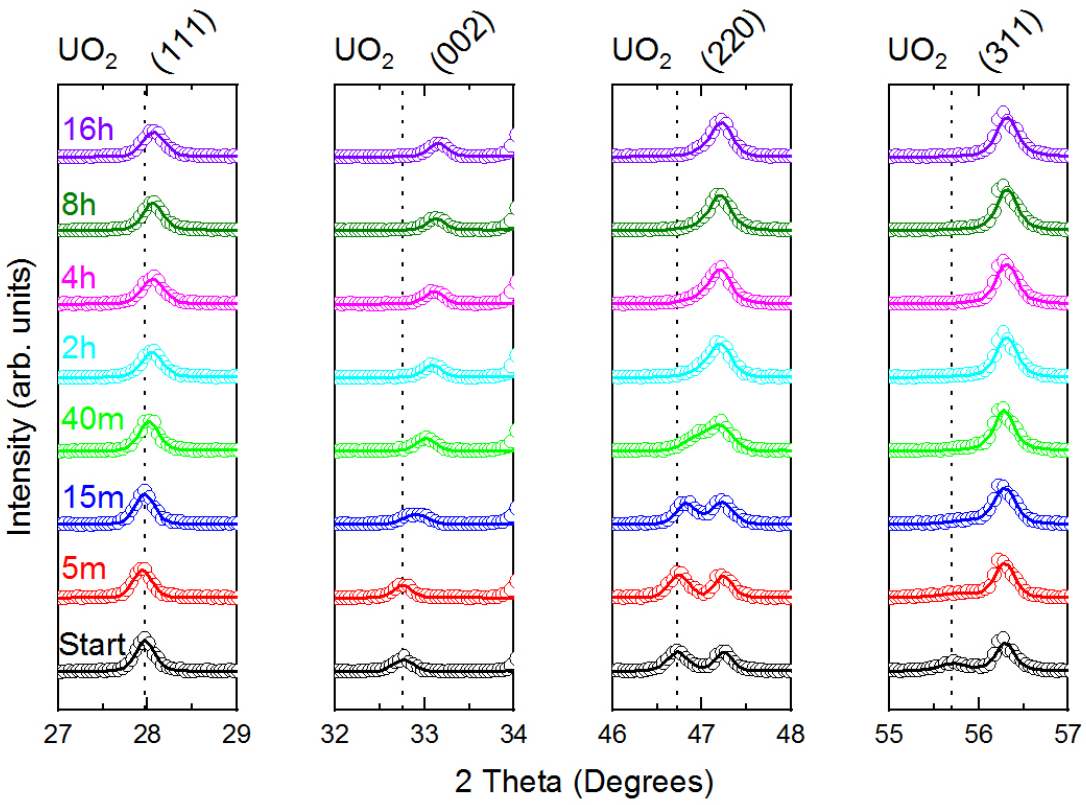

Figure 5.5: First step of second experiment. Sample SN1191 exposed to 200 mbar of Oxygen at 150°C. Unique behaviour of UO_{2+x} when system contracts then expands and again contracts is observed in first 15 minutes.

important factor is the substrate, which provides poly-epitaxial match with UO_2 which could stabilise its structure, and prevent from cracking.

During the second step of this experiment sample SN1191 was exposed to 200 m bar of oxygen at 150°C. This time, after short exposure to oxygen at high temperature for 5 minutes, a small shift towards a lower angle is observed, associated with expansion of the lattice constant. This unique behaviour of UO_{2+x} system was previously reported in the literature [179], and changes to the lattice constant as a function of extra oxygen are shown on Fig. 5.6

As mentioned previously, the lattice contraction should follow the Vegard's law in the hyper-stoichiometric range, and for UO_2 the Eq. 5.1 was proposed. This does not hold for the $0.125 < x < 0.17$ region where a lot of discrepancies arose in reported values [179, 181, 184]. For the intermediate region $0.13 < x < 0.17$, uncertainty concerning the variation of the lattice constant

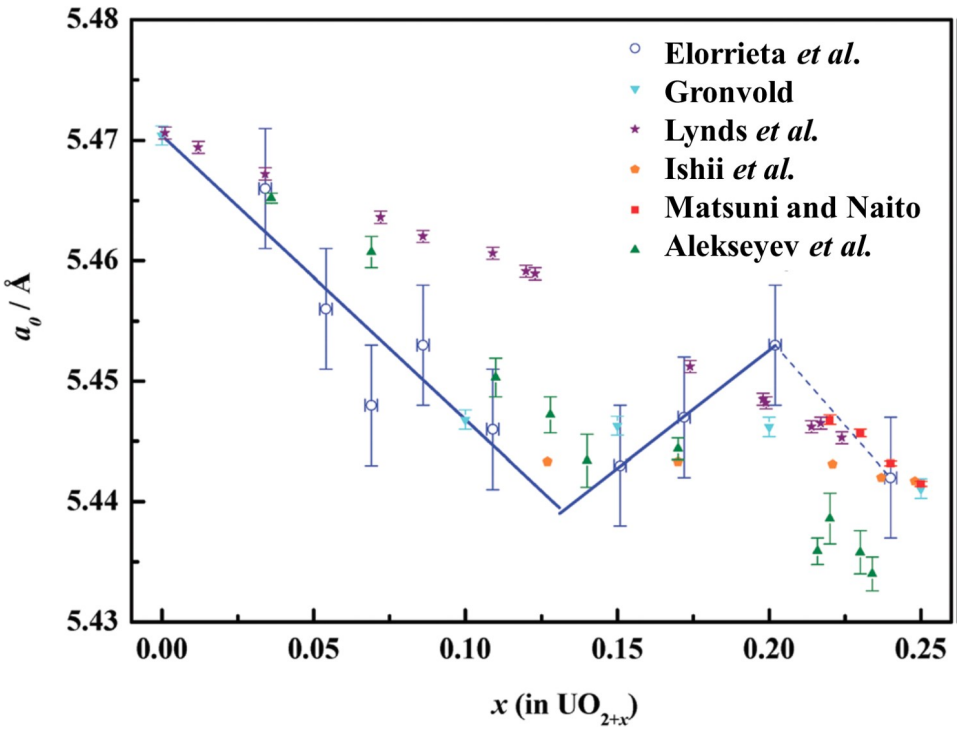

FIGURE 5.6. Changes in lattice constant as a function of x for different UO_{2+x}. Figure reproduced from [179].

was reported already by Lynds et al. [181]. Scattered results in this region did not allow to fit the whole hyperstoichiometric region with one Vegard equation, and authors proposed two different equations, above x = 0.17 and below x = 0.13. This was attributed to a transition detected at x = 0.125, based on analysis of the partial molar free energy of oxygen in UO_{2+x} [196]. Scarce values in this region were also reported by other researchers [180, 182, 184].

Detailed studies performed by Elorrieta et al. [179] demonstrated that in the region 0.13 < x < 0.20 the lattice constant of UO_{2+x} increases, and they proposed the following equation to describe this change:

$$a_0 = 5.4133 \pm 0.0005 + (0.196 \pm 0.003)x, \quad (0.13 < x < 0.20) \tag{5.2}$$

which agrees with previously published lattice parameters in this region, and also shows that a single linear equation is not sufficient to describe entire 0 < x < 0.25 region. After the region

described by Eg. 5.2, above 0.2 < x, the lattice constant in region associated with U_4O_{9-y} seems to follow again Vegard's law-like behaviour, which is shown as a dashed line on Fig. 5.6.

The changes observed during in-situ XRD oxidisation of UO_2 thin films to the lattice parameter showed on Fig 5.10, agree with the results reported in the literature [179, 180, 182, 184], where a small increase in the lattice constant is observed, just before it decreases again when approaching U_4O_9/U_3O_7 structures.

The same behaviour is observed for data shown previously on Fig. 5.1 and now on Fig. 5.5. The difference between the time needed to achieve maximum concentration of oxygen in the sample between the first oxidation experiment (less than 40 minutes) and now (less than 120 minutes), is probably caused by lower starting stoichiometry of the sample in two cases. This would also explain why in the second oxidation experiment it was possible to observe a unique expansion of the structure in region 0.13 < x < 0.17. This would indicate that the starting stoichiometry was below this point. Another less likely possibility, is that in the first part, this expansion point was missed due to a faster reaction rate.

Overnight oxidation of SN1191 in 200 mbar of oxygen at 150°C for more than 16h did not show any further changes after 2h exposure, therefore the temperature was increased to 300°C to allow the investigation of phase transition into orthorhombic U_3O_8 structure. As shown in previous steps on this experiment, the reduction of this film sample is observed when heated up to 300°C under vacuum of 5 x 10^{-4} mbar, therefore, to minimise this effect the turbo pump was not used during the heating up stage, and when the system was allowed to equilibrate for 1h. After the temperature of the system stabilised at 300°C, alignment of the XRD set-up was conducted again to compensate for the thermal expansion of the sample stage.

A higher temperature allowed further oxidation of the SN1191 sample to U_3O_8. XRD scans were taken for 19.5h overnight every 30 minutes in 2 theta range 25-70°. Data collected during that time is presented as circles on Fig. 5.7. Due to the difference in thermal expansion between the uranium oxide sample and sample stage, observation of (220) reflection became possible again. This was not true for the (311) reflection, where deconvolution of the peaks was not possible, therefore data for this peak is not presented. To fit the peak shape a pseudo-Voigt function was used, and the fit is represented by the straight line.

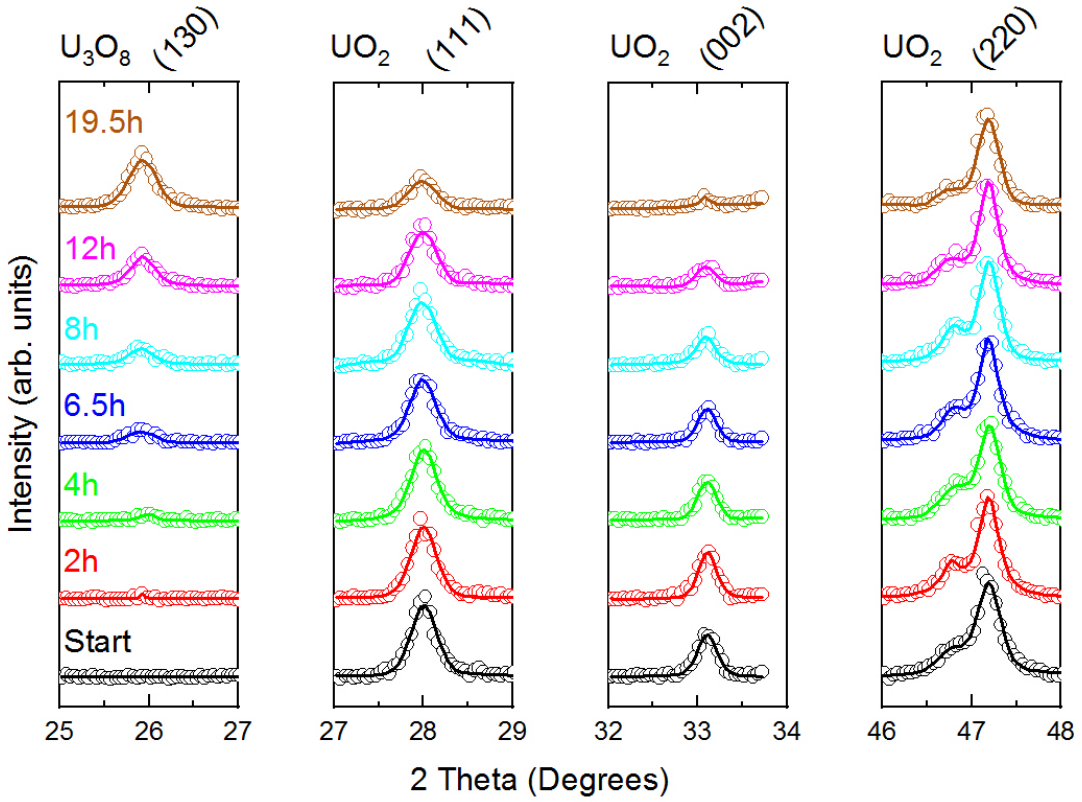

FIGURE 5.7. XRD patterns showing oxidation of SN1191 into U_3O_8 in 200 mbar of Oxygen at 300°. General decrease of UO_2 signal, and increase of U_3O_8 is observed.

Further structural changes after 21h are shown on Fig. 5.8. Scans were taken for 44h in total. In this series of measurements, scans were 1h long and 2 theta range 10-70° to allow observation of additional U_3O_8 reflection around 21/22 ° in order to distinguish between alpha and beta structures of U_3O_8. Furthermore, the (002) reflection completely disappeared, therefore, is not shown anymore on Fig. 5.8.

General decrease in the intensity is observed for (111), (002) and (220) reflection assigned to the UO_{2+x} structure as the cubic/tetragonal structure undergoes phase transition to orthorhombic structure of U_3O_8. At the same time, as expected, intensity for reflections associated with formation of U_3O_8 increase. To better illustrate this process, an area under each peak was extracted, normalised and plotted against time as shown on Fig. 5.9. The data was fitted using logistic function.

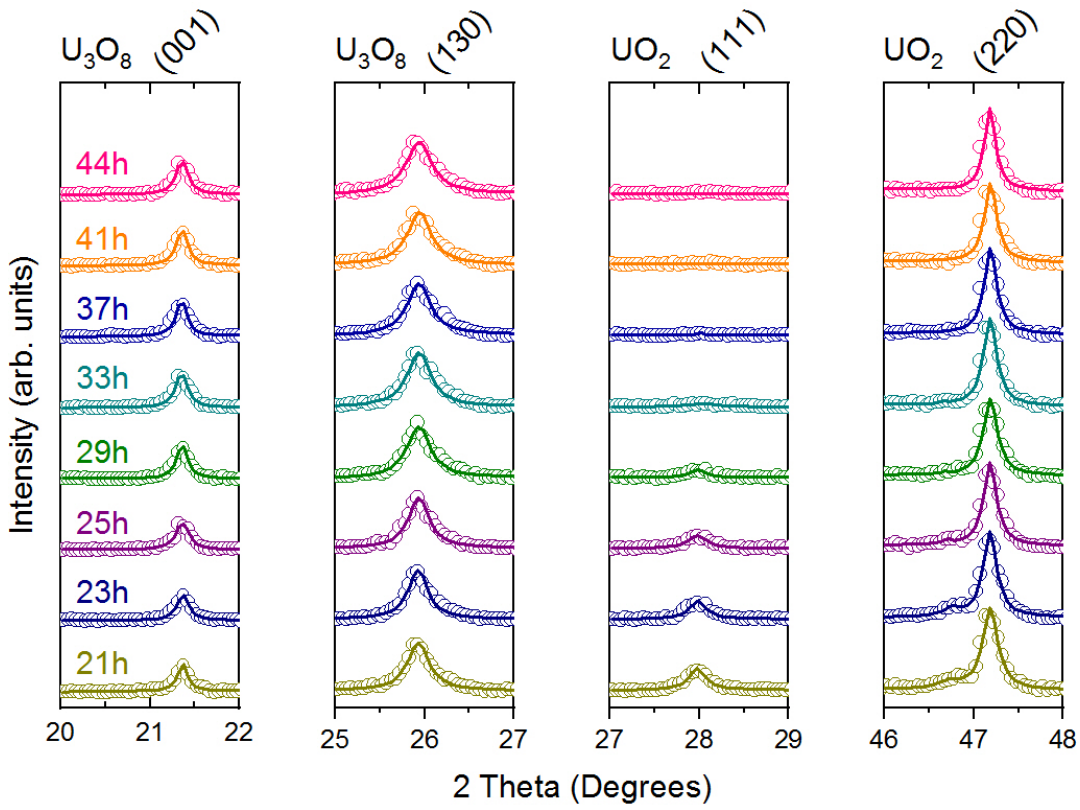

FIGURE 5.8. Further oxidation of SN1191 including (001) phase of U_3O_8. No signal was observed for (002) UO_2.

The kinetic of oxidation from UO_{2+x} to U_3O_8 presented on Fig. 5.9 are in good agreement with the sigmoidal nucleation-and-growth mechanism described in literature for this phase transition [31, 41, 41, 45, 46, 70, 70, 73, 172, 187]. The induction period, where the initial rate of oxidation is very low, takes place during first the 10 hours of the oxidation process. After this time, the oxidation rate gradually increases to a maximum, and this linear region [31] is observed from around 13 hours to 21 hours. When the reaction approaches completion, it tails off finishing after 44 hours with full sample oxidised to U_3O_8.

Data presented here is in contradiction to what was reported by Allen et al. [71, 72], where the oxidation rate of UO_2 was suggested to be highest for the (111) orientation due to epitaxial relations with U_3O_8, followed by (110) and slowest for (001). The (001) oriented grains within the SN1191 sample oxidised quickest, and no signal was observed after 23 hours. There was not

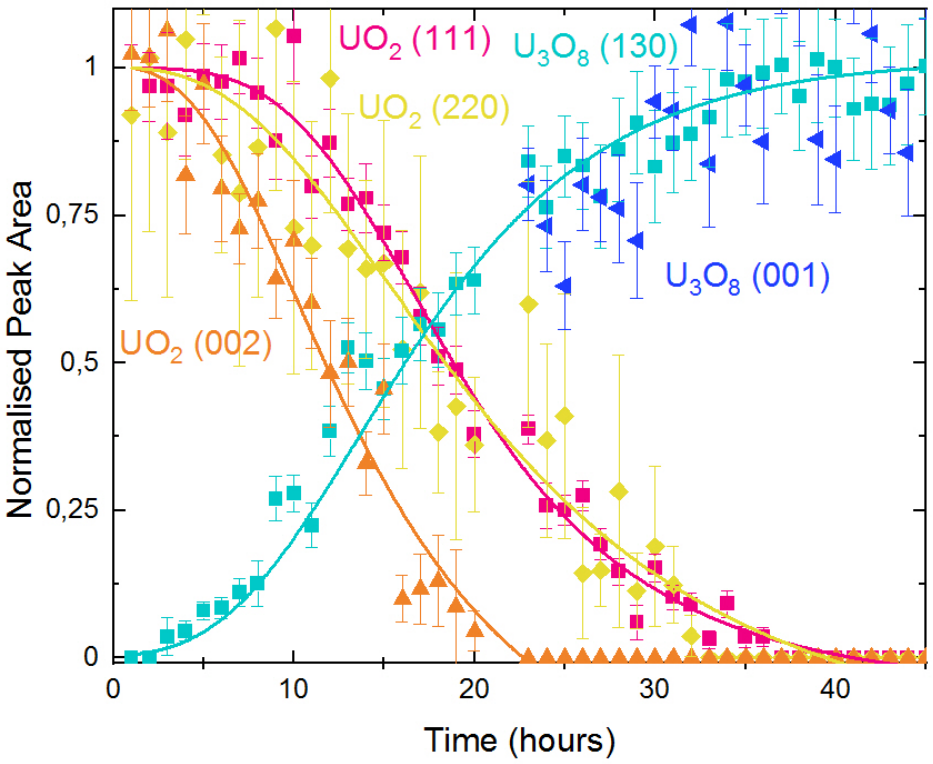

FIGURE 5.9. Integrated area of peaks against time of oxidation in 200 mbar of O_2 at 300°C. Data was fitted using logistic function. Characteristic sigmoidal kinetics for nucleation and growth of U_3O_8 are observed. The data for (001) U_3O_8 was not fitted as signal was not measured from the beginning of the oxidation.

much difference between kinetics observed for the (111) and (110), that disappeared after around 37 hours and 33 hours of oxidisation respectively. This might suggest that there is some relation between the (001) orientation of cubic UO_2 and some plane of orthorhombic U_3O_8.

Using data from the second in-situ XRD oxidation experiment (Fig. 5.5, Fig. 5.7, Fig. 5.8) center of the Bragg peaks were extracted and lattice parameters based on the Cu K_{alpha_1} wavelength were calculated, which is shown on Fig. 5.10. The panel (b) shows changes to the lattice parameter over time while oxidising UO_{2+x} in 200 mbar of O_2 at 300°C to U_3O_8. In contradiction to what has been observed at 150°C (Fig. 5.10 (a)), where due to the incorporation

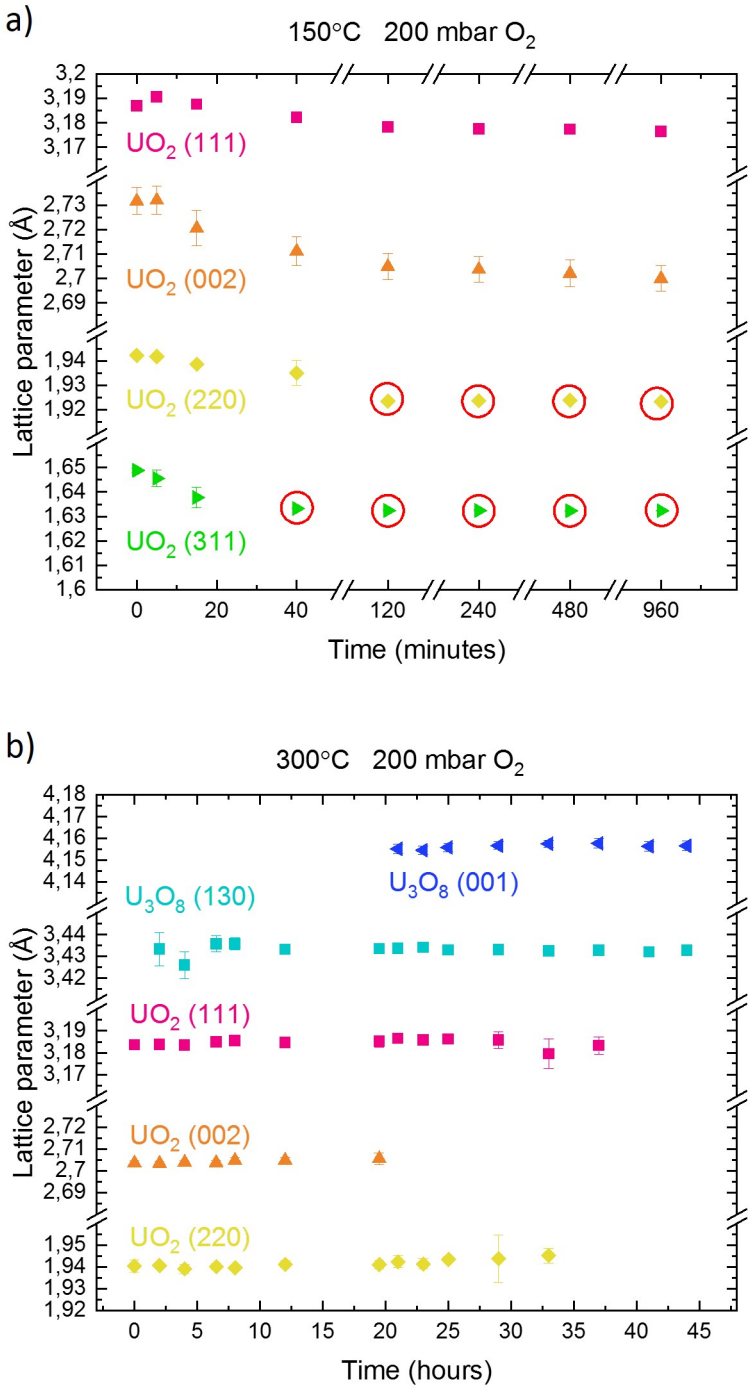

FIGURE 5.10. Changes in lattice parameter as a function of time during second in-situ XRD oxidation experiment in 200 mbar of oxygen at (a) 150°C and (b) 300°C

of oxygen into cubic structure of UO_{2+x}/U_4O_9 followed by possible distortion to tetragonal U_3O_7 the lattice parameter shrinks, here (Fig. 5.10 (b)) lattice parameter for already fully oxidised U_4O_9/U_3O_7 does not change. Furthermore, as expected, no changes are observed to the lattice parameter of U_3O_8. The first two points for the (130) reflection for U_3O_8 are slightly off compared to the rest, as due to very low signal to noise ration caused by a very small amount of U_3O_8 contributing to the signal at the beginning of phase transition.

After completing the in-situ XRD oxidation of sample SN1191 to U_3O_8, the sample was investigated again using SEM. The images taken from the sample surface after oxidation are shown on Fig. 5.11. The panel (a) shows the surface of the sample, within the ROI, before oxidation. Flat sample area with grain structure and markings made using DB system are visible. The same area captured after oxidation is shown on panels (b), and view from the top on panel(d) where crosses and dots were used for marking are easily visible. The flake structure can be seen under higher magnification on Fig. 5.11 (c). Due to disintegration of the sample EBSD mapping was not possible.

The disintegration of the thin film was caused by the volume expansion of 36% [179] associated with the phase transition from UO_2 to U_3O_8. This a well known effect that leads to loss of the UO_2 matrix integrity [31][70]. Previously reported structures of U_3O_8 after oxidising from UO_2 showing "popcorn" morphology for powder form of the sample and "cauliflower" appearance is observed for pellets [75]. In this studies a "flake" structure is most likely caused by the thin film nature of the starting material.

To verify if the observed structures on Fig. 5.11 (b-d) are related to the uranium oxide or are of different origin, an Energy-dispersive X-ray spectroscopy measurement was taken. The result of the EDX mapping is shown on Fig. 5.11 (e), where the yellow colour represents uranium. As it can be seen, a strong signal is observed from flakes, while the areas where uranium was, etched using ion beam (dots and crosses) to mark the region for EBSD, are black and no uranium signal is present within them. This in addition to the XRD signal that represents the entire sample, showed locally that the new structures contains uranium.

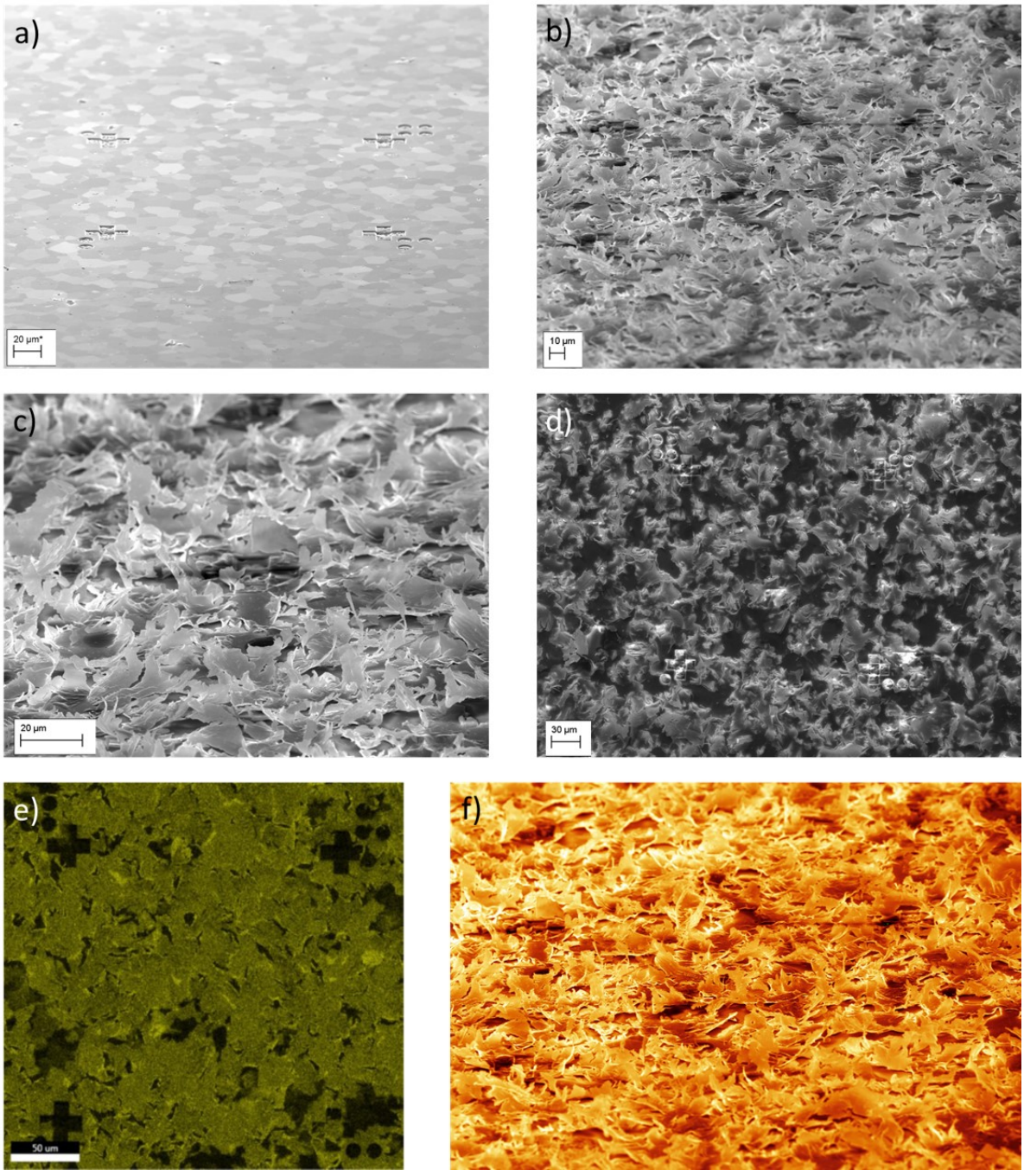

FIGURE 5.11. After oxidation, "flake" like morphology is observed under SEM on entire surface of SN1191 sample(b-d). Energy-dispersive X-ray spectroscopy (e) shows in yellow signal from uranium. Artistic visualisation of the structure as "uranium autumn leaves" is shown on panel (f).

5.2.1 Flakes studies

Unlike x-rays, the electrons interact readily with the sample limiting the thickness of the specimen to around 100 nm for a typical TEM. The thickness of the starting UO_2 thin film was around 160 nm, accounting for the volume expansion associated with phase transition into orthorhombic U_3O_8, the thickness of the flakes obtained after oxidation should be around 218 nm. This is too thick for TEM imaging, unless the material also breaks in the horizontal direction. In order to investigate the structure of the flakes, they were gently scratched from the YSZ substrate onto a copper TEM grid.

The copper grid with uranium flakes was first investigated in STEM mode on Dual-Beam system. Multiple images with different magnification in bright-field, dark-field and high-angle dark-field modes were taken, selected images are shown on Fig. 5.12. The first panel (a) shows an overview of the copper grid at low magnification. Dark field version of this area was chosen to show as it provides strong Z-contrast, and uranium flakes can be seen as white spots on the copper grid. View on the single grid is shown on Fig. 5.12 (b) and (d) in bright field and HAADF modes respectively. Multiple flakes with different size are observed, also a lot of cracking and defects within their structure. An image of the biggest flake under extreme magnification in dark field mode is presented on Fig. 5.12 (c). it shows that within a single flake, other smaller grains and cracks are present, which could be related to stress inside the structure caused by expansion.

The data collected in STEM mode on the DB system suggested that it might be possible to conduct TEM imaging on the flakes. The TEM measurements were performed by Sean Davis at the Chemistry Imaging Facility, School of Chemistry, University of Bristol, using Jeol 1400 TEM system. The images of a single flake are shown on Fig. 5.13, as presented on image (a) at lower magnification when the entire flake is visible, the central area is too thick to see its atomic structure, but when zooming into its edge (b) the thickness decreases unrevealing the structure of the material. Multiple nano grains are visible on image (c) and (d) with planes of atoms.

An image showing edge of a flake with clear boundaries between grains and nice alignment of atoms with some of the grains is shown on Fig. 5.14. Examples of boundaries are shown with a red dashed line. Multiple nanograins are visible what indicates the polycrystalline nature of the sample. Gatan software was used to extract inter-planar spacing from areas of three grains

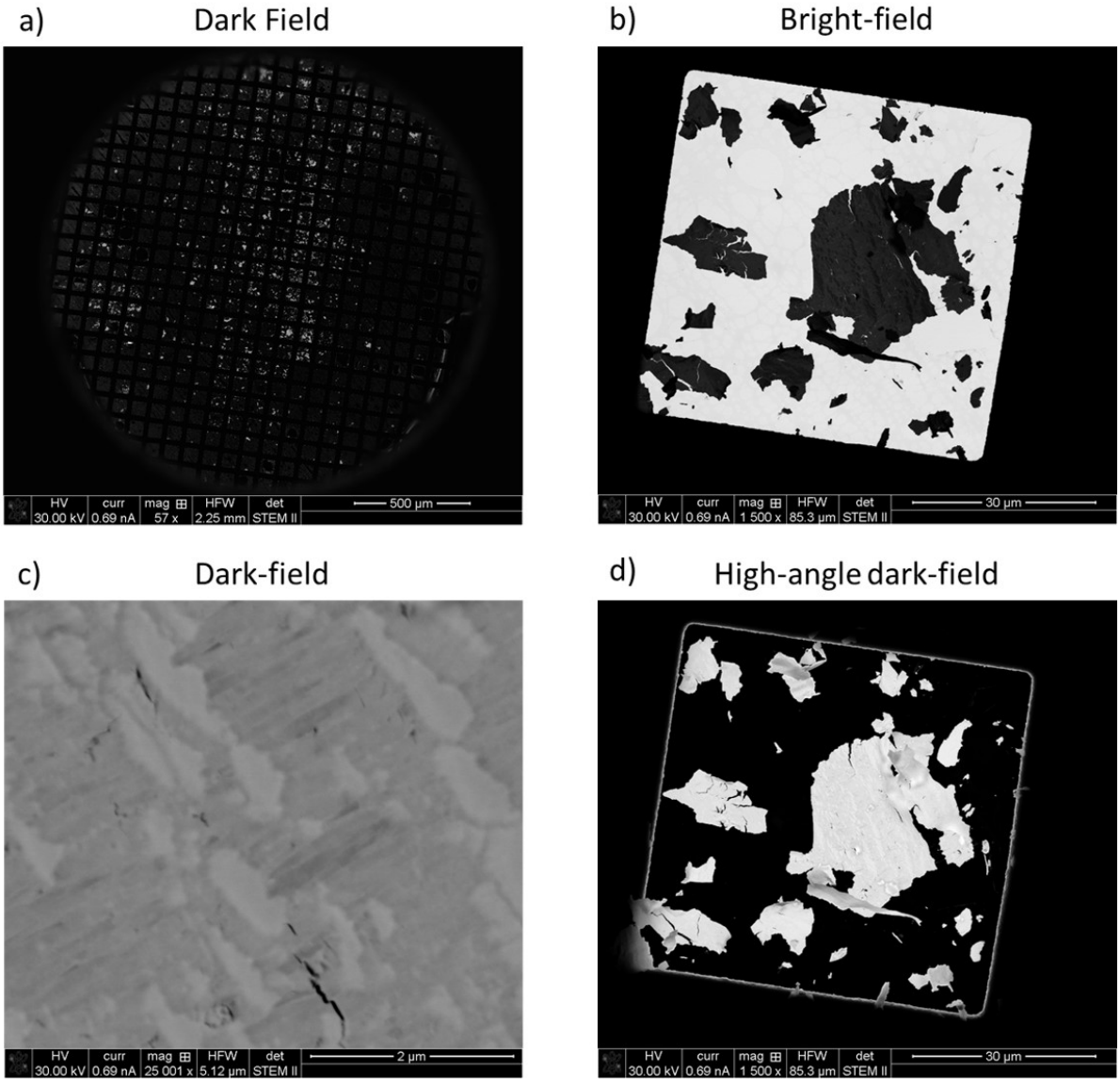

FIGURE 5.12. Scanning transmission electron microscope (STEM) images of flakes obtained by oxidising UO_2 thin film to U_3O_8. Image (a) in dark field mode shown overview of the copper grid with uranium flakes. Single grid with specimen is two different modes is visible on image (b) and (d). Nano structures and cracks can be observed under higher magnification within a flake, as shown on image (c).

labelled with yellow colour. The following procedure was applied: Fast Fourier transform (FFT) of the ROI was performed, followed by masking the area around the two symmetric brightest spots. In next step inverse FFT processing was used to create an image from which profile of repeating

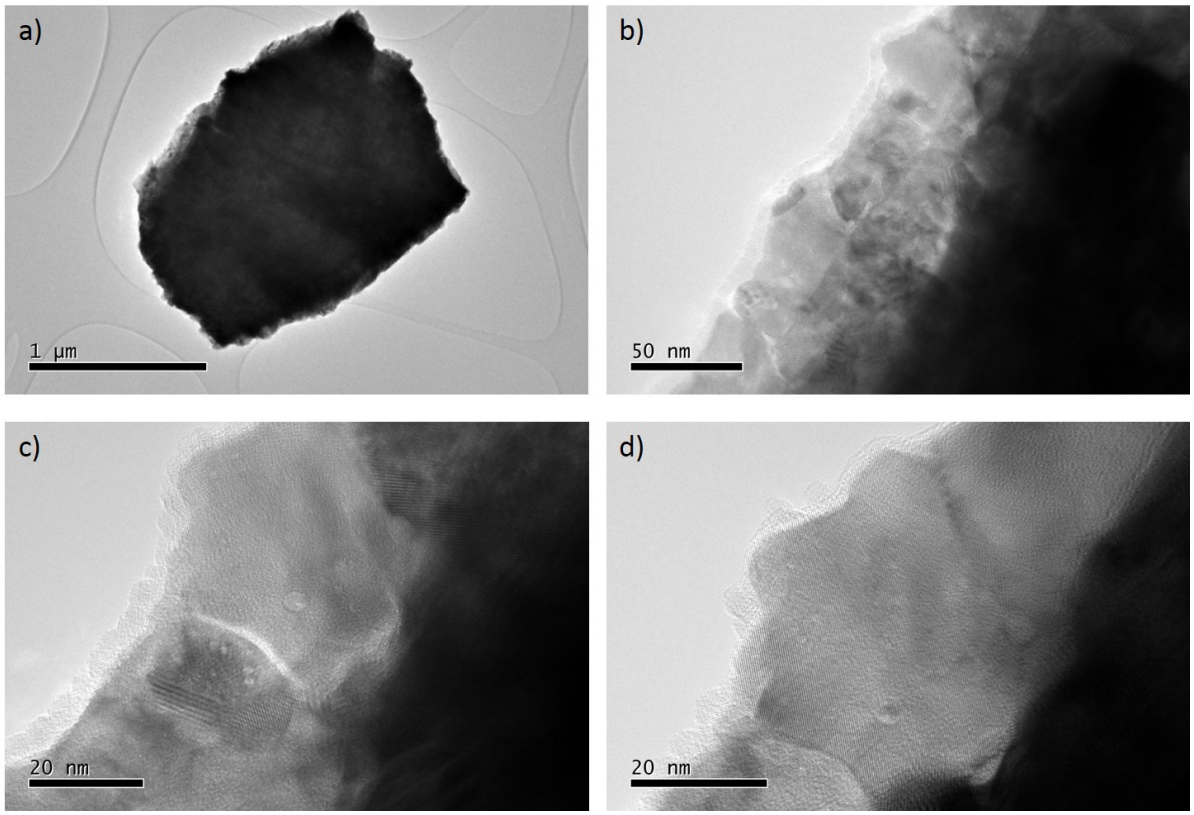

FIGURE 5.13. TEM investigation of a U_3O_8 flake. Micron size flake is shown on image (a), with thick internal area. The edges of the flake are displayed on panels (b-d), where planes of atoms arranged within nano grains are observed.

patterns was extracted. Distance between ten peaks was measured to minimise the error.

It was found that the inter-planar spacing is in range 3.28 - 3.45 Å for first ROI, 3.40 - 3.58 Å for the second ROI and 2.62 - 2.92 Å. This data was compared with the d-spacing of U_3O_8 and it was found that first two regions match well with d-spacing of 3.42971 Å (130), while the third matches with 2.64346 Å (131). This agrees well with the x-ray diffraction data and confirms the polycrystalline structure of the U_3O_8 flakes created from oxidising the UO_2 poly-epitaxial thin film.

The quality of the selected area (electron) diffraction pattern (SADP) was affected by the thickness of the sample, and its ability to only collect signal from the edges. An example of the SADP collected from the edge of a U_3O_8 is shown on Fig. 5.15. The presence of multiple spots

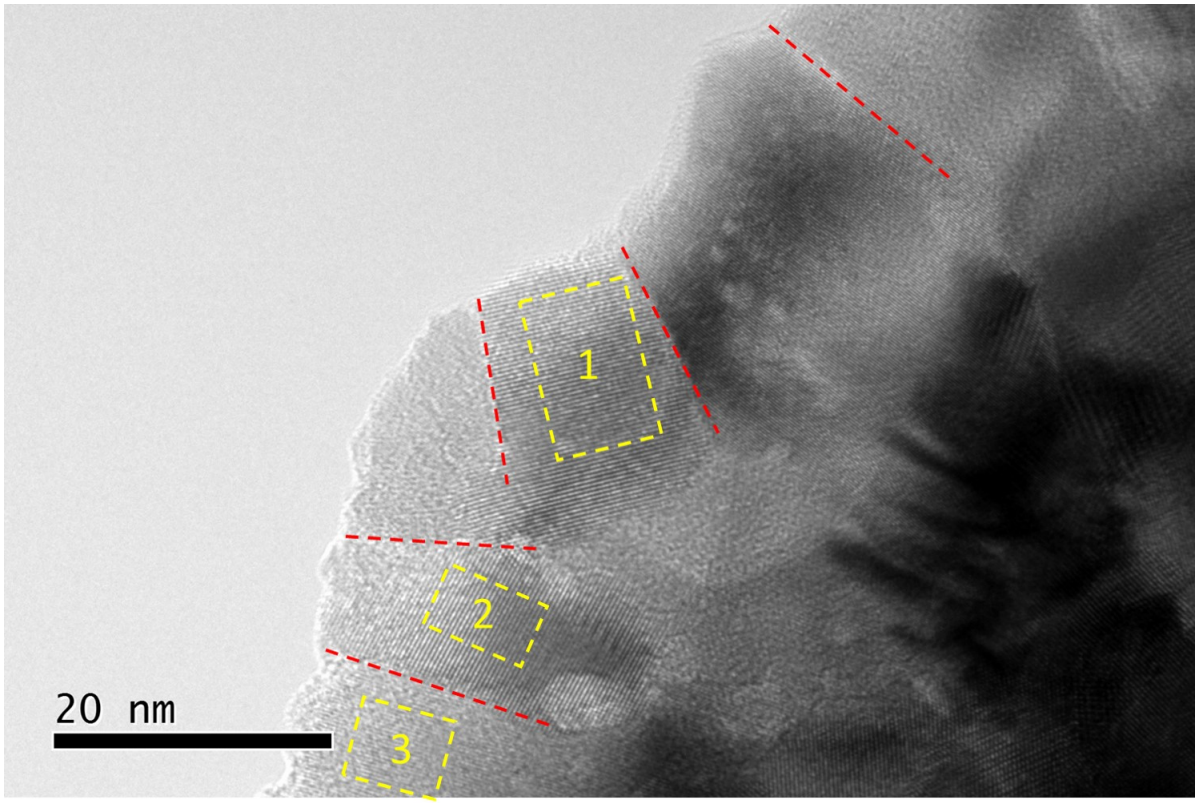

FIGURE 5.14. The lattice fringes of U_3O_8 observed on the edge of a flake. The red dashed lines show boundaries between nano size grains. Analysis of the distance between atoms within areas in yellow boxes suggest (130) orientation for the area 1 and 2, while the third area matches with (131) orientation of U_3O_8.

d spacing (Å)	
SADP Figure 5.15	U_3O_8
4.21 ± 0.11	4.149 (001)
3.45 ± 0.09	3.43 (130)
2.67 ± 0.07	2.643 (131)

Table 5.3: Calculated values of the d spacing measured from the rings shown in Figure 5.15, compared with values for orthorhombic U_3O_8.

aligned in circles indicate polycrystalline character of the specimen. Gatan Digital Micrograph software was used to analyse the d-spacing for the observed rings. The value was extracted from the center of the spot, and error was calculated based on the diameter of the spot. This data, compared with lattice spacing for different planes in U_3O_8 is shown in Tab. 5.3.

The crystallite size of polycrystalline U_3O_8 was also calculated using the Scherrer equation.

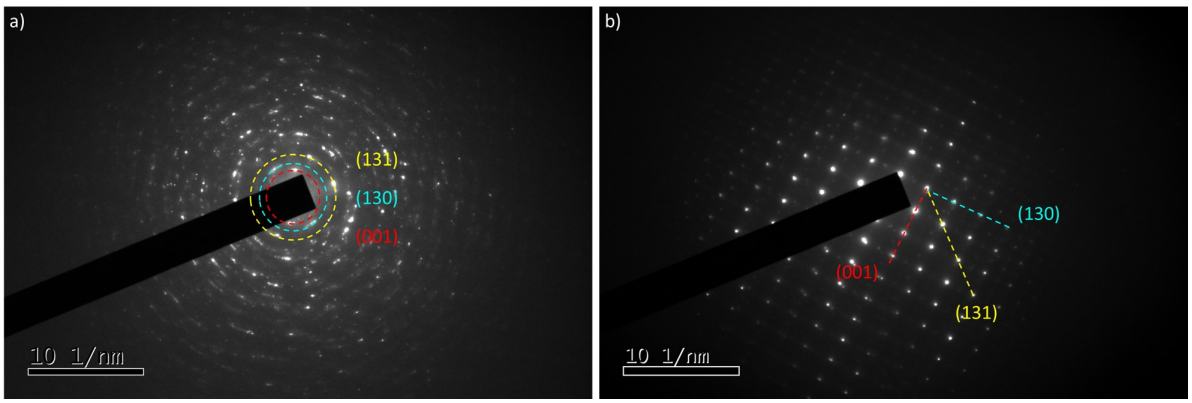

FIGURE 5.15. Selected area electron diffraction patterns (SADP) of two different flakes. First one (a) is a good representative for most of the investigated material, where polycrystalline pattern is observed. Crystal structure of orthorhombic U_3O_8 crystal is visible on image (b).

The highest intensity Bragg reflections (130) of U_3O_8 were used for this calculation. The average grain size was found to be 25 ± 2 nm, which is in very good agreement with the size of the grain observed under TEM.

The polycrystalline character of the flakes was confirmed using a combination of x-ray diffraction and electron microscopy techniques. Furthermore, flakes are made out of U_3O_8, which was expected as oxidation of UO_2 in presence of oxygen at elevated temperature leads to formation of U_3O_8, and observed in XRD, TEM, and SADP data.

5.3 In-situ HT-ESEM

The in-situ XRD oxidation of poly-epitaxial UO_2 thin films revealed that grains with (001) orientation oxidises faster than (111) and (110). Furthermore, even thin films epitaxially stabilised by substrate cracks and lose integrity while transforming to U_3O_8, due to volume expansion. To further investigate this process, and answer a new question, such as where the cracking starts and what is the influence of the grain size in addition to its petrographical orientation, an oxidation experiment in-situ High Temperature - Environmental Scanning Electron Microscope (HT-ESEM) was conducted.

The HT-ESEM used in this experiment was FEI Quanta 200 FEG ESEM (Thermo Fisher Scientific) at the Institute de Chimie Separative de Marcoule (ICMS) in Marcoule, France, and was operated by Renaud Podor. This system uses a field emission gun for imaging, which can be performed in different modes, including environmental mode with a gas pressure in range between 0.1-7 mbar. The chamber is fitted with a furnace stage allowing to increase temperature up to a 1200°C, while continuously scanning the sample surface.

The sample used in this experiment was SN1498, a poly-epitaxial 100 nm thin film of uranium dioxide grown on a ceramic YSZ substrate. Detailed characterisation of the sample was described in Chapter 4. Within the sample, an area of 200 x 200 μm was marked using a dual beam microscope, and later orientation map of the ROI was created using the EBSD system on the FEGSEM. To minimise the damage from the electron beam and carbon deposition from the EBSD mapping process, a fast scan with lower resolution was performed.

In order to conduct in-situ oxidation of the SN1498 thin film of UO_2, the sample was placed on the HT-ESEM stage. As the microscope operates in environmental mode, there was no need to create an electric bridge between the sample stage and the surface of the sample, as the discharging process is maintained by the oxygen gas. The sample was then gradually heated at oxygen partial pressure of P_{O_2} = 350 Pa. Images of the sample surface were taken every 3 to 5 seconds, at a constant acceleration voltage of 20kV.

Selected images taken during this in-situ oxidation experiment are shown in Fig. 5.16. The first image (a) was taken at 23°C just after finding and focusing on the ROI. Micron size grains of UO_2 are clearly visible with crosses and dots marking the area. The next image on Fig. 5.16 (b) shows the surface of the sample at 257°C, at this stage oxidation to U_3O_7/U_4O_9 could be taking place. Unfortunately, there was no possibility to investigate those changes, as the only indication is cracking of the structure while formation of U_3O_8 occurs. The slightly different contrast between the grains visible on image (a) compare to image (b), can not be treated as an indicator, due to the field of view and instrumental contrast being adjusted during the experiment to compensate for thermal expansion. Furthermore, a small cracking of the sample reported for formation of U_3O_7 [74] at the surface of UO_2 were not observed before in XRD measurements, where the U_3O_7/U_4O_9 presence was confirmed by lattice constant.

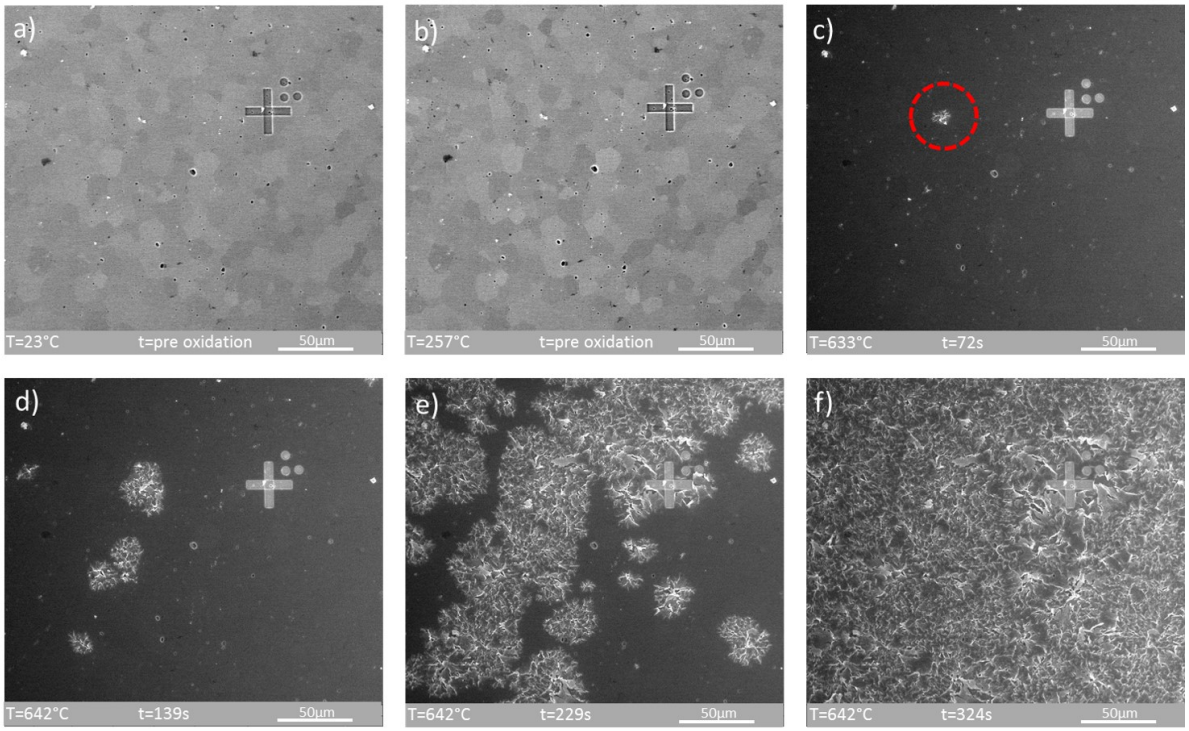

FIGURE 5.16. Images of 100 nm thick poly-epitaxial thin film sample SN1498 of UO_2 taken using FEI Quanta 200 FEG ESEM during the in-situ oxidation experiment at different time and temperatures. The surface of the sample at RT is visible on image (a). Possible oxidation to U_3O_7/U_4O_9 is shown on image (b). The start of the oxidation is marked with red circle on image (c). The images (d) and (e) show further oxidation, and final view on the sample surface is shown on image (f). Time is counted from first signs of cracking. Images were taken at ambient pressure of oxygen P_{O_2} = 350 Pa, and acceleration voltage 20 kV. (Video: https://figshare.com/s/db53671f400c57e695a9)

The slightly different contrast between the grains visible on image (a) compare to image (b), can not be treated as an indicator, due to the field of view and instrumental contrast being adjusted during the experiment to compensate for thermal expansion.

First signs of the thin film disintegration were observed at 623°C and from that point in time the heating power was kept constant. After 2 minutes the temperature stabilised at 642°C. The area where the cracking started is indicated with a red circle on Fig. 5.16 (c). This image was taken after 72s from the first signs of oxidation at 633°C. The next images (d), (e) and (f) on Fig. 5.16 show further oxidation associated with phase transition to U_3O_8, where nucleation starts at

multiple points and spread within the thin film sample. The last image (f) shows the completed process, when no more changes were observed and the entire sample was assumed to be U_3O_8.

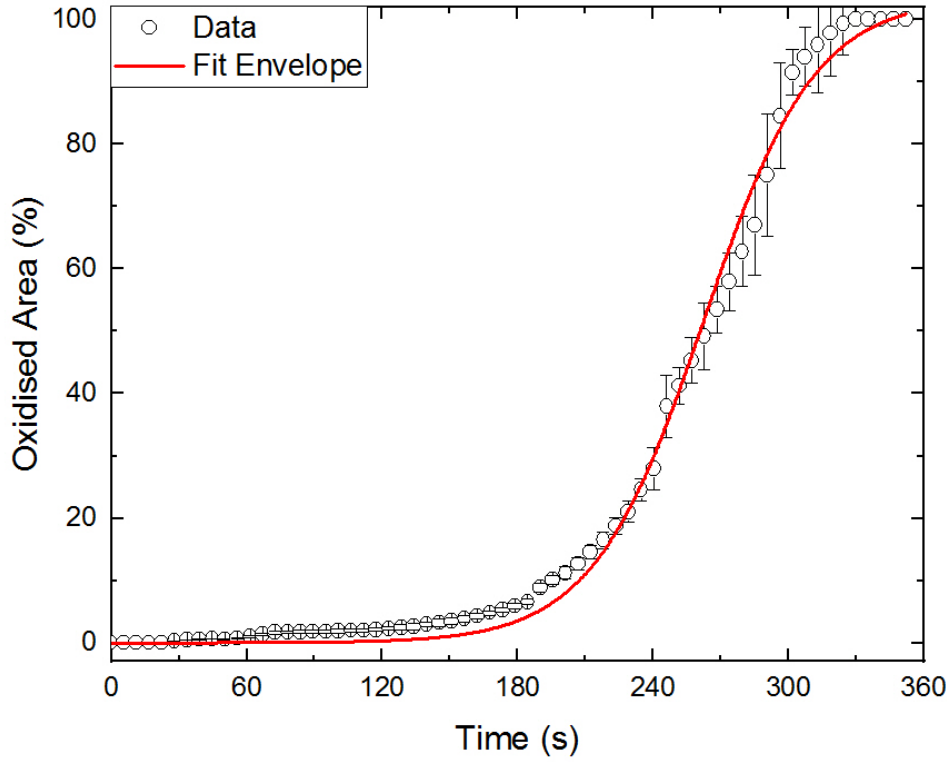

FIGURE 5.17. Kinetics for the oxidation of poly-epitaxial SN1498. The data values extracted from images are represented by black circles, while sigmoidal logistic fit is shown as red line. A typical sigmoidal nucleation-and-growth mechanism for formation of U_3O_8 is present.

To find the kinetics for the HT-ESEM in-situ oxidation of poly-epitaxial UO_2 to U_3O_8, the Fiji ImageJ software was utilised. When UO_{2+x} undergoes phase transition to orthorhombic U_3O_8, an increase of the volume by 36% causes loss of integrity. The percentage of the damaged area to the entire area of the image was extracted from a series of scans. First, to account for the difference of intensity related to the small tilt of the sample, background of each photo was subtracted using the Gaussian-blurred version of the image. The data points obtained from this process against

time are shown on Fig. 5.17.

Typical sigmoidal nucleation-and-growth kinetics for the formation of U_3O_8 are observed in good agreement with the literature[31, 49, 64, 169, 171, 197–202]. The slightly longer induction period observed for around the first 190s compared to the XRD data, can be related to the starting stoichiometry of the sample. Furthermore, due to different time frames there could be not enough time to fully oxidise the sample to U_3O_7/U_4O_9 prior to the phase transition to orthorhombic structure. The maximum oxidation rate is observed between 240-300s, and after that time it slows down to finish after 360s.

Kinetics of in-situ HT-ESEM oxidation of uranium dioxide thin films cannot be directly compared to the data collected using the XRD due to differences in three main parameters. First, the starting stoichiometry of the poly-epitaxial UO_2 sample, the thin film during the in-situ XRD is first fully oxidised during the extender treatment at 150°C in oxygen atmosphere forming U_3O_7/U_4O_9. In HT-ESEM is not possible to investigate the stoichiometry of the sample before the phase transition, as the only indication is the disintegration of the sample associated with the formation of U_3O_8. In addition, due to pressure limitations of 7 mbar inside the ESEM chamber it was not possible to perform experiments at 200 mbar of UO_2, which was the pressure used in in-situ XRD studies. Furthermore, due to limited availability of the HT-ESEM equipment and reduced amount of oxygen, temperature had to be increased further than 300°C in order to initiate the phase transition from cubic to orthorhombic system of uranium oxides.

Based on the EBSD map of the sample ROI, and SEM image taken during the oxidation experiment, an overlay was created and is shown on Fig. 5.18. The cracking process was analysed frame by frame in order to identify points where the disintegration of the UO_2 matrix begins. Those locations are marked with red dots. From a total of 28 points where the cracking started, 21 points were located on the grain boundaries. This suggests that not only the crystallographic orientation of the grain has to be take into consideration while study phase transition into U_3O_8, but also the size of the grain, which translates to the density of the grain boundaries in a polycrystalline material.

Dissolution studies performed on surrogate materials [178], showed preferential dissolution of grain boundaries and faster dissolution rate was linked with highly misoriented boundaries.

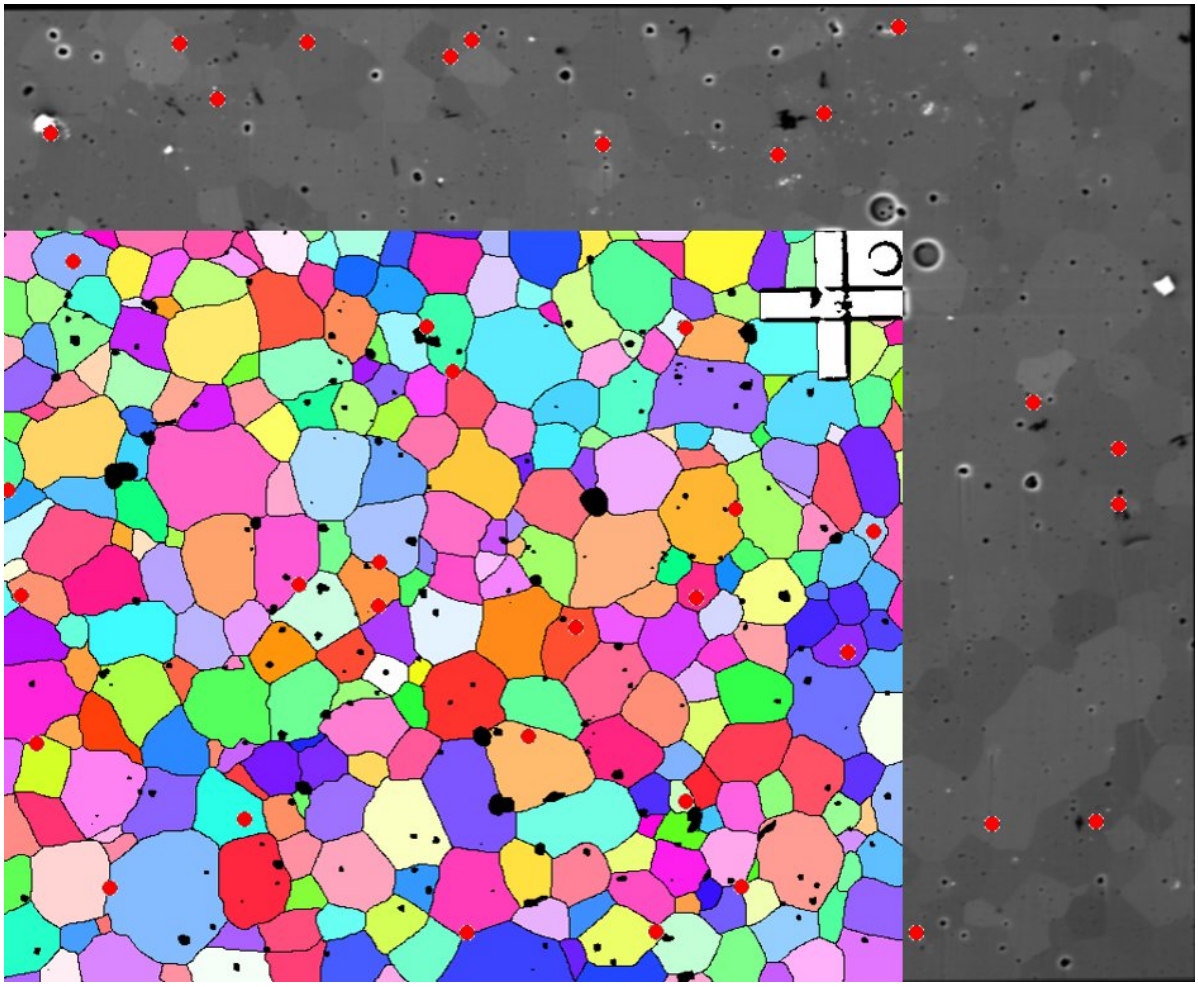

FIGURE 5.18. Inverse pole figure (IPF) map of the ROI on sample SN1498 was overlay with SEM image take during oxidation experiment. Red spots indicates locations where cracking related to formation of U_3O_8 started. Video of the oxidation process with overlay EBSD map available on the following link: https://figshare.com/s/98d896ba98b8364dbf6c

The defect-rich nature of grain boundaries was also associated with rapid oxidation, followed by simultaneous intragranular oxidation throughout the sample [31], what is observed in presented data.

Further analysis showed that the oxidation reaction prefers mostly smaller grains, with orientations close to (001). Faster oxidation of the (001)-oriented grains indicates that volume expansion associated with phase transition to U_3O_8, would first occur at those grains leading

to increased stress at the grain boundaries resulting in preferential cracking, what have been observed. This is also in good agreement with the importance of the particle size effect reported previously [169]. Those studies were performed on powder samples, where this effect is easily predictable as the smaller particle sizes, the larger surface area for the reaction to take place. For a bulk representative, such as UO_2 sintered pellets, this process is much slower [185] because samples have small surface areas. As the structure of poly-epitaxial thin film is much closer to a sintered pellet than to powder UO_2, the data collected in this experiment is mostly compared with the studies conducted on pellets and single crystals.

Early studies [171, 197] conducted on CANDU, AGR and LWR pellets showed a negative correlation between grain size and the oxidation rate of whole pellets. This was supported by more rapid oxygen diffusion along grain boundaries than into UO_2 grains, therefore oxidation proceeds initially along the grain boundaries and is followed by intragranular oxidation. This model is in very good agreement, with the data collected during the in-situ HT-ESEM oxidation of where 75% of the cracking associated with oxidation starts at the grain boundaries.

Contradictory results were presented by Wood and Bannister [198], where a positive correlation between the initial oxidation rate and grain size was suggested. However, the density of the samples was not taken into consideration, and a correlation in data with the density was observed. As the density of the sample is also very important [31], it is not clear whether the observed correlation is due to grain size or sample density. Further studies performed by the same authors [198], showed that with decreasing grain size the reaction rate increases, but only for samples with grains smaller than 5 μm . For single crystals and samples with grains larger that 5 μm, the oxidation rate was the same. The average grain size of the SN1498 sample is 13.57 μm with a standard deviation σ=4.85.

Nevertheless, in all studies presented for formation of U_3O_8 from U_3O_7/U_4O_9 [31, 49, 64, 169, 171, 197–202] it is certain that it proceeds by a nucleation and growth mechanism, as shown in this experiment (Fig. 5.17). This indicated that poly-epitaxial thin films are a good surrogate material for studies of bulk representatives of UO_2, but due to their unique structure can provide more insight into the oxidation process.

Regardless of grain size, it was found that the cracking and spalling processes begin mostly at

the boundaries of the grain close to (001) orientation. This is in good agreement to the XRD data presented earlier in this chapter, showing larger changes in the lattice parameter along the (001) grains (5.3) and faster oxidation rate for this orientation (5.9). Both data sets collected during the in-situ experiment are in disagreement with the model presented by Allen et al. [71, 72] with following oxidation rate rates [111]>[110]>[100]>[polycrystalline].

5.4 XPS mapping

Determination of UO_{2+x} stoichiometry based just on the XRD pattern can be complicated, as has been demonstrated in the in-situ XRD section. The lattice constant of UO_{2+x} does not simply follow Vegard's law-like behaviour in the whole hyperstoichiometric range, and three different equations are required to describe changes to the lattice constant. As shown on Fig. 5.6 the same lattice constant can be observed for three different stoichiometries. Furthermore, XRD provides information about volume of the sample, and without specific equipment diffraction on a single grain is not possible. However, small changes to the stoichiometry can be measured using different techniques such as Raman spectroscopy [179] and XPS [203]. Throughout this thesis both techniques were investigated, but only XPS data will be briefly discussed.

Actinide oxides have been studied for almost 50 years using XPS [203, 204], as this technique provides detailed information on the surface composition and chemical state of the near-surface which has immediate contact with its surroundings and consequently mediates most reactions. As uranium has multiple oxidation states and often a combination of them is observed in the XPS spectrum, a simple comparison of the binding energies (BEs) of core level is not enough to determine oxidation states of uranium. Fortunately, other features in the XPS of U allow for determination of the oxidation state.

In addition to comparing core level BE, a lot of information can be extracted from the most sensitive line which is the the 4f line. The shape and the broadening of this line and possibly the emergence of distinct multiplet structures provides information about bonding environment of uranium [203]. Small changes to the stoichiometry of uranium dioxide can be observed in the intensity and energies of satellite lines relative to an associated primary peak. This is also

independent from the absolute binding energy and the experiment was mainly focused on this method for determination of uranium oxidation state.

The U satellite peaks have an inter-atomic origin expressing final states due to transfer of electron(s) from the dominantly ligand 2p bonding orbital into open uranium 5f or 6 d shells [203]. The most prominent satellites come from the primary spin-orbit split $4f_7/2$ and $4f_5/2$, where the stronger $4f_7/2$ peak position is in range 379.8 to 380.1 eV [205]. The separation between the peaks and satellites for tetravalent uranium was reported to be in the range 6.6-7.1 eV, based on the oxidation state [203].

Furthermore, recent work conducted by Ilton at el. [206] showed that small changes in uranium oxidation states can be extracted using XPS of a shallow core level. In addition to data from the 4f line, researchers focused also on the U 5d and 5p multiplet structures, as those peaks are very sensitive to the oxidation state. Oxidation states for U, determined using the 4f and 5d lines were strongly correlated, showing that both can be used to investigate small changes in stoichiometry of UO_{2+x} in range $0 < x < 0.3$.

Combination of XPS methods for precise determination of UO_2 stoichiometry combined with the unique columnar sample structure of UO_2 thin films fabricated for this thesis offers new possibilities for the investigation of crystallographic orientation influence on the oxidation rate. The sample SN1545, 100 nm thin film of poly-epitaxial UO_2 grown on YSZ substrate using DC magnetron sputtering, previously characterised in Chapter 5, was used for purposes of this experiment.

Prior to XPS mapping the sample was reduced in-situ XRD at hight temperature under vacuum, in order to obtain almost stoichiometric UO_2. Then, the sample was transported in air atmosphere to Diamond Campus, where the first XPS mapping was conducted. After that, it was transported back to Bristol, where in-situ XRD oxidation was performed. The sample was slightly oxidised to UO_{2+x}, were $0.5< x <1.5$, so the limit of $UO_{2.25}$ was not reached, otherwise due to limited solubility of oxygen all grains could have the same stoichiometry. Then sample was transported back to Diamond, where post-oxidisation scanning followed by in-situ reduction under vacuum at elevated temperature was conducted.

To calibrate the lines of the integrated U 4f peaks, integrated carbon 1s lines from all 10

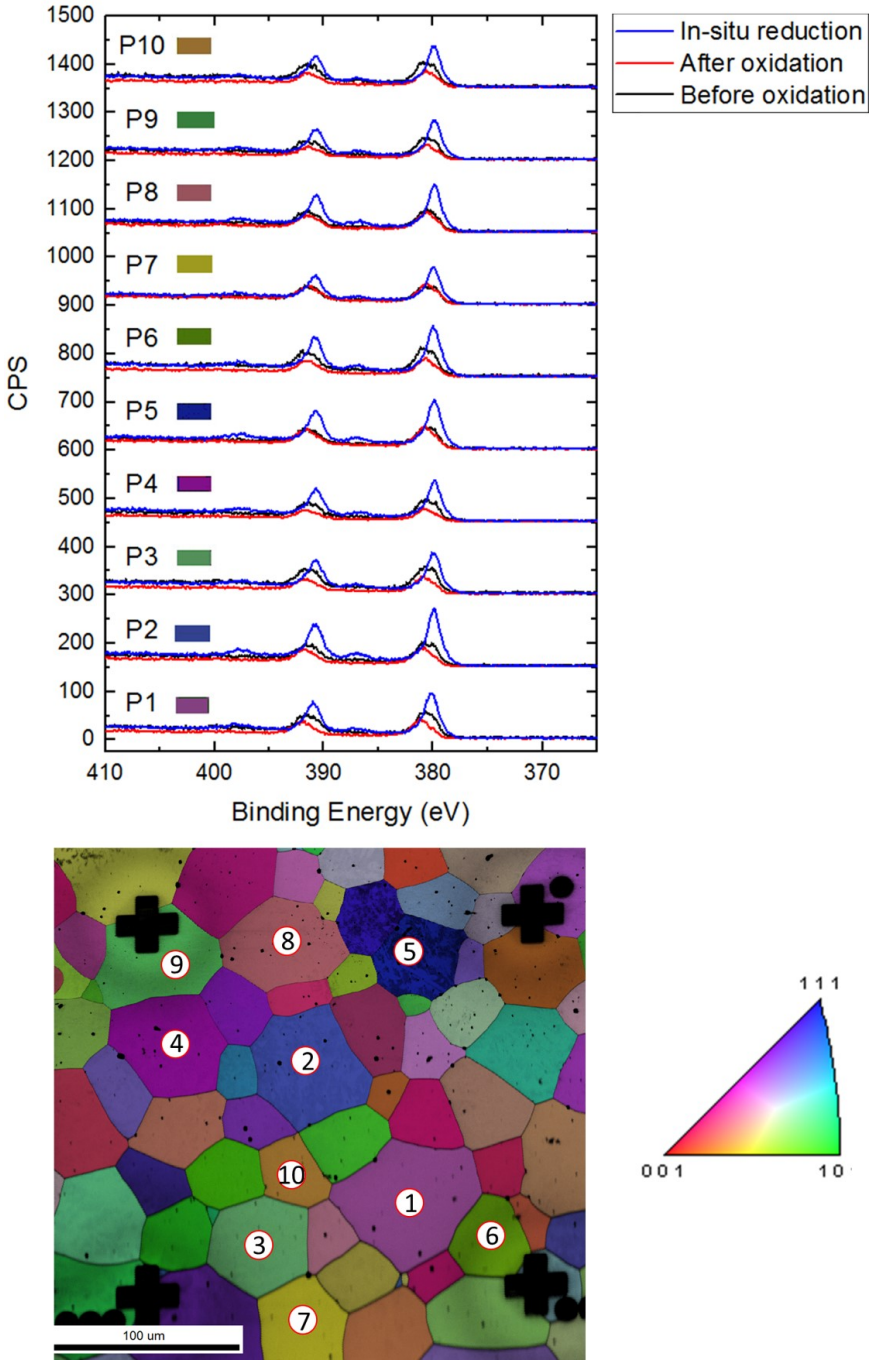

FIGURE 5.19. XPS data collected from 10 different grains before oxidation (black), after oxidation (red), and when in-situ reduced (blue). The IPF EBSD map indicated were the signal was collected.

areas were used. Fitting was performed in Origin using a Gaussian function. The small shoulder at higher binding energy on C 1s peak before oxidation might suggest presence of a small amount

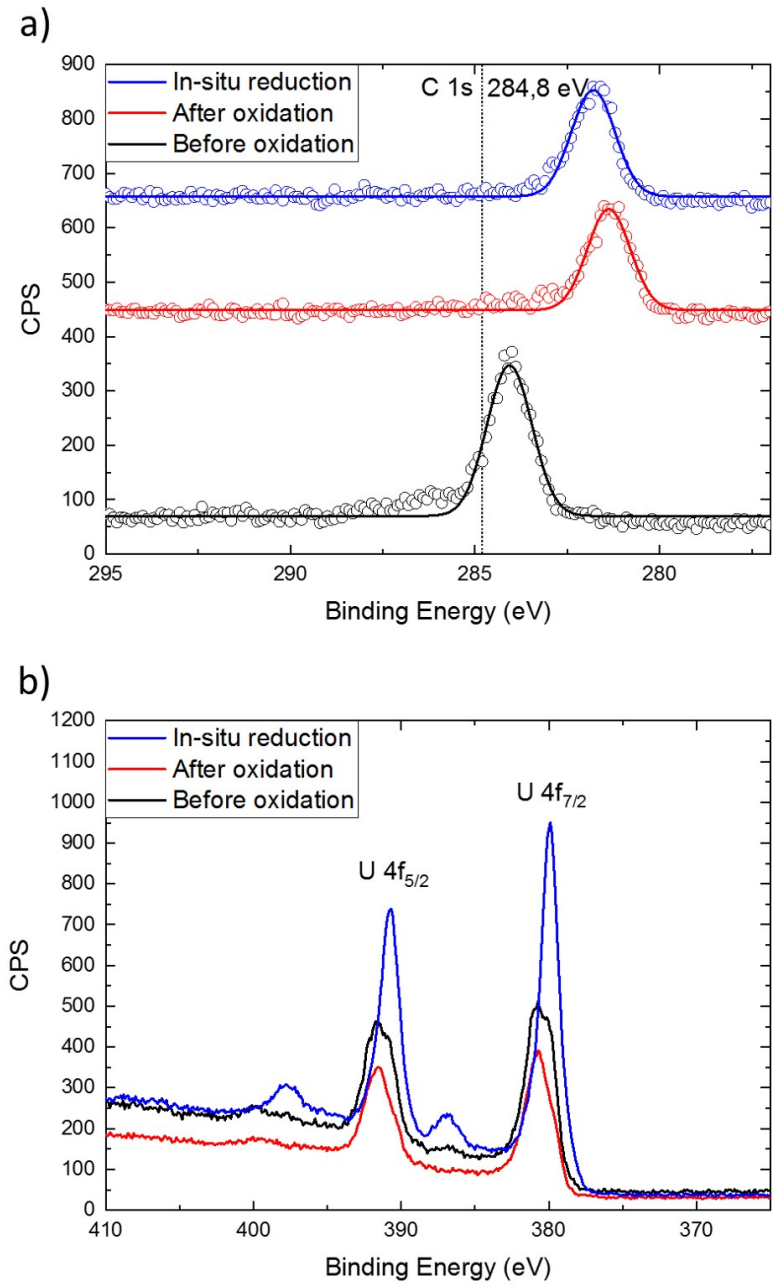

FIGURE 5.20. Integrated signal from all ten grains for (a) C 1s peak used for data calibration to 284.8 eV, and (b) signal from U 4f with satellites indicating UO_{2+x}.

of carbon oxide. Raw data with fitting of the carbon peak is shown of Fig. 5.20 (a). The position of carbon 1s was calibrated to its reference value of 284.8 eV.

Data at each stage was collected from ten different grains within the ROI, as shown on the

IPF map on Fig. 5.19. The data collected before oxidation is plotted using black colour, after oxidation with red, and scan succeeding in-situ reduction with blue color. Signal to noise ratio was unfortunately not enough to distinguish discrete changes between signals coming from grain with different orientations. Therefore, integrated intensities from all grains were plotted Fig. 5.20 (b), where positions of satellites could be only extracted from signals after annealing under vacuum.

Common practice prior collection XPS data for a sample, is annealing under vacuum which allows to reduce surface contamination, such as from oxygen or carbon. Due to the nature of this experiment, this was not possible as the stoichiometry of the sample would be highly influenced. The effect of applying this step can be visible first in reduced intensity of the C 1s peak on Fig. 5.20 (a), and increased signal from uranium dioxide visible as blue line (Fig. 5.20 (a)).

This experiment could be improved in two ways. The first improvement is related to the sample, if bigger grains could be fabricated that would allow for investigation of larger spot size, resulting in higher data output. The second possible improvement is the use of x-ray source with much higher brilliance, such as the one available one at the synchrotron facilities. Better statistic would allow for detailed analyses of the 4f and 5d line with their peak-satellites separation for each single grain, giving an inside to the oxidation rate based on the crystallographic orientation.

5.5 Discussion

The transformation of UO_2 into U_3O_8 is a two step reaction $UO_2 \rightarrow U_4O_9/U_3O_7 \rightarrow U_3O_8$ [199–201]. In the first step regular cubic fluorite structure of uranium dioxide accommodates additional oxygen atoms in its structure. That leads to the displacement of lattice oxygen atoms from their ideal lattice position and this is observed until $UO_{2.25}$ (U_4O_9) [207][208]. Further oxidation leads to a distortion of the unit cell by interstitial oxygen atoms, and change of a unit cell from cubic to tetragonal (U_3O_7). The second step of the reaction, accommodation of a higher amount of oxygen atoms results in a phase transition to orthorhombic U_3O_8 [209].

Recent synchrotron studies suggest four distinct kinetic time domains for oxidation from UO_2 to U_3O_8 [210]. The crystalline phases associated with these domains are also identified. In fact,

the first kinetic domain corresponds to the reaction of UO_2 into U_4O_9; the second one is linked to the two simultaneous reactions, UO_2 into U_4O_9 and U_4O_9 into U_3O_7. And finally, the transition from U_3O_7 into U_3O_8 corresponds to the third and fourth kinetic domains.

In the case of the oxidation of UO_2 powders, it is generally accepted that the first stage of oxidation is the incorporation of small quantities of oxygen into the fluorite-type lattice to form hyperstoichiometric UO_2+x. Then, the oxidation of UO_2 powders involves U_3O_7 formation. In the literature, two tetragonal phases are reported, α-U_3O_7 and β-U_3O_7, which only differ from their c/a ratio, respectively 0.989 and 1.031 [202][49][64]. Typically, α-U_3O_7 is considered as the normal result of the oxidation at temperatures less than 200°C [3], whereas β-U_3O_7 appears at temperatures higher than 200°C. Finally, the oxidation of powders proceeds only from β-U_3O_7 to U_3O_8, and not from α-U_3O_7 [211].

In the first step of oxidation, attributed to the formation of U_4O_9 and U_3O_7, a pseudo-parabolic weight gain curve is observed, indicating a diffusion-controlled mechanism [31]. To model this kinetics a finite difference algorithm was proposed [212]. In studies conducted on poly-epitaxial thin films of UO_2 in this Chapter it was impossible to extract kinetics of this process, as due to a very thin layer of material the entire volume of sample was oxidised in less than 40 minutes. Such short time did not allow to collect enough data points without interfering with the sample stoichiometry.

Studies conducted by Taylor et al. [185] performed on sintered UO_2 disc using XRD proffered orientation effect, were (001) oriented grains of UO_2 oxidised preferentially to (100) rather than (001) parallel to the sample surface. The rate of U_3O_7 formation from oriented slices of UO_2 were studied by Allen et al. [71, 72], showing the highest rate in the following order [111]>[110]>[100]>[polycrystalline]. The data collected during in-situ oxidation of UO_2 thin films, showed the most pronounced changes to the (001) oriented grains, while oxidising the sample to U_4O_9/U_3O_7. As mentioned previously, extraction of kinetics in the first stage of oxidation was not possible.

The data collected in the first stage of oxidation (Fig. 5.3) is in good agreement with non-Vegard character of changes observed to the lattice parameters as a function of x in UO_{2+x} system reported by Elorrieta et al. [179]. The lattice constant first shrinks in region below x = 0.13 , and

then slightly expands for 0.13 < x < 0.17 before shrinking again for x above x = 0.17.

The stoichiometry of UO_{2+x} sample could not be identified at the end of oxidation at 150°C, due to similarities between U_4O_9 and U_3O_7 structures. Although recent studies suggest cracking of the UO_{2+x} matrix when a layer of U_3O_7/U_4O_9 is formed [75]. Those macro-cracks were observed as soon as the oxidised layer of initial UO_2 reached a critical depth of about 0.4 μm, more than twice the thickness of the SN1191 sample used in this chapter, where not a single crack was observed under SEM microscopy. Studies performed on single crystal UO_2 by Desgranges et al. [74], showed that cracking is observed when a critical depth of U_3O_7 oxidised layer is reached.

The lack of the cracking in 160 nm thick poly-epitaxial film of UO_2, when oxidising U_3O_7/U_4O_9, confirmed by the shrink of the lattice constant can be explain in two ways. Firstly, the sample is too thin to form a critical thickness of oxidised layer to initiate cracking caused by the mismatch in unit cell parameter between the layer and initial UO_2. Secondly, the thin film is grown on YSZ substrate, which might stabilise the UO_{2+x} structure and prevent damage.

The in-situ XRD oxidation of the SN1191 sample to U_3O_8, revealed that grains with (001) orientation oxidise faster than (111) or (110), in contradiction to what was reported by Allen et al. [71, 72]. The XRD data are with good agreement to what was later observed under HT-ESEM, where grains with orientation close to (001) started disintegrating as first. Both techniques showed a unique behaviour for (001)-oriented UO_2. The kinetics of this process observed for both samples using different methods, are in very good agreement with data presented in the literature, where sigmoidal nucleation and growth mechanism of formation of U_3O_8 is reported.

CHAPTER 6

UNIQUE PHASE TRANSITION DURING OXIDATION OF SINGLE CRYSTAL UO2

The previous chapter of this thesis showed that (001) oriented grains of uranium dioxide behave differently than (110) and (111), as the oxidation rate was higher, in contradiction to literature data. To further explore the effect of orientation and better understand the phenomena observed in the(001) system, data from three differently oriented single crystals (100), (110) and (111) are presented.

6.1 Introduction

Majority of the studies on oxidation of uranium dioxide has been performed utilizing powder or polycrystalline solid [31, 205]. In those systems, effects associated with surface to volume ratio and grain size/grain boundary density have to be taken into account. To isolate the effect of the crystallographic orientation on the oxidation rate of UO_2, single crystal materials can be used.

Until today the work comparing three main orientations present in cubic ($Fm\bar{3}m$) UO_2 was done by Allen et al. [71, 72]. In their work, single-crystal specimens were polished and cut parallel to the [111] [110] and [001] faces. Those samples were oxidized in 1.3 mbar of oxygen at 300°C, together with a polycrystalline disk of UO_2 for comparison. Utilizing XRD, XPS and

SEM they found that the reactivity follows the sequence [111]>[110]>[001]>poly. The fast rate of oxidation in the UO_2 [111] direction was explained by the epitaxial match with the [001] direction of U_3O_8, and the slowest rate for polycrystalline system was explained with low tolerance for accommodation of lattice expansion.

Due to the epitaxial relationship between the U_3O_8 [001] direction and the UO_2 [111], a lot of studies were later performed and mostly focused on the [111]-oriented single crystal [86, 205, 213, 214], without providing proper comparison with remaining orientations. Since the studies conducted by Allen et al., the effect of crystal orientation on oxidation behaviour was not further investigated, and techniques for characterisation and methods for UO_2 fabrication have been improved and developed.

In this chapter, specially engineered single crystals of UO_2 were studied using in-situ techniques. The quality of the thin films was characterised in Chapter 5. Those systems provide excellent material for studies due to their very smooth surface and very good crystallinity. Firstly, in-situ data collected using HT-ESEM is presented, followed by a detailed investigation utilizing x-rays.

6.2 HT-ESEM experiment on single crystals

To investigate the effect of the crystal orientation on the oxidation process of UO_2 fuel in case of failed GDF, a specially engineered set of single crystals was used. Those samples: SN1493, SN1494, SN1495 were characterised and described in Chapter 5. They represent all three different crystal orientations possible in a cubic system: (111), (110) and (001), which are observed in a nuclear fuel. The experiment was conducted at specially designated High Temperature - Environmental Scanning Electron Microscope (FEI Quanta 200 FEG ESEM) at the Institut de Chimie Separative de Marcoule (ICSM) in Marcoule, France.

6.2.1 Experimental set-up

The recent development in the field of scanning electron microscopy, nowadays, allows for observation of materials at high magnification with a high depth of field and recording images at the

same time [126]. The standard SEM is restricted by sample requirements, such as conductivity to prevent sample charging, and to be stable under vacuum conditions. Furthermore, it is only possible to image a sample before and after treatment, such as oxidation. The new environmental electron microscopes, equipped with a hot stage, help to overcome some of those issues.

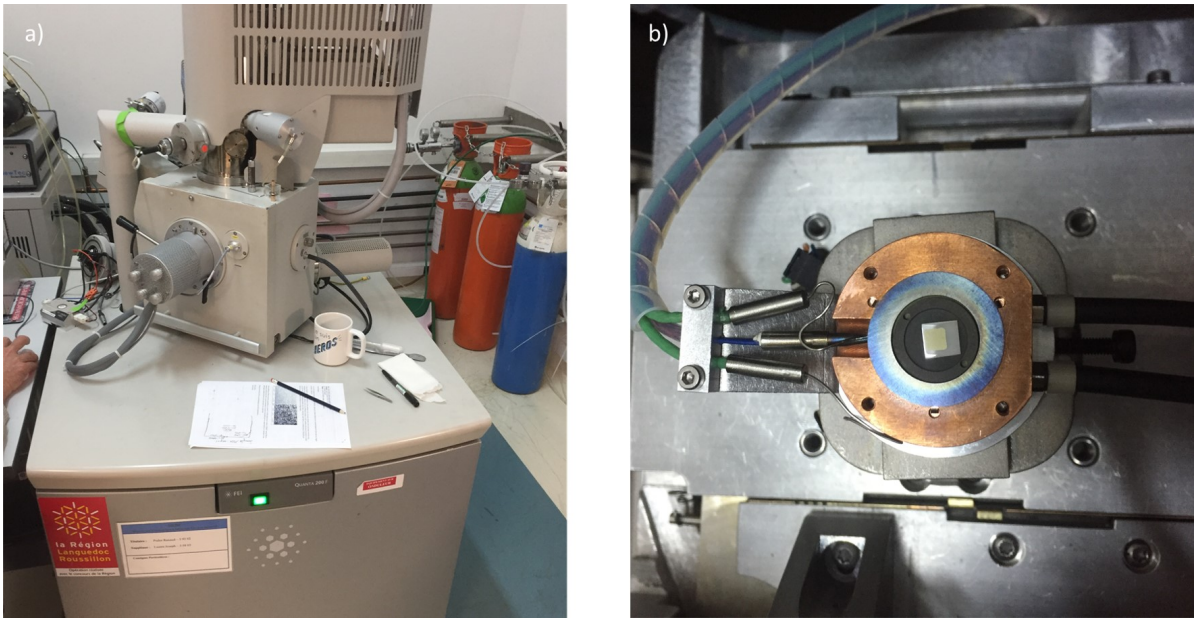

Figure 6.1: Photo (a) view on the FEI Quanta 200 FEG HT-ESEM (Thermo Fisher Scientific, Massachusetts, USA) based at ICSM in France. The heating stage, inside the microscope, with the mounted sample is shown on (b).

High Temperature Environmental Scanning Electron Microscopy (HT-ESEM) allows to work with samples that have lower conductivity as charge can be partially neutralized by gas molecules. The hot stage makes it possible to heat the sample to 1500 while still imaging the surface [215]. Combination of the possibilities to heat up a specimen and change the environmental conditions by allowing oxygen gas inside the microscope, make it an excellent tool for in-situ oxidation studies. Allowing for detailed observation of the sample surface changes during the oxidation process.

The microscope used in this experiment was a HT-ESEM at the Institut de Chimie Separative de Marcoule (ICSM) in Marcoule, France, model: FEI Quanta 200 FEG ESEM, Thermo Fisher Scientific, Massachusetts, USA. It is a scanning electron microscope fitted with a field emission gun electron source to provide high imaging resolution. This microscope operates in different

modes including environmental mode that allows to use air, pure O_2 or a mixture of O_2 and N_2. The pressure range inside the ESEM chamber can be in range between 10-750 Pa. The sample size is restricted by a 5mm circle, as shown on Fig 6.1 (b). The furnace can heat the sample up to 1200°C and be investigated under magnification between x130 to x100 000.

Procedure

The standard size of the substrate used in this experiment was $1cm \times 1cm \times 0.5mm$, which is the suitable size of the substrate holder to use with the DC magnetron sputtering system. The hot stage at the ICSM in Marcoule, France on the FEI Quanta 200 FEG ESEM allows only to mount samples that fit inside a 5 mm circle. Therefore, thin films of uranium had to be cut to make the oxidation experiment possible. In order to precisely cut a hard ceramic material, such as YSZ, and reduce damage to the thin films on top of it a diamond wire saw at the University of Bristol was used. Samples were cut first into two parts around $1cm \times 0.3cm$ and $1cm \times 0.7cm$. And next, the smaller part was cut into 3 additional rectangles.

Samples were stored in air in separate membrane boxes and transported to France. The insertion was performed in air. Samples were heated up under an atmosphere of oxygen of 350 Pa. Fig 6.1 shows images of the microscope chamber at room temperature, 300°C, and 800°C. Once the signs of the oxidation were visible, heating was stopped. A sample edge region, to study flat surface, be able to focus and see the edge effects, was continuously monitored for the entire length of the experiment and images were recorded every 3 to 5 s. All pictures were recorded with the same magnification of x250, corresponding to an area of 512 x 470 μ m^2.

Figure 6.2: Images of the FEI Quanta 200 FEG ESEM chamber taken at different temperatures: (a) room temperature, (b) 300°C, and (c) 800°C.

The Fiji ImageJ [216] software was used to analyse the surface changes during the sample treatment. The sample surface cracking due to oxidation and further expansion of the crack propagation was monitored by measuring the percentage of the damaged surface to the entire ROI. Background of each photo was crated using the Gaussian-blurred image version of the image. So extracted background was then subtracted from every image. To enhance the contrast between the oxidised and the pristine areas of the sample, a series of *find edges* and *smooth* function were used. In the next step *Gaussian-blurred* or *Medina* filters were applied. In the final step, the areas were found by choosing a threshold level in the image values contract, allowing the pristine region to be below the threshold.

6.2.2 In-situ HT-ESEM Oxidation

6.2.3 Results

Sample SN1493: (111) UO_2 / (111) YSZ

The in-situ HT-ESEM oxidation of a 100 nm single crystal (111)-oriented thin film of UO_2 was performed at oxygen partial pressure of P_{O_2} = 350 Pa. The acceleration voltage was kept constant at 20 kV and images were taken every 3 to 5 s. Fig 6.3 shows the pictures taken before oxidation started and at different stages of the oxidation process. The first image of the sample SN1493 Fig 6.3 (a) shows surface of the sample with visible edge, and the rough edge of the YSZ substrate. The area with a small dust particle was chosen in order to be able to focus the microscope. As the temperature was very low (close to room temperature), shielding of the detector was not required. Therefore the brightness/contrast looks slightly different than on the other images, were due to high temperatures (above 500°C) the detector shielding was necessary.

The fist signs of the oxidation were visible at temperature of 568°C. A tiny crack appeared almost at the center of the ROI. Heating was stopped and the temperature stabilised at 585°C for the rest of the experiment. This crack can be see on Fig 6.3 (b). Then another crack appeared and the oxidation started spreading from those cracks causing disintegration of the sample due to volume expansion associated with phase transition from UO_2 to U_3O_8, which is shown on Fig 6.3 (c). With time, more cracks appeared and disintegration process accelerated which can be seen on

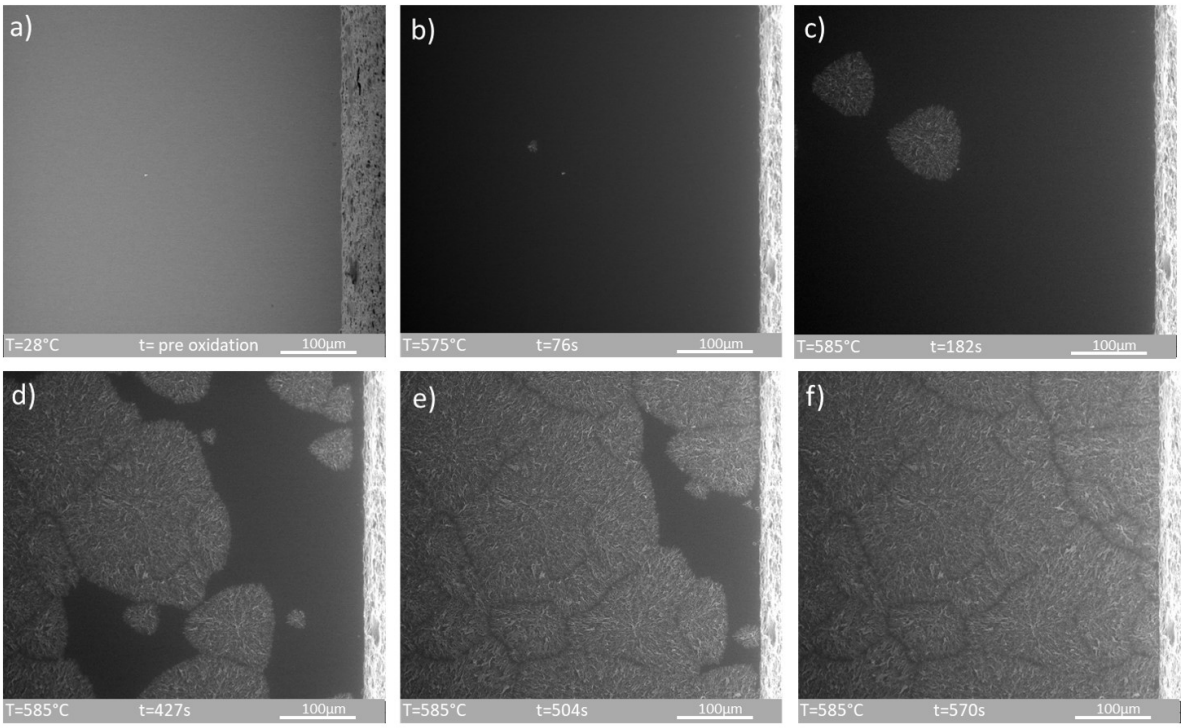

Figure 6.3: Images taken using FEI Quanta 200 FEG ESEM during the in-situ oxidation of the sample SN1493 at different times. The surface of the (111)-oriented single crystal of UO_2 thin films before oxidation is visible on image (a). Beginning of the oxidation and the associated cracking is shown of image (b). The two fronts of the disintegration from two cracks are presented on image (c). Image (d) shows disintegration process, when some of the fronts met and when still new cracks appear. The situation when most of the oxidation fronts are terminated is shown on image (e). The surface after complete oxidation is presented on image (f). Images were taken at ambient pressure of oxygen P_{O_2} = 350 Pa, and acceleration voltage 20 kV. (Video: https://figshare.com/s/9fee93dad9473a5b68f2)

Fig 6.3 (d). Once most of the oxidation fronts met, which is shown on Fig 6.3 (e) the disintegration process was retarded. The sample surface after complete oxidation is visible on Fig 6.3 (f). The total time needed for this process was 9m 16s, and on the visible area of 512 x 470 μ m^2 of UO_2 the total amount of cracking point is 20.

Using the Fiji ImageJ [216] software kinetics of the reaction were extracted by finding the percentage of the disintegrated area. The percent of oxidised area against time for (111) oriented thin film of UO_2 (SN1493) is plotted of Fig. 6.4. To fit this data the logistic function was used, where the logistic growth rate of the curve, k was found to be 0.0143 ± 0.0003, with midpoint x_c = 391 ± 2. The kinetics found during the in-situ HT-ESEM oxidation for SN1493 follow

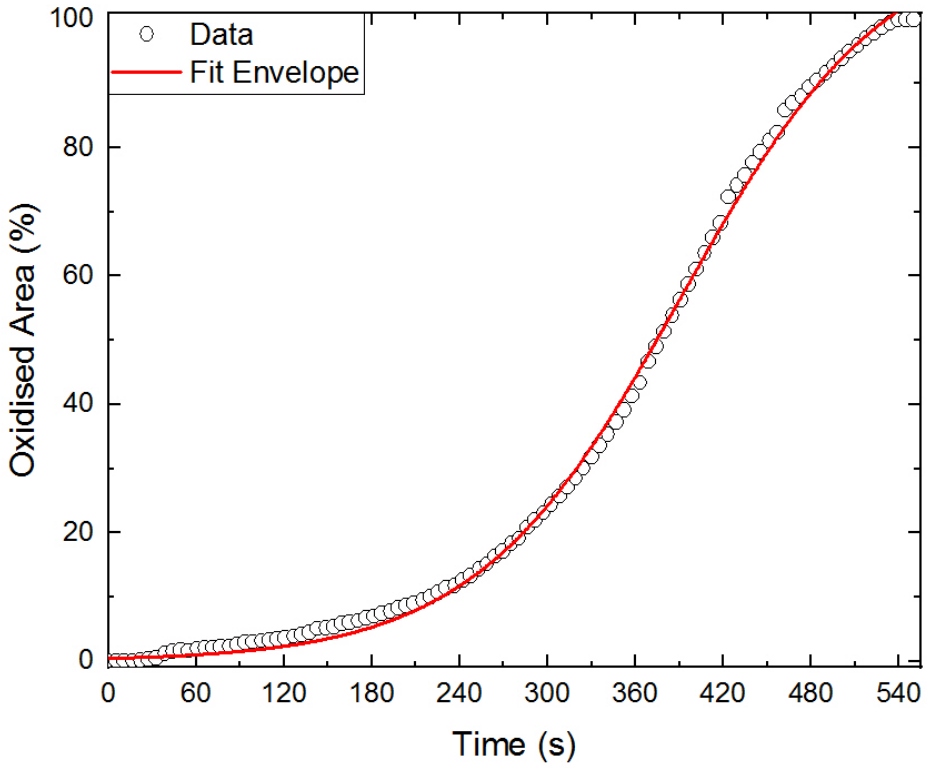

Figure 6.4: Percentage of the disintegrated area associated with the U_3O_8 against the time for SN1493 (111) oriented UO_2. Black circles represent the data, and their size is associated with the error. The logistic fit is represented by solid red line. Sample exhibits sigmoidal kinetics, typical for this reaction.

the well known mechanism of sigmoidal nucleation-and-growth of U_3O_8 reported in literature [70, 172, 197, 217–222], with clear initial very low oxidation followed by increase of oxidation rate up to a maximum, and decrease when the reaction approaches completion.

Sample SN1494: (110) UO_2 / (110) YSZ

The same procedure was applied to sample SN1494, the (110)-oriented single crystal thin film of uranium dioxide. Sample was loaded into the microscope chamber and heated up at oxygen ambient pressure of P_{O_2} = 350 Pa. Images of the sample were taken every 3 to 5 s at the acceleration voltage of 20 kV. In order to be able to focus well on the smooth surface of UO_2 thin

film, an edge with couple tiny particles was chosen as region of interest. The total visible area of the thin film sample was 515 x 470 μ m^2.

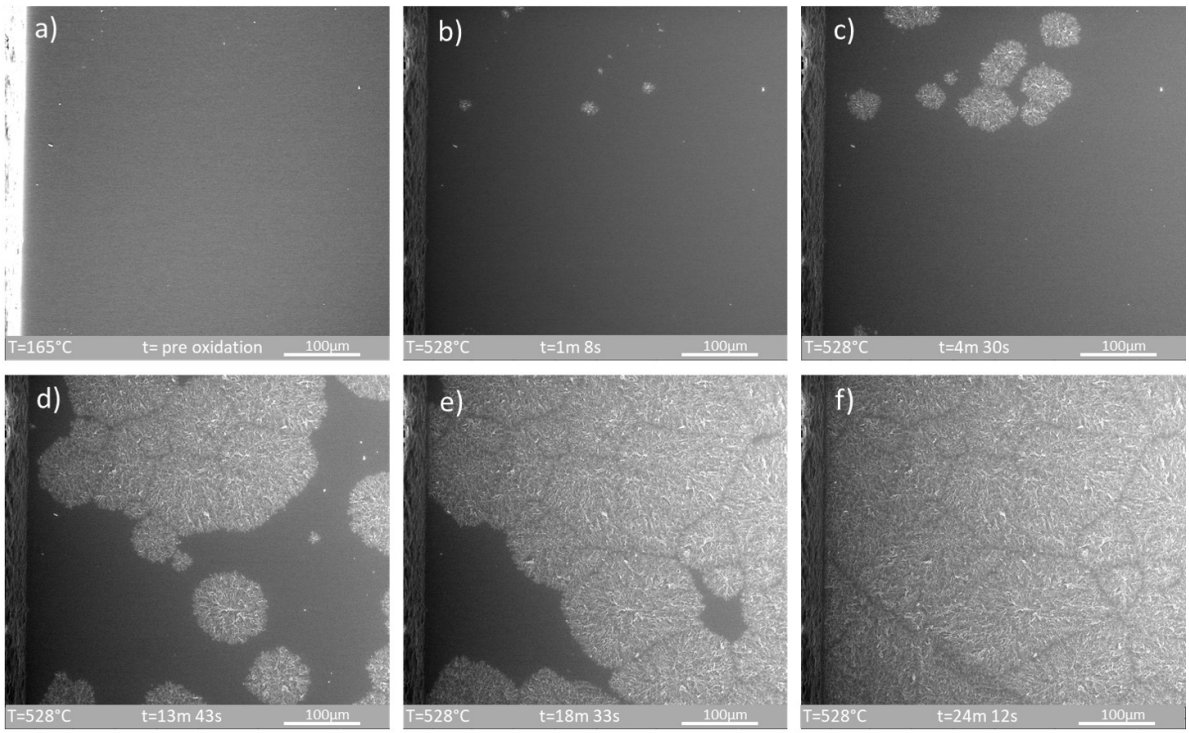

Figure 6.5: Images of sample SN1494 taken at different stages of HT-ESEM in-situ oxidation experiment. The fist image (a), taken at 165 °C, shows the area of the sample prior to the cracking. The seven first points were oxidation started are shown on image (b), the temperature at that point was 528 °C. Cracking fronts from those points are shown on image (c), where most of the sample is still intact. The surface of the sample after almost 14 m is presented on images (d), were some of the oxidation fronts terminated and still new oxidation fronts are emerging. Most of the cracking fronts is complete after 18 m what is shown on image (e), although some part of the sample is still undamaged. The total disintegration of the sample is visible on the last image (f), the time required for that to happen was 23 m and 12 s. (Video: https://figshare.com/s/05408e5fd48e60f2bc66)

The image of the sample before insertion of the detector shielding is shown on Fig 6.5 (a). The temperature inside the chamber is 165 °C and no signs of oxidation are visible. The first cracks caused by oxidation were noticed at 519 °C, and it started at few spots within seconds. Fig 6.5 (b) shows the sample surface just after 1 m, at 528 °C, where 7 oxidation centres are observed. The progression of the cracking fronts, after around 3 m, from those points can be seen on Fig 6.5 (c). The next image Fig 6.5 (d) taken after 13 m 43 s after oxidation started, at 528 °C, shows

termination of some of the cracking fronts and appearance of new oxidation points. After 18 m most of the sample was disintegrated into flakes, and some regions were still undamaged which is presented on Fig 6.5 (e). The fully oxidised structure of the sample SN1494, where all the thin films disintegrated into flakes is visible on Fig 6.5 (f). The total time necessary to fully oxidise an area of 515 x 470 μ m^2 of the (110)-oriented single crystal of UO_2 thin film at oxygen pressure of P_{O_2} = 350 Pa. and temperature of at 528 °C was 23 m and 12 s.

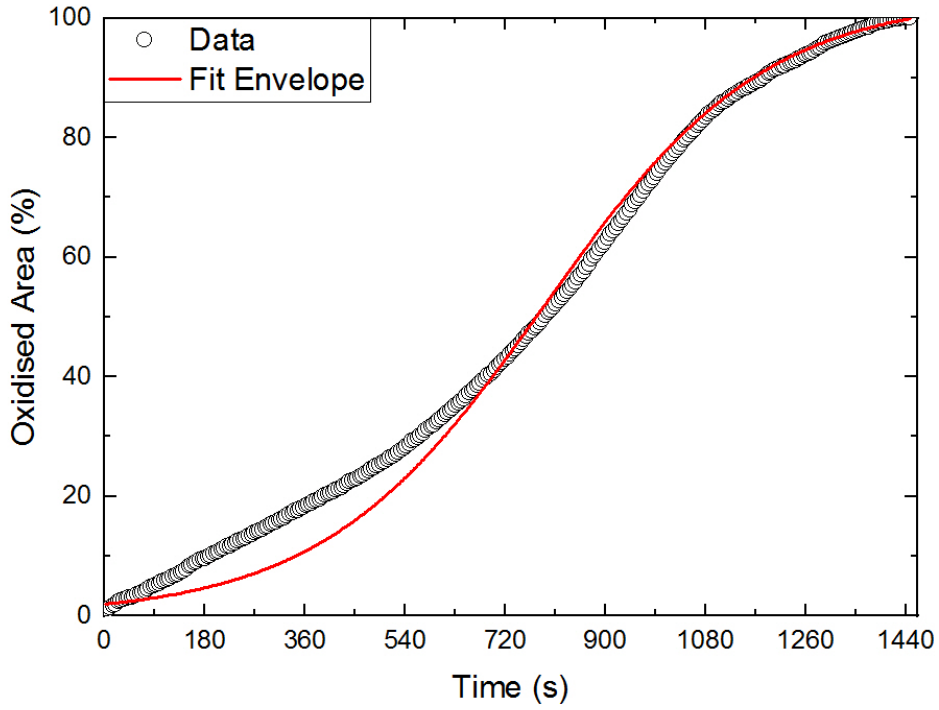

Figure 6.6: Kinetics for the oxidation of (111) oriented UO_2 to U_3O_8. Black circles represent the data, and their size is associated with the error. The logistic fit is represented by solid red line. The sigmoidal mechanism does not fit well, especially during the induction period.

The same procedure utilizing Fiji ImageJ software was used to extract the oxidation rate for SN1494, the (110) oriented single crystal thin film of UO_2. The kinetics of this reaction do not agree with the sigmoidal nucleation-and-growth formation of U_3O_8, which can be seen of Fig. 6.6. The same logistic function that was used to fit well the data for the (111) oriented sample does not match the data obtained for (110) oriented UO_2, suggesting influence of the crystal orientation

on the oxidation rate. Furthermore, the time needed to fully oxidise this sample (SN1494) at 528 °C is 2.5 times longer than time needed for the SN1493 at 585°C.

Sample SN1495: (001) UO_2 / (001) YSZ

The last sample SN1495 (001) oriented single crystal of UO_2 was also exposed to oxygen ambient pressure of P_{O_2} = 350 Pa, and heated up while taking images each 3 to 5 s at 20 kV acceleration voltage. Again, an area on the edge of the sample, with tiny contamination (dust/ leftovers from cutting process) was chosen for better focusing purposes. The total investigated area was 512 x 472 μ m^2, which can be seen on the Fig 6.7 (a) image of the sample prior to the oxidation process.

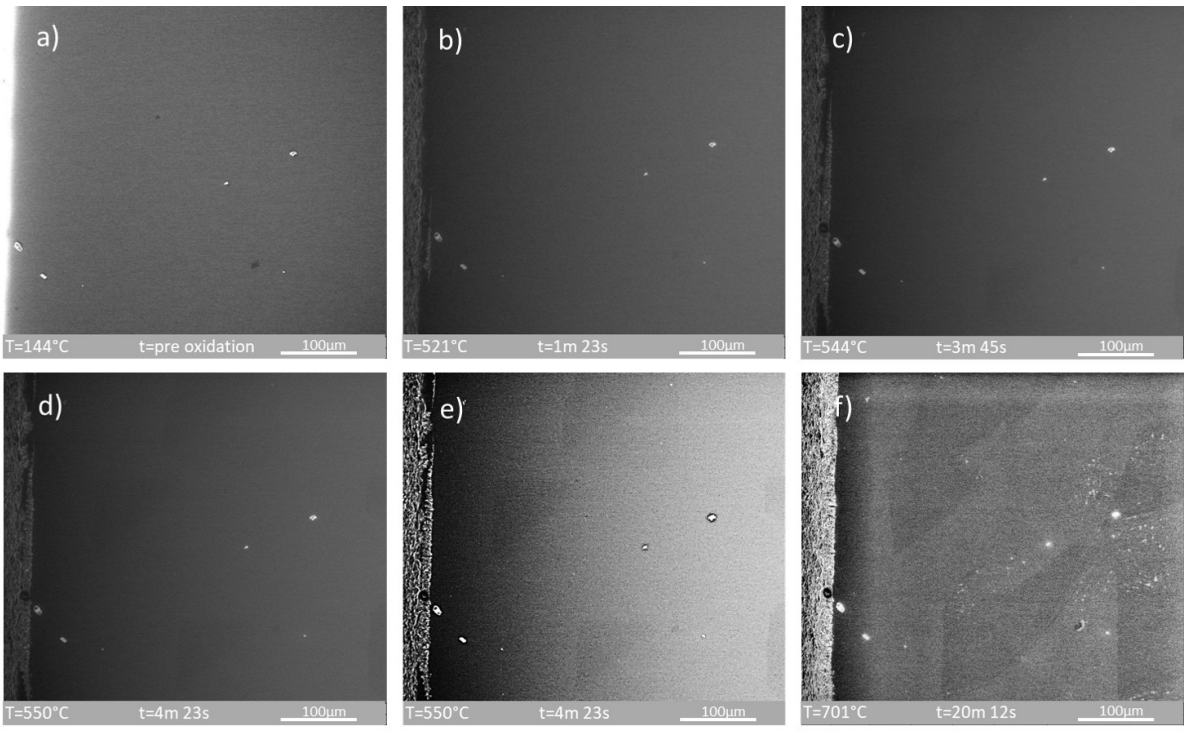

Figure 6.7: Images of sample SN1495 taken during in-situ HT-ESEM oxidation experiment. Surface of the sample before oxidation is visible on image (a). The first signs of oxidation (b) are visible at the edge of the sample at 521°C after 1m and 23s. With time, further oxidation is visible at the sample edge, and formation of triangular shapes is observed (c). The image (d) taken after 4m 23s was enhanced (e) using CLAHE method, to show formation and growth of triangular shapes. Surface of fully oxidised sample after enhancing contrast with CLAHE is shown on image (f). (Video: https://figshare.com/s/c29794e503fbe7fdcb20)

This time, changes caused by oxidation were not as pronounced as in the two previous cases. Therefore, it was not possible during the experiment to clearly state at what point the oxidation started and to stop the heating. As a result, the final temperature that the sample SN1494 was exposed to was 701°C. Even at such a high temperature, there were no signs of thin film disintegration. The only cracking can be observed at the edge of the sample, where a single crystal structure might not be maintained and a lot of defects are present. The first signs can be spotted on Fig 6.7 (b), very close to the edge, and spreading along the edge over the exposure time. Changes in the main area of the sample as a darker triangles are shown on Fig 6.7 (c) and (d). To better illustrate those changes Fig 6.7 (e) was created by enhancing the brightness and contrast of Fig 6.7 (d), by using Fiji software. The final image of the oxidation experiment of the sample SN1495 is shown on Fig 6.7 (d). The local contrast on this image was enhanced using the Contrast Limited Adaptive Histogram Equalization (CLAHE) method [223].

The sample SN1495 (001) behaved in a completely different way than SN1493 (111) and SN1494 (110). Excluding the thin line at the edge on the thin film, no other part of the surface exhibited any signs of cracking. The UO_2 underwent transformation from fluorite cubic structure to orthorhombic structure of U_3O_8 maintaining the structure integrity, even due to the volume expansion associated with this phase transition. The nature of observed changes suggest creation of (130)-oriented domains of U_3O_8 single crystal.

6.2.4 Discussion

The role of the crystallographic orientation on the oxidation behaviour of uranium dioxide was investigated in-situ using HT-ESEM, on three specially engineered epitaxial thin film samples with different crystal orientations: (001), (110) and (111). For each sample a series of images over time of exposure were recorded along with temperature and oxygen pressure inside the chamber. Images were recorded at acceleration voltage of 20 kV and magnification of x250. Experiments were conducted at ICSM in France on FEI Quanta 200 FEG HT-ESEM.

The in-situ oxidation of samples SN1493 (111), SN1494 (110) and SN1495 (001) showed that the initiation starts at different temperatures. The lowest temperature to initiate the oxidation process was observed for sample (001) oriented sample at 518 °C. Signs of oxidation could be

visible at the edges of the sample where high amount of defects were present and material did not adhere well to the substrate. Another indication were the visible changes after enhancing contrast of the images. Those appeared as small triangles/pyramids and increased their size until their edges met, which was shown on Fig 6.7 (e-f). The time needed to oxidise the ROI of 515 x 470 μ m^2 was 8 minutes and 9 seconds. The second orientation to exhibit signs of oxidation was (110), and the cracks in the structure started appearing at 528°C. As the sample surface was smooth and without visible defects in the spots where the cracking started, it might suggest that the oxidation starting points were random. The total time needed for full disintegration of the sample surface of 515 x 470 μ m^2, was 23 m and 12 s. For the (111) oriented sample no signs of oxidation were visible until the temperature inside the chamber reached 568 °C. A similar process, with different dynamic, to (110) oriented sample was observed, this sample started oxidising at random points from which cracking was progressing. A total time of 9m and 16s was needed to fully oxidise the sample.

This experiment showed that two different oxidation mechanisms can be distinguished. The first one shared between (111) and (110) crystal orientation of UO_2, where the volume expansion of 36% associated with formation of U_3O_8 leads to disintegration of the structure. Outbreak of cracking are observed at multiple random spots, from which it spreads to the entire sample surface. Although, the dynamic in those two cases is different, what is shown on Fig 6.8. This figure presents percentage of the oxidised area of the sample to total area of the sample. As it can be seen, (111) oriented sample exhibits first the induction period, where the cracking spots start appearing followed by increased oxidation rate up to the maximum when the oxidation progresses from those points and disintegrates the structure. By the end, when most of the cracking fronts are terminated, and only a small area of the sample remained intact, the process slows down and the oxidation curves tails off.

As shown on Fig. 6.6 the logistic function used to describe the kinetics of nucleation-and-growth mechanism for U_3O_8 from (110) single crystal of UO_2 does not fit the data well, and was substituted with the linear fit divided into three regions. The first region, called the induction period, was set to be from 0 to 470 seconds and fitting with linear function gave the slope of 0.049 ± 0.003. The second region with the fastest oxidation rate was set for fitting in range 570-1060

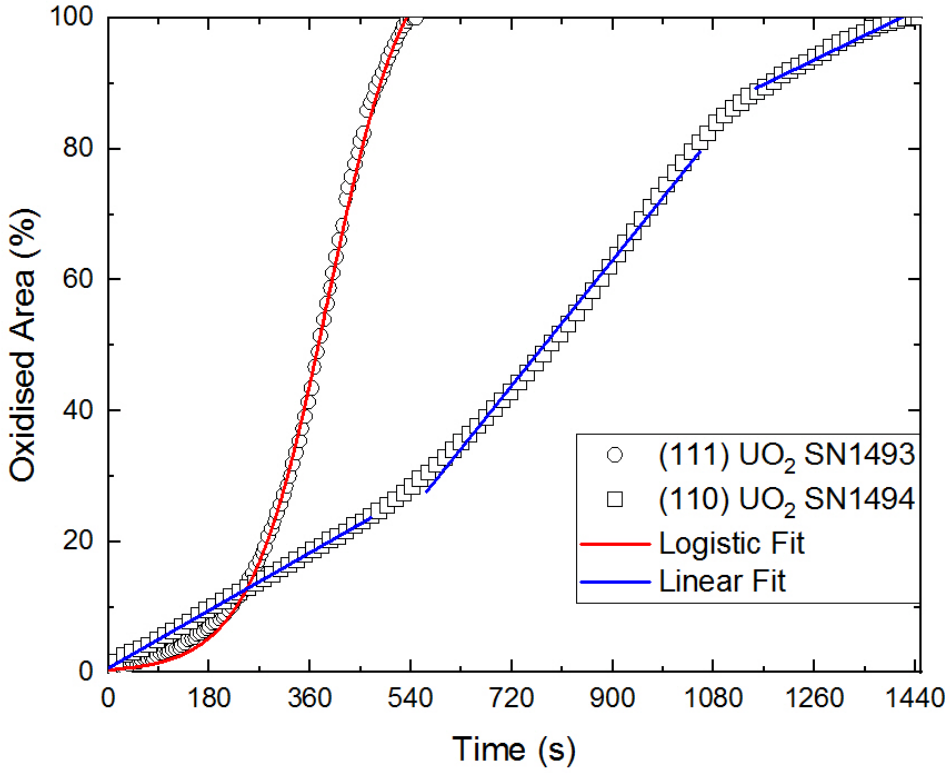

Figure 6.8: Comparison between the oxidation kinetics observed for (111) (circles) and (110) (squares) oriented single crystal of UO_2. For clarity, only each third data point is shown for the (110) oriented sample. The fits are represented with straight lines, where red is for logistic fit and blue for linear. The first sample exhibits sigmoidal growth, while the second exhibits different behaviour at the induction period, and the total time need for oxidation is much longer.

seconds , and the slope was 0.106 ± 0.018. This indicated that oxidation in this region is 2.16 times faster than at the beginning of the process. The third region 1150-1447 had a slope of 0.042 ± 0.008, which is very similar to the starting rate.

A unique behaviour is observed for the (100) oriented epitaxial thin film of UO_2 on YSZ substrate. The sample does not disintegrate while exposed to oxygen at high temperatures, instead formation of domain is observed. This suggests that the volume expansion associated with formation of U_3O_8 can be accommodated in the new structure without loss of integrity. This specific orientation was further investigated using a hot stage mounted on x-ray diffractometer for in-situ studies, what is described in the next part of this chapter.

6.3 In-situ XRD oxidation

6.3.1 Experimental set-up

The in-situ oxidation experiments were performed using a PANalytical X'pert diffractometer at the School of Physics (IAC), University of Bristol. The X-ray source of this diffractometer has a coper node, and set of filters, allowing only two Cu wavelengths K_{α_1} = 1.54060Å and K_{β_1} = 1.54443Å. The environmental chamber used for those studies was Anton Par HTK 1200, with possibility to heat up sample up to 1200 °C under a vacuum, and with an inlet allowing for a gas insertion. The detailed description of this set-up can be found in Chapter 3.

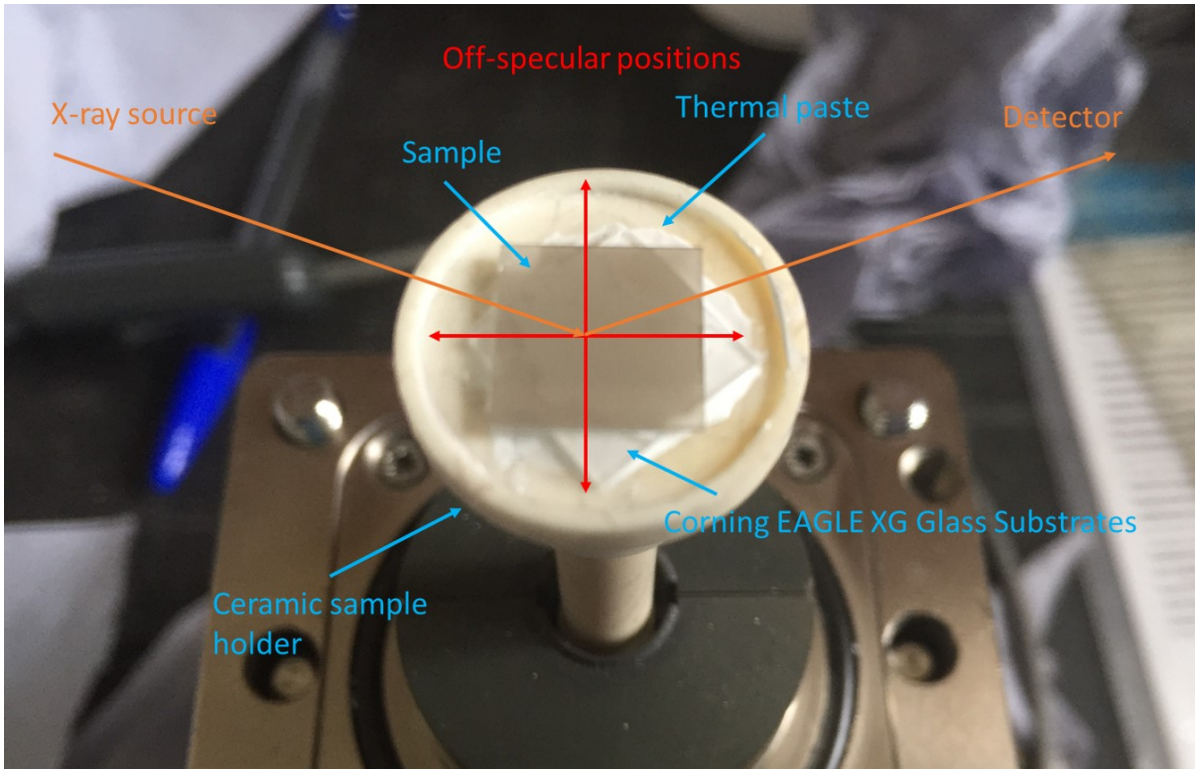

Figure 6.9: Set-up of the sample holder for Anton Paar HTK 1200 chamber.

Samples were mounted in the way shown on Fig 6.9. First on the ceramic sample holder for Anton Paar HTK 1200 chamber, a Corning EAGLE XG Glass Substrates (MTI) was stuck using heat conducting grease (Anton Paar) and a lot of pressure was applied to make sure that the substrate sits as flat as possible. Such sample elevation is required, otherwise the sample surface level would be below the level of the sample stage holder, and x-ray reflectivity measurements

as well as precise alignment of the sample would not be possible. The angle between the glass substrate and the sample was around 45 °, to facilitate sample removal process.

To mount the sample on the glass substrate again, the heat conducting grease was used, and special care was taken to make sure that the sample sticks as flat as possible to the sample holder. As there is no possibility to control the spinning of the sample stage, samples were aligned in between x-rays source and detector, in the way to make observation of off-specular vectors from (001) oriented thin films of uranium dioxide possible.

Procedure

Prior to the oxidation studies, all samples were characterised on the Open Eulerian Cradle stage, for better quality of the data due to higher x-ray intensity and possibility of aligning sample in χ. Once the sample was mounted on the sample holder, the holder was inserted into the chamber, and secured using four screws. The system was pumped out first for around an hour using an oil pump and, additionally overnight with a turbomolecular pump to reach a vacuum of low 10^{-4} mbar. Then samples were heated up to the required temperature, and additional time was allowed to let the temperature stabilise. During heat up, the chamber was always under vacuum, provided at lest by a rotary pump.

When the temperature stabilised, another alignment of the experimental set-up was required due to the thermal expansion of the components. Height of the sample was adjusted using half-cut method, and new omega offset was applied every time. Then a series of scans were taken to define the starting parameters at each temperature, before introducing oxygen gas to the chamber. After letting oxygen into the system, scans were taken every hour.

At the end of the XRD in-situ oxidation experiment, oxygen was pumped out and samples were cooled down under vacuum at room temperature. The hot chamber was then replaced with the Open Eulerian Cradle stage, and a series of scans were conducted in order to determine the final parameters of the samples with higher quality, than the quality obtained at the hot stage set-up.

6.3.2 Oxidation and characterization of (001) UO_2

The mechanisms proposed for the phase transition from UO_2 to to U_3O_8, after initial formation of U_3O_7/U_4O_9 shows a volume expansion of 36% [179]. In studies conducted to this day, this volume increase is associated with loss of the UO_2 matrix integrity [31, 70]. Although, as shown previously the (001) oriented epitaxial thin film of UO_2 on YSZ substrate, does not disintegrate after exposure to oxygen at elevated temperatures.

This suggests an epitaxial relation between hyperstoichiometric UO_2 and U_3O_8, that allows for coexistence of one phase on another. The mechanisms proposed by Allen et. al. [187] indicate a relation between the cubic close-packed (111) plane of UO_2 and the (001) basal plane of the layered orthorhombic U_3O_8. However, these models are not satisfactory due to symmetry break in the hexagonal uranium sub-lattice of the (111) plane [224], and does not match the system observed in previous HT-ESEM studies.

To further investigate the unique behaviour of the (001) oriented single crystal thin film of UO_2, grown using a DC magnetron sputtering system, on YSZ substrate, a series of XRD in-situ experiment were performed. The primary goal of this experiment is to find the epitaxial relationship between (001) oriented UO_2 and U_3O_8, which will be described in the first part of this section. The second objective is to provide detailed description of the kinetics and mechanism behind the formation of U_3O_8 without loss of integrity to the sample matrix.

Fig. 6.10 shows XRD data collected for a 50 nm thick film of (001) oriented single crystal UO_2 before (a, b), and after oxidation (c, d). As shown on a longitudinal $\omega - 2\theta$ scan prior to oxidation (Fig. 6.10 (a)) only two peaks with high intensity are present, corresponding to (002) reflections from UO_2 and YSZ. This XRD profile was modelled using two asymmetric Pearson VII functions to fit the Bragg peak arising from the thin film and YSZ substrate. The central Bragg peak positions were extracted from those fits, which allowed to calculate specular lattice parameters for the thin film and substrate, which are 5.46 ± 0.03Å and 5.15 ± 0.02Å respectively.

The single crystal character of the sample is suggested by presence of only one reflection family, with high intensity. To confirm that this system is a real single crystal an off-specular scan was performed and the data is shown on Fig. 6.10 (b). The peaks exhibit expected four fold symmetry with 90°spacing, and relative position of the peaks from the sample and the substrate

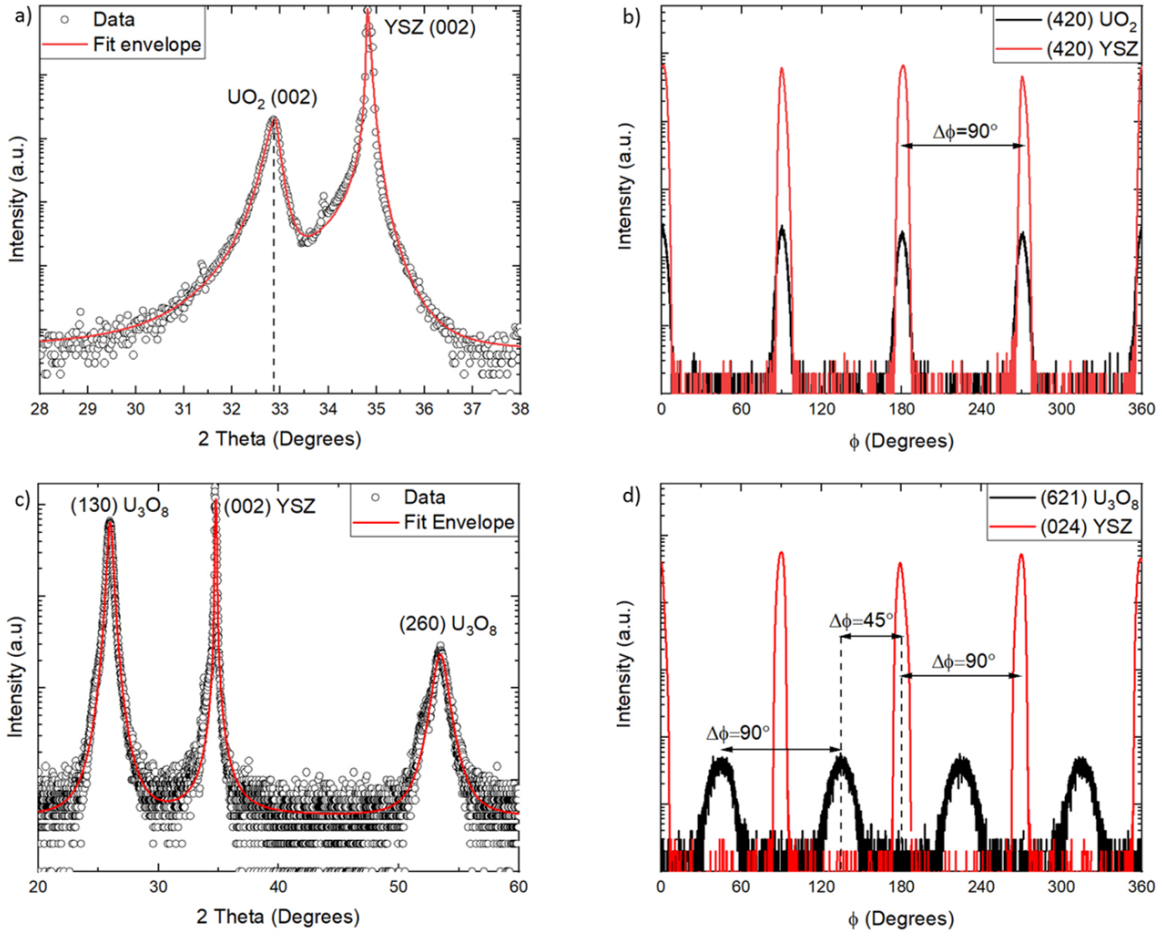

Figure 6.10: XRD scans of 50 nm (001) oriented thin film of UO_2 (SN1627) before and after oxidation. The first longitudinal $\omega - 2\theta$ scan (a), shows high intensity peaks for (002) reflections from both, the thin film and the substrate. The off-specular scan with four fold symmetry (b), confirms it single crystal nature. Scans taken after oxidation (c) and (d) show formation of single crystal orthorhombic U_3O_8 with 45°rotation to the substrate planes.

showed a cube on cube match.

The high angle scan of the same sample, taken at open eulerian cradle stage and after the oxidation experiment at room temperature are shown on Fig. 6.10 (c) and (d). The new peaks arising close to 26°and 53.4°were fitted using Pearson VII functions, while for the sharper peak from the substrates a pseudo-Voigt function was used. Based on the central Bragg peak position from those model, the lattice spacing was calculated for the U_3O_8 which was 3.428 ± 0.006Å and 1.713 ± 0.006Å and those peaks were assigned with the (130) and the (260) planes respectively. The values reported for bulk material [225] are 3.429Å and 1.714Å, which is in great agreement

with the data from the measured samples. The position of Bragg reflection associated with the YSZ substrate remained unchained giving the same lattice parameter of 5.15 ± 0.02Å, what indicates no changes to the substrate during the oxidation process.

The off-specular scan shown on Fig. 6.10 (d) reveals two very important details about the formation of U_3O_8 from (001) oriented single crystal of UO_2. Firstly, the presence of off-specular reflection indicates a single crystal nature of orthorhombic (130) α-U_3O_8 structure. This is observed for the first time, that a single crystal of UO_2 can undergo non destructive phase transition to a single crystal of U_3O_8. Secondly, the epitaxial relationship between the (00l) YSZ and (130) U_3O_8 planes was extracted from this scan and the average separation angle between film and substrate was found to be $\Delta\phi$=45°.

Illustration of this epitaxial relationship is shown on Fig. 6.12. Its a view on the (001) plane of UO_2 (blue dash line), where uranium atoms are represented as gray spheres. Two possible arrangements of the (130) plane of the U_3O_8 structure on the (001) plane of UO_2 are indicated by the red and green dashed lines. Due to very similar structures of UO_2 and YSZ, the same model applies also to the epitaxial relation between (001) YSZ and (130) U_3O_8.

The calculation conducted for UO_2 with lattice spacing of 5.47Å shows that the strain between U_3O_8 and UO_2 on the shorter axis is 1.07 %, while on the longer axis is 7.26 %. That suggests this is more preferential than on the YSZ structure, where the associated stain would be 7.36 % and 13.93% respectively. Furthermore, when the cubic UO_2 structure absorbs oxygen forming U_4O_9/U_3O_7 shrinks, and if we take the values measured even at 150°C 5.41Å, the strain in between this layer and U_3O_8 is slightly higher 2.2 % and 8.46 %. Therefore, from the strain point of view, the preferential way of U_3O_8 structure is on UO_2. The lowest stress would be obtained for the cubic structure with lattice spacing of 5.86Å, in which case the strain would be -5.65 % and 0.13 %, where minus indicates that bottom layer is wider than the U_3O_8 shorter axis on (130) plane.

6.3.3 Detailed in-situ studies of phase transition from (001) UO_2 to (130) U_3O_8

For a better understanding of the oxidation process responsible for the formation of (130) single crystal, layered orthorhombic U_3O_8 from (001) oriented single crystal of cubic UO_2, a series of

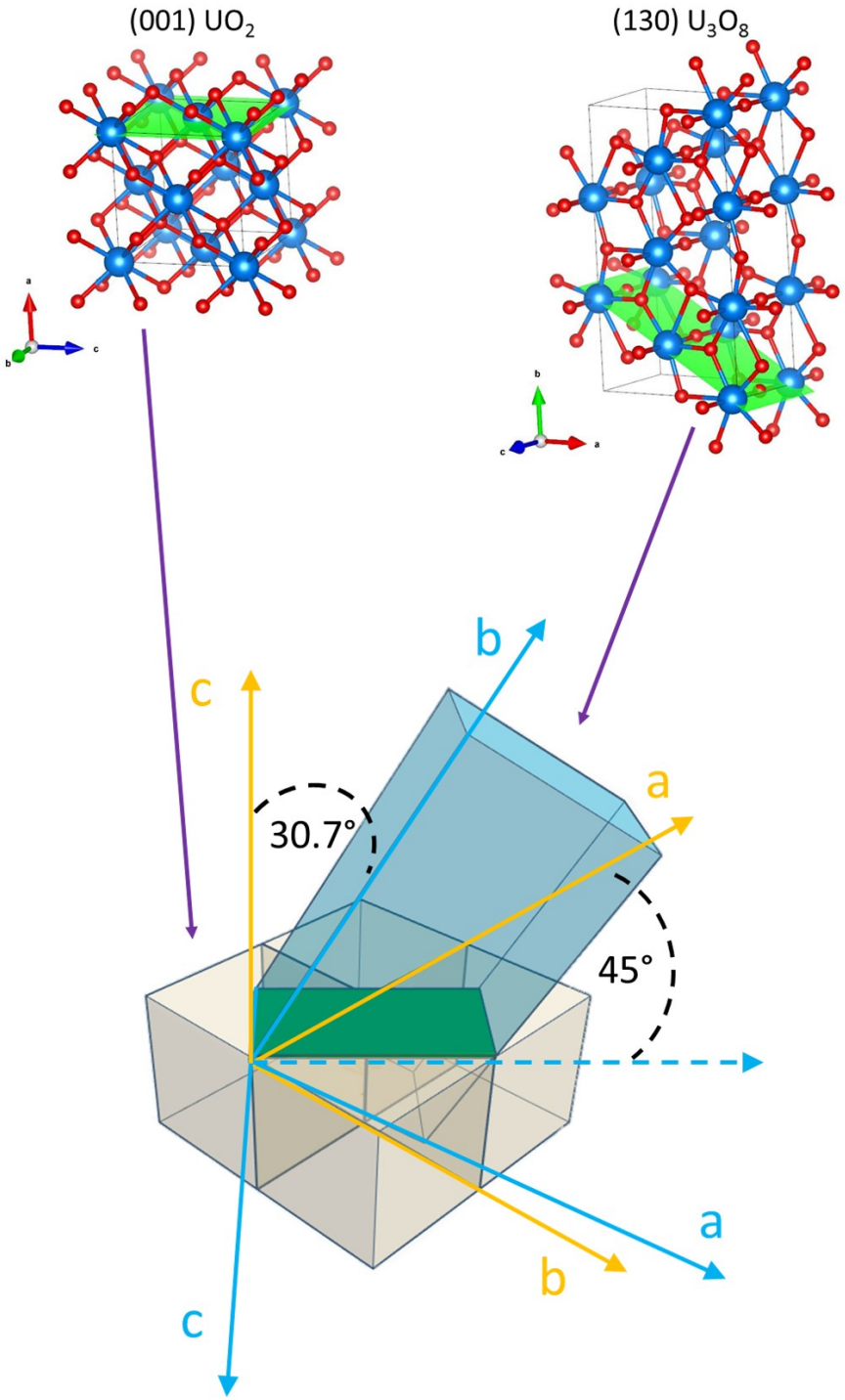

Figure 6.11: Schematic representation of epitaxial relationship between the (001) plane of UO_2 and the (130) plane of U_3O_8. Atoms of uranium are represented by the blue spheres, and oxygen atoms by the red spheres.

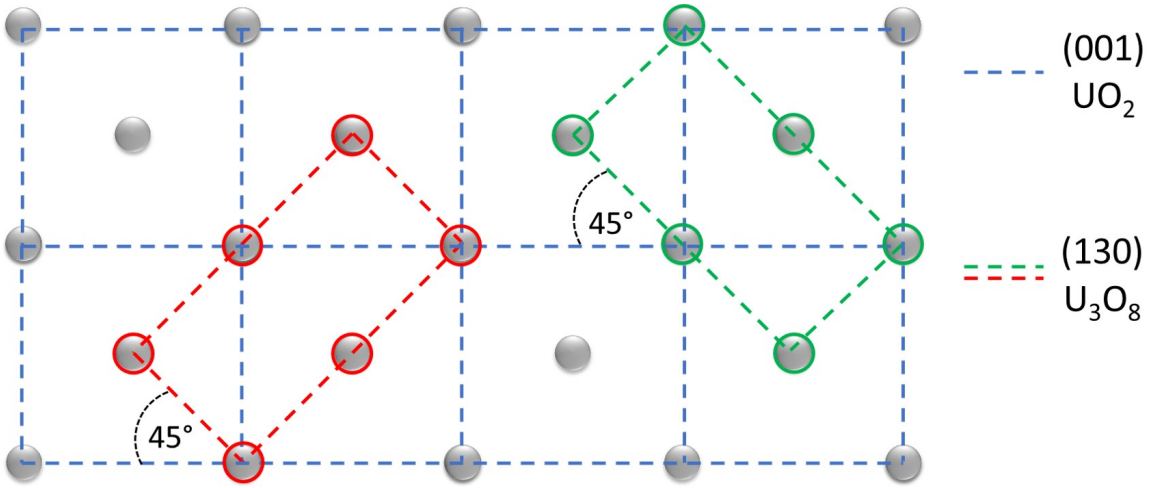

Figure 6.12: Atoms of uranium are represented by the gray spheres. Blue dash lines show the cubic structure of the UO_2 (001) phase. The red and green lines represent possible arrangement of the (130) plane of U_3O_8 on top of UO_2.

samples were oxidised in-situ. Those samples were SN1535, SN1614 and SN1627, with thickness of 100nm, 20nm and 50nm respectively. Samples were characterised by conducting high angle scan, off specular scan and rocking curves. In addition and where possible, x-ray reflectivity measurements were performed.

In the first step of the in-situ oxidation experiment, samples were exposed to 150°C. The temperature was increased up to 150°C in 15°C steps with the chamber evacuated all the time using oil and turbo pump. When temperature reached 150°C, the system was left under vacuum for an hour to let the temperature stabilise. The scan taken at 150°C prior to introduction of oxygen into the system is shown on Fig. 6.13 with black colour. The red and blue colours show the diffraction pattern collected after exposing the sample to 200 mbar of oxygen for in total 10 minutes and 30 minutes, respectively.

To fit the data an asymmetric Pearson VII function was used, and the lattice spacing was calculated based on the central positions of the Bragg peaks. The lattice parameter was found to be 5.46 ± 0.01Å for the sample at 150°C prior to oxidation. The data measured after exposing the sample to oxygen for 10 minutes (red) was fitted using two peaks. The first one associated with leftovers of UO_2 structure that did not oxidized yet into U_4O_9/U_3O_7, gave the same lattice spacing as the starting point as expected. From the second component of the fit envelope related

to the U_4O_9/U_3O_7 structure, the lattice spacing was calculated to be 5.41 ± 0.02Å. This behaviour is typical for oxidation of UO_2 which lattice spacing shrinks with increasing the amount of oxygen absorbed into the structure. The measurement taken after 30 minutes of the sample being exposed to 200 mbar of oxygen at 150°C (blue colour), shows the full transition from UO_2 to U_4O_9/U_3O_7 .

The higher angle data collected from the (004) Bragg peak was modelled also taking into account contribution from $K_{\alpha_2} = 1.5444$Å additionally to $K_{\alpha_1} = 1.5406$Å, as the difference at the peak spreading at high angles becomes more noticeable. That was labelled as a short dot line and dot line respectively.

A general trend with peak position moving to the higher angle is observed. This is associated with shrinking of the cubic UO_2 lattice parameter due to incorporation of additional oxygen and formation of U_4O_9, then transition to tetragonal structure of U_3O_7. As it can be seen on Fig. 6.13 10m is not enough to fully oxidise the thin film and two phases are visible. Half an hour was sufficient to incorporate the maximum possible amount of oxygen into the sample structure at 150°C. Further exposure of the sample at this conditions did not show any changes to the structure.

The possibility of obtaining two cubic structures of uranium oxide with different stoichiometry is important from a semiconductor point of view. Based on oxidation level of UO_{2+x} it can be either p-type or n-type material. As only part of the sample thin film has higher amount of oxygen, that leads to creation of n-p junction.

Oxidation of UO_2 to U_3O_8 is a two step process, where in the first step the tetragonal oxide of composition $UO_{2.34 \pm 0.03}$ is formed [41]. This was observed for the UO_2 thin film samples at temperatures below 300°C and pressure 200 mbar of oxygen. Due to the limited resolution of the equipment, huge similarities between the U_4O_9 and U_3O_7 structures [187], and uncertainties about their crystal structure [31, 41, 45, 73], it is almost impossible to distinguish between those two phases. The recent model proposed by Rousseau et al. [70] indicates that formation of the cubic U_4O_9 phase occurs prior to the formation of tetragonal U_3O_7, in contradiction to what was previously reported [41, 46, 172]. Nevertheless, the shift in the XRD to the higher angle (Fig. 6.13) indicate a decrease of the lattice parameter, what was calculated to be 0.67 ± 0.05 %, and it

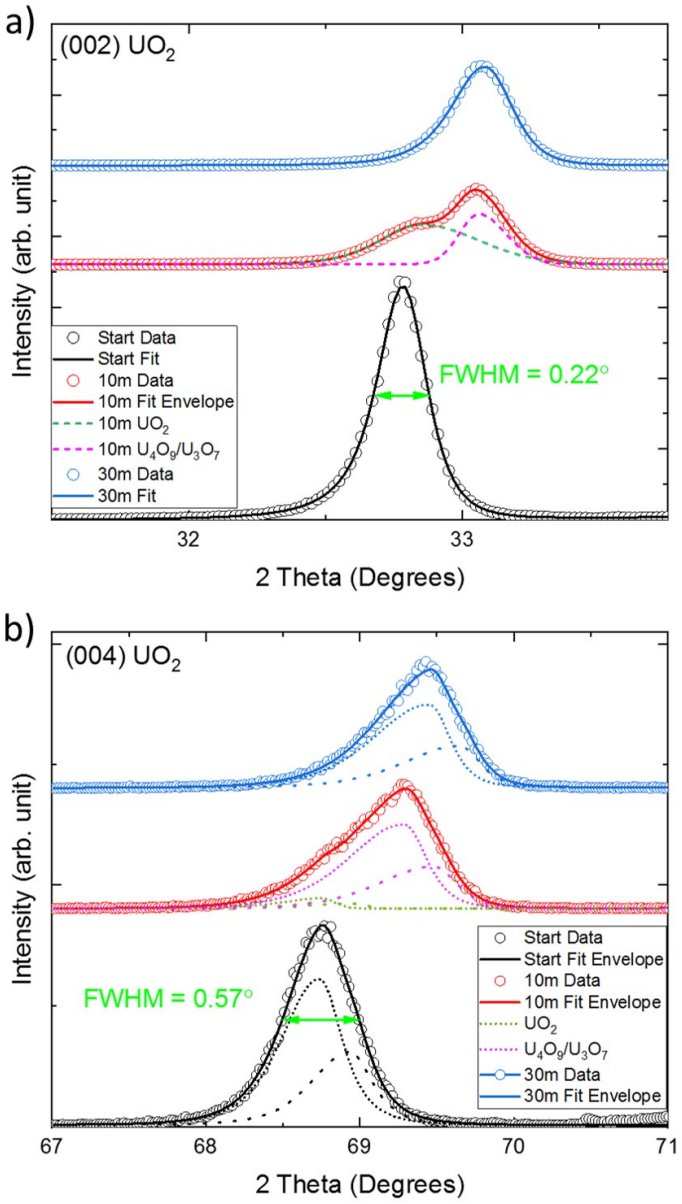

Figure 6.13: XRD patters of the sample SN1535 collected at 150°C. Data in black colour represents scans taken prior to oxidation. The red colour shows the pattern obtained after 10 minutes of exposure the sample to 200 mbar of oxygen, with contribution from UO_2 (green dash line) and U_4O_9/U_3O_7 (purple dash line). The fully oxidised sample to U_4O_9/U_3O_7 after 30 minutes is represented by blue colour. Data points are indicated as circles, while the line represent the fit model. Panel (a) shows data for (002) Bragg peak and panel (b) for the (004) Bragg peak. To fit the (004) peak two Cu wavelengths were taken into consideration K_{α_1} = 1.5406Å and K_{α_2} = 1.5444Å represented as short dot line and dot line respectively

is in consistent with the 0.7% reported in literature [70] for the first step of the oxidation from UO_2 to U_3O_8.

Until that point of transition from UO_2 to U_3O_8, the oxidation of (001) oriented UO_2 thin film follows what have been reported in literature, and described in Chapter 6, without any new insights. This also indicates that thin films can be used as surrogate material to study the bulk behaviour of nuclear fuel.

In the next step, the temperature of the chamber was raised up to 250°C, and after letting the temperature stabilise the sample was realigned and exposed to 200 mbar of oxygen. Scans were taken every hour, but no changes were observed under those conditions even after 16 hours, therefore, the temperature was increased again. The new temperature was set to be 300°C.

Once the experimental set-up reached and stabilised at 300°C, it was realigned to compensate the thermal expansion of the components. The 200 mbar of oxygen were introduced into the system, and a longitudinal $\omega - 2\theta$ was taken every hour. Data from the different time points for (002) and (004) Bragg peaks for cubic UO_{2+x}, together with (130) (260) reflections from orthorhombic U_3O_8 are presented on Fig. 6.14

The slits setting for the experiment were adjusted in the way that only signal from a material with good crystal structure, such as single crystals, will be visible. At the beginning of the oxidation process a small reflection associated with the (130) Bragg peak for U_3O_8 structure started appearing at around 26°, while there was not much change observed at the (002) reflection from the UO_{2+x} structure. Significant change to the structure of the sample occurs after around two days, when the decrease of the UO_{2+x} structure intensity is noticeable and the signal for the orthorhombic U_3O_8 becomes much stronger. The positions of diffraction peaks for both structures do not shift during the progressive transformation.

This experiment was conducted for 11 days, during which, the phase transition for uranium oxide from cubic to orthorhombic was observed. Although, the process took a long time, afterwards a small contribution from the (002) Bragg peak associated with the UO_{2+x} was observed. This can be attributed to the oxygen permeability at given conditions to reach the lower levels of the sample, or what is more likely to the stabilisation of the cubic UO_{2+x} due to the epitaxy from the YSZ substrate and migration of zirconium.

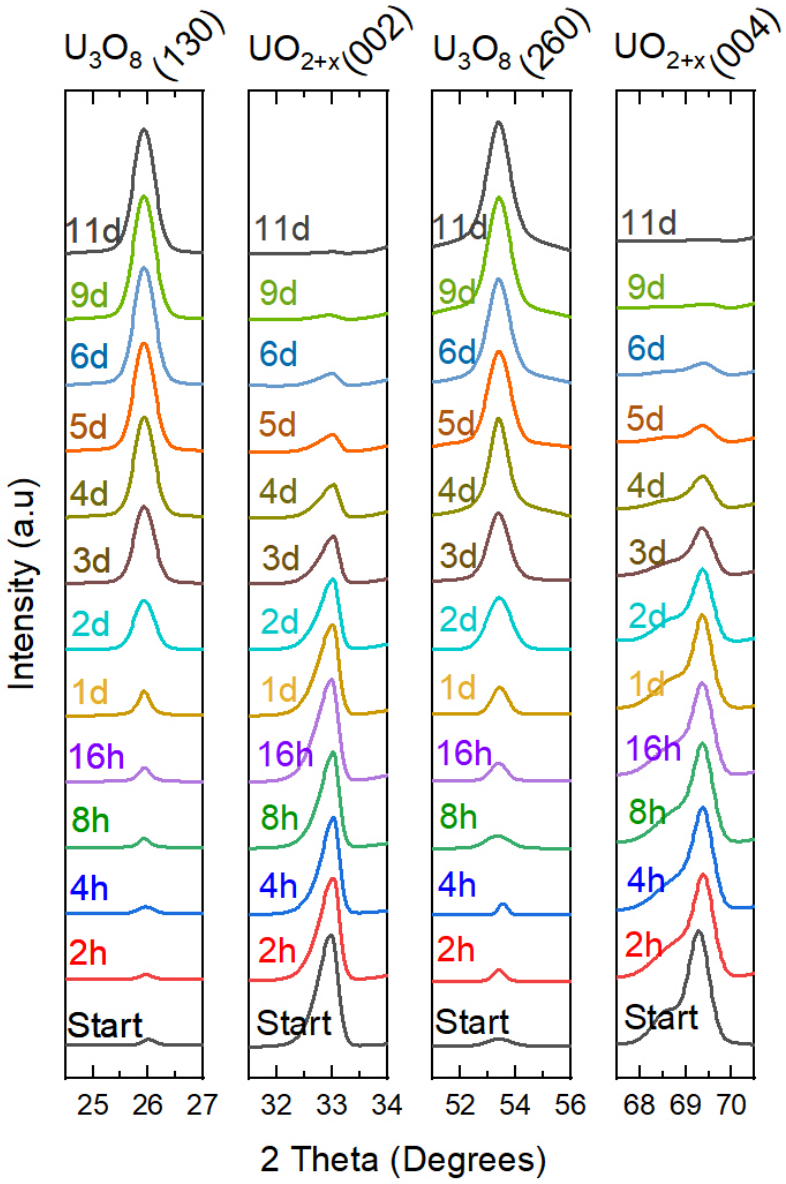

Figure 6.14: XRD in-situ oxidation of (SN1535) [001] UO_2 single crystal at 300°C at 200 mabr of oxygen. This graph focuses on four main areas where crystal planes associated with [001] single crystal hyperstoichiometric cubic structure of UO_2 and [130], [$\bar{1}$30] of orthorhombic U_3O_8 are observed. For clarity, not all the data are shown.

To find the kinetics of the oxidation process, the area of the Bragg peaks was used. The increase of the (002) UO_{2+x} and decrease of the (130) U_3O_8 peaks is indicative for the rate at

which single crystal of U_3O_8 is formed. From similar data to the one presented on Fig. 6.14, but for a 50 nm thick film of (001) UO_2 thin film, the peaks area was extracted using LIPRAS software. The area with associated error against time is shown on Fig. 6.15.

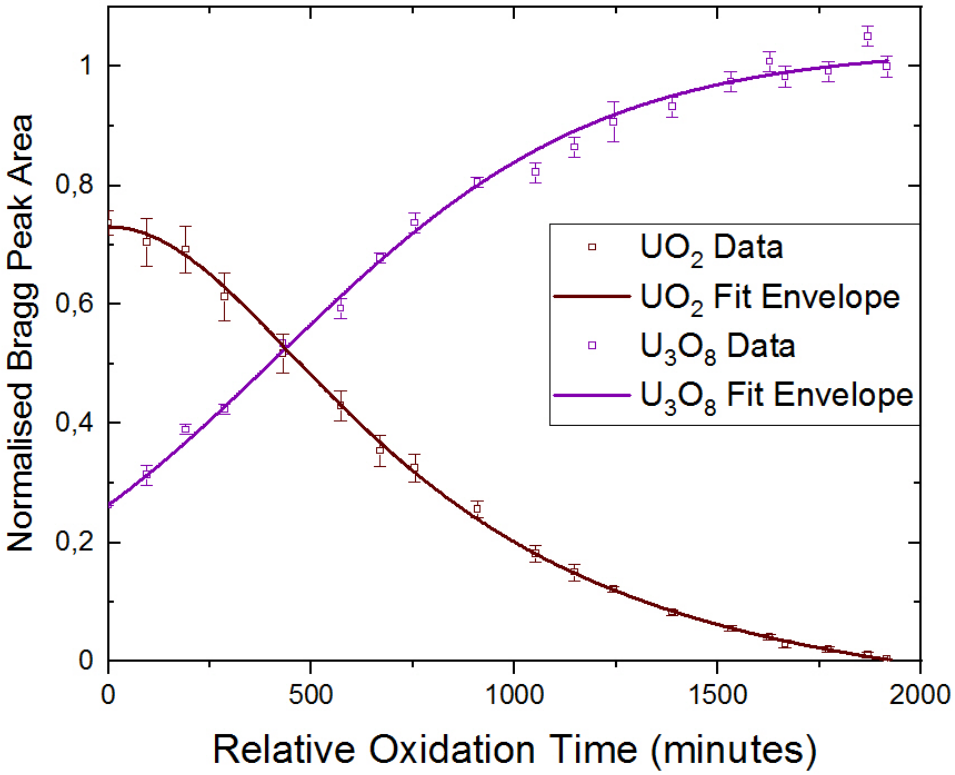

Figure 6.15: Normalised area of the Bragg peaks of UO_{2+x} (brown) and U_3O_8 (purple). Open squares represent the data with associated error bar, and straight line is fitting done using Logistic functions. Kinetics of changes in both oxides exhibit sigmoidal behaviour.

To model the sigmoidal behaviour of the data, the logistic function given by [226] was used:

$$f(x) = \frac{L}{1 + e^{-k(x - x_m)}} \tag{6.1}$$

where x_m is the midpoint, L is the curve's final value, and k is the logistic growth rate of the curve. This function was applied to increasing intensity from the U_3O_8 layer.

As formation of U_3O_8 is linked with decrease of UO_{2+x}, which is related to the area of those

peaks, proportion between them can be established. If the amount of U_3O_8 at a given time is expressed by percentage from 0% to 100%, then for sigmoidal growth given by Eq. 6.1 the amount of UO_{2+x} should decrease according to 100%-$\%_{U_3O_8}$. Therefore, the changes in the peak area of UO_{2+x} can be modelled using dose-response logistic relationship given by:

$$f(x) = L + \frac{L_0 - L}{1 + (\frac{x}{x_m})^p} \tag{6.2}$$

Where L_0 is the initial value.

The mechanism proposed by Aronson et. al. [41] for formation of U_3O_8 assumes nucleation-and-growth of U_3O_8 after initial formation of $UO_{2.34}$ with rate limited by diffusion of oxygen through the uranium dioxide lattice. This assumption is supported by two experimental facts. The presence of the induction periods or plateaus and the fact that the second step of the reaction begins before the first step is finished at higher temperatures. Therefore, if the the activation energy for growth is lower than for nucleation, the rate of nucleation increases more rapidly with increasing temperature than the rate of growth does. To model the rate of this conversion to orthorhombic U_3O_8, Aronson et. al. [41] suggest expressions proposed by Johnson and Mehl [227]:

$$\alpha = 1 - \exp(-\frac{\pi}{3} N_v G^3 t^4) \tag{6.3}$$

where α is the the fraction of the converted material, N_v is the rate of nucleation, G is the isotropic growth rate of $_3O_8$ nuclei and t is the time. The more general formation of U_3O_8 has also been described by Avrami-Erofeev equation [228–230]:

$$-\ln(1-\alpha) = kt^n \tag{6.4}$$

where n and k are empirically determined constants. Later, kinetics of the U_3O_8 formation revised and expanded by McEachern et al., using a two-dimensional model to describe simultaneous nucleation and growth processes on a sintered UO_2 disk:

$$\alpha(t) = \exp\left\{-\frac{\pi\kappa t^3}{3} + \frac{\pi^2\kappa^2 t^6}{180} - \frac{11\pi^3\kappa^3 t^9}{45360} + \frac{5\pi^4\kappa^4 t^1 2}{399168}\right\} \text{ where } \kappa = K_g^2 K_N \tag{6.5}$$

where K_g is the linear increase of the U_3O_8 circular islands and K_N is the nucleation rate. Those models for nucleation-and-growth mechanisms assume a constant rate of nucleation, where more sophisticated models including time-dependent nucleation, multistep nucleation or U_3O_8 grain-size limitation could describe the process in more detail [231]. Nucleation-and-growth are generally in good agreement with data collected for the oxidation of coarse powders and sintered pellets [31], but the sigmoidal reaction kinetics observed for oxidation of UO_2 microspheres did not fit this model [217].

Furthermore, parameters such as the surface roughness of polished UO_2 can influence the rate of U_3O_8 nucleation. A more general approach to describe kinetics was recently proposed by Rousseau et al [70]:

$$\frac{d\alpha}{dt} = \Phi(T, P_i)E(t) \tag{6.6}$$

where Φ is the growth rate per unit area and it is time independent but may be a function of temperature and thermodynamic chemical potential of the reacting gases P_i, and Ecorresponds to the reaction zone where the rate limiting step is located [70]. However, the thin films system used in this experiment is different to the pellet or powder samples and those equations might not be the most optimal to describe the kinetics of non-destructive oxidisation mechanism for (001) oriented single crystal of UO_2 to (130) single crystal of U_3O_8. Therefore, an alternative equation to describe the growth rate of U_3O_8 is proposed based on the logistic model with respect to time:

$$\frac{d\alpha}{dt} = \frac{df_{logictic}}{dt} = \frac{-kLe^{-k(t-t_m)}}{(1+e^{-k(t-t_m)})^2} \tag{6.7}$$

Consequently, the mechanism proposed for oxidation of (001) oriented single crystal of UO_2 exhibit sigmoidal kinetics, as well as (111) and (110) sample (Fig. 6.8), which is generally accepted for this process [70, 172, 197, 217–222]. The difference between some of the studies and models

presented in literature is the starting stoichiometry of the sample. Where the entire process of transformation from UO_2 to U_3O_8 is taken into consideration, the initial curve has slightly different kinetics as overlapping formation of U_3O_7/U_4O_9 and U_3O_8 is observed. In the case presented in this chapter, the first step of oxidation is finished, as shown on Fig. 6.13 where U_3O_7/U_4O_9 structure is formed with excess of oxygen. Therefore, kinetics are only associated with formation of (130) single crystal of U_3O_8, which provides more details about this step of oxidation.

The suspected mechanism for conversion of a single crystal UO_{2+x} to a single crystal of U_3O_8, is formation and growth of a layer U_3O_8 on top of UO_{2+x}. This can be verified by performing in-situ XRR scan while oxidising the sample. If the system is layered, signals associated with the interface between UO_{2+x} and U_3O_8 will be present, in addition to thin film/substrate and air/thin film interfaces.

The XRR results of (001) UO_2 thin film sample exposed to 200 mbar of oxygen at 330°C are shown on Fig. 6.16. Prior to that, the sample was first oxidise at lower temperatures (150-200 °C) to fully convert into U_3O_7/U_4O_9. Scans were taken approximately each 48 minutes. The first scan, for clarity was labelled as *0 minutes*, where in reality data was collected in between 0 to 48 minutes, therefore a small amount of U_3O_8 is already present. The data (open circles) have been also offset for clarity together with associated fit (solid lines).

The first information that can be extracted from Fig. 6.16 is change in the critical angle of the sample. The critical angle is the point on which and above total reflection of incident X-rays occurs, therefore provides information about the average electron density of the layer. The lower the electron density of a material, the lower the critical angle. At the beginning of the oxidation, critical angle is at what is associated mostly with UO_2. With time the critical angle shifts to the lower angle as the electron density of the sample decreases, and reaches minimum value which is associated with the electron density of U_3O_8.

The XRR data also provides information about the sample thickness. A general trend in decreasing the fringe separation is observed as a function of oxidation time. As discussed in Chapter 3, the fringe separation will decrease with thicker layers, what is observed in this case. The total thickness calculated of the starting point is 474 ± 7 Å consisting of 446 ± 6 Å UO_2

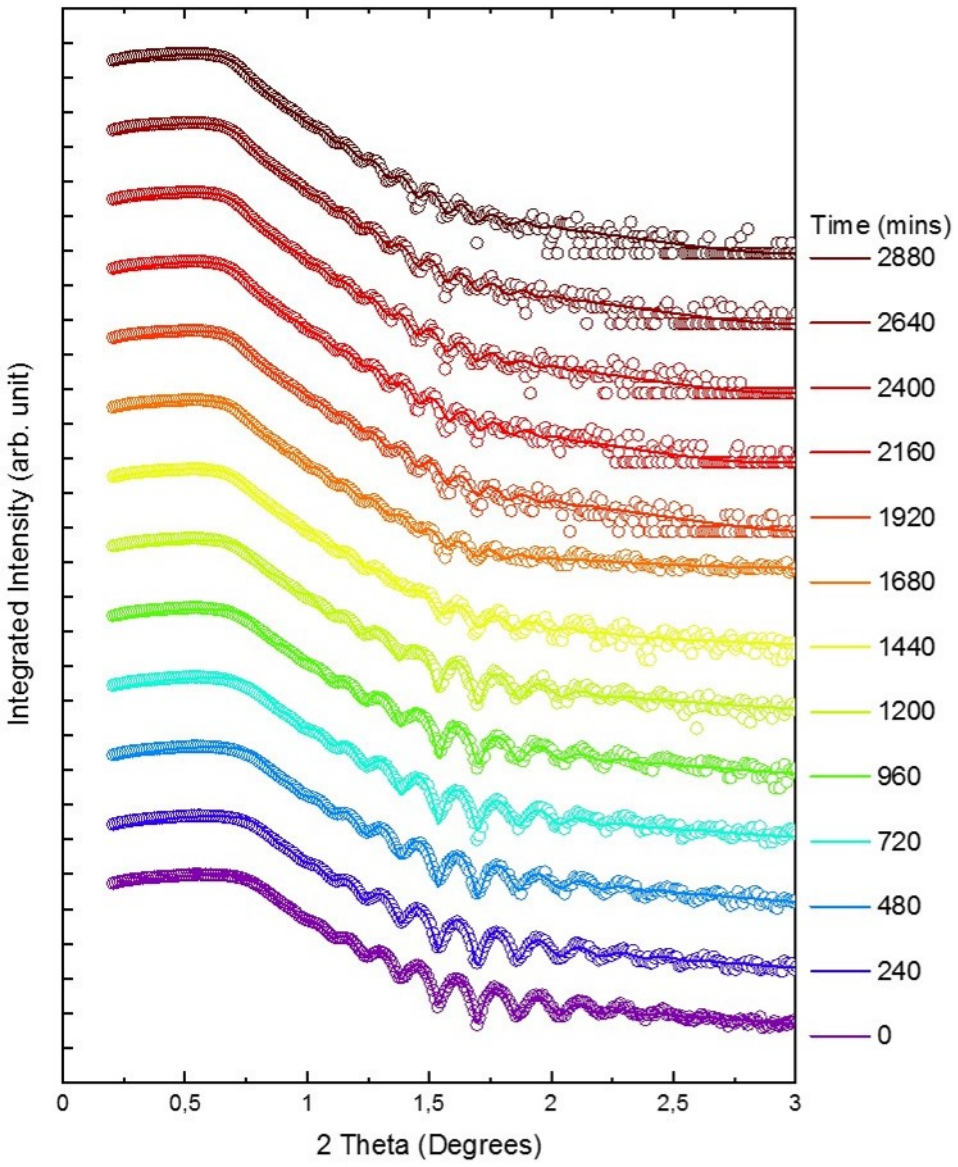

Figure 6.16: XRR measurements taken during in-situ oxidation of 50 nm thick (001) UO_2 single crystal (SN1627) at 330°C at 200 mabr of oxygen. Data is represented by open circles and modelled fit with straight line, colour indicates exposure time. Intensity offset between scans was applied for clarity and not all the data are shown.

and 28 ± 1 Å U_3O_8. Small changes to the thickness are observed until 1440 minutes where the sample composition is estimated to be 435 ± 6 Å UO_2 and 33 ± 1 Å U_3O_8. The scan taken after, at 1680 minutes of oxidation shows significant changes attributed to formation of U_3O_8 and associated volume expansion with this process. The parameters for the final points are 630 ± 1 Å

U_3O_8 and a very thin layer 9 ± 1 Å with electron density between UO_2 and YSZ.

As the oxidation of the UO_2 and phase transition to U_3O_8 proceeds, the total thickness of the film increases. This is attributed to the volume expansion associated with the phase transition from a cubic/tetragonal system of UO_2/U_4O_9/U_3O_7 to orthorhombic U_3O_8 [31]. Therefore, the thickness of the U_3O_8 layer, $D_{U_3O_8}$, and the total thickness of the film, D_{total} are a function of the thickness of the UO_2 layer:

$$D_{U_3O_8}(D_{UO_2}) = (D_0 - D_{UO_2})\alpha_{phase} \tag{6.8}$$

and:

$$D_{total}(D_{UO_2}) = D_{UO_2}(1 - \alpha_{phase}) + \alpha_{phase}D_0 \tag{6.9}$$

where the α_{phase} is volume expansion associated with phase transition.

Higher error in XRR data is present during in-situ oxidation scans. The first two factors come from the experimental set-up. The lack of a motor at the hot stage for alignment of the sample along χ axis, results in misalignment and loss of intensity. Furthermore, 5% to 10% of the x-ray beam intensity is absorbed on the kapton/aluminium foil windows used on the hot stage. Another factor is associated with scan set-up during in-situ experiment. Oxidation of uranium oxide sample is an ongoing process at high temperatures as with presence of oxygen the sample will oxidise and under vacuum conditions reduction of the sample will occur. Therefore, there is no possibility to stop this process to take a scan and a balance between scan resolution and time and probing period has to be made. Shorter scans allow to probe the state of the sample more often, but at cost of the resolution. Additionally, the status/structure/composition of the sample will be changing while the scan is performed resulting in additional error.

This sample was therefore analysed performing XRR measurements on the Open Eulerian Cradle stage before and after oxidation, and data is presented in Fig. 6.17. The displayed XRR for sample before oxidation (Fig. 6.17 (a)) was modelled using three layers: the YSZ substrate, a very thin layer of mix between YSZ and UO_2, and the main layer of the sample as UO_2. Each layer

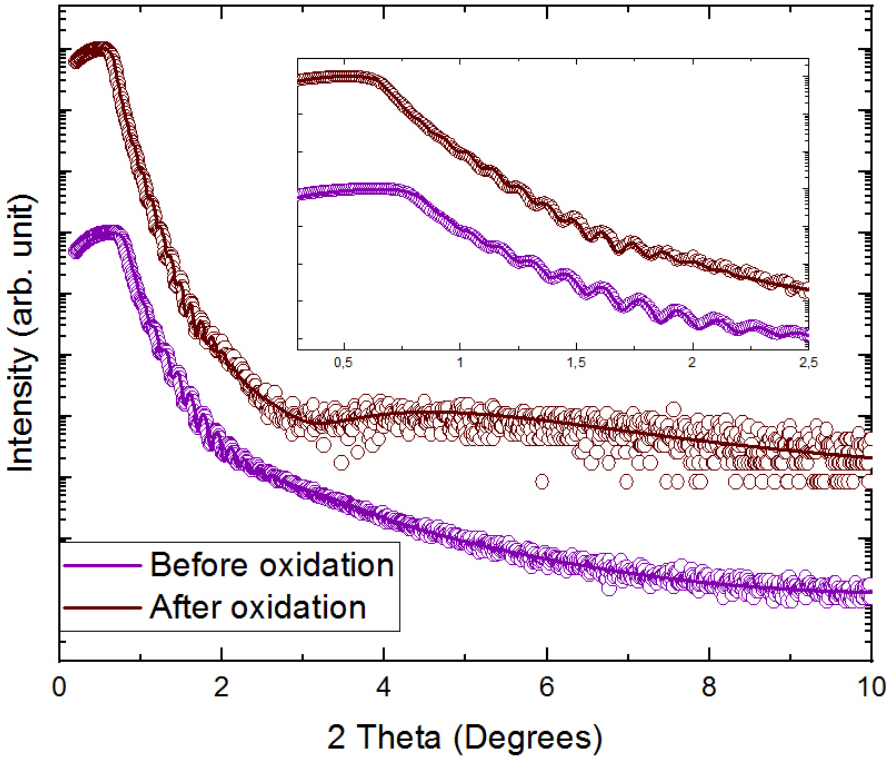

Figure 6.17: XRR measurements taken during using the Open Eulerian Cradle stage (a) before and (b) after oxidation. Data is represented by open circle and fit with straight line. Sample after oxidation is thicker by 36.4% and exhibit three beating frequencies associated with formation of three layers of different electron density.

was defined by the material density (r_{YSZ}, r_{mix}, r_{UO2}) given in atoms per Å^2, the layer thickness (t_{YSZ}, t_{mix}, t_{UO2}) in Å, and the average roughness of each interface (s_{YSZ}, s_{mix}, s_{UO2}) in Å. The calculated density for substrate was 0.028 atoms per Å^2, the thickness was defined as infinity, and roughness was found to be 4.3 ± 0.8 Å. The density of the mixed layer was fitted to be slightly higher than the substrate but lower than UO_2, limiting the thickness to 10 Å, and roughness was found to be 2.3 ± 0.2Å. The main layer of the sample, UO_2 was fitted with density of 0.025 atoms per Å^2, the thickness was found to be 47.5 ± 0.3 nm.

The data collected after the in-situ oxidation experiment (Fig. 6.17 (b)), was modelled using four layers: the substrate, mixed layer, and two layers of U_3O_8 first with slightly higher density

than the second one. Substrate density was kept the same, and roughness was allowed to be fitted to accommodate for any material diffusion on the interface due to elevated temperature, and was found to be 5.8 ± 0.5Å. The mixed layer was allowed to be fitted, giving a density between substrate and UO_2, the thickenss was found to be 13 ± 1 Å and the fringe beating was marked with blue colour. The density of the first U_3O_8 was found to be 0.0057 atoms per $Å^2$ with a thickness of 62 ± 4 Å and roughness of 15 ± 4 Å. The top layer of U_3O_8 was found to be 553 ± 4 Å thick with density of 0.0053 atoms per $Å^2$ and roughness 22.2 ± 0.5 Å. In total the thickness of the sample was found to be 639.4 ± 5 Å, which results in volume increase in the vertical direction of 36.4% what is with very good agreement with the value of 36% reported in the literature [31].

Reduced electron density on the interface between the YSZ substrate and the bulk of the uranium oxide thin film can be caused by a few factors. Firstly, the migration of zirconium from the substrate to the thin film, zirconium with much less electrons than uranium would substitute uranium, decreasing the electron density. This exchange of atoms might occur during both, the deposition process when uranium atoms hit the heated substrate with high kinetic energy and high temperature of 500°C and above of the substrate increases the chance of implementation of uranium to the structure. Another factor allowing for the atoms migration on the interface is the high temperature used during the XRD in-situ experiment. The lower density of the electron can be caused also by grading and roughness of the interface itself. The observed decrease of the electron density in the area near the substrate is more likely to be resultant of all those effects.

Nevertheless, the collected XRR data during and after the in-situ oxidation clearly indicates the existence of a very thin layer, thinner than couple nanometres, between the substrate and the bulk of the thin film. The electron density of this layer is slightly higher than the SLD of the YSZ substrate, and at the same time lower than the SLD of the uranium dioxide. This suggests that the composition of this layer is a mix of ZrO_2 and UO_2. As the highest oxidation state of zirconium is +4, the incorporation of zirconia into position of UO_2 atoms at very limited range might stabilise this very thin layer from further oxidation. This explains why at the final scan (Fig. 6.17) performed with higher accuracy/precision, a very thin layer is still clearly visible.

Recent studies of oxygen defects in UO_{2+x} conducted by Spurgeon et. al. [76] using scanning transmission electron microscopy and electron energy loss spectroscopy suggest that excess

oxygen can be incorporated at far greater levels than previously thought while still maintaining the cubic structure. Furthermore, they showed that there is no evidence for a large scale transition from the fluorite structure. The sample oxidised in their experiment had the same orientation (001), as the sample with unique behaviour described in this chapter. The in-situ XRR data (Fig. 6.16, generally agrees with the work presented by Spurgeon et. al. [76], although there is no clear evidences for a formation of the fluorite structure closer to $UO_{2.67}$ at the area near the sample surface.

In addition to performing the specular and off-specular scan of the (001) oriented UO_2 sample before and after oxidation, a rocking curves scan was also conducted to investigate the mosaicity of the sample. The data collected prior to the oxidation experiment, on (002) UO_2 Bragg peak is shown on Fig. 6.18. To fit the profile (red) two functions were used, Gaussian (blue) for the narrow component and Pearson VII (green) for the broad part. The FWHM for the sharp part is 0.072 ± 0.002 and for the wide part is 1.52 ± 0.02 with $m = 3.94$.

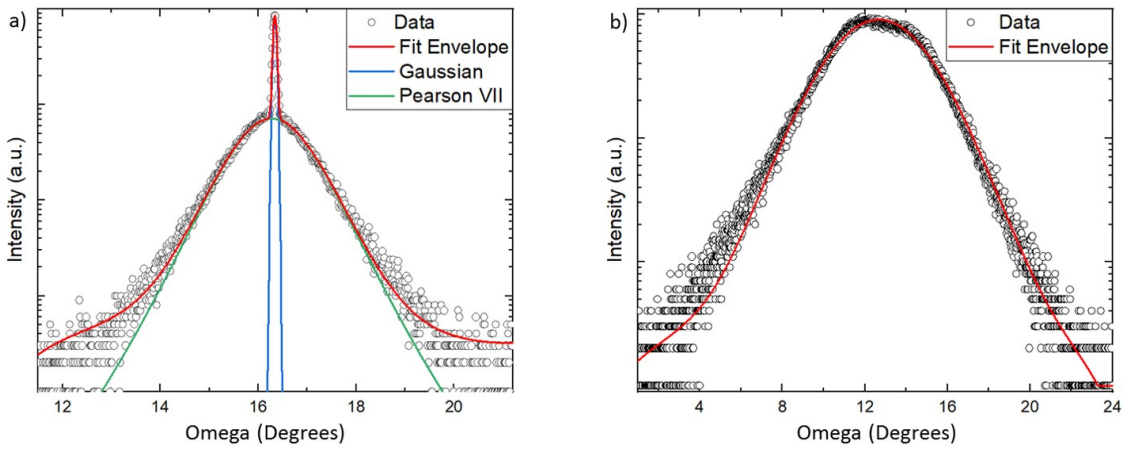

Figure 6.18: Rocking curve measurements taken for (a) the (002) Bragg peak of UO_2 before oxidation, and (b) scan of the (130) Bragg peak of U_3O_8 formed after oxidation of the sample. Significant broadening from (a) $1.52 \pm 0.02°$ to (b) $4.91 \pm 0.03°$ is observed. Data is represented by open circles and fit models by straight lines.

The rocking curve profile for the (130) Bragg peak of U_3O_8 after oxidation is shown at Fig. 6.18 (b). To fit this data a Pearson VII function was used, giving the FWHM of 4.91 ± 0.03 °. No sharp Gaussian component is observed which could suggest that there is not a good long range

arrangement of atoms. The very broad FWHM would also indicate a high mosaicity of the sample.

The change from a narrow FWHM observed for (002) UO_2 Bragg peak to very broad profile of the (130) U_3O_8 Bragg peak indicates a worse alignment of the crystallites. This might be connected with formation of large domains observed in HT-ESEM experiment (Fig. 6.7), and was further investigated by performing SEM scan of the sample surface before and after oxidation. The images of UO_2 taken before oxidation are shown on Fig. 6.19 (a) and (c).

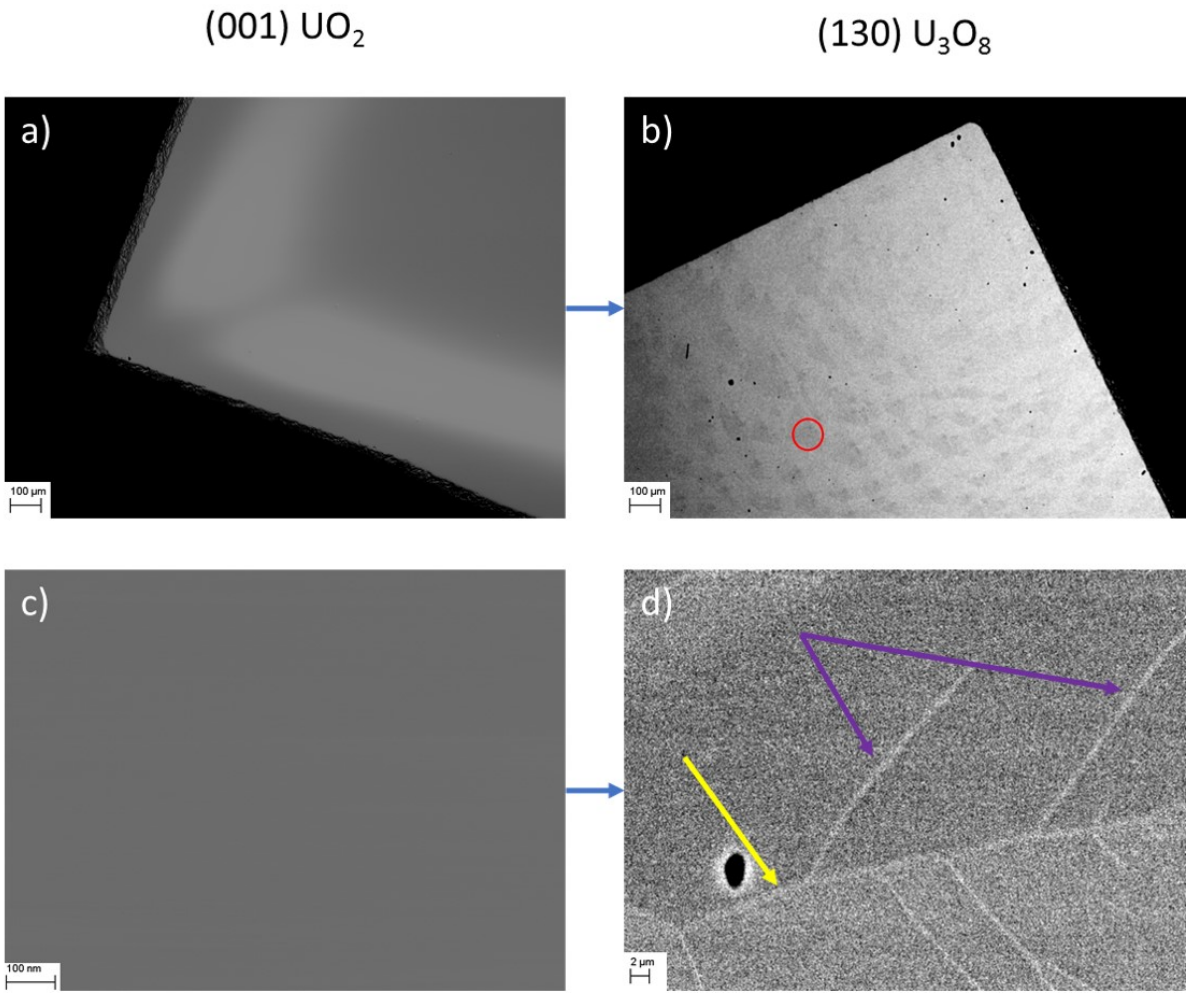

Figure 6.19: SEM images of 100 nm thick film of (001) oriented UO_2 (SN1535). Images (a) and (c) show the surface of the sample before oxidation, with different magnification. Very smooth surface is observed on both, what is with agreement with XRR data. Images on the right, (b) and (d), show sample after oxidation to single crystal of (130) U_3O_8. Contrast of both images was enhanced using Fiji software. Image (b) shows possibly domains of single crystal, what can be associated with broadening of the rocking curve. Boundaries are shown under higher magnification of image (d).

Before oxidation, the sample exhibited a uniform homogeneous and extremely flat surface, which can be seen at lower magnification on Fig. 6.19 (a) where also a bit of charging effect is present. To show the flatness of the sample better, image shown on Fig. 6.19 with 100 000x magnification was taken, showing extremely flat surface what finds in confirmation in XRR data, where roughness is lower than 5Å. The images taken after oxidation, of U_3O_8 are shown on Fig. 6.19 (b) and (d). Based on those images, it is suspected that domains are formed, with at least two types of defects.

As shown on Fig. 6.12, the (130) plane of U_3O_8 can be arranged on (001) plane of UO_2 in two different ways rotated by 90°with respect to each other. Because of that formation of areas/domains might be possible, which is probably observed on the Fig. 6.19 (b), where the domains might be visible as areas with different shades of grey. This would also explain the formation of shapes visible on the images taken during the in-situ HT-ESEM oxidation experiment (Fig. 6.7) where first one of the possible orientations is formed and expands until it meets the front of the other domains. This would be also in agreement with well known model of nucleation and growth of U_3O_8.

As a consequence of this model, two different boundaries within the U_3O_8 would be possible. The first type of boundary, shown with yellow colour on Fig. 6.20, would be formed between two domains where unit cells of U_3O_8 are rotated by 90°with respect to each other. The second type would be defect within the same domain, where unit cells are parallel to each other but shifted by a half of unit cell in longer axis, what is shown on Fig. 6.20 with purple colour. That could explain defects visible on Fig. 6.19 (d).

Generally, the presence of such domains and at least of those two types of defects in a single crystal structure would lead to a very broad profile of a rocking curve due to a high mosaic spread. Therefore, this would explain the huge broadening of the rocking curve after oxidation of UO_2 to U_3O_8 shown of Fig. 6.18

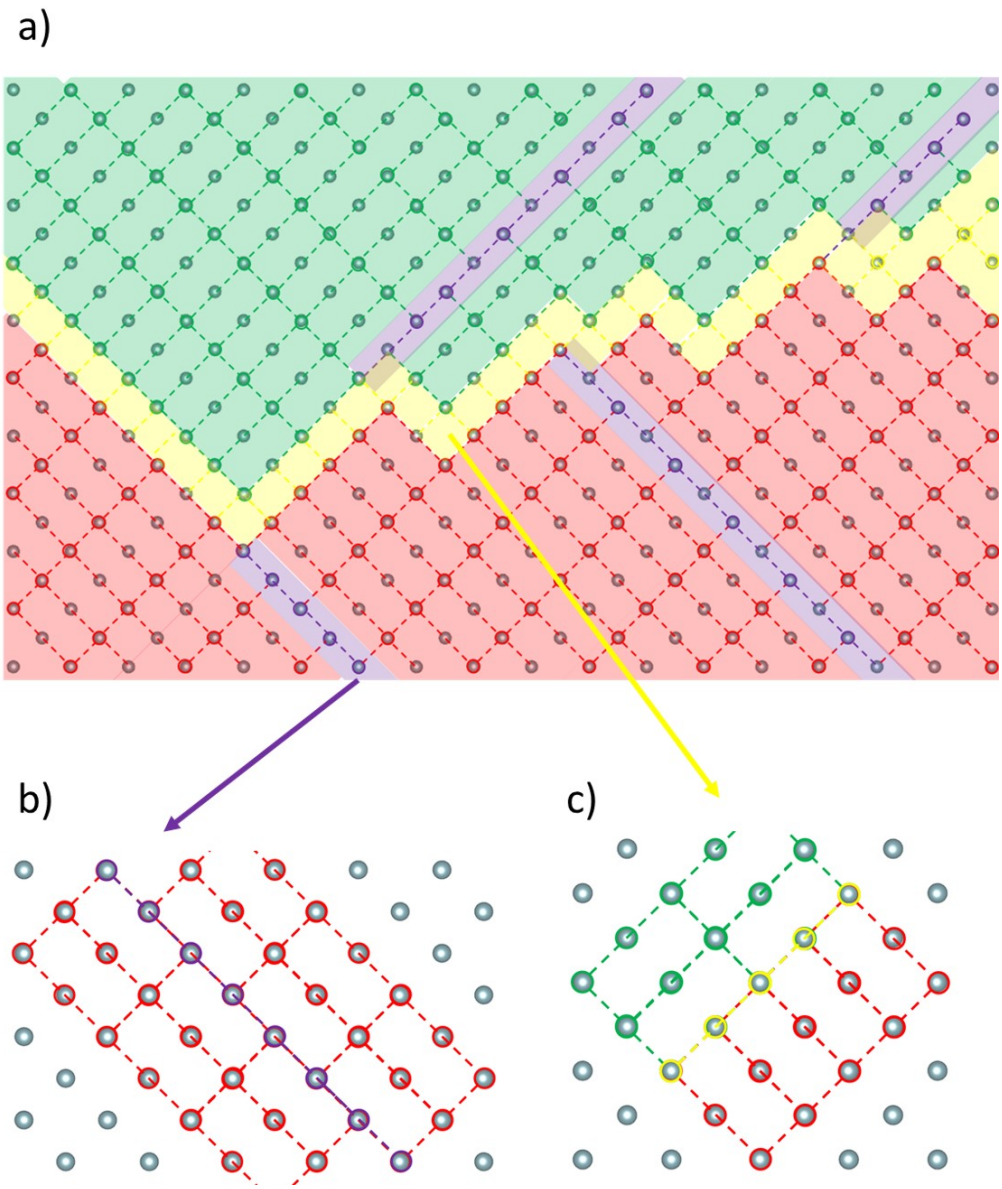

Figure 6.20: Atoms of the uranium are represented by the gray spheres. Blue dash line show the cubic structure of the UO_2 (001) phase. The red and greens lines represent possible arrangement of the (130) plane of U_3O_8 on top of UO_2. Panel (b) shows possible creation of the U_3O_8 on the surface structure of (001) UO_2.

6.4 Discussion

The orientation of uranium dioxide has significant influence on its oxidation mechanism, which has been shown by in-situ experiments using XRR, XRD and HT-ESEM. The oxidation of the (110) and (111) leads to the disintegration of the thin film structure, and formation of U_3O_8 flakes

as can be seen on Fig 6.3 and Fig 6.5. Although, the final effect of the sample exposure to high temperatures in atmosphere of oxygen leads to total film destruction in both cases, the dynamic of the process seems to be slightly different. Both orientations follow sigmoidal nucleation-and-growth kinetics for the formation of U_3O_8 reported in literature [70, 172, 197, 217–222], and volume expansion causing formation of the so called "popcorn" morphology [31]. The (111) oriented thin film of UO_2 exhibits more clearly a visible mechanism where the initial rate of oxidation is very low, called the "induction period", followed by a gradually increasing oxidation rate, named sometimes the linear region, and finally the curve tails off as the reaction is almost completed [31]. In the the (110) oriented sample those stages are less pronounced, and there is no clear distinction between the induction period and the linear region. The temperature at which the oxidation initiates is also different 568°C and 528°C for (111) and (110) respectively. The difference in temperatures could have also influenced the kinetics of the oxidation process.

The evidence that the formation rate of U_3O_8 is dependent on the crystallographic orientation of UO_2 was shown by Allen et al. [71, 72]. Single-crystal specimens with polished surfaces cut parallel to the [111], [110] or [100] faces, were studied in 1.3 mbar of oxygen at 300°using XPS, SEM and XRD. They found that the reactivity follows the sequence [111]>[110]>[100]>[polycrystalline], which is with good agreement to the data collected during HT-ESEM oxidation experiment for (111) and (110) single crystals. The rapid oxidation rate in the UO_2 [111] direction was explain by epitaxial match with the [001] direction of U_3O_8. They proposed that ordered interstitial oxygen clusters in the fluorite structure may be related to the $(UO_2)O_5$ pentagonal bipyramids in the layer orthorhombic U_3O_8 structure and that the changes in the oxygen lattice are the driving force for the formation of U_3O_8. This led them to conclusion that the rapid rate is due to the relative ease with which the lattice can expand in the direction normal to this surface. The slower rate for other directions and polycrystalline samples was assigned to lack of readily accommodation of lattice expansion. This theory does not match with the oxidation of (001) UO_2 single crystal to (130) U_3O_8, as this system also exhibits an epitaxial match.

A unique behaviour is observed for the (001) oriented sample of UO_2 thin film. During the in-situ HT-ESEM oxidation experiment, apart of the volume expansion, no cracking/disintegration of the sample was observed. The film transformed from a single crystal of (001) UO_2 to a nice

thin film of U_3O_8. After enhancing contrast, and using CLAHE processing it was possible to see domains of the U_3O_8, and their expansion until full phase transition of the sample.

The further investigation of oxidation mechanism for the (001) UO_2 system utilizing x-ray diffraction revealed growth of the (130) α-U_3O_8 single crystal phase. The off-specular taken after oxidation showed that this layered orthorhombic structure is 45°rotated to cubic UO_2/YSZ. Based on this relationship, it was calculated that the crystallographic b-axis of the U_3O_8 is oriented at 30.7° with respect to the cubic vertical axis. (ref to figure)

Due to similarities between the UO_2 structure and the YSZ structure, it is possible to grow epitaxial single crystal thin films. This could also suggest the relation between the (001) UO_2, could hold for the (001) YSZ. The confirmation of the theory that (130) single crystal of U_3O_8 is formed on (001) oriented single crystals of UO_2 can be found in both, the XRD and XRR data collected during in-situ oxidation experiments. The longitudinal $\omega - 2\theta$ scans taken during the oxidation of the sample show the coexistence of both structures at the same time. This scenario is only possible if there is an epitaxial relationship between structures, otherwise formation of polycrystalline material or loss of the material integrity would be observed. The x-ray reflectivity profile during the oxidation, shows presence and growth of U_3O_8 layer on top of UO_{2+x}.

The calculation conducted for UO_2 with lattice spacing of 5.47Å shows that the stress between the U_3O_8 and UO_2 on the shorter axis is 1.07 %, while on the longer axis its 7.26 %. That suggests this is more preferential than on the YSZ structure, where the associated stress would be 7.36 % and 13.93 respectively. Furthermore, when the cubic UO_2 structure absorbs oxygen forming U_4O_9/U_3O_7 shrinks, and if we take the values measured even at 150°C 5.41Å, the stress in between this layer and U_3O_8 is slightly higher 2.2 % and 8.46 %. Therefore, from the stress point of view, the preferential way of the U_3O_8 structure is on UO_2. The lowest stress would be obtained for the cubic structure with lattice spacing of 5.86Å , in which case the stress would be -5.65 % and 0.13 %, where minus indicates that the bottom layer is wider than the U_3O_8 shorter axis on (130) plane.

Once the oxidation of (001) UO_2 to (130) U_3O_8 is finished, a very thin layer that could be associated with the (002) peak form a cubic structure with lattices parameter close to UO_2 is still observed in the XRD scan. Furthermore, XRR scan performed after the oxidation shows presence

of an extremely thin layer with scattering length density lower than one expected from UO_2, and at the same time higher scattering length density than YSZ. This might suggest formation of a buffer layer in between the YSZ substrate and the (130) U_3O_8.

Formation of this buffer layer with reduced electron density when compared to UO_2, can occur during the sample growth process and during the oxidation experiment. Deposition process involves high temperatures at which the substrate is held and high kinetic energy of the sputtering material that hits the substrate. In this case uranium can be implemented into the YSZ structure and zirconium can migrate to UO_2. This might result in formation of a very thin layer of mixed ZrO_2/UO_2, with electron density between the values for pure layers. Migration of atoms at the interface might also occur during the oxidation process due to elevated temperatures. Presence of the zirconium atoms in UO_2 structure would not only reduce the electron density, but also can stabilise the cubic structure preventing oxidation of uranium dioxide to U_3O_8.

Formation of U_3O_7/U_4O_9 from UO_2 involves a slight volume reduction, which was associated with lattice parameter shrinking by 0.7%, and calculated from data presented in this chapter to be 0.67 ± 0.05%. This stage of the oxidation of UO_2 to U_3O_7/U_4O_9 is in very good agreement with literature [31, 41, 41, 45, 46, 70, 70, 73, 172, 187]. In the second stage, at elevated temperatures, the thickness of the sample increases with formation of the orthorhombic phase. This distinctly different crystal structure [232] has a density that is 23% less than that of UO_2 what leads to 36% net volume increase [233]. The thickness of the sample was investigated before and after the oxidation to U_3O_8, the calculated increase of the thickness from that data is 36.4% which is in very good agreement with the ratio of 1.36:1 between the crystallographic volumes per uranium atom in U_3O_8 and UO_2 [233].

The kinetics of the U_3O_8 formation were extracted by fitting (002) UO_2 Bragg peak area and (130) area of the Bragg peak for U_3O_8 against time. The difference between some of the data provided for oxidation kinetics in literature is the starting oxidation of the sample. Firstly, there is lack of overlapping formation of U_3O_7/U_4O_9 and U_3O_8, as commonly observed for UO_2 powders. In this case, thin film accommodated oxygen to form U_3O_7/U_4O_9 when exposed to 200 mbar of oxygen at 150°. Secondly, a thin layer of U_3O_8 is already presence during the initial scan. This results in missing the induction period where oxidation is very low, and showing only the

following linear behaviour ended with the curve tailing off at the end of the process, which is typical for the sigmoidal kinetics. The data was fitted using logistic growth curve. Combining the HT-ESEM data collected for (111) and (110) orientations with XRD data for (001) it can be seen that all three main orientations follow the sigmoidal nucleation-and-growth kinetics for the formation of U_3O_8.

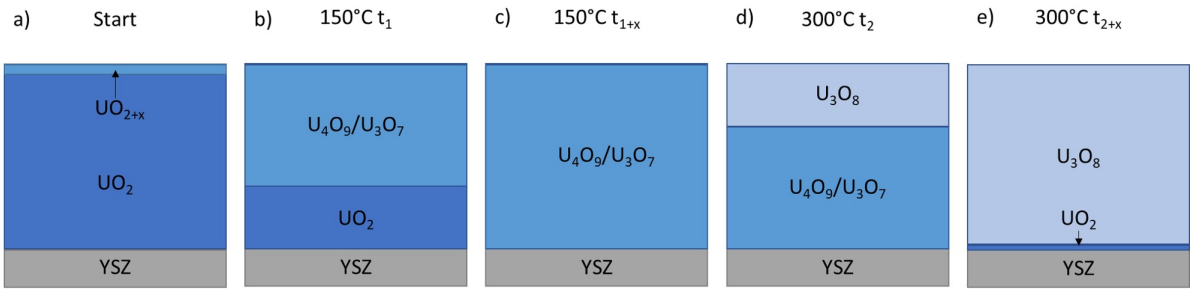

Figure 6.21: The schematic representation of the changes to the structure of a (001) thin film of uranium dioxide when exposed to oxygen at different temperatures

The schematic of the oxidation process from (001) oriented thin film of UO_2 to (130) oriented thin film of U_3O_8 is shown on Fig 6.21. At the starting point (a) most of the uranium dioxide is closed to stoichiometry. The surface of the sample can be slightly oxidized to form hyperstoichiometric UO_{2+x}, as the UO_2 oxidises slowly even at room temperature when exposed to air. In the next stage (generally at temperatures below 300°C) (b) when the sample is heated up to 150 °C and exposed to oxygen, formation of U_4O_9/U_3O_7 occurs. Two phases of uranium oxide can be observed for the time until the sample fully oxidised (c) to U_4O_9/U_3O_7. At this temperature, formation of higher oxides is impossible. To force oxidation further, to U_3O_8 an increase of temperature up to 300 °C is required. Again, two phases can be distinguished, associated with a cubic/tetragonal crystal system and orthorhombic structure, which coexists at the same time due to epitaxial relationship. At the end of the oxidation, a thin layer which is probably a mix of the zirconium and uranium dioxides remains between the YSZ substrate and the (130) U_3O_8 thin film, which suggested by the XRD and XRR data combined with stress calculations.

The oxidation process where (001) oriented single crystal of UO_2 undergoes phase transition into (130) oriented single crystal of U_3O_8, could be classified as a topotactic transition. In the topotactic reaction, the orientations of the product crystals are determined by the orientation

of the initial crystal [234]. This process of topotactic phase transitions has been reported for other oxides including cobaltites, ferrites and manganites [235–237]. In manganites usually stable perovskite structure can be topotactically transformed to a layered vacancy ordered brownmillerite structure.

The similarities between the mentioned materials exhibiting the topotactical transformation and reported here formation of (130) U_3O_8 from (001) UO_2, can be found is their structures. The perovskite structure has also cubic symmetry, therefore the mechanism for accommodation of oxygen might be similar. Both final structures Brownmillerite an orthorhombic U_3O_8 are layered structures. This might suggest that the mechanism for topotactical phase transition from cubic like structure to a layered structure might be common or similar for a variety of oxides following those criteria.

The preferential formation of (130) U_3O_8 structure can be found in work of Sont et al. [238]. They observed formation of columnar U_3O_8 grains while oxidizing the UO_2 pellets in air at 900°C. The layer of columnar grains showed a single U_3O_8 phase, where the intensity of the (001) reflection is anomalously diminished but those of the (130) and (260) reflections are enhanced. Authors attribute this effect to the accommodation of the transformation-induced strain in this preferred orientation not as shown here to the epitaxial relationship.

CHAPTER 7

CONCLUSIONS

Understanding the fundamental properties of nuclear fuel, such as the oxidation mechanism, is necessary for improvements to safety and economic efficiency. Uranium dioxide is the most commonly used nuclear fuel, and has been extensively studied utilising various techniques to probe its chemical, structural, and mechanical properties at different stages of the fuel cycle. Earlier research in this area was based on a real "bulk" fuel sample, where the complexity of the system lead to general conclusions based on many factors that could not be measured separately. More recent studies based on thin films showed promising results that, due to reduced complexity, are an excellent comparison to theoretical studies.

A thin film approach was used to study the oxidation of UO_2 to U_3O_8. In order to fabricate those samples, a reactive DC magnetron system was used. The construction of the UHV deposition system was described in Chapter 3. The new one-gun system offers standard deposition capabilities, with the possibility to mount a system for in-situ optical characterisation of the deposited material, such as Raman spectroscopy.

The (111), (110), and (001) oriented single crystal samples were grown on YSZ substrates, which have been previously reported to provide excellent epitaxial match. This approach was developed even further to produce, for the first time, poly-epitaxial thin films of columnar UO_2, with controlled grain size. The special substrate preparation technique, based on annealing of

the YSZ system in order to achieve the required grain size, was developed and is described in Chapter 3.

Samples grown on different substrates at various conditions, specified in Chapter 3, were characterised using x-ray reflectivity (XRR), x-ray diffraction (XRD), and electron backscatter diffraction (EBSD). X-ray reflectivity allowed to measure precisely the thickness of the thin films, which can be controlled with Angstrom precision, as well as interfacial roughness and electron density profiles for samples below 100 nm. The single crystal character of the sample was confirmed by XRD measurement, that not only allowed to identify the orientation, but also the quality of the crystal structure by performing rocking curve scan, and epitaxial matches by conducting off-specular measurements. It was found that the best quality structure with long range order is observed for (001) oriented single crystals of UO_2.

The XRD characterisation of the new poly-epitaxial system of UO_2 deposited on YSZ, revealed a polycrystalline system without preferred orientation. Due to size and nature of those samples, it was not possible to estimate the average grain size of UO_2 utilizing the Scherrer equation. This was performed using electron backscatter diffraction (EBSD), which showed excellent quality of the columnar grains, and demonstrated that those systems can be easily fabricated with grains ranging from 10 μm to 50 μm. In areas were long precise mapping of the surface was conducted, unwanted carbon deposition was observed using XPS mapping, and small damage from electron beam was also observed under SEM.

The poly-epitaxial UO_2 thin films were oxidised in-situ using hot stage mounted on x-ray diffractometer, and high temperature environmental scanning electron microscope. The first experiment conducted on 160 nm thin film showed that the oxidation process from UO_2 to U_3O_7/U_4O_9 is reversible just under elevated temperatures at high vacuum conditions. The most significant changes during both oxidation and reduction processes, were observed to (001) oriented grains. Also, it was not possible to oxidise the poly-epitaxial thin film further than U_3O_7/U_4O_9 at temperatures below 300°C. No cracking was observed at the sample surface at any point of this experiment.

The second XRD in-situ experiment performed on the sample at 300°C allowed for formation of U_3O_8. During this experiment a unique behaviour of UO_2 where lattice parameter does not

simply follow Vegard's law was observed. By investigating kinetics of this process it was found that (001) oriented grain oxidised to U_3O_8 faster than (111) and (110), which is contradictory to data presented in the literature. All the orientations followed the well-know sigmoidal nucleation and growth mechanism. The electron microscopy studies of the sample after oxidation to U_3O_8, showed a flaky structure. Those flakes were further investigated using TEM, and their polycrystalline U_3O_8 structure was confirmed.

The in-situ HT-ESEM oxidation of poly-epitaxial UO_2, showed that cracking of the structure associated with volume expansion during phase transition from fluorite structure to orthorhombic U_3O_8, exhibit sigmoidal kinetics . Further investigation involving grain orientation and boundaries showed that loss of the sample matrix integrity begins mostly at grain boundaries, and grain with orientation close to (001) are affected firstly.

Following the unique behaviour of the (001) oriented grains, single crystal systems were explored for better understanding in Chapter 6. Investigation of the oxidation mechanism under ESEM showed a small difference between the (111) and (110), which could originate from the sample starting conditions or oxidation temperature. Generally, oxidation kinetics with three distinguished regions are observed. The oxidation gradually increases from a slow initial rate in the induction period, to a maximum in the linear region, tailing off as the reaction approaches completion. The (001) oriented sample exhibited unique behaviour when oxidised to U_3O_8, no surface disintegration was observed, instead, formation and growth of pyramid-like shapes was observed.

The extraordinary mechanism for formation of U_3O_8 from (001)-oriented thin films of UO_2 was further investigated by in-situ XRD. Data indicated formation of (130)-oriented single crystal of α-U_3O_8, was confirmed also by performing off-specular scans. The epitaxial relation was found between the U_3O_8 and cubic structure of YSZ/($UO_{2+x)}$ as a 45°rotation. This indicates a topotactical phase transition from (001)-oriented single crystal UO_2 to (130)-oriented single crystal α-U_3O_8. This is the first time such a transition has been detected in the uranium oxide system.

Extracting the kinetics of the unique phase transition from SEM images was not possible, although nucleation and growth of U_3O_8 areas were observed. The in-situ XRD oxidation allowed

to demonstrate that the nucleation-and-growth mechanism is true. The process follows the sigmoidal kinetics observed for formation of U_3O_8.

The thickness of the initial UO_2 film and final U_3O_8 layer was accessed using x-ray reflectivity. Calculated XRR profiles showed increase of the thickness by 36.4%, which is in very good agreement with previously observed 36% of net volume increase for phase transition from cubic/tetragonal UO_{2+x} to layer orthorhombic U_3O_8.

The topotactical growth of (130) U_3O_8 has a lot of defects, these can be seen as domain boundaries under SEM. Formation of those boundaries was associated with existence of two identical ways, rotated 90°relatively to each other, that U_3O_8 can fit on UO_2. This also gives a significant rise to the broadening of the rocking curve between initial UO_2 and final U_3O_8 sample state.

Strain calculation and final XRR profile also indicates existence of buffer layer between the YSZ substrate and (130) oriented U_3O_8. This very thin buffer layer with electron density between UO_2 and YSZ could form during the deposition process, followed by additional migration of UO_2 to YSZ when samples were oxidised at high temperatures.

There are two important consequences of this work:

1. Fabrication of poly-epitaxial samples with engineered grains, allowing to reduce 3-dimensional problem to 2-dimensions. This is very useful for studying the influence of orientation and grain boundaries on water fuel interaction, thermal conductivity, fission products migration or radiation damage.

2. We have shown that the epitaxial relation between UO_2 and U_3O_8 proposed by Allen et al. is not valid, nor the oxidation rates for different crystal orientations. We report a new topotactic transition between (100)-UO_2 and (130)-U_3O_8, which has an implication on faster oxidation rate observed for (001)-oriented uranium dioxide, compared to other crystallographic orientations. This oxidation route shows the lowest energy mechanism for transforming from one oxide crystal to another with higher anion valence state; this is important for the U-O system, but could be applicable across a variety of other metal-oxides.

BIBLIOGRAPHY

[1] Enerdata.
Sluggish growth of world energy demand in 2011.
https://www.enerdata.net/about-us/press-release/sluggish-growth-world-energy-demand-in-2011.html.

[2] WorldOMeters.
World population.
http://www.worldometers.info/world-population/.

[3] Clara Franziska Heuberger and Niall Mac Dowell.
Real-world challenges with a rapid transition to 100% renewable power systems.
Joule, 2(3):367–370, 2018.

[4] European Commission.
2030 energy strategy.
https://ec.europa.eu/energy/en/topics/energy-strategy-and-energy-union/2030-energy-strategy.

[5] Nuclear Energy Institute.
Nuclear energy around the world.
https://www.nei.org/Knowledge-Center/Nuclear-Statistics/World-Statistics.

[6] Nuclear Energy Institute.
Nuclear units under construction worldwide.
https://www.nei.org/Knowledge-Center/Nuclear-Statistics/World-Statistics/Nuclear-Units-Under-Construction-Worldwide.

[7] Euronews.
Poland among europe's worst for smog.
http://www.euronews.com/2017/11/30/poland-among-europe-s-worst-for-smog.

[8] Columbia Electronic Encyclopedia (6th ed.).
Uranium.
Columbia University Press., 2000.

[9] World Nuclear Association.
Chemistry of conversion.
http://www.world-nuclear.org/information-library/nuclear-fuel-cycle/conversion-enrichment-and-fabrication/conversion-and-deconversion.aspx.

[10] United States Buclear Regulatory Commision.
Conventional uranium mills.
https://www.nrc.gov/materials/uranium-recovery/extraction-methods/conventional-mills.html.

[11] European Nuclear Society.
Yellow cake.
https://www.euronuclear.org/info/encyclopedia/y/yellow-cake.htm.

[12] D. M. Hausen.
Characterizing and classifying uranium yellow cakes: A background.
JOM, 50(12):45–47, Dec 1998.

[13] World Nuclear News.
Paducah enrichment plant to be closed.
http://www.world-nuclear.org/information-library/nuclear-fuel-cycle/conversion-enrichment-and-fabrication/uranium-enrichment.aspx.

[14] World Nuclear Association.
Uranium enrichment.

http://www.world-nuclear-news.org/ENF-Paducah-enrichment-plant-to-be-closed-2805132.html.

[15] U. Ehrfeld E.W Becker, P.Bley and W.Ehrfeld.
Separation nozzle: an aerodynamic device for large-scale enrichment of uranium-235.
Progress in Astronautics and Aeronautics, 51(15):3–16, 1977.

[16] David Albright, Frans Berkhout, and William Walker.
World inventory of plutonium and highly enriched uranium, 1992.
Oxford University Press, 1993.

[17] Chuan-Chou Shen, R Lawrence Edwards, Hai Cheng, Jeffrey A Dorale, Rebecca B Thomas, S Bradley Moran, Sarah E Weinstein, and Henrietta N Edmonds.
Uranium and thorium isotopic and concentration measurements by magnetic sector inductively coupled plasma mass spectrometry.
Chemical Geology, 185(3-4):165–178, 2002.

[18] Jack Boureston and Charles D Ferguson.
Laser enrichment: Separation anxiety.
Bulletin of the Atomic Scientists, 61(2):14–18, 2005.

[19] World Nuclear Association.
Nuclear fuel and its fabrication.
http://www.world-nuclear.org/information-library/nuclear-fuel-cycle/conversion-enrichment-and-fabrication/fuel-fabrication.aspxl.

[20] World Nuclear Association.
Radioactive waste management.
http://www.world-nuclear.org/information-library/nuclear-fuel-cycle/nuclear-wastes/radioactive-waste-management.aspx.

[21] Robert A Rich, Heinrich D Holland, and Ulrich Petersen.
Hydrothermal uranium deposits.
1977.

[22] Lionel Desgranges, Gianguido Baldinozzi, Gurvan Rousseau, Jean-Claude Niepce, and Gilbert Calvarin.
Neutron diffraction study of the in situ oxidation of UO_2.
Inorganic chemistry, 48(16):7585–7592, 2009.

[23] C Guéneau, A Chartier, and L Van Brutzel.
Thermodynamic and thermophysical properties of the actinide oxides.
2012.

[24] GC Allen and PM Tucker.
Surface oxidation of uranium metal as studied by x-ray photoelectron spectroscopy.
Journal of the Chemical Society, Dalton Transactions, (5):470–474, 1973.

[25] GC Allen, IR Trickle, and PM Tucker.
Surface characterization of uranium metal and uranium dioxide using x-ray photoelectron spectroscopy.
Philosophical Magazine B, 43(4):689–703, 1981.

[26] Judy WL Pang, William JL Buyers, Aleksandr Chernatynskiy, Mark D Lumsden, Bennett C Larson, and Simon R Phillpot.
Phonon lifetime investigation of anharmonicity and thermal conductivity of UO_2 by neutron scattering and theory.
Physical review letters, 110(15):157401, 2013.

[27] JG Tobin and S-W Yu.
Orbital specificity in the unoccupied states of UO_2 from resonant inverse photoelectron spectroscopy.
Physical review letters, 107(16):167406, 2011.

[28] S Carretta, P Santini, R Caciuffo, and G Amoretti.
Quadrupolar waves in uranium dioxide.
Physical review letters, 105(16):167201, 2010.

[29] CA Colmenares.

Oxidation mechanisms and catalytic properties of the actinides.

Progress in Solid State Chemistry, 15(4):257–364, 1984.

[30] Tommy Wadsten.

The oxidation of polycrystalline uranium dioxide in air at room temperature.

Journal of Nuclear Materials, 64(3):315, 1977.

[31] Rod Joseph McEachern and P Taylor.

A review of the oxidation of uranium dioxide at temperatures below 400°C.

Journal of Nuclear Materials, 254(2-3):87–121, 1998.

[32] Bella Belbeoch, JC Boivineau, and P Perio.

Changements de structure de l'oxyde U_4O_9.

Journal of Physics and Chemistry of Solids, 28(7):1267–1275, 1967.

[33] Naito Keiji.

Phase transitions of U_4O_9.

Journal of Nuclear Materials, 51(1):126–135, 1974.

[34] NORIO Masaki et al.

Analysis of the superstructure of U_4O_9 by neutron diffraction.

Acta Crystallographica Section B: Structural Crystallography and Crystal Chemistry, 28(3):785–791, 1972.

[35] Aurélien Soulié, Gianguido Baldinozzi, Frédérico Garrido, and Jean-Paul Crocombette.

Clusters of oxygen interstitials in UO_{2+x} and α-U_4O_9: Structure and arrangements.

Inorganic Chemistry, 58(19):12678–12688, 2019.

[36] RI Cooper and BTM Willis.

Refinement of the structure of β-U_4O_9.

Acta Crystallographica Section A: Foundations of Crystallography, 60(4):322–325, 2004.

[37] L Desgranges, G Baldinozzi, David Simeone, and HE Fischer.

Structural changes in the local environment of uranium atoms in the three phases of U_4O_9.
Inorganic Chemistry, 55(15):7485–7491, 2016.

[38] DK Smith, BE Scheetz, Ch AF Anderson, and KL Smith.
Phase relations in the uranium-oxygen-water system and its significance on the stability of nuclear waste forms.
Uranium, 1(1):79–111, 1982.

[39] L Nowicki, F Garrido, A Turos, and L Thomé.
Polytypic arrangements of cuboctahedral oxygen clusters in U_3O_7.
Journal of Physics and Chemistry of Solids, 61(11):1789–1804, 2000.

[40] PA Tempest, PM Tucker, and JW Tyler.
Oxidation of UO_2 fuel pellets in air at 503 and 543 k studied using x-ray photoelectron spectroscopy and x-ray diffraction.
Journal of Nuclear Materials, 151(3):269–274, 1988.

[41] S Aronson, RB Roof Jr, and J Belle.
Kinetic study of the oxidation of uranium dioxide.
The Journal of Chemical Physics, 27(1):137–144, 1957.

[42] KB Alberman and JS Anderson.
S 62. the oxides of uranium.
Journal of the Chemical Society (Resumed), pages S303–S311, 1949.

[43] H Hering and P Perio.
Equilibria of uranium oxides between UO_2 and U_3O_8.
Bull. soc. chim. France, 19:351–357, 1952.

[44] P Perio.
Oxidation of uranic oxide at low temperatures.
Bull. soc. chim. France, 20:256–263, 1953.

[45] HR Hoekstra, A Santoro, and S Siegel.

The low temperature oxidation of UO_2 and U_4O_9.

Journal of Inorganic and Nuclear Chemistry, 18:166–178, 1961.

[46] Edgar F Westrum Jr and F Grønvold.

Triuranium heptaoxides: Heat capacities and thermodynamic properties of α-and β-U_3O_7 from 5 to 350 k.

Journal of Physics and Chemistry of Solids, 23(1-2):39–53, 1962.

[47] Roderick J McEachern, Sham Sunder, Peter Taylor, Diane C Doern, Neil H Miller, and Donald D Wood.

The influence of nitrogen dioxide on the oxidation of UO_2 in air at temperatures below 275°C.

Journal of Nuclear Materials, 255(2-3):234–242, 1998.

[48] EU Kuz'micheva, LM Kovba, and EA Ippolitova.

Oxidation of uranium dioxide at temperatures below 270°C.

Radiokhimiya, pages 852–857, 1971.

[49] Peter Taylor, Elizabeth A Burgess, and Derrek G Owen.

An x-ray diffusion study of the formation of β-$UO_{2.33}$ on UO_2 pellet surfaces in air at 229 to 275°C.

88:153–160, 1980.

[50] LE Thomas, RE Einziger, and HC Buchanan.

Effect of fission products on air-oxidation of LWR spent fuel.

Journal of Nuclear Materials, 201:310–319, 1993.

[51] DA Andersson, Gianguido Baldinozzi, Lionel Desgranges, DR Conradson, and SD Conradson.

Density functional theory calculations of UO_2 oxidation: Evolution of UO_{2+x}, U_4O_{9-y}, U_3O_7, and U_3O_8.

Inorganic chemistry, 52(5):2769–2778, 2013.

[52] F Garrido, RM Ibberson, L Nowicki, and BTM Willis.
Cuboctahedral oxygen clusters in U_3O_7.
Journal of Nuclear Materials, 322(1):87–89, 2003.

[53] Gregory Leinders, Rene Bes, Kristina O Kvashnina, and Marc Verwerft.
Local structure in U (IV) and U (V) environments: The case of U_3O_7.
Inorganic chemistry, 59(7):4576–4587, 2020.

[54] Gregory Leinders, Remi Delville, Janne Pakarinen, Thomas Cardinaels, Koen Binnemans, and Marc Verwerft.
Assessment of the U_3O_7 crystal structure by x-ray and electron diffraction.
Inorganic chemistry, 55(19):9923–9936, 2016.

[55] BO Loopstra.
On the crystal structure of alpha-U_3O_8.
1977.

[56] KO Kvashnina, Sergei M Butorin, P Martin, and P Glatzel.
Chemical state of complex uranium oxides.
Physical review letters, 111(25):253002, 2013.

[57] Kaushik Sanyal, Ajay Khooha, Gangadhar Das, MK Tiwari, and NL Misra.
Direct determination of oxidation states of uranium in mixed-valent uranium oxides using total reflection x-ray fluorescence x-ray absorption near-edge spectroscopy.
Analytical chemistry, 89(1):871–876, 2017.

[58] Nicholas A Brincat, Stephen C Parker, Marco Molinari, Geoffrey C Allen, and Mark T Storr.
Ab initio investigation of the uo3 polymorphs: Structural properties and thermodynamic stability.
Inorganic chemistry, 53(23):12253–12264, 2014.

[59] Lucas E Sweet, Thomas A Blake, Charles H Henager, Shenyang Hu, Timothy J Johnson, David E Meier, Shane M Peper, and Jon M Schwantes.

Investigation of the polymorphs and hydrolysis of uranium trioxide.
Journal of Radioanalytical and Nuclear Chemistry, 296(1):105–110, 2013.

[60] Lucas E Sweet, Charles H Henager, Shenyang Y Hu, Timothy J Johnson, David E Meier, Shane M Peper, and Jon M Schwantes.
Investigation of uranium polymorphs.
Technical report, Pacific Northwest National Lab.(PNNL), Richland, WA (United States), 2011.

[61] Y Podkovyrina, I Pidchenko, T Prußmann, S Bahl, J Gottlicher, A Soldatov, and T Vitova.
Probing covalency in the UO_3 polymorphs by UM 4 edge HR-XANES.
In *J. Phys.: Conf. Ser*, volume 712, page 012092, 2016.

[62] KJ Schneider and SJ Mitchell.
Foreign experience on effects of extended dry storage on the integrity of spent nuclear fuel.
Technical report, Pacific Northwest Lab., 1992.

[63] KJ Schneider, SJ Mitchell, and AB Johnson Jr.
International status of dry storage of spent fuels.
Technical report, Pacific Northwest Lab., Richland, WA (United States), 1992.

[64] Peter Taylor, Donald D Wood, and A Michael Duclos.
The early stages of U_3O_8 formation on unirradiated UO_2 fuel oxidized in air at 200-300°C.
189:116–123, 1992.

[65] Silvio Rainho Teixeira and Kengo Imakuma.
High temperature x-ray diffraction study of the U_4O_9 formation on UO_2 sintered plates.
Journal of Nuclear Materials, 178(1):33–39, 1991.

[66] LE Thomas and RE Einziger.
Grain boundary oxidation of pressurized-water reactor spent fuel in air.
Materials characterization, 28(2):149–156, 1992.

[67] Kenneth M Wasywich, William H Hocking, David W Shoesmith, and Peter Taylor.

Differences in oxidation behavior of used CANDU fuel during prolonged storage in moisture-saturated air and dry air at 150°C.

Nuclear technology, 104(3):309–329, 1993.

[68] KK Bae, BG Kim, YW Lee, MS Yang, and HS Park.

Oxidation behavior of unirradiated UO_2 pellets.

Journal of Nuclear Materials, 209(3):274–279, 1994.

[69] MJ Bannister.

The storage behaviour of uranium dioxide powders.

Journal of Nuclear Materials, 26(2):174–184, 1968.

[70] G Rousseau, L Desgranges, F Charlot, N Millot, JC Niepce, M Pijolat, F Valdivieso, Gianguido Baldinozzi, and JF Bérar.

A detailed study of UO_2 to U_3O_8 oxidation phases and the associated rate-limiting steps.

Journal of Nuclear Materials, 355(1-3):10–20, 2006.

[71] GC Allen, PA Tempest, and JW Tyler.

The formation of U_3O_8 on crystalline UO_2.

Philosophical Magazine B, 54(2):L67–L71, 1986.

[72] Geoffrey C Allen, Paul A Tempest, and Jonathan W Tyler.

Oxidation of crystalline UO_2 studied using x-ray photoelectron spectroscopy and x-ray diffraction.

Journal of the Chemical Society, Faraday Transactions 1: Physical Chemistry in Condensed Phases, 83(3):925–935, 1987.

[73] Lionel Desgranges, Gianguido Baldinozzi, David Simeone, and HE Fischer.

Refinement of the α-U_4O_9 crystalline structure: New insight into the U_4O_9 -> U_3O_8 transformation.

Inorganic chemistry, 50(13):6146–6151, 2011.

[74] Lionel Desgranges, Hervé Palancher, M Gamaléri, Jean-Sébastien Micha, Virgil Optasanu, Laura Raceanu, Tony Montesin, and Nicolas Creton.

Influence of the U_3O_7 domain structure on cracking during the oxidation of UO_2.
Journal of Nuclear Materials, 402(2-3):167–172, 2010.

[75] Ludovic Quémard, Lionel Desgranges, Vincent Bouineau, Michèle Pijolat, Guido Baldinozzi, Nadine Millot, Jean-Claude Nièpce, and Arnaud Poulesquen.
On the origin of the sigmoid shape in the UO_2 oxidation weight gain curves.
Journal of the European Ceramic Society, 29(13):2791–2798, 2009.

[76] Steven R Spurgeon, Michel Sassi, Colin Ophus, Joanne E Stubbs, Eugene S Ilton, and Edgar C Buck.
Nanoscale oxygen defect gradients in UO_{2+x} surfaces.
Proceedings of the National Academy of Sciences, 116(35):17181–17186, 2019.

[77] R Springell, B Detlefs, GH Lander, RCC Ward, RA Cowley, N Ling, W Goetze, Rajeev Ahuja, Wei Luo, and Börje Johansson.
Elemental engineering: Epitaxial uranium thin films.
Physical Review B, 78(19):193403, 2008.

[78] Z Bao, R Springell, HC Walker, H Leiste, K Kuebel, R Prang, G Nisbet, S Langridge, RCC Ward, T Gouder, et al.
Antiferromagnetism in UO_2 thin epitaxial films.
Physical Review B, 88(13):134426, 2013.

[79] AM Adamska, E Lawrence Bright, J Sutcliffe, W Liu, OD Payton, L Picco, and TB Scott.
Characterisation of electrodeposited polycrystalline uranium dioxide thin films on nickel foil for industrial applications.
Thin solid films, 597:57–64, 2015.

[80] TT Meek, B Von Roedern, PG Clem, and RJ Hanrahan Jr.
Some optical properties of intrinsic and doped UO_2 thin films.
Materials Letters, 59(8-9):1085–1088, 2005.

[81] IO Usov, RM Dickerson, PO Dickerson, ME Hawley, DD Byler, and KJ McClellan.

Thin uranium dioxide films with embedded xenon.

Journal of Nuclear Materials, 437(1-3):1–5, 2013.

[82] Melissa M Strehle, Brent J Heuser, Mohamed S Elbakhshwan, Xiaochun Han, David J Gennardo, Harrison K Pappas, and Hyunsu Ju.

Characterization of single crystal uranium-oxide thin films grown via reactive-gas magnetron sputtering on yttria-stabilized zirconia and sapphire.

Thin Solid Films, 520(17):5616–5626, 2012.

[83] S Rennie, E Lawrence Bright, JE Sutcliffe, JE Darnbrough, R Burrows, J Rawle, C Nicklin, GH Lander, and R Springell.

The role of crystal orientation in the dissolution of UO_2 thin films.

Corrosion Science, 145:162–169, 2018.

[84] Ross Springell, Sophie Rennie, Leila Costelle, James Darnbrough, Camilla Stitt, Elizabeth Cocklin, Chris Lucas, Robert Burrows, Howard Sims, Didier Wermeille, et al.

Water corrosion of spent nuclear fuel: radiolysis driven dissolution at the UO_2/water interface.

Faraday Discussions, 180:301–311, 2015.

[85] Yury A Teterin, Aleksej J Popel, Konstantin I Maslakov, Anton Yu Teterin, Kirill E Ivanov, Stepan N Kalmykov, Ross Springell, Thomas B Scott, and Ian Farnan.

Xps study of ion irradiated and unirradiated UO_2 thin films.

Inorganic chemistry, 55(16):8059–8070, 2016.

[86] Konstantin I Maslakov, Yury A Teterin, Aleksej J Popel, Anton Yu Teterin, Kirill E Ivanov, Stepan N Kalmykov, Vladimir G Petrov, Ross Springell, Thomas B Scott, and Ian Farnan.

Xps study of the surface chemistry of UO_2 (111) single crystal film.

Applied Surface Science, 433:582–588, 2018.

[87] Aleksej J Popel, Vladimir G Petrov, Vasily A Lebedev, Jason Day, Stepan N Kalmykov, Ross Springell, Thomas B Scott, and Ian Farnan.

The effect of fission-energy xe ion irradiation on dissolution of UO_2 thin films.
Journal of Alloys and Compounds, 721:586–592, 2017.

[88] Otto Glasser.
Wilhelm conrad rontgen and the early history of the roentgen rays.
Norman Pub, 1993.

[89] J. G. Anderson.
William morgan and x-rays.
Transactions of the Faculty of Actuaries, 17:219,Äì221, 1945.

[90] Lawrence Berkeley National Laboratory The Center for X-Ray Optics.
http://www.cxro.lbl.gov/bl612/index.php?content=research.html.
http://www.cxro.lbl.gov/BL612/index.php?content=research.html.

[91] X ray applications.
X-ray applications.
https://en.wikipedia.org/wiki.

[92] WAYNE T. SPROULL.
X-rays in practice.
62:196, 1946.

[93] *X-rays and their interaction with matter*.
John Wiley and Sons, Ltd, 2011.

[94] A Level Physics HQ.
X ray production animation.
https://www.youtube.com/watch?v=IsaTx5-KLT8.

[95] Prof. Dr. Philippe Cattin.
Basics of x-ray. principles of medical imaging.
https://miac.unibas.ch/PMI/01-BasicsOfXray.html.

[96] Armel Le Bail, Ian Madsen, Lachlan M D Cranswick, Jeremy Karl Cockcroft, Poul Norby, A D Zuev, Andy Fitch, Juan Rodriguez-Carvajal, Carmelo Giacovazzo, Robert B Von Dreele, Paolo Scardi, Nicolae C Popa, Rudolf Allmann, Leonid A Solovyov, Bernd Hinrichsen, Ulrich Schwarz, Angela Altomare, Anna Moliterni, Rocco Caliandro, Rosanna Rizzi, Nicola V Y Scarlett, and Martin Jansen.

Powder Diffraction.

The Royal Society of Chemistry, 2008.

[97] ALBA.

Insertion devices.

https://www.albasynchrotron.es/en/accelerators/insertion-devices.

[98] Alex von Bohlen and Metin Tolan.

Editorial for synchrotron radiation.

J. Anal. At. Spectrom., 23:790–791, 2008.

[99] D. McLachlan.

X-ray crystal structure.

McGraw-Hill, 1957.

[100] William Henry Bragg and William Lawrence Bragg.

The reflection of x-rays by crystals.

Proceedings of the Royal Society of London. Series A, Containing Papers of a Mathematical and Physical Character, 88(605):428–438, 1913.

[101] John Katsaras and Jeremy Pencer.

Neutron and x-ray scattering from isotropic and aligned membranes.

09 2019.

[102] Janez Megusar.

Low temperature fast-neutron and gamma irradiation of kapton polyimide films.

Journal of Nuclear Materials, 245(2):185 – 190, 1997.

[103] JM Chivall.

Growth and characterisation of uranium nanostructures.

PhD thesis, UCL (University College London), 2012.

[104] Giovanni Esteves, Klarissa Ramos, Chris M Fancher, and Jacob L Jones.

Lipras: Line-profile analysis software.

Preprint at https://www. researchgate. net/publication/316985889_LIPRAS_Line-Profile_Analysis_Software, 2017.

[105] Vitalij Pecharsky and Peter Zavalij.

Fundamentals of powder diffraction and structural characterization of materials.

Springer Science & Business Media, 2008.

[106] John Elliott Daniels, JL Jones, and Trevor Roy Finlayson.

Characterization of domain structures from diffraction profiles in tetragonal ferroelastic ceramics.

Journal of Physics D: Applied Physics, 39(24):5294, 2006.

[107] Heinz Kiessig.

Interferenz von rontgenstrahlen an dunnen schichten.

Annalen der Physik, 402(7):769–788, 1931.

[108] Lyman G Parratt.

Surface studies of solids by total reflection of x-rays.

Physical review, 95(2):359, 1954.

[109] L Nevot and P Croce.

Characterization of surfaces by grazing x-ray reflection: Application to the study of the polishing of various silicate glasses.

Rev. Phys. Appl., 15:761–779, 1991.

[110] SK Sinha, EB Sirota, Garoff, S, and HB Stanley.

X-ray and neutron scattering from rough surfaces.

Physical Review B, 38(4):2297, 1988.

[111] Krassimir Stoev and Kenji Sakurai.

Recent theoretical models in grazing incidence x-ray reflectometry.

The Rigaku Journal, 14(2):22–37, 1997.

[112] RA Cowley.

Theory of the x-ray scattering from surfaces and interfaces.

In *Synchrotron Techniques in Interfacial Electrochemistry*, pages 67–84. Springer, 1994.

[113] Matts Björck and Gabriella Andersson.

Genx: an extensible x-ray reflectivity refinement program utilizing differential evolution.

Journal of Applied Crystallography, 40(6):1174–1178, 2007.

[114] HyperPhysics.

Order of filling of electron states.

http://hyperphysics.phy-astr.gsu.edu/hbase/pertab/perfill.html.

[115] Cynon.

X-ray photoelectron spectroscopy (XPS).

https://www.slideshare.net/cynon/xps-3529469.

[116] János Végh.

The shirley background revised.

Journal of electron spectroscopy and related phenomena, 151(3):159–164, 2006.

[117] Neal Fairley.

Peak fitting in XPS.

http://www.casaxps.com/help-manual/manual-updates/peak-fitting-in-xps.pdf.

[118] JJ Thomson MAFRS.

Xl. cathode rays.

Philosophical Magazine Series, 5(44):293–316, 1897.

[119] John R Haase and David B Go.

Analysis of thermionic and thermo-field emission in microscale gas discharges.

Journal of Physics D: Applied Physics, 49(5):055206, 2016.

[120] Alex Ilitchev.
How do you make an electron beam? electron source fundamentals.
https://www.thermofisher.com/blog/microscopy/.

[121] P.W. Hawkes.
Advances in Imaging and Electron Physics.
ISSN. Elsevier Science, 2007.

[122] J.I. Goldstein, D.E. Newbury, J.R. Michael, N.W.M. Ritchie, J.H.J. Scott, and D.C. Joy.
Scanning Electron Microscopy and X-Ray Microanalysis.
Springer New York, 2017.

[123] Ali S. Ali.
Application of Nanomaterials in Environmental Improvement.
03 2020.

[124] Thomas E Everhart and RFM Thornley.
Wide-band detector for micro-microampere low-energy electron currents.
Journal of scientific instruments, 37(7):246, 1960.

[125] Ray Fitzgerald, Klaus Keil, and Kurt FJ Heinrich.
Solid-state energy-dispersion spectrometer for electron-microprobe x-ray analysis.
Science, 159(3814):528–530, 1968.

[126] R. Podor, G.I. Nkou Bouala, J. Ravaux, J. Lautru, and N. Clavier.
Working with the ESEM at high temperature.
Materials Characterization, 151:15 – 26, 2019.

[127] K Wetzig, J Edelmann, W Fischer, and H Mueller.
LASEM-a novel combined device for laser modification in SEM.
Scanning, 9(3):99–107, 1987.

[128] Dirk M Kirch, Arndt Ziemons, Thomas Burlet, Ingo Lischewski, Xenia Molodova, Dmitri A Molodov, and Günter Gottstein.
Laser powered heating stage in a scanning electron microscope for microstructural investigations at elevated temperatures.
Review of Scientific Instruments, 79(4):043902, 2008.

[129] Andreas H Foitzik, Manfred W Füting, Georg Hillrichs, and Ludolf-Johannes Herbst.
In situ laser heating in an environmental scanning electron microscope.
Scanning, 19(2):119–124, 1997.

[130] Joseph W Brouillette and William E Leyshon.
Hot sub-stage for a scanning electron microscope, November 11 1975.
US Patent 3,919,558.

[131] D.B. Williams and C.B. Carter.
Transmission Electron Microscopy: A Textbook for Materials Science.
Number v. 1 in Cambridge library collection. Springer, 2009.

[132] BJ Inkson.
Scanning electron microscopy (SEM) and transmission electron microscopy (TEM) for materials characterization.
In *Materials characterization using nondestructive evaluation (NDE) methods*, pages 17–43. Elsevier, 2016.

[133] Mahmoud Z Ibrahim, Ahmed AD Sarhan, Farazila Yusuf, and M Hamdi.
Biomedical materials and techniques to improve the tribological, mechanical and biomedical properties of orthopedic implants–a review article.
Journal of Alloys and Compounds, 714:636–667, 2017.

[134] A. Ichimiya, P.I. Cohen, P.I. Cohen, and Cambridge University Press.
Reflection High-Energy Electron Diffraction.
Cambridge University Press, 2004.

[135] Yoshimi Horio, Yasuyuki Hashimoto, and Ayahiko Ichimiya.
A new type of RHEED apparatus equipped with an energy filter.
Applied Surface Science, 100:292–296, 1996.

[136] W. Braun.
Applied RHEED: Reflection High-Energy Electron Diffraction During Crystal Growth.
Springer Tracts in Modern Physics. Springer Berlin Heidelberg, 1999.

[137] J.F. O'Hanlon.
A User's Guide to Vacuum Technology.
Wiley, 2005.

[138] Vacuum Science World.
Vacuum physics - basic terms.
https://www.vacuumscienceworld.com/.

[139] Kkmurray.
Schematic of a turbomolecular vacuum pump.
https://commons.wikimedia.org/wiki/File:Turbo-pump-schematic-2011-05-02.gif.

[140] M Von Pirani.
Selbszeigendes vakuum-mefsinstrument.
Verhandlungen der Deutschen Physikalischen Gesellschaft, 1906:686–694, 1906.

[141] S. Borichevsky.
Understanding Modern Vacuum Technology.
CreateSpace Independent Publishing Platform, 2017.

[142] Scienta Omicron GmbH.
Spare parts catalogue systems.

[143] CORNING.
Machinable glass ceramic for industrial applications.

[144] GoodFellow.

Macor - machinable glass ceramic.

[145] JB Ainscough, BW Oldfield, and JO Ware.

Isothermal grain growth kinetics in sintered UO_2 pellets.

Journal of Nuclear Materials, 49(2):117–128, 1973.

[146] DW Shoesmith.

Fuel corrosion processes under waste disposal conditions.

Journal of Nuclear Materials, 282(1):1–31, 2000.

[147] John D Verhoeven.

Fundamentals of physical metallurgy.

New York : Wiley, 1975.

Text on lining papers.

[148] Rajiv Kohli and Kashmiri L Mittal.

Developments in Surface Contamination and Cleaning, Vol. 1: Fundamentals and Applied Aspects.

William Andrew, 2015.

[149] JB Durkee.

Developments in surface contamination and cleanning.

Willian Andrew, pages 759–872, 2008.

[150] Werner Kern.

Cleaning solution based on hydrogen peroxide for use in silicon semiconductor technology.

RCA review, 31:187–205, 1970.

[151] John R Vig.

Uv/ozone cleaning of surfaces.

Journal of Vacuum Science & Technology A: Vacuum, Surfaces, and Films, 3(3):1027–1034, 1985.

[152] S Baunack and A Zehe.
A study of uv/ozone cleaning procedure for silicon surfaces.
physica status solidi (a), 115(1):223–227, 1989.

[153] Kyunsuk Choi, Tae-Jong Eom, and Chongmu Lee.
Comparison of the removal efficiency for organic contaminants on silicon wafers stored in plastic boxes between UV/O3 and ECR oxygen plasma cleaning methods.
Thin Solid Films, 435(1-2):227–231, 2003.

[154] Gottlieb S Oehrlein, Gerald J Scilla, and Shwu-Jen Jeng.
Efficiency of oxygen plasma cleaning of reactive ion damaged silicon surfaces.
Applied physics letters, 52(11):907–909, 1988.

[155] VB Menon, LD Michaels, RP Donovan, and DS Ensor.
Effects of particulate size, composition, and medium on silicon-wafer cleaning.
Solid State Technology, 32(3):S7–S12, 1989.

[156] M. Ohring and Knovel (Firm).
Materials Science of Thin Films.
Elsevier Science, 2002.

[157] Brian Lewis and Joseph Chapman Anderson.
Nucleation and growth of thin films.
Academic Press, 1978.

[158] DG Schlom, JH Haeni, J Lettieri, CD Theis, W Tian, JC Jiang, and XQ Pan.
Oxide nano-engineering using mbe.
Materials Science and Engineering: B, 87(3):282–291, 2001.

[159] LW Martin, Y-H Chu, and RJMS Ramesh.
Advances in the growth and characterization of magnetic, ferroelectric, and multiferroic oxide thin films.
Materials Science and Engineering: R: Reports, 68(4-6):89–133, 2010.

[160] Peter Ehrhart.

Properties and interactions of atomic defects in metals and alloys.

PhD thesis, Verlag nicht ermittelbar, 1992.

[161] A Lavakumar.

Crystal imperfections.

In *Concepts in Physical Metallurgy*, 2053-2571, page 41 to 49. Morgan and Claypool Publishers, 2017.

[162] PW Tasker.

The stability of ionic crystal surfaces.

Journal of Physics C: Solid State Physics, 12(22):4977, 1979.

[163] Max Knoll.

Aufladepotentiel und sekundäremission elektronenbestrahlter körper.

Zeitschrift für technische Physik, 16:467–475, 1935.

[164] Manfred Von Ardenne.

Das elektronen-rastermikroskop.

Zeitschrift für Physik, 109(9-10):553–572, 1938.

[165] Stuart I Wright, Matthew M Nowell, and David P Field.

A review of strain analysis using electron backscatter diffraction.

Microscopy and microanalysis, 17(3):316–329, 2011.

[166] AJ Popel, Anna Maria Adamska, Peter George Martin, Oliver D Payton, GI Lampronti, Loren Picco, Liam Payne, Ross Springell, Thomas Bligh Scott, I Monnet, et al.

Structural effects in UO_2 thin films irradiated with U ions.

Nuclear Instruments and Methods in Physics Research Section B: Beam Interactions with Materials and Atoms, 386:8–15, 2016.

[167] Hongyu Sun, Gede WP Adhyaksa, and Erik C Garnett.

The application of electron backscatter diffraction on halide perovskite materials.

Advanced Energy Materials, 10(26):2000364, 2020.

[168] LEJ Roberts.

The oxides of uranium. Part V. The chemisorption of oxygen on UO_2 and on UO_2–ThO_2 solid solutions.

Journal of the Chemical Society (Resumed), pages 3332–3339, 1954.

[169] JS Anderson, LEJ Roberts, and EA Harper.

The oxides of uranium. part vii. the oxidation of uranium dioxide.

Journal of the Chemical Society (Resumed), pages 3946–3959, 1955.

[170] Todd K Campbell, Edgar Robert Gilbert, George D White, Gregory F Piepel, and Bernard J Wrona.

Oxidation behavior of nonirradiated UO_2.

Nuclear Technology, 85(2):160–171, 1989.

[171] RJ Guenther, ER Gilbert, SC Slate, JR Devine, DK Kreid, and WL Partain.

Ensuring safety in monitored retrievable storage.

Nuclear Engineering International, 29(363):36–40, 1984.

[172] DEY Walker.

The oxidation of uranium dioxides.

Journal of Applied Chemistry, 15(3):128–135, 1965.

[173] R Wang.

Spent fuel special studies progress report: Probable mechanisms for oxidation and dissolution of single-crystal UO_2 surfaces. pnl-3566.

Pacific Northwest Laboratory, Richland, WA, 1981.

[174] Rod J McEachern and Peter Taylor.

On the reported anisotropic rate of formation of U_4O_9 on UO_2.

Journal of Nuclear Materials, 217(3):322–324, 1994.

[175] Pablo Maldonado, JRA Godinho, LZ Evins, and Peter M Oppeneer.

Ab initio prediction of surface stability of fluorite materials and experimental verification.

The Journal of Physical Chemistry C, 117(13):6639–6650, 2013.

[176] José RA Godinho, Sandra Piazolo, and LZ Evins.
Effect of surface orientation on dissolution rates and topography of caf2.
Geochimica et Cosmochimica Acta, 86:392–403, 2012.

[177] Jose RA Godinho, Christine V Putnis, and Sandra Piazolo.
Direct observations of the dissolution of fluorite surfaces with different orientations.
Crystal growth & design, 14(1):69–77, 2014.

[178] Claire L Corkhill, Emmi MyllykylaÃà, Daniel J Bailey, Stephanie M Thornber, Jiahui Qi, Pablo Maldonado, Martin C Stennett, Andrea Hamilton, and Neil C Hyatt.
Contribution of energetically reactive surface features to the dissolution of ceo2 and tho2 analogues for spent nuclear fuel microstructures.
ACS applied materials & interfaces, 6(15):12279–12289, 2014.

[179] JM Elorrieta, LJ Bonales, N Rodríguez-Villagra, VG Baonza, and J Cobos.
A detailed raman and x-ray study of UO_{2+x} oxides and related structure transitions.
Physical Chemistry Chemical Physics, 18(40):28209–28216, 2016.

[180] Fredrik Grønvold.
High-temperature x-ray study of uranium oxides in the UO_2 - U_3O_8 region.
Journal of Inorganic and Nuclear Chemistry, 1(6):357–370, 1955.

[181] Lahmer Lynds, WA Young, JS Mohl, and GG Libowitz.
X-ray and density study of nonstoichiometry in uranium oxides.
ACS Publications, 1963.

[182] T Ishii, K Naito, and K Oshima.
X-ray study on a phase transition and a phase diagram in the U_4O_9 phase.
Solid State Communications, 8(9):677–683, 1970.

[183] T Matsui and K Naito.
Phase relation and defect structures of nonstoichiometric u $sub4$ o/sub 9+-y/and uo/sub 2+ x/at high temperatures.
Technical report, Nagoya Univ.(Japan). Faculty of Engineering, 1975.

[184] VA Alekseyev, LA Anan'yeva, and RP Rafal'skiy.
Effects of composition on lattice parameter of UO_{2+x}.
International Geology Review, 23(10):1229–1236, 1981.

[185] Peter Taylor, Elizabeth A Burgess, and Derrek G Owen.
An x-ray diffraction study of the formation of β-UO_2. 33 on UO_2 pellet surfaces in air at 229 to 275°C.
Journal of Nuclear Materials, 88(1):153–160, 1980.

[186] RE Einziger, LE Thomas, HC Buchanan, and RB Stout.
Oxidation of spent fuel in air at 175 to 195°C.
Journal of Nuclear Materials, 190:53–60, 1992.

[187] GC Allen and NR Holmes.
A mechanism for the UO_2 to α-U_3O_8 phase transformation.
Journal of Nuclear Materials, 223(3):231–237, 1995.

[188] Michèle Pijolat, Catherine Brun, Françoise Valdivieso, and Michel Soustelle.
Reduction of uranium oxide U_3O_8 to UO_2 by hydrogen.
Solid State Ionics, 101:931–935, 1997.

[189] H Chevrel, P Dehaudt, B Francois, and JF Baumard.
Influence of surface phenomena during sintering of overstoichiometric uranium dioxide UO_{2+x}.
Journal of Nuclear Materials, 189(2):175–182, 1992.

[190] C Brun, Françoise Valdivieso, Michèle Pijolat, and Michel Soustelle.
Reduction by hydrogen of U_3O_8 into UO_2: nucleation and growth, influence of hydration.
Physical Chemistry Chemical Physics, 1(3):471–477, 1999.

[191] Kun Woo Song, Keon Sik Kim, and Youn Ho Jung.
Densification behavior of U_3O_8 powder compacts by dilatometry.
Journal of Nuclear Materials, 279(2-3):356–359, 2000.

[192] Françoise Valdivieso, Michèle Pijolat, Michel Soustelle, and J Jourde.
Reduction of uranium oxide U_3O_8 into uranium dioxide UO_2 by ammonia.
Solid state ionics, 141:117–122, 2001.

[193] Jae Ho Yang, Young Woo Rhee, Ki Won Kang, Keon Sik Kim, Kun Woo Song, and Seung Jae Lee.
Formation of columnar and equiaxed grains by the reduction of U_3O_8 pellets to UO_{2+x}.
Journal of Nuclear Materials, 360(2):208–213, 2007.

[194] Jae Ho Yang, Ki Won Kang, Kun Woo Song, and Youn Ho Jung.
Reduction behavior of U_3O_8 in ar and co2 gas atmospheres.
In *Proceedings of the Korean Nuclear Society Conference*, pages 373–374. Korean Nuclear Society, 2005.

[195] Sang-Chae Jeon, Jae-Won Lee, Sang-Jun Kang, Ju-Ho Lee, Jung-Won Lee, Guen-Il Park, and In-Tae Kim.
Temperature dependences of the reduction kinetics and densification behavior of U_3O_8 pellets in ar atmosphere.
Ceramics International, 41(1):657–662, 2015.

[196] CF Miller, Ulrich Merten, and JT Porter.
Chemistry of uranium-oxygen systems. final report.
Technical report, General Atomic Div., General Dynamics Corp., San Diego, Calif., 1961.

[197] Todd K Campbell, Edgar Robert Gilbert, Cheryl Knox Thornhill, and Bernard J Wrona.
Oxidation behavior of spent UO_2 fuel.
Nuclear Technology, 84(2):182–195, 1989.

[198] G.H Bannister P Wood.
Workshop on chemical reactivity of oxide fuel and fission product release.
CEGB, 19(19):19, 1987.

[199] By Paul E Blackburn, Joseph Weissbart, and Earl A Gulbransen.

Oxidation of uranium dioxide.

357(10):902–908, 1956.

[200] G C Allen and N R Holmes.

A mechanism for the UO_2 to α-U_3O_8 phase transformation.

223:231–237, 1995.

[201] Jianliang Lin, Isaac Dahan, Billy Valderrama, and Michele V. Manuel.

Structure and properties of uranium oxide thin films deposited by pulsed dc magnetron sputtering.

Applied Surface Science, 301:475–480, 2014.

[202] P A Tempest, P M Tucker, and J W Tyler.

Oxidation of UO_2 fuel pellets in air at 503 and 543 k studied using x-ray photoelectron spectroscopy and x-ray diffraction.

151:251–268, 1988.

[203] Eugene S Ilton and Paul S Bagus.

XPS determination of uranium oxidation states.

Surface and Interface Analysis, 43(13):1549–1560, 2011.

[204] BW Veal, DJ Lam, H Diamond, and HR Hoekstra.

X-ray photoelectron-spectroscopy study of oxides of the transuranium elements Np, Pu, Am, Cm, Bk, and Cf.

Physical Review B, 15(6):2929, 1977.

[205] Hicham Idriss.

Surface reactions of uranium oxide powder, thin films and single crystals.

Surface Science Reports, 65(3):67–109, 2010.

[206] Eugene S Ilton, Yingge Du, Joanne E Stubbs, Peter J Eng, Anne M Chaka, John R Bargar, Connie J Nelin, and Paul S Bagus.

Quantifying small changes in uranium oxidation states using XPS of a shallow core level.

Physical Chemistry Chemical Physics, 19(45):30473–30480, 2017.

[207] R J Mceachern and P Taylor.
A review of the oxidation of uranium dioxide at temperatures below 400°C.
1998.

[208] Ludovic Quémard, Lionel Desgranges, Vincent Bouineau, Michèle Pijolat, Guido Baldinozzi, Nadine Millot, Jean-Claude Nièpce, and Arnaud Poulesquen.
On the origin of the sigmoid shape in the UO_2 oxidation weight gain curves.
Journal of the European Ceramic Society, 29(13):2791–2798, 2009.

[209] Lionel Desgranges, Gianguido Baldinozzi, Gurvan Rousseau, Jean-Claude Niepce, and Gilbert Calvarin.
Neutron diffraction study of the in situ oxidation of UO_2.
Inorganic chemistry, 48(16):7585–7592, 2009.

[210] G Rousseau, L Desgranges, F Charlot, N Millot, JC Niepce, M Pijolat, F Valdivieso, Gianguido Baldinozzi, and JF Bérar.
A detailed study of UO_2 to U_3O_8 oxidation phases and the associated rate-limiting steps.
Journal of Nuclear Materials, 355(1-3):10–20, 2006.

[211] JM Elorrieta, LJ Bonales, N Rodríguez-Villagra, VG Baonza, and J Cobos.
Physical Chemistry Chemical Physics, 18(40):28209–28216, 2016.

[212] A Poulesquen, L Desgranges, and C Ferry.
An improved model to evaluate the oxidation kinetics of uranium dioxide during dry storage.
Journal of Nuclear Materials, 362(2-3):402–410, 2007.

[213] Sanjaya D Senanayake, Kumudu Mudiyanselage, Anthony K Burrell, Jerzy T Sadowski, and Hicham Idriss.
Surface reactions of ethanol over UO_2 (100) thin film.
The Journal of Physical Chemistry C, 119(44):24895–24901, 2015.

[214] K Mudiyanselage, AK Burrell, SD Senanayake, and H Idriss.

XPS and NEXAFS study of the reactions of acetic acid and acetaldehyde over UO_2 (100) thin film.

Surface Science, 680:107–112, 2019.

[215] W Ralph Knowles and Thomas A Hardt.

High temperature specimen stage and detector for an environmental scanning electron microscope, February 15 2000.

US Patent 6,025,592.

[216] Caroline A Schneider, Wayne S Rasband, and Kevin W Eliceiri.

NIH Image to ImageJ: 25 years of image analysis.

Nature Methods, 9(7):671–675, 2012.

[217] K To Harrison, Co Padgett, and KT Scott.

The kinetics of the oxidation of irradiated uranium dioxide spheres in dry air.

Journal of Nuclear Materials, 23(2):121–138, 1967.

[218] KA Simpson and P Wood.

Uranium dioxide fuel oxidation in air below 350°C.

Technical report.

[219] Derek G Boase and Tjalle T Vandergraaf.

The canadian spent fuel storage canister: some materials aspects.

Nuclear Technology, 32(1):60–71, 1977.

[220] Gil-Sung You, Keon-Sik Kim, Duck-Kee Min, Seung-Gy Ro, and Eun-Ka Kim.

Oxidation behavior of UO_2 in air.

Nuclear Engineering and Technology, 27(1):67–73, 1995.

[221] Jinichi Nakamura, Takashi Otomo, and Satoru Kawasaki.

Oxidation of UO_2 under dry storage condition.

Journal of Nuclear Science and Technology, 30(2):181–184, 1993.

[222] JL Collins.

Chemical reactivity of oxide fuel and fission product release.

Technical report, Oak Ridge National Lab., TN (USA), 1987.

[223] Karel Zuiderveld.

Contrast limited adaptive histogram equalization.

In *Graphics gems IV*, pages 474–485. Academic Press Professional, Inc., 1994.

[224] Nicholas A Brincat, Stephen C Parker, Marco Molinari, Geoffrey C Allen, and Mark T Storr.

Density functional theory investigation of the layered uranium oxides U_3O_8 and U_2O_5.

Dalton Transactions, 44(6):2613–2622, 2015.

[225] R.J. Ackermann, A.T. Chang, and Charles A. Sorrell.

Thermal expansion and phase transformations of the U_3O_8-z phase in air.

Journal of Inorganic and Nuclear Chemistry, 39(1):75 – 85, 1977.

[226] Pierre-François Verhulst.

Resherches mathematiques sur la loi d'accroissement de la population.

Nouveaux memoires de l'academie royale des sciences, 18:1–41, 1845.

[227] WA Johnson and RF Mehl.

Reaction kinetics in processes of nucleation and growth.

American Institute of Mining, Metallurgical, and Petroleum Engineers, pages 1–27, 1939.

[228] M Avrami.

Close kinetics of phase change.

J. Chem. Phys, 7:1103–1112, 1939.

[229] BV Erofeyev.

Granulation, phase change, and microstructure kinetics of phase change.

J. Chem. Phys, 9:177, 1941.

[230] M Avrami.

Transformation-time relations for random distribution of nuclei kinetics of phase change, ii.

J. Chem. Phys, 8:212, 1940.

[231] GM Rosenblatt and NB Hannay.

Treatise on solid state chemistry.

In *Surfaces*, volume 6. Plenum New York, 1976.

[232] Bert Onno Loopstra.

Neutron diffraction investigation of U_3O_8.

Acta Crystallographica, 17(6):651–654, 1964.

[233] Peter Taylor, Donald D Wood, A Michael Duclos, and Derrek G Owen.

Formation of uranium trioxide hydrates on UO_2 fuel in air-steam mixtures near 200°C.

Journal of Nuclear Materials, 168(1-2):70–75, 1989.

[234] Ulrich Müller.

Symmetry relationships between crystal structures: applications of crystallographic group theory in crystal chemistry, volume 18.

OUP Oxford, 2013.

[235] Topotactic phase transformation of the brownmillerite $SrCoO_{2.5}$.

[236] Amit Khare, Dongwon Shin, Tae Sup Yoo, Minu Kim, Tae Dong Kang, Jaekwang Lee, Seulki Roh, In-Ho Jung, Jungseek Hwang, Sung Wng Kim, et al.

Topotactic metal–insulator transition in epitaxial srfeox thin films.

Advanced Materials, 29(37):1606566, 2017.

[237] Hyoungjeen Jeen, Woo Seok Choi, Michael D Biegalski, Chad M Folkman, I-Cheng Tung, Dillon D Fong, John W Freeland, Dongwon Shin, Hiromichi Ohta, Matthew F Chisholm, et al.

Reversible redox reactions in an epitaxially stabilized srcoo x oxygen sponge.

Nature materials, 12(11):1057–1063, 2013.

[238] Kun Woo Song and Myung Seung Yang.

Formation of columnar U_3O_8 grains on the oxidation of UO_2 pellets in air at 900°C.

Journal of Nuclear Materials, 209(3):270–273, 1994.